The Growth and Microstructural Characterization of ZnSe/GaAs Quantum Wells and Double Heterostructures

Jody Lee House

S.M.E.E., Massachusetts Institute of Technology 1994

Submitted to the Department of Electrical Engineering in partial fulfillment of the requirements for the degree of

Science Doctorate
[Doctor of Science]

at the

MASSACHUSETTS INSTITUTE OF TECHNOLOGY

February 1997
[February 1997]

Signature of Author:_____
Department of Electrical Engineering
September 12, 1997

Certified by:_____
Professor Leslie A. Kolodziejski
Esther & Harold Edgerton Associate Professor of Electrical Engineering
Thesis Supervisor

Approved by:_____
Professor Arthur C. Smith
Chair of the Committee on Graduate Students

The Growth and Microstructural Characterization of ZnSe/GaAs Quantum Wells and Double Heterostructures

by

Jody Lee House

Submitted to the Department of Electrical Engineering on 10 September, 1997 in partial fulfillment of the requirements for the degree of Science Doctorate

Abstract

Dielectric quantum wells composed of ZnSe barriers with a GaAs well have the potential to increase the excitonic binding energy in the GaAs to 25 meV. The fabrication of such a heterostructure has a potential application for high-speed (sub-picosecond switching times) optical switches for 1.3 μm light. The epitaxial growth and characterization of ZnSe/GaAs quantum wells and double heterostructures are investigated in this study. The double heterostructure is grown by molecular beam epitaxy. During fabrication, the material is characterized by reflection high energy electron diffraction. Ex situ, the ZnSe/GaAs double heterostructure is characterized optically via photoluminescence, microstructurally by a combination of electron microscopy and x-ray diffraction techniques, and compositionally by energy dispersive x-ray spectroscopy. Control structures composed of ZnSe/III-V materials and all III-V materials also contribute to an understanding of the complete ZnSe/GaAs double heterostructural properties.

Thesis supervisor: Leslie A. Kolodziejski
Title: Associate Professor of Electrical Engineering

TABLE OF CONTENTS

Index of figures

Index of tables

ACKNOWLEDGEMENTS

The work presented in this thesis was made possible by many people.

Undergraduate research at UMASS with Neal Anderson gave me the opportunity to come to MIT, and Leslie Kolodziejski gave me the opportunity to stay at MIT. Working and interacting with such very kind people as Gerry Power, Katie Hall, Rich Perilli, Christian Honeker and Angela Mickunas have made my time at MIT enjoyable and less daunting. Late night phone calls to my family, Stacy Pollard, Abby Reicken, David Greenberg, Barry Coleman, Deb Trivedi, Lousie and Fred Wing, and Jack Chang showed me that life is quite different outside MIT and that the time spent on the degree would alter my future experiences in a positive way. Lenore Rainey, David Bell. Mike Frongillo, and Tony Garrett-Reed provided me with the ability to learn about electron microscopy which has been one of my greatest MIT experiences. Jan Wright provided me with support and much needed thesis editing.

Babette Wils, Dana Meadows, and Jim Hines have provided me with the vision of what to do with myself for the near future...and the opportunity to pursue it. My experiences with the Dorchester Dolphins, Ted Loska, and Linda Loska have also helped me along in determining my future activities.

I would like to thank all of these people.

I would also like to thank my dissertation committee: Professor Linn Hobbs, Professor Erich Ippen, and Professor Leslie Kolodziejski for walking with me through the final stages of this degree. The final year of this research was possible due to the generous support of the people at Intel.

1. Introduction

Speed, size, and sensitivity are the measures of quality for communications electronics. Photonic devices composed of compound semiconductors have proven to be fast, small, and less susceptible to electromagnetic interference than electronic devices. However, the sensitivity of the compound semiconductor-based photonic devices varies with temperature. Photonic devices comprised of ZnSe/GaAs QWs holds promise for reducing the effects of temperature on device performance.

This study includes the analysis of ZnSe/III-V heterostructures, ZnSe/GaAs double heterostructures (DBHs), and all-III-V heterostructures. The final goal of the study was to understand the formation of the ZnSe/III-V heterointerface from a microstructural perspective. However, a complete investigation of the ZnSe/GaAs heterostructure involves four aspects besides microstructural analysis; epitaxial growth, optical and electrical characterization, composition analysis, and theoretical analyses. To some degree, all five aspects of the study of the ZnSe/GaAs system are present in this body of research. The combined results from each of these processes provide a better understanding of properties of the mixed II-VI/III-V heterostructure. Where relevant, the results from the collaborative efforts of David Dougherty will be presented [1].

For photonic devices that require quantum confinement, the temperature-related sensitivity is largely a function of the excitonic binding energy in the region of carrier confinement. In general, these photonic devices are composed of III-V compound semiconductors that have been extensively studied in order to optimize the excitonic binding energy in quantum confined layers. In 1989, Kumagai and Takagahara sought to push the limits of the excitonic binding energy in GaAs by proposing the fabrication of GaAs QWs with ZnSe barriers [2]. Such a ZnSe/GaAs QW heterostructure would have an increased excitonic binding energy of 25 meV as compared to the AlGaAs/GaAs QW heterostructure value of 15 meV for a 25 Å thick GaAs QW. This increase in the excitonic

binding energy yields room temperature carrier dynamics that have excitonic contributions. The increase in excitonic binding energy in the ZnSe/GaAs QW system is in part due to the large difference in the dielectric constant between the ZnSe (7.6) and GaAs (12.9). The smaller ZnSe dielectric constant has the advantage of confining an optical signal within the GaAs material.

The large excitonic binding energy is not the only interesting property of the ZnSe/GaAs QW system. There is a large difference between the band-gap energy of ZnSe (2.67 eV) and GaAs (1.43 eV). A heterostructure of a thin layer of GaAs (1 - 100 nm) surrounded by ZnSe "barriers" has a large potential well in the valence band for holes in the GaAs (~ 1eV, depending upon whose theory is invoked). The electrons are similarly confined, albeit with much smaller barriers (~ 200 meV). Such large potential barriers for the holes result in a number of possible confined energy states that the holes can have in the GaAs [2, 3]. When such a ZnSe/GaAs DBH is excited, either electrically or optically, the transitions of holes between these confined levels (intersubband transitions) in the valence band can be detected. Furthermore, by coupling several ZnSe/GaAs DBHs into a superlattice structure the density of hole intersubband transitions can be engineered to achieve a large signal at the optical communications wavelength of 1.3 μm (~0.8 eV).

The potential to achieve high-speed optical switching with devices comprised of ZnSe/GaAs QWs is the motivation for this thesis. The fabrication and optimization of the ZnSe/GaAs QWs, and the optical measurement of carrier confinement in the GaAs are the experimental challenges. The combination of the ability to manipulate a GaAs/ZnSe superlattice to achieve a significant population of holes traversing across inter-valence band states at the optical fiber communications wavelength of 1.3 μm, coupled with the large variation in the other optical properties of GaAs and ZnSe (including a variation in the index of refraction of ~1), make the mixed II-VI/III-V heterostructure a candidate for high-speed optical switching (switching times of < 1 picosecond). Further, ZnSe and GaAs have very similar lattice constants (0.25% lattice mismatch), which enables the materials to be grown epitaxially to form a heterostructure. However, the fabrication of ZnSe/GaAs

DBHs and QWs is complicated by the large difference in the optimal growth parameters for ZnSe and GaAs.

The individual bulk properties of both ZnSe and GaAs are well understood. However, a ZnSe/GaAs DBH cannot entirely be considered a stack of independent materials. At the interfaces between the ZnSe and the GaAs there is a complex interaction between the constituent species of each respective layer. For example, III-V heterostructures that employ layers of GaAs and AlGaAs have characteristics related to how abrupt the transition is between the two semiconductors [4, 5]. If the interfacial region is wide or rough, the resultant electronic and optical properties of the heterostructure are degraded. Essentially, the interfacial transition region has to be treated as another layer in the heterostructure.

In the ZnSe and GaAs case, the two materials are composed of elements with different valences, which affect the heterointerfacial properties. As one material is formed on top of the other, the bonding of the four different elements can have several orientations. Theoretically, an abrupt interface can be formed with interfacial layers of Ga, Zn, Se, and As; in this instance, an electronic imbalance results and an associated electric field creates a carrier-depleted region for stability. On the other hand, if a few transitional monolayers are formed, the heterostructure is no longer entirely ZnSe and GaAs, and the interfacial region contributes to the electronic and optical properties of the overall structure.

The fabrication of a ZnSe/GaAs QW is complicated by the difference in the optimal growth parameters between ZnSe and GaAs. In this study, the heterostructures are fabricated by molecular beam epitaxy (MBE). MBE is a proven method for obtaining high quality single crystal semiconductor heterostructures with monolayer control of the planar dimensions. Fabrication of ZnSe/GaAs QWs by MBE has the advantage of being able to control and monitor the heterointerface formation. However, the challenge remains in addressing the different growth parameters for the two materials while producing a heterostructure that is of high quailty both microstructurally and optically. This thesis

investigates the fabrication of the ZnSe/GaAs QW heterostructure by MBE, and evaluates the heterostructure by optical and microstructural characterization.

1.1 Overview of dissertation contents

A literature review on the fabrication and characterization of the heterostructure systems related to the ZnSe/GaAs QW is presented in Chapter Two. The fabrication and optimization of ZnSe/GaAs QWs, DBHs, and related all-III-V heterostructures are discussed in Chapter Three, followed by the optical characterization of these heterostructures by photoluminescence in Chapter Four. Chapter Five is a summary of the results from both the fabrication and optical characterization of the ZnSe/GaAs QWs and DBHs and proposes a set of explanatory hypotheses. A discussion of the two approaches taken to address each hypothesis is also given in Chapter Five as an introduction to the microstructural analysis presented in the second part of this thesis. Compositional analysis of the ZnSe/GaAs QWs and DBHs by energy dispersive x-ray spectroscopy is contained in Chapter Six. Long-range microstructural characterization by triple-axis x-ray diffraction measurements follows in Chapter Seven. The final set of experimental results, where the ZnSe/GaAs QWs and DBHs are examined by transmission electron microscopy are presented in Chapter Eight. The experimental results are synthesized in Chapter Nine, with the combined results discussed in relationship to the hypotheses presented in Chapter Five. Finally, recommendations for future work are made.

Two appendices have been added. Appendix 1 is a description of the transmission electron microscopy sample preparation procedure. Appendix 2 is a description of the surface preparation efforts for the ZnSe substrates.

2. Literature Review

The series of experimental techniques developed for this study of ZnSe/GaAs DBHs was based on current theoretical and experimental results in the field. To provide some background into the approach taken in this study of ZnSe/GaAs DBHs, the following sections discuss the research presented in the scientific literature on the material fabrication and some of the issues associated with semiconductor heterostructures.

2.1 Material Fabrication

The ZnSe/GaAs mixed heterostructures in this study are fabricated by molecular beam epitaxy (MBE). The details and optimization of the MBE growth process for each material and for the corresponding heterostructure have been studied in the literature. The different stages of growth are the nucleation of ZnSe on GaAs, the growth of ZnSe, the nucleation of GaAs on ZnSe, and the growth of GaAs. Each stage of growth is discussed below along with supporting relevant information.

2.1.1 Nucleation of ZnSe on GaAs

GaAs is a natural choice of substrate material for ZnSe-based devices, as it has a similar lattice constant to ZnSe, is inexpensive, and is consistently of high quality. Because the GaAs substrate has a clean and fairly defect-free oxidized surface, it can be directly loaded into the growth system. Upon thermal- or hydrogen-driven oxide removal, a GaAs buffer layer is grown on the substrate at a temperature close to 600°C. The buffer layer has been shown to improve the quality of the crystal structure of the subsequent semiconductor layers.

The above procedure is fairly well accepted within the II-VI and III-V semiconductor growth community. The controversy to be addressed is the method for the nucleation of the highest quality ZnSe on the GaAs layer. The arguments surround the proper starting III-V surface stoichiometry and the ZnSe nucleation sequence. The study of the nucleation

of ZnSe on III-V semiconductor materials, such as GaAs, is of interest because there are two instances of ZnSe nucleation on a III-V layer in the ZnSe/GaAs quantum well heterostructure. First, there is the growth of ZnSe upon the substrate buffer layer which can be InGaP, GaAs, or InGaAs, depending upon the experiment. The second ZnSe nucleation occurs on the GaAs QW layer surface. In both cases, the literature was studied in order to decide upon the best possible procedure for the nucleation and growth of ZnSe on GaAs.

At the onset of this study, the researchers of the epitaxial growth of compound semiconductors had realized the following:

- an As-terminated or As-rich GaAs surface was optimal for ZnSe nucleation [6-9];
- Ga diffuses into ZnSe at elevated temperatures [10];
- a Ga-rich GaAs surface leads to the formation of a Ga(As,Se) compound for a few monolayers at the onset of ZnSe nucleation [10, 11];
- from an interface state density perspective, a Ga-rich GaAs surface at the onset of ZnSe nucleation results in the lowest number of interface states [12, 13].

The formation of a potentially non-FCC type lattice (as would be the case for a Ga(As,Se) compound) for even a few monolayers at the ZnSe/GaAs heterointerface is undesirable for the successful growth of a GaAs QW with optical emission capability, because it complicates the expected confinement properties theoretically expected of a semiconductor quantum well. Also, the potential for Ga diffusion into the ZnSe layer would mandate that the ZnSe/GaAs QW would be modulation doped at the interfaces.

2.1.2 Nucleation of GaAs on ZnSe

The growth of GaAs on ZnSe is complicated by the large difference in the optimal growth temperature for GaAs (~ 600°C) and ZnSe (~ 300°C). A variety of approaches has been used to nucleate and grow GaAs on ZnSe, with the common approach being that the growth temperature of the substrate for the initial GaAs growth is reduced from that of the standard growth temperature. Unfortunately, when a semiconductor is not grown at

the optimal temperature, the possibility of impurity incorporation, defect and vacancy generation, and three-dimensional growth increases.

Several approaches to the growth of GaAs on ZnSe surfaces have been presented in the literature and were investigated in order to understand the range of growth parameters and the resultant GaAs properties. First, there has been an effort to grow GaAs "microcrystals" on the ZnSe surface [14, 15]. Second, ZnSe has been studied as a buffer layer between a GaAs layer and a Si substrate [16, 17]. Third, GaAs has special properties when grown at substrate temperatures at or below 250°C, and these characteristics have led to the study of low-temperature GaAs (LT-GaAs). Finally, there has also been a serious effort to grow high quality GaAs layers on ZnSe for ZnSe/GaAs/ZnSe single quantum wells (QWs). A survey of the results of each of these four efforts is given in the following sections.

2.1.2.1 Growth of GaAs microcrystals on ZnSe

The growth of GaAs microcrystals on ZnSe was motivated by the formation of low-dimensional structures for electron confinement [14, 15]. In work presented by Chikyow, *et al*, both a Zn- and a Se-rich surface were studied as the starting ZnSe surface stoichiometries for GaAs nucleation. The surface stoichiometry was determined using the reflection high-energy electron diffraction (RHEED) patterns, where a c(2x2) pattern is indicative of a Zn-rich surface and a (2x1) pattern corresponds to a Se-rich surface. In all cases [14, 15], roughly one monolayer of Ga was deposited on the ZnSe surface at a substrate temperature of 200°C. Arsenic was introduced into the growth chamber and allowed to incorporate the Ga atoms, resulting in GaAs molecules. Microcrystals (or pyramids) of GaAs formed as a result of these processes. The size and orientation of the GaAs crystal were a function of the ZnSe starting surface stoichiometry; smaller GaAs crystals formed on a Zn-stabilized surface.

2.1.2.2 ZnSe as a buffer layer between a GaAs layer and a Si substrate

Historically, there has been an interest in using compound semiconductor materials to integrate materials with optical emission capabilities with silicon-based technology. This ability would enable the integration of optoelectronic and photonic devices with VLSI technology. One approach to the integration of compound semiconductors and Si is the epitaxial growth of GaAs on Si. Unfortunately, the lattice mismatch between the two materials is large enough that only very thin layers of GaAs can be grown on Si before strain-relieving defects form in the GaAs. A conceivable solution to this issue has been studied by Romano, *et al* [17], and Bringans, *et al* [16], in the use of ZnSe as an interlayer between GaAs and Si. The ZnSe interlayer is more ionic than GaAs, and the generation of defects during lattice relaxation in the compound semiconductors is expected to be concentrated in the ZnSe layer.

Romano and Bringans took different approaches to the growth of GaAs on the ZnSe surface. In one case, standard MBE growth of GaAs was initiated on a Zn-stabilized surface at 200°C [17]. The growth temperature was ramped to 500°C during the course of 20 nm of GaAs growth. In the second case, GaAs was deposited at room temperature by solid phase epitaxy and then the substrate temperature was ramped to 500°C to anneal the GaAs [16]. Beginning the growth of GaAs on the ZnSe surface below 200°C has implications on the electronic quality of the GaAs. Also, if the GaAs is deposited at room temperature, the first 8 nm of the GaAs are polycrystalline. It is important to note, however, that the cross-sectional TEM analysis of these heterostructures does show evidence of high-quality GaAs away from the ZnSe/GaAs heterointerface. The nucleation of GaAs on ZnSe was successful, in that the GaAs was structurally of high-quality away from the heterointerface.

2.1.3 ZnSe/GaAs/ZnSe Quantum Wells

Along with specific studies of the formation of the ZnSe/GaAs and the GaAs/ZnSe interface, there has been prior work on the growth and characterization of ZnSe/GaAs QWs. Two separate efforts by researchers in Japan have been made to form high quality

GaAs QWs with ZnSe barriers. In one case, the entire heterostructure was grown by a combination of migration enhanced epitaxy (MEE) and solid phase epitaxy (SPE) in a single MBE chamber [18-22]. In the other case, the growth was completed by metal-organic vapor phase epitaxy (MOVPE) at atmospheric pressure in a single growth reactor [23-25]. The MOVPE-grown ZnSe/GaAs QWs were grown by raising the ZnSe growth temperature to between 450°C and 550°C. The GaAs "well" material was grown at the same temperature as the ZnSe.

These heterostructures were investigated by cross-sectional TEM, x-ray diffraction, Auger spectroscopy, Nomarski phase-contrast microscopy, and photoluminescence. The microstructural results demonstrate that the growth procedure results in heterostructures of fairly high crystal quality. This is demonstrated by intense and well-defined satellite peaks in the x-ray diffraction rocking curve [24, 25]. The cross-sectional TEM also shows a defect free region of the heterostructure [23-25]. In one instance, Fujita, *et al,* present photoluminescence data that they attribute to an optical signal from 100 nm of GaAs grown between 300 nm Zn(S)Se barriers, as a function of annealing temperature. Unfortunately, the accurate identification of the source of the optical signal from this heterostructure is complicated because its energy range and intensity are both similar to that of a defect-band often seen in ZnSe-based material that has a sufficiently high impurity level. Given the growth conditions of this study, it is possible that such an impurity level did exist in the ZnSe layers.

In another study of ZnSe/GaAs QWs, the heterostructures were grown by MEE. In MEE, the substrate is exposed alternately to the equivalent of one full monolayer of coverage of each constituent source. For example, GaAs is grown by opening the Ga shutter for an amount of time that has been determined to provide a full monolayer coverage on the substrate. Next, one monolayer of As is deposited on the substrate surface. The GaAs well material was nucleated by first depositing two atomic layers of As at room temperature, followed by the introduction of the equivalent amount of Ga. The MEE growth was continued at 250°C (or ramping from 250°C to 400°C) for the remainder of the GaAs

growth. It seems that this approach deposits at least two atomic layers of LTGaAs at the GaAs on ZnSe heterointerface. These heterostructures were assessed microstructurally via x-ray diffraction, cross-sectional TEM [18-20, 22] and RHEED. During the growth of these heterostructures, the RHEED pattern was either weak or spotty [22]. However, the x-ray diffraction results indicate the presence of a uniformly high-quality structure as indicated by narrow Bragg peaks and interference fringes [18, 20, 21]. There was some effort to assess the interface quality using SIMS and Auger spectroscopy, though the spatial resolution of both characterization methodologies is below that necessary to measure the interfacial properties accurately [19]. The optical properties of the GaAs QW were measured by low-temperature photoluminescence measurements, and appear to be very close in energy to the band-edge of the GaAs substrate [18, 20].

2.1.4 Low-temperature GaAs

The study of low temperature GaAs (LTGaAs) is relevant to the investigation of ZnSe/GaAs QWs in that the disparity in the optimal growth temperatures of ZnSe and GaAs, as well as the approaches to the nucleation of GaAs on ZnSe reported in the technical literature, place the growth of GaAs in or close to the regime of LTGaAs. The growth of LTGaAs is usually at a substrate temperature ranging from 200°C to 300°C, with a range of As:Ga ratios [26-37]. LTGaAs is characterized by a short carrier lifetime (sub-picosecond) that results from the incorporation of excess arsenic during the growth. The additional As atoms reside interstitially in the GaAs lattice, sitting close to the normally present As atoms with a projected displacement of roughly 0.03 nm [26, 37]. In general, the optical properties of LTGaAs are such that there is no measurable level of photoluminescence across the energy band-gap, although there is evidence of deep-level low-temperature photoluminescence at 0.8 eV [33, 35, 38-40]. This is largely a function of the low carrier lifetime [41].

There is some evidence that the properties of LTGaAs are tied to the ratio of As:Ga used during the GaAs growth [31-34, 42, 43]. Essentially, the closer the LTGaAs As:Ga growth ratio is to 1:1, the longer the carrier lifetime in the material as grown. This is a

logical result, since the presence of excess arsenic in the lattice behaves as a defect of the GaAs with a measured non-ionized impurity band of 0.2 eV width centered 0.5 eV from the top of the conduction band [44].

The details on the properties of GaAs when it is grown near and within the regime of low temperature GaAs have bearing on the understanding of the properties of the ZnSe/GaAs QWs under investigation. Table 2-1 lists the measured carrier lifetimes of GaAs grown with a beam equivalent pressure (BEP) ratio of 10 [41] (where a BEP of 3 is roughly equivalent to an As:Ga ratio of 1:1 [34]). The carrier lifetime of GaAs grown even at a slightly lower temperature (400°C) is much shorter than that of GaAs grown under optimal conditions. The further degradation of the carrier lifetime for GaAs grown at lower temperatures should be considered in conjunction with the issues associated with growing a high-quality optical GaAs QW with ZnSe barriers.

T_{sub}	τ (psec)
580	> 1 nsec
400	65
350	62
300	60
260	58
200	< 0.4
190	< 0.4

Table 2-1. Carrier lifetimes (τ) for GaAs grown at different temperatures (T_{sub}) [41].

Table 2-2 gives the results of x-ray diffraction studies of GaAs grown at a reduced temperature with different ratios of the As to Ga in the growth reactor [28, 34]. The presence of an extra Bragg feature in an x-ray rocking curve indicates that there is a periodicity of the atomic planes other than that of the standard GaAs lattice. This feature can result from strain in the lattice or compositional shifts. For the case of LTGaAs, the excess arsenic incorporated into the lattice alters the lattice constant and shows up as a compressively-strained feature compared to the GaAs substrate. The intensity and FWHM (or the integrated intensity) of the extra x-ray feature seems to dissipate as stoichiometric growth conditions are approached.

As to Ga BEP	Δ(arcsec)	FWHM (arcsec)	T_{sub} (°C)
20	-160	60	225
10	-200	100	200
6	-100	100	250
5	-75	100	250
4	-75	100	250
3	0	25	250

Table 2-2. Effect of As to Ga BEP on the structural properties of LTGaAs [28, 34]. Δ corresponds to the shift in the LTGaAs Bragg peak from the GaAs substrate Bragg peak. The full width at half maximum (FWHM) is for the LTGaAs Bragg peak. The growth temperature (T_{sub}) is also given.

The prior sections represent the survey of the experimental work that has been done on ZnSe/GaAs QWs. This information is important because it led the starting point of the present experimental work on the growth of the mixed ZnSe/GaAs heterostructures.

2.2 Analysis at the heterointerfaces

In addition to the experimental research on the fabrication of ZnSe/GaAs heterostructures, there were research efforts to tackle some of the problems associated with a mixed ZnSe/GaAs heterointerface (as well as the heterointerfaces of other semiconductor material systems). One issue addressed was the energy-band alignment between ZnSe and GaAs. A related issue was the type of interface that forms between the two materials and the properties of that interface. Finally, the limitations in the material fabrication that ultimately determine the heterostructure properties were also explored. Relevant information available in the technical literature follows. In some cases, experimental methods were used to find solutions to these questions, though the work still falls into the theoretical realm.

2.2.1 Energy-band alignment

When two different semiconductor materials are joined to form a single heterostructure (which in the present study was done by MBE), there is often a discontinuity in the band-gap energy of the heterostructure. It is important to have an understanding of how the two different band-gaps align at the heterointerface in order to have a sense of the carrier dynamics within the heterostructure. There are several theories of how semiconductor band-gaps align [45-51]. The theories on the energy-band alignment agree that an

interfacial dipole results in charge transfer between the two materials which must be accounted for by more than the electron affinity rule. The electron affinity rule assigns the energy band alignment between two materials according to the relative separation of the conduction band levels for each material from a reference vacuum energy level (the energy required to completely remove an electron from the material). The theoretical work presented specifically on the ZnSe/GaAs heterointerface predicts an energy-band alignment that results in a valence-band offset (ΔE_v) ranging from 0.83-1.09 eV. The range of the predicted valence-band offset for the ZnSe/GaAs system is partially determined by the use of a range of material constants for both materials. This range in material parameters for ZnSe is due to an incomplete understanding of the electronic properties of bulk ZnSe. At a more fundamental level, many of the energy-band alignment theories assume that the heterointerface is comprised of all III-V or all group IV elements. This issue is discussed more thoroughly below, as it also affects the thickness of the heterointerface.

2.2.1.1 ZnSe/GaAs energy-band alignment

To date, extensive experimental research has been carried out on the formation of the mixed interface formed in a ZnSe/GaAs heterostructure. These efforts have tried to provide an understanding of the nature of the stoichiometry of the II-VI/III-V heterointerface and the alignment of the electronic energy bands across the heterostructure. Work by Nicolini, *et al*, [52] ascertained that the ZnSe/GaAs heterointerface can have four permutations, each with a different energy band alignment. Figure 2-1 presents an illustration of the atomic arrangement for the four cases with the valence band-offsets given below each one.

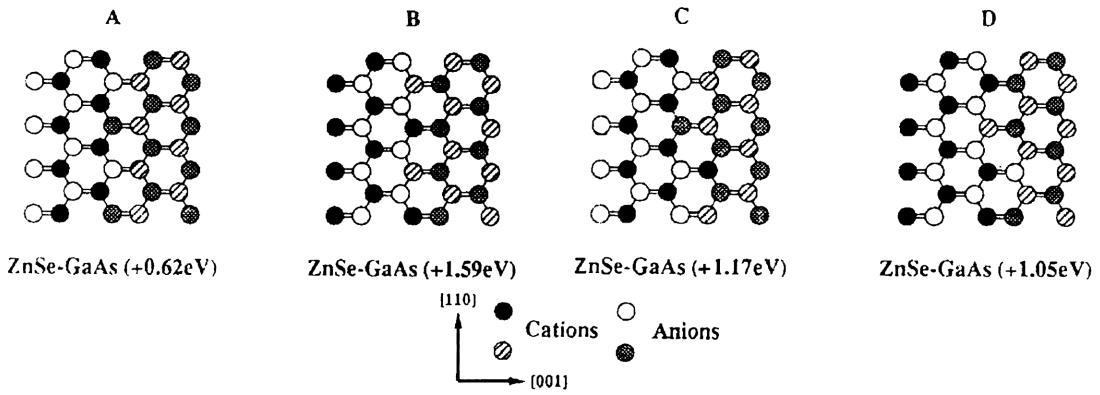

Figure 2-1. Illustration showing possible atomic arrangements of Zn, Se, Ga, and As at the ZnSe/GaAs heterointerface and the corresponding valence band-offsets [52].

The Nicolini group was also able to identify and control the energy-band alignment between ZnSe on a GaAs(001) surface which was As-stabilized as represented by a (2x4) surface reconstruction. The valence-band offset was measured to be a function of the ratio of Se to Zn in the growth reactor [52-57]. ZnSe nucleated on GaAs in highly Se-rich conditions will have a smaller valence-band offset (as small as 0.6 eV) than when nucleated in Zn-rich conditions (as large as 1.2 eV), as is shown in Figure 2-2 [53]. These results were also found to be independent of GaAs doping and/or surface reconstruction although this study did not thoroughly cover the spectrum of doping and starting surface reconstruction for each ratio of Zn:Se tested [52].

Bonanni, *et al*, studied the effect of the ratio of Zn:Se during ZnSe growth on the ZnSe/GaAs energy-band alignment. The value of the valence-band offset (ΔE_v) was derived from x-ray photoemission spectroscopy (XPS) measurements of the binding energies of the constituent elements for the heterostructures. In Figure 2-2, ΔE_v is measured as a function of the thickness of ZnSe grown on GaAs [53]. The first 2 nm of the ZnSe in the ZnSe/GaAs heterostructures in this study were grown with Zn:Se ratios ranging from 0.1 to 10. The remainder of the ZnSe layer was grown under stoichiometric conditions. As shown, the energy-band alignment can be engineered by setting the ratio of Zn:Se during the ZnSe growth within the first 2 nm.

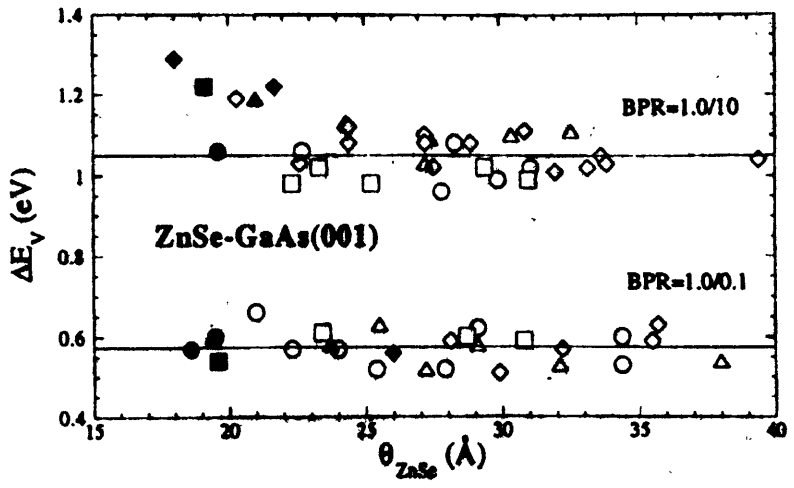

Figure 2-2. XPS-derived values of ΔE_v for ZnSe-GaAs(001) heterostructures as a function of the thickness of the overall ZnSe layer. Solid symbols denote data obtained from the first 2 nm of ZnSe. Open symbols denote data obtained after deposition of a ZnSe overlayer with BPR=1. Similar symbols (diamonds, squares, circles, and triangles) denote data obtained in the same experimental run with a Zn-rich nucleation (topmost section), or Se-rich nucleation (bottom-most section). Average values of ΔE_v=1.05± 0.05 eV for samples with Zn-rich nucleations, and ΔE_v= 0.58± 0.05 eV for Se-rich nucleations are indicated by horizontal lines [53].

The effect of the growth ratio of Zn:Se on the ZnSe/GaAs energy-band alignment is further presented by Nicolini, *et al* [52]. In this work, the stoichiometry and doping concentration of the GaAs surface were varied in conjunction with a range of Zn:Se ratios during the ZnSe growth. A summary of the results on the energy-band alignment for this set of ZnSe/GaAs heterostructures is shown in Figure 2-3. The graph of ΔE_v as a function of the Zn:Se ratio shows that the starting GaAs stoichiometry or doping concentration does not contribute to the energy-band alignment between ZnSe and GaAs.

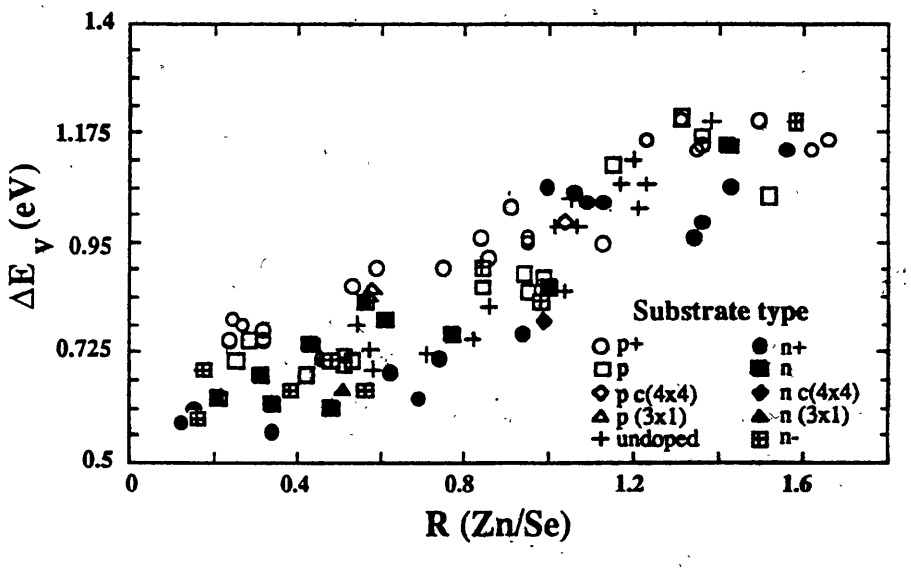

Figure 2-3. Experimental valence band offset (ΔE_v) for ZnSe interfaces fabricated on GaAs(001) substrates with different type of doping. Unless noted otherwise, the substrate reconstruction was As-stabilized 2x4. The offsets are plotted as a function of the Zn:Se ratio R observed for each interface in the early growth stage (at a ZnSe coverage of 0.3 nm) [52].

The experimental work on the energy-band lineup between a layer of ZnSe grown on GaAs addresses one of the problems associated with the heterointerface of a II-VI/III-V material. However, the same group of researchers relied on a 2 nm thick ZnSe nucleation layer to engineer the energy-band alignment of the subsequent structure successfully. This choice has ramifications for the interfacial quality when the ZnSe nucleation layer is grown under extreme Zn:Se ratios.

2.2.2 Interface roughness

For a quantum well heterostructure, an abrupt transition between the different layers is desired for several reasons. First, if the heterointerface is abrupt, the properties of the heterostructure are easier to understand once the bulk properties of each layer are known. Second, if the final destination of the heterostructure is within an optoelectronic or photonic device, a more abrupt heterointerface implies a more precise optical signature. Finally, once an abrupt heterointerface has been achieved and the growth parameters optimized, the heterostructure can be built with reproducible characteristics.

All semiconductor heterostructures have interface quality issues. For a stack of semiconductors with alternating layers consisting of group V elements of P or As, there is an issue of interdiffusion of phosphorus into the neighboring layer [58, 59]. In the growth of AlGaAs on GaAs, the formation of the heterointerface is complicated by the difference in optimal growth temperatures (AlGaAs, ~800°C). This has a degrading effect on the interface roughness and purity [60, 61]. In all III-V heterostructures, the use of growth interruption (of a few minutes) between layers of different material types has been studied to optimize the interfacial roughness [60-66].

The ZnSe/GaAs heterostructure is complicated by the different valences of the four elements at the heterointerface. Gallium has been shown to act as a donor-type dopant in ZnSe [67-69]. Similarly, zinc has been shown to dope GaAs. There has also been documentation of surface-exchange of Se with As atoms on the GaAs surface, to form a Ga(As)Se compound [11, 70, 71]. All of these results indicate that there is the possibility for interfacial diffusion between ZnSe and GaAs.

The orientation of the growth surface also affects the interfacial properties. The (001) compound semiconductor surface is polar, in that there is a periodic absence of one of the surface dimers [72]. For the case of GaAs, this has been shown to be manifested by the absence of every fourth arsenic dimer [73]. For ZnSe, the surface is more complicated. A Se-rich surface (as indicated by a (2x1) surface reconstruction) is terminated with Se dimers with the same periodic absence of the fourth dimer as in the GaAs case. However, in the Zn-rich case, the Zn dimers are unstable due to excessive back-bonding strain, and the surface is terminated in a half-monolayer of Zn [74, 75]. As a result, the formation of the ZnSe/GaAs heterointerface is complicated by the different types of stable (001) surfaces for each material. Theoretically, a truly abrupt heterointerface formed by GaAs in its most stable form (As-stabilized) and ZnSe in its most stable form (Zn-rich) would result in interfacial charge.

2.3 Summary

The complexity of the ZnSe/GaAs heterostructure has been illlustrated. The fabrication of the mixed structure is complicated by a mismatch in the optimal growth temperatures for ZnSe and GaAs. Furthermore, the formation of a ZnSe/GaAs/ZnSe single QW requires engineering of the growth of GaAs on ZnSe while remaining outside of the regime of LTGaAs.

The electronic properties of the ZnSe/GaAs heterostructure are discussed on both the theoretical and experimental levels. In all cases, the energy-band alignment between the materials has been shown to vary greatly depending upon the growth parameters. The theory behind energy-band alignment of a compound semiconductor heterostructure assumes, in part, an abrupt heterointerface, and the issues associated with this assumption have been surveyed. The probability of interfacial diffusion and/or the presence of interfacial charge has been discussed.

3. Material fabrication

The II-VI and III-V compound semiconductor materials studied were grown by molecular beam epitaxy. The epitaxial growth process and the system employed are presented in the subsequent sections, followed by a discussion of the optimal growth procedure for ZnSe and GaAs. The initial description of ZnSe and GaAs growth aids the understanding of the growth of the complete ZnSe/GaAs/ZnSe heterostructure. Each compound semiconductor has a unique set of optimal growth parameters. The optimal growth parameters for a heterostructure composed of different material systems requires some engineering of these conditions to achieve the best quality material from both an optical and electrical perspective. The final sections of this chapter present the results on the growth and optimization of the ZnSe/GaAs DBH.

3.1 Description of method: GSMBE and MBE

Molecular beam epitaxy (MBE) is a commonly used method of building heterostructures by controlling the formation of each atomic layer. Molecular beams of the source materials are generated when the source temperatures reach a point at which the material vaporizes. The amount of each material in the growth chamber at a given time can be controlled by changing the source temperature and then analyzed by measuring the beam fluxes. The molecular beams impinge upon a heated substrate and bond to the surface if the bond can be electronically formed. This entire process occurs in an ultra-high vacuum environment (base chamber pressure is ~ $1x10^{-10}$ Torr) to ensure that the only atoms which interact with the substrate surface are from the desired source materials. The critical parameters in this process are the chamber pressure, the source temperatures and fluxes, and the substrate temperature.

Various forms of molecular beam epitaxy employ either solid elemental, gaseous hydride, or metal-organic source materials with known vapor pressures. In this study, for the growth of ZnSe, solid elemental Zn and Se are used as the source materials, whereas for

the growth of GaAs and all III-V semiconductors, solid Ga (or group III source) is used with the gaseous hydride arsine (or phosphine) as the group V source. The two materials are grown in separate chambers that are interconnected. Transfers between the two chambers are performed in an ultra-high vacuum environment. The epitaxial growth system employed in this environment is described below.

3.2 System Description

The experimental system employed for the epitaxial growth of the ZnSe/GaAs DBHs is basically a combination of stainless steel cavities (or chambers) welded together and connected to a hierarchy of pumps to maintain the inside pressure at or below 10^{-10} Torr. Access to the inside of the growth system is made possible by a series of valves which allow for samples to be loaded into the chamber without altering the base system pressure. There are also a number of viewports throughout the system to aid in transferring the sample and monitoring the sample during analysis or growth. Finally, a number of attachments are fed through the stainless steel walls via a system of bolted flanges that are sealed at the chamber/flange interface by either copper or aluminum gaskets. Every attachment to the growth system has a specific purpose, as does each chamber of the growth system. The following paragraphs describe more thoroughly each part of the growth system.

The overall growth system consists of six interconnecting chambers; a transfer chamber, two introduction chambers, a II-VI compound semiconductor dedicated reactor, a III-V compound semiconductor dedicated reactor, and an analytical chamber (Figure 3-1). Centered in the transfer chamber, a robotic arm allows the samples to be maneuvered between each connecting chamber.

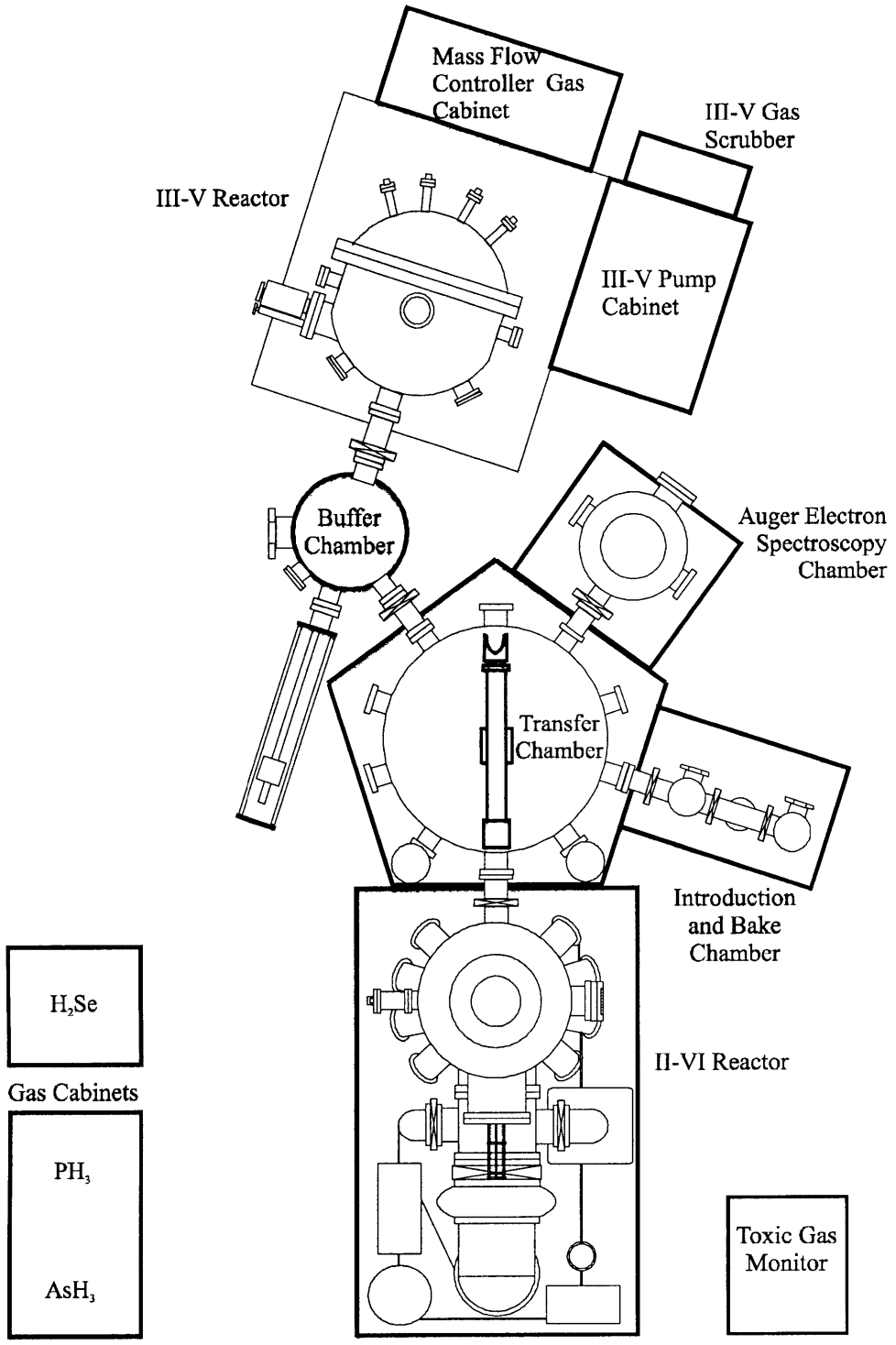

Figure 3-1. Schematic showing the growth system. Shown are the II-VI growth reactor, III-V growth reactor, analytical chamber, transfer chamber, and the supporting equipment necessary to maintain an ultra-high vacuum and to monitor for toxic gases.

The introduction chamber consists of two separate vacuum chambers. These two areas share a cryogenic pump allowing only one chamber to be pumped at a time. The first contains a heater and a platform for desorbing the residual acids and water from the surface of a clean sample block or holder prior to loading a substrate. The second chamber acts as a load lock for the clean substrate and sample block prior to the introduction into the transfer chamber which is connected through a gate valve. From the introduction chamber, the carrier and sample are transported into the transfer chamber using the robotic arm in the transfer chamber. Inside the transfer chamber, a clean sample block with a mounted sample can be baked at another bake station to desorb water.

The III-V chamber has a buffer chamber which acts as another load lock for the sample prior to being loaded into the III-V growth reactor. The buffer chamber allows for *in situ* transfer between the growth reactors and the analytical chamber via the transfer chamber.

Two growth chambers are used for the growth of the III-V layers and the II-VI layers: a Riber 32P gas-source MBE (GSMBE) system for the growth of III-V compound semiconductors, and a chemical-beam epitaxy (CBE) system for the growth of ZnSe. The different families of compound semiconductors are grown in separate systems to avoid cross-contamination during the respective film growth. As the growth chambers were manufactured by different companies, the details of each tend to differ. However, each system is equipped with a substrate heater, a thermocouple and a pyrometer to measure the substrate temperature, effusion cells containing ceramic crucibles sitting in heaters for each solid element employed in the growth, cracking cells for removing the hydrogen from the hydride molecule for the gas sources, an ion gauge for measuring source fluxes, and an electron gun and phosphorus screen for reflection high energy electron diffraction (RHEED) analysis. Both chambers utilize liquid-nitrogen-cooled shrouds or traps to minimize the background pressure during growth. A cryso-shroud is used in the III-V chamber to thermally isolate the cells, while the II-VI chamber uses water cooling since the cells operate at lower temperatures.

In the II-VI chamber, the sample is suspended by a rotating platform under the substrate heater in the center of the reactor. The substrate heater can be raised and lowered to allow for sample transfers. A quartz crystal oscillator sits at the substrate holder to measure the source fluxes close to the sample surface. The elemental sources are directed upward towards the substrate surface. Each source's flux can be interrupted by manually controlled shutters.

In the III-V chamber, the sample is connected to a rotating stage with a fixed separation from the substrate heater. The elemental sources and the cracking cells are aimed at the substrate, and are mechanically shuttered. An ionization gauge is used to determine the source fluxes at the substrate surface prior to growth.

Both growth reactors employ RHEED analysis to evaluate the quality of the substrate surface at all stages of the growth. The RHEED pattern is formed by focusing a 10 keV electron beam at a shallow angle onto the substrate (< 2° from the sample's surface) causing the electrons to diffract according to the crystal structure. The desired pattern is a series of well defined dots. The primary forward scattered beam has the additional property that in the case of layer-by-layer growth, the beam intensity oscillates with the same period as the material growth rate. RHEED intensity oscillations are usually taken at the onset of growth, when the growth surface is smooth.

3.3 Calibration of the growth environment

The growth parameters for a semiconductor depend upon the types of sources employed and the surface kinetics of the material grown. There are five stages of interaction of the constituent species of a compound semiconductor with the growth surface: adsorption, migration, desorption, reaction and incorporation. The substrate temperature must be low enough such that it is thermodynamically feasible for the sources to adsorb, migrate along the sample surface, and become incorporated before the sources are desorbed. Hence, the optimal growth temperature for a semiconductor material is a function of the vapor pressure of the constituent element(s). Since Ga and As_2 have much lower vapor pressures than Zn and Se, the GaAs growth temperature is much higher than that of ZnSe.

3.3.1 GaAs growth

The growth of GaAs begins with the removal of the native oxide on the GaAs substrate surface. The oxide is removed by heating the substrate to 620°C while observing the RHEED surface reconstruction. A background pressure of roughly 10^{-5} Torr of As_2 is maintained to protect the surface as the oxide is removed. Usually, the oxide-free GaAs surface shows a (2x4) reconstructed surface on the RHEED screen, which indicates that ~75% of the GaAs surface is occupied by As and is As-stabilized. A summary of the GaAs RHEED patterns is given in Figure 3-2.

GaAs is typically grown at a temperature of 580°C - 600°C. Growth is initiated by opening the Ga cell shutter, as there is already a background pressure of As_2 in the system. The (2x4) RHEED pattern remains throughout the GaAs growth. RHEED intensity oscillations are measured to determined the growth rate. Once the layer has reached the desired thickness, the Ga cell shutter is closed. When the substrate temperature is reduced to roughly 400°C following growth, the GaAs surface transforms to an As-rich surface as indicated by a c(4x4) RHEED surface reconstruction.

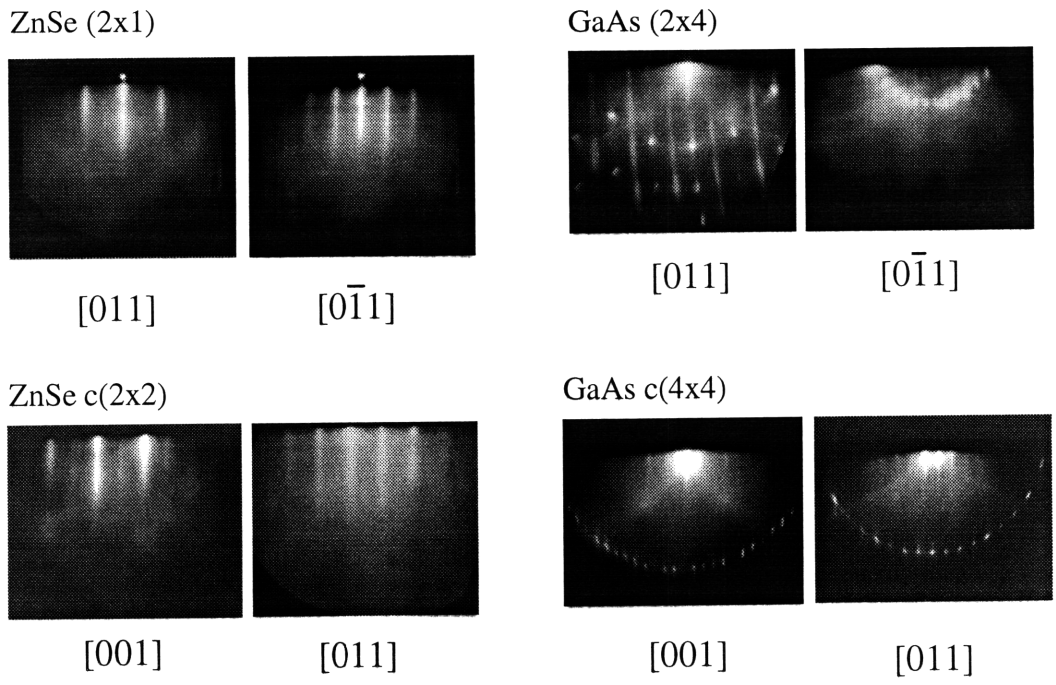

Figure 3-2. RHEED patterns of ZnSe and GaAs surface reconstructions. ZnSe (2x1) and c(2x2) patterns are shown. GaAs (2x4) and c(4x4) patterns are shown.

3.3.2 ZnSe growth

The ZnSe material studied was grown on either GaAs or ZnSe substrates. When a GaAs substrate is used, the starting surface is either a GaAs or an InGaP buffer layer. When a ZnSe substrate was used, the substrate surface must be treated *in situ* before growth can begin. Upon direct entry into the growth reactor, the ZnSe substrate shows a faintly streaky bulk surface RHEED reconstruction. The presence of a RHEED pattern indicates that any oxide on the ZnSe surface is thin. Auger electron spectroscopy revealed that the ZnSe substrate surface in fact had less oxygen than it did carbon. As a result, a starting surface treatment of hydrogen plasma cleaning is performed to remove the carbon. Once the ZnSe surface is prepared, the growth of the subsequent ZnSe layer is the same as for the growth on the III-V surface.

For ZnSe, the sources are usually set by adjusting the cell temperatures and measuring the corresponding molecular beam flux with a crystal oscillator to achieve a Se-rich surface during growth. ZnSe is typically grown at a substrate temperature between 280°C and

300°C. The ZnSe nucleation begins by manually opening the Zn and Se shutters simultaneously. During the ZnSe growth the substrate surface exhibits a Se-rich (2x1) RHEED reconstruction. RHEED intensity oscillations are measured to determine the growth rate. Once the layer has reached its desired thickness, the Zn and Se cells are shuttered off, and the substrate heater is raised away from the sample. At this point, the ZnSe surface becomes Zn-rich, as indicated by a c(2x2) surface reconstruction. A summary of the ZnSe RHEED patterns is given in Figure 3-2.

Table 3-1 summarizes the evolution of the RHEED pattern during the oxide removal and the GaAs and ZnSe growth process.

Start Surface	End Surface	RHEED Pattern	T_{sub} °C
GaAs oxide on substrate	Oxide off	bulk	620
GaAs (sub)	GaAs (epi)	2x4	580-600
GaAs	ZnSe Se-rich	2x1	280-300
ZnSe Se-rich	ZnSe Zn-rich	2x2	280-300

Table 3-1. Typical RHEED patterns during the course of GaAs and ZnSe epitaxial growth.

3.4 Growth rate and stoichiometry

The dependence on the growth rates and stoichiometries of the GaAs and the ZnSe layers on the elemental and hydride source parameters were determined by a combination of system calibration using control samples and *in situ* characterization using RHEED intensity oscillations. The ZnSe material was grown under standard conditions, and the calibration of the stoichiometry using control samples is given in more detail elsewhere [76-84].

3.4.1 ZnSe growth rate

The barrier layers in the ZnSe/GaAs heterostructure are thin enough that the short growth duration results in a compromise between achieving RHEED intensity oscillations and a uniform film growth via rotation of the sample. In general, the RHEED oscillation measurement was attempted on the first barrier layer to measure the ZnSe growth rate for a given set of Zn and Se beam fluxes (as measured by a water-cooled crystal oscillator located at the substrate position). The first ZnSe barrier layer was nucleated on a smooth

III-V buffer layer surface grown under standard conditions, allowing for a higher probability of measuring RHEED intensity oscillations. The second ZnSe barrier layer was nucleated on a reduced-temperature GaAs layer, and although a c(4x4) GaAs surface reconstruction was achieved for this layer, when RHEED intensity oscillations were attempted, the fluctuation in the specular beam intensity was within the noise range of the detection system. As a result, an effort was made to maintain the II-VI growth parameters measured for the first ZnSe barrier layer in order to achieve a similar growth rate for the second ZnSe barrier layer. Cross-sectional TEM results show that the thickness of the ZnSe barriers in a given heterostructure vary by 10%.

3.4.2 GaAs growth

Unlike ZnSe, the epitaxial growth of GaAs at the standard substrate temperature of 580°C is not self-limited by monolayer coverage of the constituent species. On a GaAs surface at standard MBE growth temperatures, the Ga atoms have a unity sticking coefficient. The As_2 molecules, require the presence of vacant bonds on Ga atoms to react with the GaAs surface and are otherwise thermally desorbed from the substrate surface. As a result, the two-dimensional growth of GaAs is Ga-limited at a standard growth temperature. A RHEED intensity oscillation measurement of a high-quality GaAs growth surface reflects the rate of Ga growth. However, the ratio of As_2:Ga during the GaAs growth can also affect the final layer quality. This is particularly the case for the reduced temperature GaAs, as the increased possibility for excess As_2 incorporation can lower the carrier lifetime in the GaAs. Hence, it is important to understand the growth rate of GaAs as a function of the Ga cell temperature and the AsH_3 flow rate. As the GaAs was also grown at reduced temperatures, the growth rates are also studied as a function of temperature.

3.4.2.1 As_2 incorporation rate

The As_2 dependence of the GaAs growth rate was studied as a function of the AsH_3 flow rate (sccm) and the growth temperature. When a flow of AsH_3 results in a growth rate of As_2 on the GaAs surface that is equivalent to the growth rate of GaAs at a given flux of Ga, the As_2:Ga ratio is 1:1. To measure the growth rate as a function of AsH_3 flow rate, a smooth GaAs(100) surface was heated to around 600°C with a surface (2x4) RHEED

reconstruction. An optical fiber attached to a photomultiplier tube was centered at the specular beam of the RHEED pattern. Ten monolayers of Ga were deposited on the GaAs surface, during which time the RHEED pattern disappeared and a diffuse background level of scattering was visible. At this point, the AsH_3 shutter was opened allowing for the As_2 to bond with the Ga atoms on the GaAs surface. The specular beam both recovered in intensity and oscillated with a cycle time of one monolayer of GaAs growth. Upon the growth of ten monolayers of GaAs the oscillations stopped and the surface exhibited a (2x4) RHEED reconstruction. The data points in Figure 3-3 indicate the growth rate determined by the period of the RHEED intensity oscillations from the As_2 contribution to the GaAs growth rate. As expected, the growth rate increases with increasing AsH_3 flow.

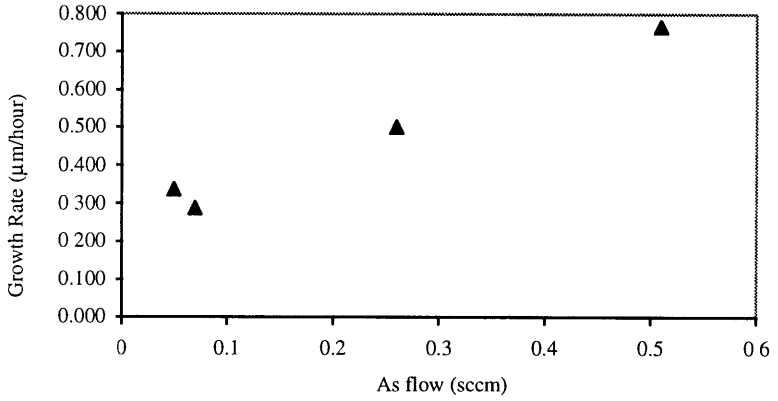

Figure 3-3. Growth rate as a function of the AsH_3 flow rate in the growth reactor as measured by RHEED intensity oscillations.

The contribution of As_2 to the growth rate of GaAs was also studied as a function of the substrate temperature. The motivation for this measurement was to understand how the As_2 would interact with the GaAs surface at reduced growth temperatures, which would help in establishing stoichiometric GaAs growth conditions. To measure the contribution of As_2 to the GaAs growth rate as a function of substrate temperature, the same procedure was followed in the comparison of GaAs growth rate as a function of AsH_3 flow except the AsH_3 flow was kept constant at 0.07 sccm (the minimum flow rate that can be maintained by the mass flow controller) and the substrate temperature was varied. As the substrate temperature was reduced, between As_2 oscillation measurements, the GaAs

substrate temperature was raised to around 600°C to anneal and smooth the surface. The smoother GaAs surface was necessary for detecting RHEED intensity oscillations.

Figure 3-3 shows the relationship between the contribution of As_2 to the GaAs growth rate and the substrate temperature. The data shows that the growth rate of GaAs becomes independent of substrate temperature temperatures below 550°C (at an AsH_3 flow of 0.07 sccm). Compared to the growth rate at the standard growth temperature of 600°C, the growth rate levels off to a value that is 30% higher (0.475 μm/hr).

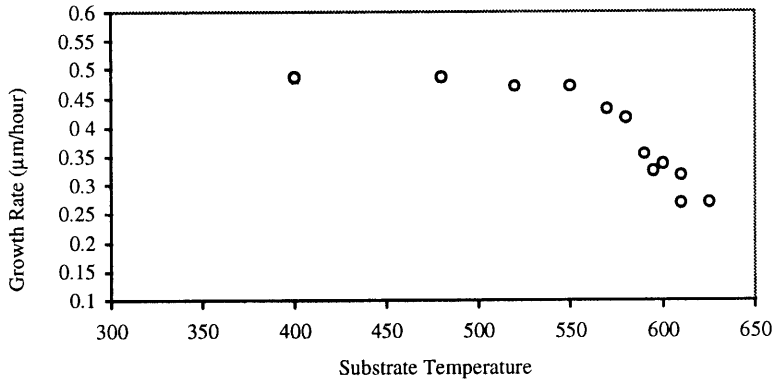

Figure 3-4. GaAs growth rate as a function of substrate temperature (°C). RHEED intensity oscillations resulting from As_2 incorporation were used to measure this relationship as Ga has a unity sticking coefficient on the GaAs surface over the range of temperatures measured

The combination of the results from the As_2 oscillations as a function of AsH_3 flow and substrate temperature can be used to calculate the conditions under which stoichiometric GaAs can be grown at reduced temperatures. The Ga incorporation rate is also needed to make this calculation.

3.4.2.2 Ga incorporation rate

The Ga incorporation rate is the limiting factor in the growth of GaAs at the standard growth temperature. Therefore, RHEED intensity oscillations of GaAs growth at 600°C as a function of Ga cell temperature directly measures the contribution of Ga to the GaAs growth rate. The GaAs growth rate was measured with a similar arrangement to that for the As_2 oscillations, except both the As_2 and Ga shutters were open during the RHEED

oscillation measurement. Figure 3-5 shows the relationship between the Ga cell temperature in °C and the growth rate. The relationship is non-linear with roughly a doubling in the growth rate for a 20° - 30° increase in cell temperature.

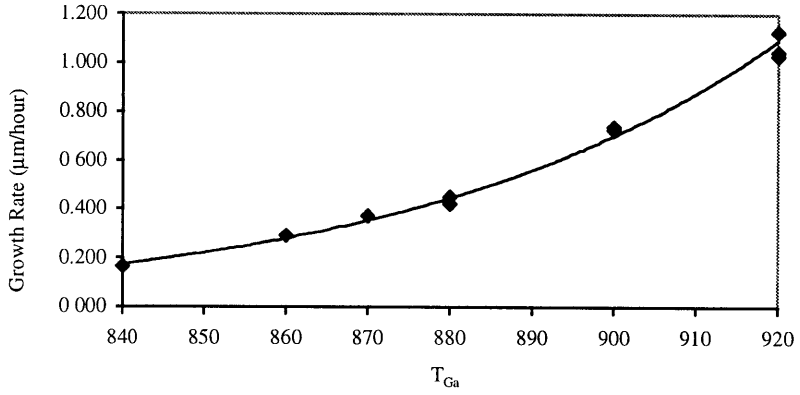

Figure 3-5. Growth rate as a function of the Ga temperature (°C) as measured by RHEED intensity oscillations.

3.4.2.3 GaAs stoichiometry determination

The previous three measurements of the As_2 incorporation rate as a function of AsH_3 flow and substrate temperature, and the Ga incorporation rate as a function of the Ga cell temperature can be combined to determine the ratio of Ga:As_2 for reduced temperature GaAs growth. The ratio is calculated by the following equation:

$$Ratio\left(\frac{Ga}{As_2}\right)=\frac{R_{Ga}\left(T_{Ga}\right)}{R_{As_2}\left(r_{As_2}\right)}*\frac{R_{As_2}\left(350^{o}C\right)}{R_{As_2}\left(600^{o}C\right)}$$

where R is the growth rate, T is the cell temperature, and r is the AsH_3 flow. The results of this calculation are shown in Figure 3-6 as a function of Ga cell temperature for an AsH_3 flow of 0.07 sccm.

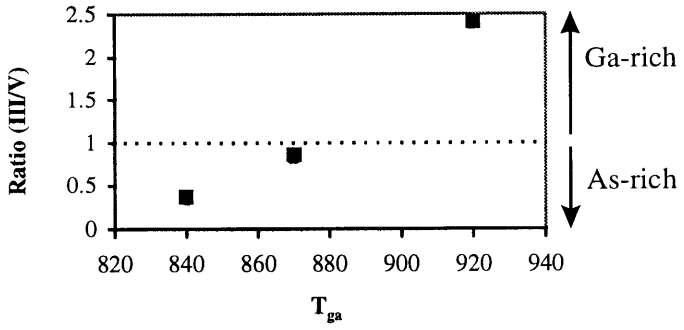

Figure 3-6. Ratio of Ga:As_2 as a function of Ga temperature for an AsH_3 flow of 0.07 sccm. The substrate temperature is between 350°C and 400°C.

The calibration process for the growth of reduced temperature GaAs led to the determination of a growth rate of 0.4 μm/hr with a Ga cell temperature of 875°C and an AsH_3 flow rate of 0.07 sccm for stoichiometric, or 1:1. growth conditions at a reduced growth temperature.

3.5 Epitaxy of ZnSe/GaAs/ZnSe

The following sections discuss the fabrication of the ZnSe/GaAs mixed heterostructure by epitaxial growth. A general description of the growth method is given, as well as the specifics of the method used in this study. The issues regarding optimization of the growth of the GaAs "well" material are presented, followed by a discussion of the nucleation of GaAs on ZnSe. The growth-related results are presented for the optimized growth of the entire ZnSe/GaAs/ZnSe DBH, including the growth parameters and sequence. Also, the surface RHEED pattern during the growth is shown. Characterization of the heterostructures after growth are presented in subsequent chapters.

3.5.1 GaAs quantum well material

Due to the disparity in optimal growth temperatures for ZnSe and GaAs, the effects of reducing the GaAs growth temperature have been investigated. The difference in the growth temperatures is an issue in the formation of a high-quality ZnSe/GaAs QW because the GaAs QW layer is optimally grown at a high enough temperature to destroy the quality of the lower ZnSe barrier layer.

The limits to achieving high quality optical GaAs material while preserving the ZnSe barrier layers have been probed. It was important to isolate the GaAs growth temperature effects from the issues associated with the formation of the II-VI/III-V heterointerfaces in the ZnSe/GaAs QW heterostructure. GaAs/InGaP multiple quantum well (MQW) structures were grown with the GaAs at a temperature that would preserve the ZnSe layer quality. The GaAs/InGaP MQW heterostructure grown under standard conditions have been extensively studied [85]. A GaAs/InGaP MQW structure has been used to show the presence of low temperature photoluminescence for GaAs material grown at 350°C with an As:Ga ratio of 1:1. At low growth temperatures, an As:Ga ratio of 1:1 is expected to be optimal for achieving a high quality GaAs crystal structure [30-34].

As the ultimate goal of the study of ZnSe/GaAs heterostructures is to fabricate photonic devices, the GaAs material must be of high optical quality. The reduced growth temperature employed for the growth of the GaAs approaches the regime of low temperature GaAs (LTGaAs). LTGaAs currently has the interest of the semiconductor research community due to its ability to eliminate backgating effects in transistors as well as to fabricate high-speed photoconductors [86-88]. The characteristic feature of LTGaAs is the incorporation of excess arsenic during the growth of the material. When LTGaAs is annealed near 600°C, the excess arsenic forms a fairly uniform distribution of precipitates. The resultant carrier lifetimes are significantly reduced (sub-picosecond) in LTGaAs as compared to standard GaAs [89]. Also the absorption profile for LTGaAs is characteristically less abrupt at the band-edge [90]. Both properties can be potentially related to the presence of excess As in the material.

For the formation of ZnSe/GaAs DBHs, an attempt was made to inhibit the incorporation of excess As in the reduced temperature GaAs by adapting the As:Ga ratio. It is possible that the properties of the reduced temperature GaAs are a combination of those seen for the LTGaAs and standard GaAs. The investigation of the reduced temperature GaAs requires the integration of research results from the fields of photoluminescence, compositional analysis, and microstructural analysis, including cross-sectional TEM and high resolution double crystal x-ray diffraction.

3.5.2 Nucleation of GaAs on ZnSe

Another component of the fabrication of the ZnSe/GaAs DBH studied is the nucleation of GaAs on ZnSe. Because the initial stages of nucleation involves several monolayers of GaAs, the affected material has been named the nucleation layer. Past literature on the nucleation of GaAs on ZnSe has employed standard MBE with a substantially reduced growth rate and migration enhanced epitaxy (MEE) [7, 18-22, 24, 25, 91]. These methods have been also repeated in the CBE laboratory as starting points for future research. However, in both cases, the resultant GaAs material was of poor quality from a microstructural perspective. A third method for nucleation was employed in which the GaAs was nucleated on a Zn-stabilized ZnSe surface using a high arsenic over-pressure with monolayer control of the growth for the first 10 monolayers (single layer MBE or SM-MBE). Figure 3-7 shows the surface morphologies over a 100 μm^2 area of the three different methods of nucleating GaAs on ZnSe as determined via atomic force microscopy (AFM) of the sample surface.

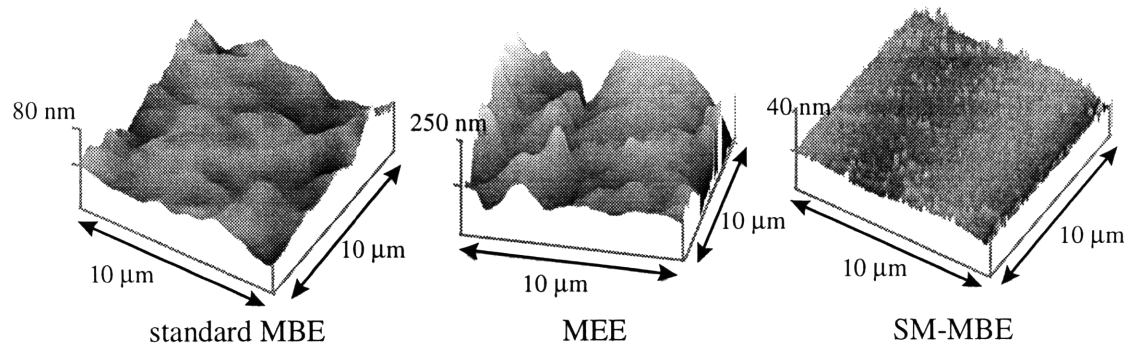

Figure 3-7. AFM images of the surface of 250 nm of GaAs grown on ZnSe by the three different methods: standard MBE, MEE, and the optimized SM-MBE. The z-axis denoting surface height is scaled to according to the roughness of the respective sample.

Based upon the results of the initial study of the nucleation of GaAs on ZnSe, a standard methodology for the growth of further heterostructures was established. In an effort to minimize the amount of GaAs in the heterostructure grown in the regime of LTGaAs, the substrate temperature was raised as soon as a streaky GaAs surface reconstruction was evident. This type of RHEED pattern was indicative of a complete coverage of GaAs on

the ZnSe surface, and occurred after 3 monolayers of material were deposited at 250°C with an As:Ga ratio of 12:1. At this point, the substrate temperature was ramped to 300°C, which further annealed the GaAs surface. An additional 3 monolayers of GaAs were deposited at this point, after which the As:Ga ratio was reduced to 3:1, and the substrate temperature was raised to 350°C. Four monolayers of GaAs were deposited one at a time. Finally, the As:Ga ratio was reduced to 1:1, and the remainder of the GaAs layer was grown at 350°C in stoichiometric conditions. This growth procedure is summarized in Figure 3-8. The first 10 monolayers of GaAs constitute the nucleation layer in the GaAs on ZnSe heterostructure. Figure 3-9 shows the RHEED patterns corresponding to the three transition points in the GaAs nucleation layer: the 3rd, 6th, and 9th monolayers.

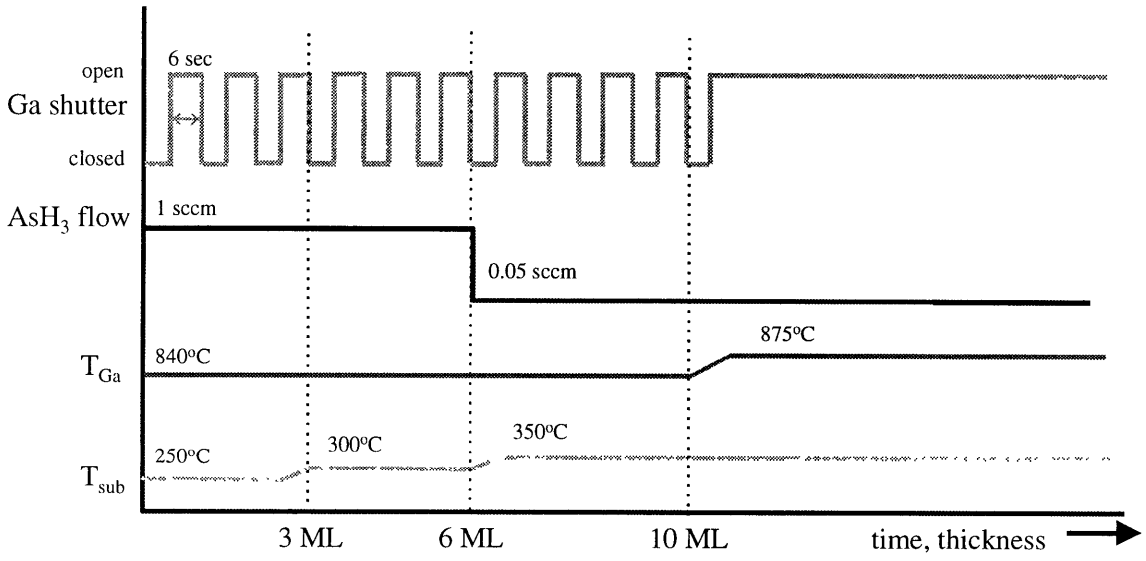

Figure 3-8. Growth sequence for the nucleation of GaAs on a ZnSe surface.

The growth sequence indicated in Figure 3-8 achieves two-dimensional growth because the Ga atoms are always in the presence of an abundance of As in the growth reactor. This limits the formation of Ga pools, or bonding between Ga and Se which would ultimately result in the formation of a Ga(Se) compound. The low growth temperature at the onset of the growth is necessary both to protect the ZnSe surface reconstruction, maintaining a smooth starting surface for GaAs nucleation, and to lower the Ga mobility. The monolayer-by-monolayer growth rate was very low, with a 6 second deposition time

for one monolayer of Ga and an interval of several minutes during which the surface RHEED pattern was documented. The subsequent RHEED patterns in Figure 3-9 demonstrate a significant improvement over the results presented in the scientific literature.

However, the presence of even three monolayers of GaAs grown in non-stoichiometric conditions at 250°C will affect the ultimate optical properties of the QW. Such material is estimated to have a carrier lifetime of roughly 50 picoseconds (as compared to 1 nsec for high-quality GaAs). This characteristic has implications for the optical properties of the heterostructure and will be discussed in later sections.

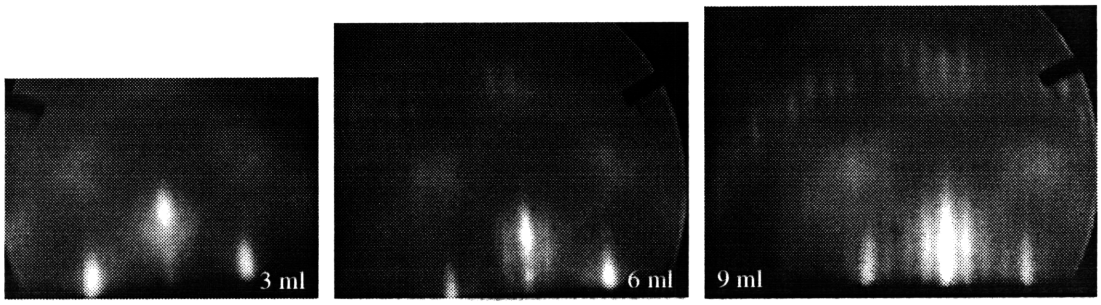

Figure 3-9. RHEED pattern of GaAs surface at the 3, 6 and 9 monolayer thickness on ZnSe. Reconstruction of the GaAs layer is apparent after 6 monolayers of growth, a full c(4x4) reconstruction is evident after 9 monolayers of GaAs growth.

3.5.3 The ZnSe/GaAs double heterostructure

The third stage of the investigation of the ZnSe/GaAs DBH involves the whole structure, incorporating the results from the optimization of the reduced temperature GaAs and the nucleation of GaAs on ZnSe. There are several competing factors which ultimately control the final properties of the mixed heterostructure. The heterovalent interfaces have the potential to create local electric fields which can control the location of carriers in the heterostructure. The theoretical model of an abrupt II-VI/III-V heterointerface shows the excess of one charge (either positive or negative depending upon interfacial stoichiometry) for each unit cell. This uncompensated charge is the source of any interfacial electric fields, and has the potential to control carrier dynamics across the heterostructure. In

addition, the nucleation procedures at the two heterojunctions can result in a variety of energy-band alignment profiles. The potential for interdiffusion of the constituent species at the heterojunctions can further alter the energy band alignment and change the amount of interfacial excess charge.

The full ZnSe/GaAs/ZnSe QW was grown, unless otherwise indicated, by a standard growth sequence. The first ZnSe layer was nucleated on the III-V buffer layer surface at a substrate temperature ranging from 280°C - 300°C, with a slightly Se-rich Zn:Se ratio. For the first 60-90 seconds of ZnSe growth, the Se source was shuttered off from the growth reactor and Zn was deposited on the III-V surface. The surface RHEED reconstruction at this point usually remained the same, with an increase in the intensity of the primary diffraction spot. Next, the Se-shutter was opened and ZnSe growth was initiated. Within 30 seconds, the reconstruction transformed to a (2x1) pattern. RHEED intensity oscillations were taken, indicating a growth rate of roughly 0.5 μm/hour. After the growth of a 50 nm ZnSe layer was complete, the substrate heater was immediately removed from the substrate and ramped to 100°C to maintain a smooth ZnSe surface. The ZnSe surface reconstruction would change from a slightly Se-rich (2x1) pattern present during the ZnSe growth to a Zn-rich c(2x2) pattern once the source shutters were closed.

After the ZnSe growth, the substrate temperature is reduced to 150°C. When sufficiently cool enough for transfer to the III-V growth reactor, the sample is transferred *in situ*. By maintaining the elemental sources at the proper temperature for growth and the gaseous hydrides at the proper flows, the III-V growth reactor was always ready for the growth of GaAs, apart from the substrate temperature. Since the substrate temperature was low, the ZnSe surface reconstruction was barely detectable upon immediate introduction into the III-V system. As the substrate temperature was ramped to 250°C, the reconstruction began to appear, and the c(2x2) surface reconstruction remained in roughly 50% of the growths. In other cases, a (2x1) reconstruction was evident, possibly indicating that the surface was interacting with As atoms in the III-V growth reactor.

At this point, the nucleation of GaAs was initiated and carried out as previously discussed, using SM-MBE. Once the nucleation layer was complete, the GaAs was grown by standard MBE, at a substrate temperature of 350°C with an As:Ga ratio of 1:1. The surface reconstruction during this growth, c(4x4), indicated an As-rich surface. Once the growth of the GaAs layer was complete, the substrate temperature was lowered, and the sample was transferred back into the II-VI growth reactor.

The ZnSe growth for the second ZnSe barrier layer was performed just as the first, although the starting growth surface was always a c(4x4) GaAs surface. RHEED intensity oscillations were achieved during the growth of the ZnSe layer on only one occasion. Hence, the growth rate from the first layer was referred to in setting the growth time for the second ZnSe layer.

The formation of the ZnSe/GaAs DBH by MBE growth was grown with the general procedure outlined in the above sections. However, this process did not result in a heterostructure with the optical quality required to produce photoluminescence from the central GaAs layer. An attempt was made to optimize the nucleation layer, and these results follow.

3.5.3.1 Optimization of nucleation layer

Due to the lack of a photoluminescence signal detected from previously grown ZnSe/GaAs single quantum well structures, the nucleation of the GaAs on the ZnSe has been examined. The 250°C grown GaAs has a short carrier lifetime and ultimately limits the optical properties of the quantum well. Four samples were grown in an attempt to probe the quality of the nucleation layer under different conditions. In addition, two samples were grown to probe the relationship between the final GaAs QW growth temperature and the structural quality of the ZnSe/GaAs QW. A summary of the samples and the growth conditions are provided in Table 3-2 for reference.

#	Sample ID	Nucleation layer thickness (ML)	GaAs QW Growth T (°C)	Final RHEED
1	z302r345	0	350	fishnet
2	z306r358	1	350	spotty bulk
3	z307r356	2	350	spotty faint c(4x4)
4	z304r351	3	350	c(4x4)
5	z308r357	3	400	c(4x4)
6	z313r368	3	450	fishnet bulk
7	z305	0	no QW	

Table 3-2. Nucleation study sample descriptions: nucleation layer thickness, GaAs QW growth temperature, and final RHEED reconstruction.

In the first case, the 250°C nucleating layer was removed, and nucleation was performed at 350°C. The resultant surface diffraction pattern showed an unreconstructed GaAs layer with a strong fishnet pattern. The fishnet pattern became evident within 1 monolayer, indicating a rough surface Figure 3-10.

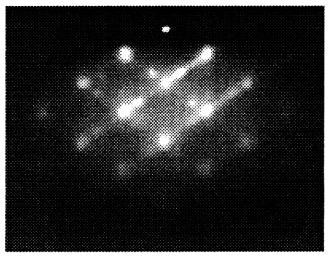

Figure 3-10. An example of the fishnet pattern seen during the nucleation of the GaAs on the lower ZnSe barrier layer without the nucleation layer.

In the second case, 1 ml of 250°C GaAs was nucleated on the ZnSe surface. The remainder of the GaAs layer was grown at 350°C, with 4 monolayers of SM-MBE. While this case showed no fishnet pattern, the surface never reconstructed and a spotty bulk pattern remained. The spotty bulk RHEED pattern for the GaAs surface is a slight improvement over the fishnet pattern, however the pattern is still not indicative of a two-dimensional growth surface.

In the third case, 2 monolayers of 250°C GaAs were nucleated on the ZnSe surface. The remainder of the GaAs was grown at 350°C, with the first 3 monolayers by SM-MBE. In this instance, a c(4x4) reconstructed surface was visible after the 2nd monolayer was deposited and the substrate was ramped to 350°C. However, the final reconstruction showed broad integer order streaks along with the reconstruction. The presence of integer order streaks in the RHEED pattern for the GaAs indicates that the surface is showing signs of two-dimensional reconstruction. However, the broadening of the streaks indicates surface roughness.

In the last case, 3 monolayers of 250°C GaAs were nucleated on the ZnSe surface. As in the previous growth, c(4x4) reconstruction was visible by the completion of the ramp to 350°C. The final RHEED pattern showed a reconstructed As-rich surface, and was somewhat of an improvement over the previous case.

Based upon these four experiments, the successful nucleation of GaAs on ZnSe requires 3 monolayers of GaAs grown at 250°C. It seems that full surface coverage of the ZnSe occurs at this point. This result is further supported by atomic force microscope measurements of the surfaces of the samples grown for this nucleation study.

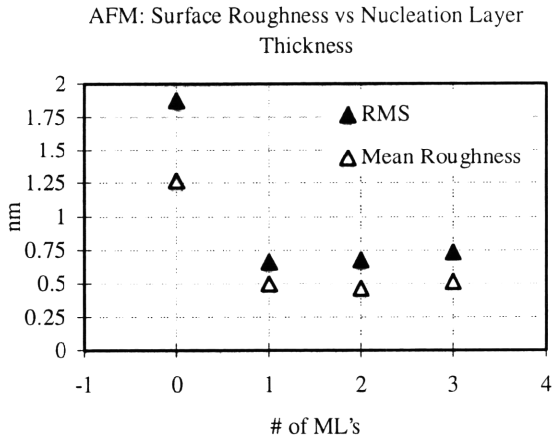

Figure 3-11. AFM measurements of the root-mean square (RMS) and mean surface roughness over a 1 mm square area of the ZnSe/GaAs QW samples from the nucleation study as a function of the number of monolayers (ML's) of GaAs deposited at 250°C.

This series of nucleation studies was expanded by increasing the temperature of the GaAs grown beyond the first three monolayers. The remainder of a 6 nm GaAs single quantum well was grown at 400°C and 450°C. The resultant RHEED reconstruction was an improvement upon the same structure grown at 350°C. However, at the 400°C temperature, the reconstruction of the 3 monolayers of GaAs grown at 250°C showed a 3-fold reconstruction in the [011] direction and a 4-fold reconstruction in the [001] direction. This suggests either Zn diffusion into the three monolayers or a Ga-rich surface.

For the growth at 450°C, the starting surface of 3 monolayers of GaAs grown at 250°C showed a spotty bulk diffraction pattern. Two monolayers of GaAs were grown at 450°C by single layer MBE with an As:Ga ratio of 3:1. The resultant RHEED pattern remained spotty. The remainder of the 6 nms of GaAs was grown by standard MBE. The surface diffraction during this growth was bulk with a fishnet pattern. The results from this experiment suggest that although 3 monolayers of the LTGaAs are sufficient to cover the ZnSe surface, they are not sufficient to avoid the formation of islands as the substrate temperature was raised. Atomic force microscopy (AFM) measurements of the surface of the ZnSe/GaAs QWs with the GaAs well material grown at different substrate temperatures shows a marked increase in the surface roughness as the growth temperature increases (Figure 3-12).

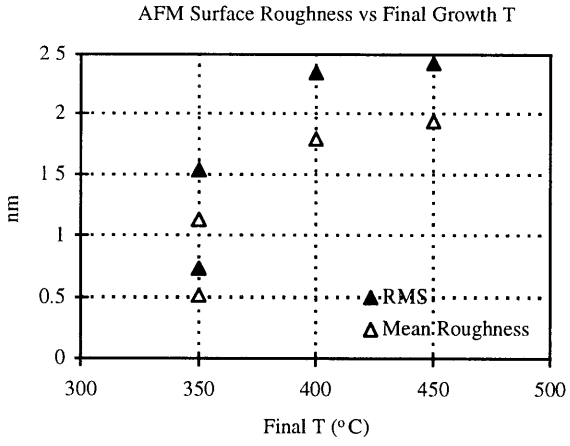

Figure 3-12. Atomic force microscope surface roughness results from the ZnSe/GaAs QWs that were grown with a variation in the final growth temperature of the GaAs well material.

In summary, the successful growth of a "two-dimensional" GaAs single quantum well with ZnSe barriers requires the presence of a low-temperature GaAs nucleation layer. The nucleation layer is grown by single layer MBE, with a high As:Ga ratio of 12:1 at 250°C. The dimensions of the nucleation layer depend upon the ultimate temperature of the GaAs grown for the remainder of the quantum well width. A layer of 3 monolayers is sufficient to achieve full surface coverage of the ZnSe when followed by growth of GaAs at 350°C or 400°C. However, for GaAs grown at 450°C, the 3 monolayer nucleation layer forms islands and does not provide a smooth starting surface.

3.6 Summary

The fabrication of ZnSe/GaAs QWs and DBHs by molecular beam epitaxy has been presented. Background information regarding the optimal growth conditions for the ZnSe and GaAs layers and the growth system employed was given. This was followed by the calibration of the III-V growth parameters.

Next, the nucleation of GaAs on ZnSe was examined; three methods were compared. The highest quality GaAs layer resulted when a methodology called single monolayer MBE (SM-MBE) was employed. The SM-MBE GaAs nucleation requires an As_2 over-pressure maintained in the growth reactor and the equivalent of single monolayer exposures to Ga followed by short anneals of the surface. The substrate temperature begins at 250°C and, by the tenth monolayer, is ramped to 350°C. The As_2 :Ga ratio is varied from 12:1 to 1:1 by the tenth monolayer. By the third monolayer of GaAs nucleation, the surface RHEED pattern exhibits integer order beams. RHEED surface reconstruction appears by the sixth monolayer, indicating a c(4x4) As-rich GaAs surface, and remains throughout the GaAs layer growth. The ten monolayers of GaAs that are grown by SM-MBE constitute the nucleation layer. The remainder of the GaAs layer was grown at 350°C under stoichiometric conditions.

The epitaxial growth of the entire ZnSe/GaAs QW and/or DBH follows the standard parameters for ZnSe growth and the SM-MBE parameters for the GaAs layer. The growth

of the ZnSe layers was initiated by 60 seconds of Zn exposure and followed by MBE growth under slightly Se-rich conditions (as indicated by a (2x1) RHEED surface reconstruction. The sample was transferred *in situ* between the growth reactors for each layer. The GaAs layer was nucleated on the lower ZnSe barrier layer by SM-MBE for the first ten monolayers and then grown by MBE at 350°C for the remainder of the layer.

A series of 6 nm ZnSe/GaAs QWs were grown with variations in the GaAs nucleation layer thickness and the substrate temperature of the GaAs QW growth. Four QWs were grown with the number of monolayers of GaAs grown at 250°C varied from 0 monolayers to 3 monolayers. RHEED patterns monitored during the GaAs growth indicate that the highest quality GaAs layer resulted when the full 3 monolayers were deposited. The substrate temperature of the GaAs QW growth was varied in three heterostructures from 350°C to 450°C. The RHEED patterns of the GaAs layer during the growth indicate that the highest quality GaAs QW resulted when the substrate temperature was either 350°C or 400°C. Atomic force microscope measurements of the surface of the 6 nm ZnSe/GaAs QWs show similar trends in the surface roughness to the results from the RHEED surface analysis.

4. Optical characterization

One of the motivating forces behind the study of ZnSe/GaAs quantum wells (QWs) is the ability to excite an optical signal from the GaAs well material or detect an optical signal directed at the GaAs well material. It is important to have an understanding of the optical properties of the materials grown in this study; two simultaneous efforts were made to investigate the optical properties of the ZnSe/GaAs QWs. Work by David Dougherty investigated the carrier lifetime and the photoreflectance of the ZnSe-on-GaAs heterointerface, as well as in the ZnSe/GaAs single QW [1]. Secondly, an investigation was made of all heterostructures grown by a technique called photoluminescence (PL) which is presented in this study.

Photoluminescence serves as a non-destructive optical measurement of a semiconductor material that has a direct energy band-gap. During the course of the measurement, an excitation source such as a laser is focused upon the sample surface at a known angle. The photonic excitation penetrates the semiconductor surface according to the absorption length of the material and excites the electrons in the sample to higher energy levels. Depending upon the time of electron decay back to the equilibrium energy level, the electrons either emit a photon characterized by an energy equal to the energy difference between the excited state and the equilibrium state, or the electron is absorbed into a non-radiative recombination site which decreases the PL signal from a material. In the instance that the electron non-radiatively recombines, the photonic excitation serves to provide energy for the recombination. For this study, the measurement was made at low-temperatures (10 K). At higher temperatures, the PL signal from a material would be reduced by the thermal ionization of impurities and dopants in the ZnSe and GaAs layers.

The following sections describe the information that can be obtained from a PL measurement, the PL system, and the results from the optical measurements made on the materials in this study.

4.1 Information to be obtained from PL

The photoluminescence of a material has three important characteristics: the optical energy, the intensity of the signal, and the full width at half maximum (FWHM) of the signal. The following paragraphs discuss the information provided by these different parameters.

The optical energy of a PL feature is indicative of the energy states in the material. For example, the PL of a semiconductor often shows a feature near or at the band-gap energy. Impurity doping in the semiconductor will shift the band-gap feature energy to a lower level since the impurity band in a semiconductor sits inside the energy band-gap. Strain in a semiconductor material will cause the light and heavy hole energy bands to separate energetically by a few meV, and the band-gap energy-related PL feature will be split according to the degree of strain. For quantum well structures, the first electron and hole confinement levels are detected using PL. The energies of the confined carrier states are a function of the width of the potential well in a QW (i.e. the width of the GaAs). Hence, the peak PL energy of a QW gives some information about the thickness of the well material.

The intensity of the PL signal is a function of both the experimental set-up and the material being measured. The angle of impingement from the excitation source, as well as the excitation power density will affect the depth over which the sample signal can be detected. Also, the low-temperature measurement of the sample allows for more intense band-edge related PL features. With the optimization (or at least the consistent operational set-up) of the angle of impingement, the power density, and the measurement temperature, the changes of the PL signal intensity across different semiconductor samples is a function of the sample quality. At one extreme, PL signal intensity at the band-edge is reduced by impurity states and non-radiative recombination sites. At the other extreme, the band-edge related PL signal is reduced by a high incidence of free-exciton generation and recombination. Free-excitons are electron-hole pairs that form with a few meV, and are free to move around the material once formed. As a result, the probability of optical

emission is reduced as the free-exciton moves away from the original site of the photonic excitation.

The FWHM of the PL feature of a semiconductor is related to the quality of the material. A broadened feature means that there is a range of energies over which the electrons can recombine. In a QW structure, broadening often indicates that the well material is not of uniform thickness, or that the heterointerfaces are rough. For a single layer of semiconductor material, the FWHM of the PL features can indicate that there is an impurity band of energy levels within the energy band-gap.

All three properties of a PL signal are important in the study of the ZnSe/GaAs QW. The energy of the PL signal is indicative of both the presence of electron and hole confinement and the thickness of the well material. The intensity of the PL signal provides information regarding the purity of the materials in the heterostructure. Finally, the FWHM of the PL signal provides information about the structural uniformity of the QW and the impurity levels in the heterostructure.

4.2 System description

The experimental set-up for the photoluminescence measurement is divided into four subsystems: temperature control, optical pumping, optical detection, and data acquisition (Figure 4-1). The first of these, temperature control, consists of a closed-cycle compressed helium Janis cryostat. The cryostat is evacuated to less than 10^{-4} Torr with a combination of a mechanical roughing pump and a molecular drag pump. The cryostat is capable of maintaining a stable temperature of 10 K. Several samples are simultaneously mounted inside the cryostat. The sample temperature is monitored and controlled, with a range of 10 K to 330 K, using a silicon diode attached to the base of the sample holder.

Simultaneously mounting multiple samples has several advantages. Not only is the experiment less time-consuming, the conditions under which the PL data is taken are assuredly the same for each sample. This allows for a more accurate comparison of the

energies and intensities of the PL features, especially when the measurements are taken over a range of temperatures.

The PL system was calibrated for power density and chromatic aberration. The details of this calibration process are presented in [92].

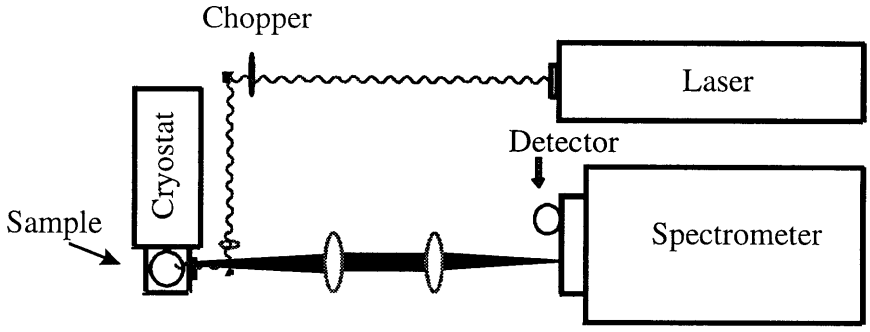

Figure 4-1. The photoluminescence system used in this study.

4.2.1 Optical Pumping

The sample is optically pumped by a laser beam. Three different types of lasers were implemented in this study: a 325 nm He-Cd laser (for II-VI and large band gap III-V materials), a 632.8 nm He-Ne laser (for narrow band gap III-V materials), and a 514.5 nm Ar laser (for narrow band gap III-V materials). The laser emission energy must be larger than the band gap energy of the material in order to excite electrons across the band gap. The power density can be varied from a few mW/cm^2 to hundreds of W/cm^2 by changing the laser spot diameter on the sample's surface. The laser power can also be varied using neutral density filters. Both the He-Cd and the He-Ne lasers are similar in power (~ 8 mW), but the He-Ne laser has a slightly larger spot size than the He-Cd laser. The Ar laser has up to 6 Watt emission capability with a variable spot size.

The lasers travel similar paths to the sample. First, the beam passes through an optical chopper and is focused with a lens onto the sample surface. A large power loss occurs mainly at an interference filter, which transmits about 25% of the primary laser line. An example of the final laser power at the sample surface for a He-Cd or He-Ne source is around 0.45 mW, and the spot diameter is approximately 300 μm, corresponding to a

power density of 0.64 W/cm^2. The laser is optically chopped to create a modulated signal at the sample surface. As a result, it is possible to differentiate between the PL signal and any spurious noise at the data acquisition stage.

4.2.2 Optical Detection

The optical detection subsystem consists of two lenses, a Hamamatsu photomultiplier tube or a silicon photodetector, and a 1/2 meter Jarrell Ash spectrometer. The luminescence from the sample surface is collected using two lenses. The first lens collects and collimates the luminescence from the sample. The second lens focuses the luminescence onto the slits of the spectrometer. The spectrometer is scanned over a range of wavelengths. As the spectrometer passes a wavelength corresponding to the luminescence, the light leaves the spectrometer at a second set of slits. A photomultiplier tube detects and amplifies this light with a gain of up to 10^6. The wavelength calibration of the spectrometer is made by collecting a second harmonic laser line from the He-Cd laser at 650 nm.

4.2.3 Data Acquisition

The signal from the photomultiplier tube and the corresponding wavelength setting of the spectrometer are collected in the data acquisition subsystem. This part of the PL system is primarily a lock-in amplifier, a preamplifier, and a computer. The frequency of the optical chopper is sent to the lock-in amplifier, along with the signal from the photomultiplier tube (which has been first sent through a preamplifier-amplifier). For a given time constant, the lock-in demodulates the signal from the photomultiplier tube and sends the average to the output and, eventually, to the computer. This process reduces the level of background noise, and allows for the detection of signals as small as 1 μV. The analog output of the lock-in amplifier is digitized by a computer equipped with an analog-to-digital converter. The data over a given range of wavelengths is analyzed with the aid of computer software [93].

The resulting PL spectra are an indication of the optical quality of the material. Changes in the PL parameters (measurement temperature and excitation power density) can be used

to study different effects in the PL, such as the introduction of increasing levels of ionized impurity levels contributing to the optical signal of a material as the PL temperature is increased.

4.2.4 System Limitations

The spectrometer has a resolution limitation on the order of 0.8 nm, or 4 meV at energies near 2.7 eV and 3 meV at energies near 2.4 eV when the slit width used is 50 μm. For a higher resolution system (with a 1 meter spectrometer), the FWHM for the same feature has been reported to be as small as 0.3 meV [94]. However, the spectrometer in the PL system has an optimal resolution of 0.2 nm, or 0.6 meV, for narrower slit widths. Closing the slits further reduces the collected luminescence to the extent that the noise in the detection and acquisition electronics exceeds and distorts the PL signal. Hence, a compromise between resolution and signal level is maintained with a less than optimum slit width. The set-up described in the previous sections is nearly identical to that used in [92].

4.3 Results

The following sections provide the experimental results from the PL measurements of the materials investigated in the study of ZnSe/GaAs heterostructures. The PL of multiple GaAs quantum wells with InGaP barriers is presented, with the GaAs grown at different temperatures. These results are followed by the PL of ZnSe grown on GaAs. Finally, the full ZnSe/GaAs/ZnSe mixed heterostructure results are provided. In all cases, the results are given in comparison to PL spectrum provided in the technical literature.

4.3.1 Measurement of control structures

Multiple GaAs quantum wells with InGaP barriers were grown to study the properties of GaAs grown at a reduced temperature. These results were compared with PL data presented in the literature by Seifert, *et al* of a multiple QW of InGaP/GaAs (see Figure 4-2) [95]. In Figure 4-2 the x-axis denotes energy (eV) and the y-axis denotes the intensity (arbitrary units). Each peak in the PL spectra originates from a different layer in the InGaP/GaAs multiple QW, as a function of either material composition or thickness. The

thickness of each QW is labeled above the corresponding PL feature. As shown, luminescence is detected from each quantum well as the thickness of the well is varied. The GaAs substrate peak and InGaP buffer layer PL is also visible. Siefert's data also shows broadening in the narrower QWs of 3 monolayers and 1 monolayer (1 monolayer is ~ 0.28 nm). This broadening is a function of excitonic interaction with irregular interfaces. The excitonic diameter in GaAs is roughly 10 nm.

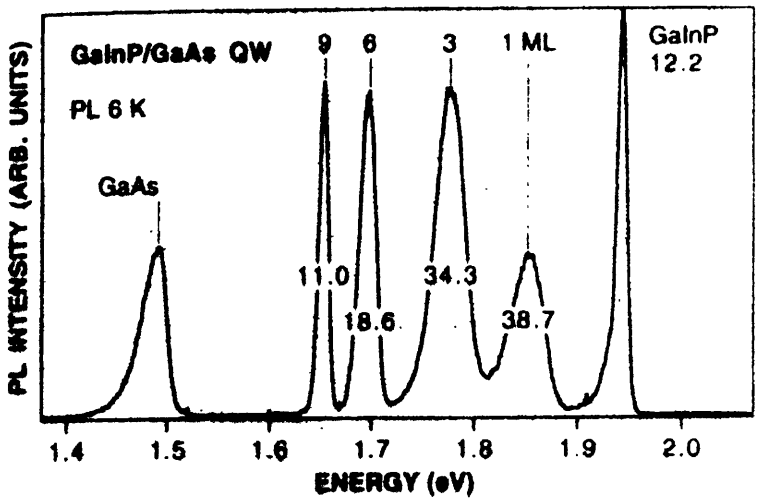

Figure 4-2. The 6 K PL spectra of GaAs/GaInP QWs. The thickness of each QW is given above the corresponding PL feature in units of nm unless otherwise noted. The FWHM (meV) of the QW PL features are superimposed on the corresponding feature. Also shown are the PL features from the GaAs substrate and the GaInP barrier layers [95].

In order to understand the optical properties of the GaAs grown at reduced temperatures, for this study a series of InGaP/GaAs multiple QW structures were grown, where the substrate temperature was stepped down in 50°C increments from the standard InGaP growth temperature of 470 °C to 250 °C, at an As:Ga ratio of 1:1. The PL results for the heterostructures are shown in Figure 4-3 and Figure 4-4. The GaAs QWs were grown with decreasing widths such that the PL feature energy corresponding to the first confined state would shift to a higher energy. Hence, each QW was grown at a different thickness and substrate temperature, enabling direct characterization of the GaAs grown at each substrate temperature.

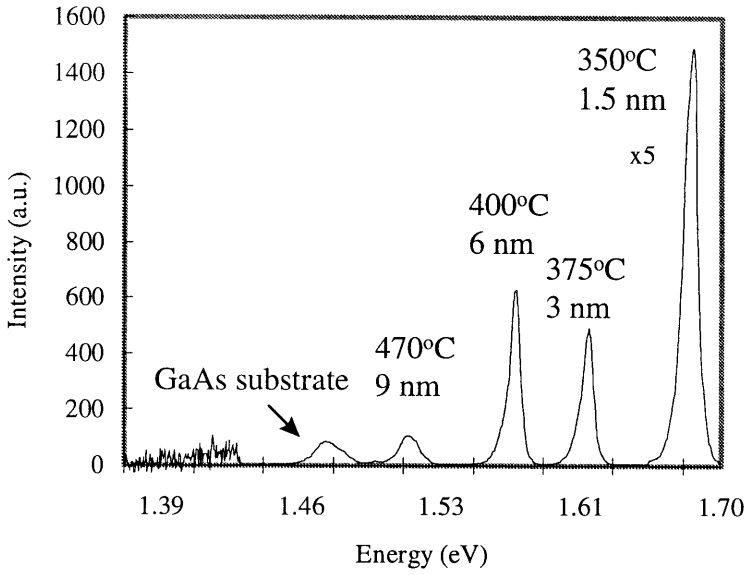

Figure 4-3. The 10 K PL of InGaP/GaAs MQW showing PL from GaAs grown at 350°C. A PL feature is seen from each QW grown at incrementally lower substrate temperatures. The intensity of the luminescence from the 1.5 nm QW grown at 350°C has been magnified 5x.

Figure 4-3 shows the 10 K PL from an InGaP/GaAs multiple QW consisting of a 9, 6, 3, and 1.5 nm thick QW grown at 470 °C, 400 °C, 375°C, and 350°C, respectively. The presence of PL from the first confined state of the 1.5 nm thick GaAs QW indicates that at an As:Ga ratio of 1:1, the GaAs material has a long enough carrier lifetime to achieve a detectable level of radiative recombination. This result is further supported from the PL spectrum of a 9, 6, 3 and 1.5 nm InGaP/GaAs multiple QW heterostructure with the QW's grown at substrate temperatures of 470°C, 350°C, 300°C, and 250°C respectively (Figure 4-4).

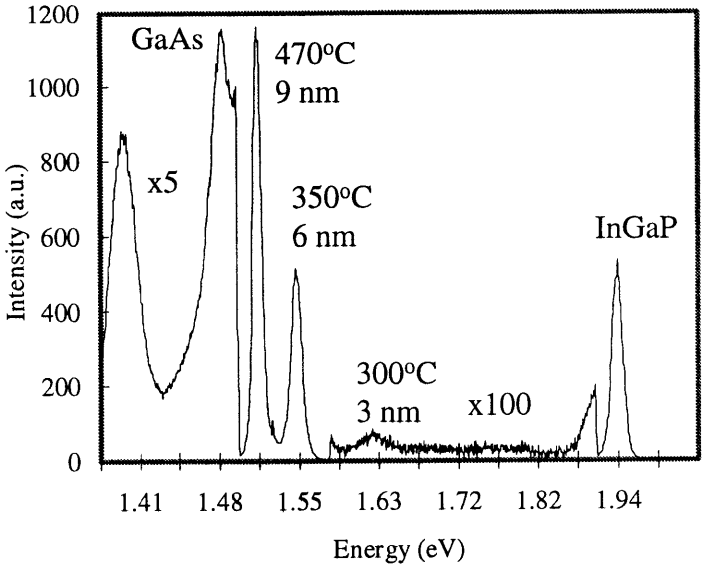

Figure 4-4. The 10 K PL of InGaP/GaAs MQW showing luminescence from GaAs grown at 350°C and 300°C. A PL signal is seen from the GaAs QWs grown at substrate temperatures as low as 300°C. The feature from the 3 nm QW grown at 300°C is significantly weaker than that of the rest of the PL spectra, magnified by a factor of 100. The PL from both the substrate and the InGaP barriers and buffer layer are also shown. The low energy feature at and energy of 1.39 eV is believed to result from type II energy-band alignment between the InGaP and the GaAs resulting from the growth of the InGaP at the same reduced temperatures as the GaAs.

In Figure 4-4, the PL signal is not detected for GaAs grown at 250°C, and the signal from the material grown at 300°C is less-intense than the optical signal from the GaAs grown at 350°C by two orders of magnitude. While the presence of an optical signal from GaAs grown at 300°C is encouraging, the small signal intensity suggests a deterioration in the quality of the GaAs material. The reduced signal intensity could also suggest that the InGaP/GaAs heterointerfaces are rough. However, the FWHM of the PL signal for the 3 nm QW is not significantly broadened, which would be expected in the case of interfacial roughness [66].

Based upon the PL results from the InGaP/GaAs multiple QW's, achieving GaAs of optical quality as a function of substrate temperature at stoichiometric growth conditions has a lower limit of roughly 300°C. This limit has implications on the optical properties of the ZnSe/GaAs QWs in this study. It is encouraging that the bulk of the GaAs material in the ZnSe/GaAs QW is grown at 350°C under stoichiometric conditions, because this

material has been shown to be of optical quality. However, the marked reduction in the PL intensity at 300°C suggests that the GaAs nucleation layer in the ZnSe/GaAs QW, grown at substrate temperatures from 250°C to 300°C is not of optical quality. The combination of the low substrate temperature and the off-stoichiometric conditions moves the GaAs nucleation material away from the conditions necessary to achieve a long carrier lifetime and a low impurity level for a PL signal. This result is supported further by work by Missous, *et* al [87, 88]. Since the nucleation layer is thin (6 monolayers), however, its presence is not believed to be the only determinant in the optical properties of the ZnSe/GaAs heterostructure from the GaAs well layer.

4.3.2 Measurement of ZnSe/III-V interface

Work by Franciosi, *et al* indicates a correlation between the PL signal of the ZnSe band-edge and the ratio of Zn:Se used during the nucleation of ZnSe on GaAs [57]. This relationship is demonstrated in Figure 4-5, where the peak energy and the line-shape of the PL feature changes according to the Zn:Se ratio during the ZnSe growth. However, fairly thick layers of ZnSe (1.5 μm) were analyzed in this study.

In comparison, in this thesis the ZnSe in the ZnSe/GaAs DBHs is seldom thicker than 50 nm. The rationale behind this choice was to maintain a heterostructure that was well below the critical thickness of ZnSe on GaAs (~180 nm), and thus to avoid the issue of strain relaxation between the ZnSe and the GaAs in the characterization of the heterostructures. The PL signal from such a small layer will be significantly less intense and more difficult to analyze.

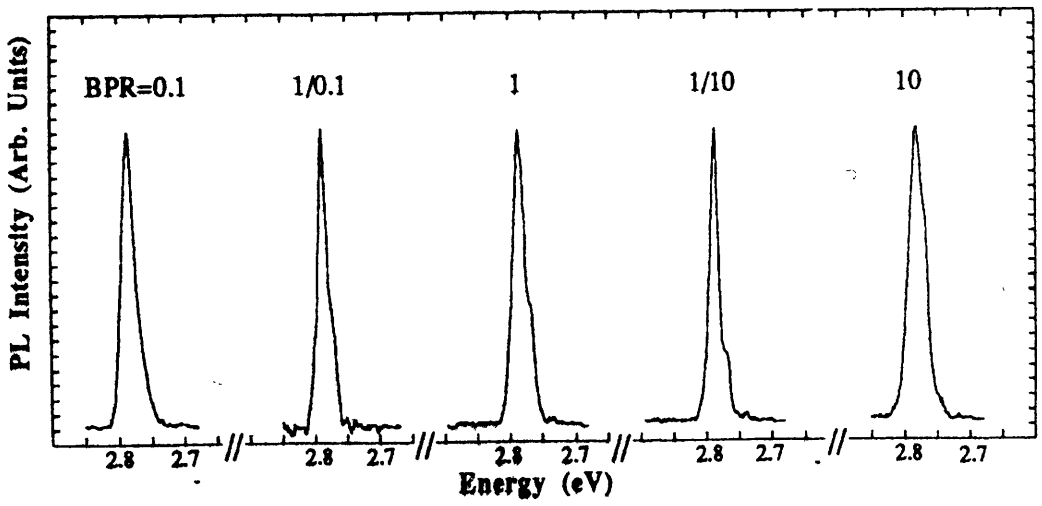

Figure 4-5. Photoluminescence spectra at 18 K emphasizing the extrinsic emission in ZnSe-GaAs(001) heterostructures grown with different Zn:Se beam pressure ratios [57].

Figure 4-6 shows a typical 10 K PL spectrum at the ZnSe band-edge from a ZnSe/GaAs QW. In this case, the QW was 6 nm thick. The band-edge feature is fairly weak, about 3 orders of magnitude below the optical signal from a ZnSe layer that is 1 μm thick. In comparison to the results shown in Figure 4-5, the fairly symmetric lineshape of band-edge ZnSe PL feature is conducive with the Se-rich growth conditions for the ZnSe/GaAs QWs.

The FWHM of the PL feature (12.7 meV) is roughly double that of the FWHM of a single ZnSe layer grown under optimal conditions on a GaAs substrate (~5 meV) [96]. The PL signal from the ZnSe/GaAs QW originates from both ZnSe barrier layers. The broadening in the FWHM for the band-edge signal could come from the top barrier contribution to the PL signal, since the starting surface for the growth of this ZnSe layer is rougher as a result of the reduced temperature GaAs well growth. Figure 4-7 shows the PL spectra from 100 nm of ZnSe grown on InGaP. The FWHM (as indicated on Figure 4-7) of the band-edge PL feature for this ZnSe layer is closer to that of a thicker ZnSe layer. Because the ZnSe layer thickness is the same as the combined thickness of the two ZnSe barriers in a ZnSe/GaAs QW, it provides a useful comparison for determining the origin of the PL feature broadening shown in Figure 4-6. The PL intensity in both cases is similar,

indicating that the ZnSe in the ZnSe/GaAs QW is not significantly reduced by non-radiative recombination sites which would reduce the radiative emission from the ZnSe.

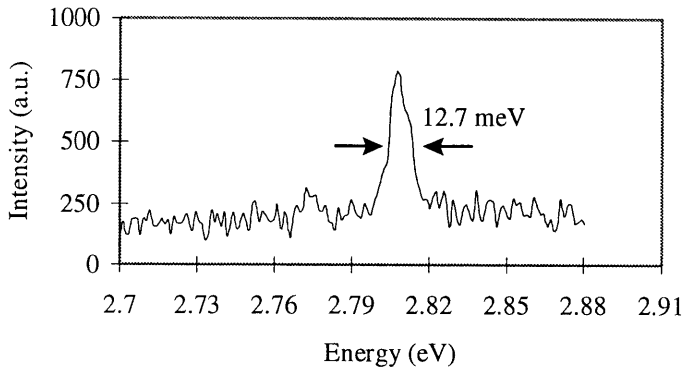

Figure 4-6. Typical PL spectra from the ZnSe band-edge for a ZnSe/GaAs QW. The FWHM of 12.7 meV is broader than that for thicker ZnSe layers or for single ZnSe layers grown on III-V surfaces.

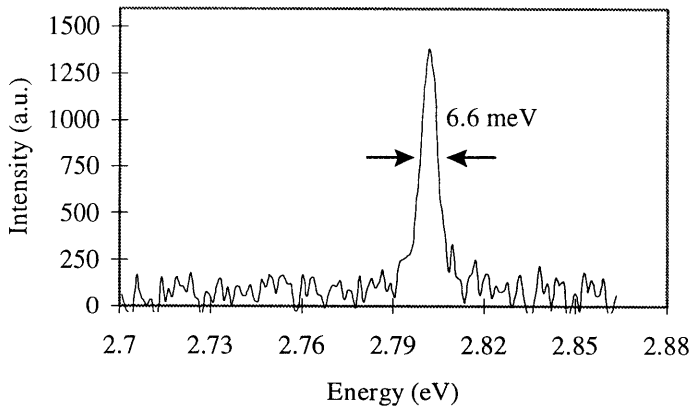

Figure 4-7. The 10 K PL spectra from 100 nm of ZnSe grown on InGaP. The FWHM of 6.6 meV is closer to the FWHM from the band-edge PL of thicker ZnSe layers grown on III-V layers than that originating from a ZnSe/GaAs QW.

The thin ZnSe barrier layers in the ZnSe/GaAs QWs did not exhibit a PL signal solely from the band-edge. A defect band centered at an energy ranging from 2.15 eV to 2.3 eV with an intensity of the same order of magnitude of the band-edge PL feature was evident as well. The defect band offers evidence of a deep-level impurity within the ZnSe energy gap. Thin ZnSe layers grown on InGaP do not exhibit the same defect-related PL feature.

The defect-band in the ZnSe/GaAs QW PL is hypothesized to originate from the bottom ZnSe barrier. This analysis is supported by the resultant FWHM of the defect band PL feature as a function of the final growth temperature of the GaAs well material (see Figure 4-8). The FWHM of the defect-band feature increases with increasing GaAs substrate growth temperature. The higher substrate temperature effectively anneals the lower ZnSe barrier layer and generates a broader band of impurity states within the ZnSe energy-gap. The higher growth temperature of the GaAs well material is expected to reduce the surface roughness of the GaAs surface for the top ZnSe barrier layer. Hence, it would be expected that the PL feature from this layer would be improved by higher GaAs growth temperatures.

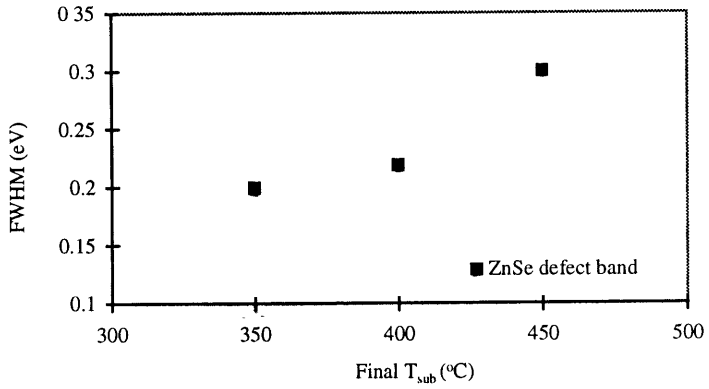

Figure 4-8.The FWHM of the ZnSe defect band PL feature increases as a function of the final GaAs growth temperature for a 6 nm GaAs QW with ZnSe barriers.

The optical properties of the ZnSe layers in the ZnSe/GaAs QWs and DBHs have been investigated by low-temperature PL. A band-edge signal indicates that the ZnSe layers in combination are of fairly high optical quality. However, the FWHM of the band-edge feature is broadened in comparison to the band-edge feature of a 100 nm ZnSe layer grown on InGaP. The broadening is believed to originate from the top ZnSe barrier layer, as a result of the rough starting surface of the GaAs well material upon which the ZnSe barrier was nucleated. A deep-level impurity band is also evident in the ZnSe PL from the ZnSe/GaAs QWs and DBHs. Since the defect band feature broadens with the final growth

temperature of the GaAs well, the bottom ZnSe barrier layer is believed to be the primary source of this PL feature.

4.3.3 PL of GaAs (ZnSe on reduced temperature GaAs)

In order to understand the interaction of the reduced temperature GaAs layer with the ZnSe barriers, heterostructures were grown with GaAs sandwiched between one layer of ZnSe and one layer of InGaP. The InGaP material was selected because the PL of the reduced temperature GaAs QWs with InGaP barriers indicated that the InGaP/reduced temperature GaAs heterointerface was of high enough quality to achieve luminescence from the first confined state of the GaAs QW. In the first case, heterostructures of a 50 nm ZnSe barrier grown on a GaAs QW of either 6 nm or 100 nm thickness on a 1.5 μm InGaP layer were grown. In the case of the heterostructure with the 100 nm GaAs layer, an InGaAs layer was grown before the InGaP layer to block luminescence from the GaAs substrate.

Low temperature PL measurements of the 100 nm heterostructures using an argon laser excitation source with a wavelength of 514.5 nm indicate luminescence from the reduced temperature GaAs material (Figure 4-9). However, the PL from the reduced temperature GaAs has an intensity that is 3 orders of magnitude lower than that of the InGaP PL feature. For the case of the 6 nm GaAs heterostructure, there is no evidence of a PL signal from the reduced temperature GaAs. Figure 4-10 shows the 10 K PL from the 6 nm GaAs heterostructure, indicating PL from the GaAs band-edge and the InGaP buffer layer.

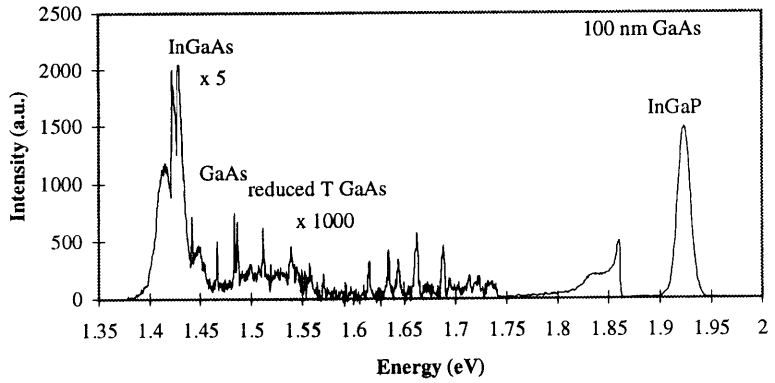

Figure 4-9. 10 K PL from a ZnSe/GaAs 100 nm/InGaP/InGaAs heterostructure. Features from all of the III-V layers are detected, however the luminescence from the reduced T 6 nm GaAs layer is less intense by 3 orders of magnitude than the PL from the InGaP features.

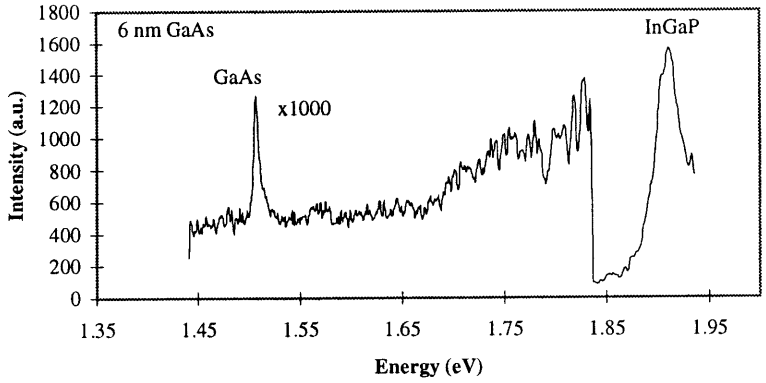

Figure 4-10. 10 K PL spectra of a ZnSe/GaAs 6 nm/InGaP heterostructure. Features from the GaAs substrate and the InGaP buffer layer are present.

The combined results from the 100 nm and the 6 nm GaAs heterostructures indicate that the thickness of the reduced temperature GaAs material is important in achieving a detectable level of luminescence. It is important that the "well" material in these two heterostructures was grown without the nucleation layer, as the GaAs was grown on InGaP. Hence, the interface that is potentially limiting the successful detection of PL from the reduced temperature GaAs is the one formed by the growth of ZnSe on reduced temperature GaAs.

4.3.4 PL of GaAs (reduced temperature GaAs on ZnSe)

The PL properties of a GaAs layer grown on ZnSe were also investigated. An InGaP cap layer was grown on the surface of the GaAs material in order to ensure that the GaAs material was not depleted due to surface states which would reduce the GaAs PL efficiency. Two heterostructures were investigated with a 6 nm and a 100 nm thick GaAs layer sandwiched above a 50 nm ZnSe layer and below a 50 nm InGaP layer. The PL spectrum of the 6 nm GaAs heterostructure shows luminescence from the reduced temperature GaAs, with an intensity that is 2 orders of magnitude less than that of the PL from the GaAs substrate. The PL spectrum for the 100 nm GaAs heterostructure is complicated by the InGaAs buffer layer, which overlaps the expected PL feature energy of the reduced temperature GaAs. As a result, it is difficult to ascertain whether or not a PL feature can be detected from the reduced temperature GaAs in the 100 nm GaAs heterostructure. However, measuring PL from the reduced temperature GaAs in the 6 nm GaAs heterostructure indicates that the nucleation layer does not have far reaching effects on the optical properties of the GaAs QW.

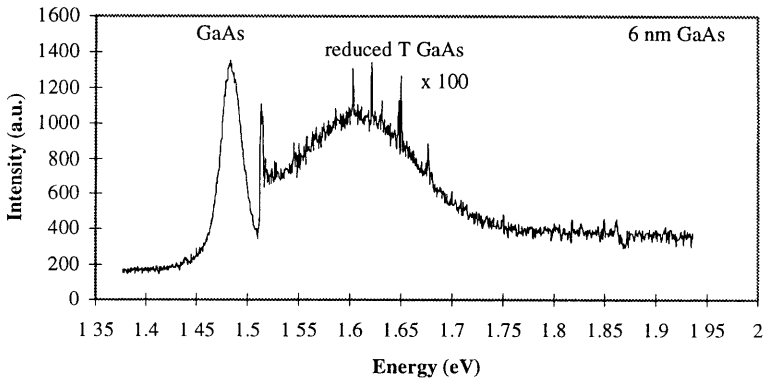

Figure 4-11. The 10 K PL spectra of an InGaP/GaAs 6 nm/ZnSe/GaAs substrate heterostructure. Features from both the GaAs substrate and the reduced temperature GaAs are shown.

Up to this point in this study, the results have been presented regarding the optical quality of the reduced temperature GaAs measured by low temperature PL using InGaP/GaAs multiple QW structures. The reduced temperature GaAs has been shown to be of optical quality when grown at substrate temperatures as low as 300°C under stoichiometric

conditions. The ZnSe in the ZnSe/GaAs QW structure has also been evaluated by PL. The ZnSe barrier layers have exhibited both band-edge luminescence and a deep-level impurity band. The band-edge luminescence is slightly broader than a single 100 nm ZnSe layer grown on InGaP, and this broadening is believed to result from the nucleation of the ZnSe on the reduced temperature GaAs "well" layer. The defect band PL feature has been shown to result from deterioration of the ZnSe layer quality during the elevated substrate temperature of the GaAs QW.

The optical properties of the reduced temperature GaAs QW layer have also been evaluated in conjunction with each ZnSe barrier layer. A ZnSe/GaAs/InGaP heterostructure shows PL spectra originating from the reduced temperature 100 nm GaAs layer. However, there is no evidence of a PL signal from the reduced temperature 6 nm GaAs layer. The results from these two ZnSe/GaAs/InGaP heterostructures indicates that the properties of the ZnSe on GaAs interface affects the reduced temperature GaAs layer for at least 6 nm. The inverted heterostructure, InGaP/GaAs/ZnSe, has a detectable level of PL from the reduced temperature GaAs for a 6 nm GaAs layer thickness. This result indicates that the nucleation layer does not have far-reaching effects on the optical properties of the reduced temperature GaAs layer.

4.3.5 PL of ZnSe/GaAs QWs and DBHs

Based upon the PL results presented thus far, a logical progression in the study of the ZnSe/GaAs QWs would be to probe for luminescence from the central GaAs layer with ZnSe barriers. PL measurements have been taken of a series of ZnSe/GaAs QWs and DBHs:

- GaAs layer thickness ranging from 3 nm - 100 nm
- 8 nm ZnSe/GaAs QWs grown on ZnSe and GaAs substrates
- 100 nm ZnSe/GaAs DBHs grown on ZnSe and GaAs substrates
- p- and n-type doped 3 nm ZnSe/GaAs QWs
- p-type delta-doped heterointerfaces in a 3 nm ZnSe/GaAs QW

- nucleation layer thickness ranging from 0 monolayers to 3 monolayers in a series of 6 nm ZnSe/GaAs QWs
- GaAs QW growth temperature ranging from 350°C to 450°C in a series of 6 nm ZnSe/GaAs QWs

Regardless of the central GaAs layer dimensions, the growth parameters for the GaAs, the substrate type, and the doping in the QW- no PL signal was detected from this layer.

4.4 Summary

The key result in this chapter is the unexpected absence of PL detected from the central GaAs layer in the ZnSe/GaAs QWs and DBHs. Each part of the ZnSe/GaAs QW and/or DBH has been separately shown to be of optical quality except for the first 3-6 monolayers of the nucleation layer. The ZnSe barrier layers exhibit band-edge luminescence and, in some instances, a defect band. The presence of the defect band is a function of the quality of the ZnSe/III-V layer heterointerface.

A PL signal from the GaAs QW material grown at 350°C under stoichiometric conditions is detected when the QW is grown with InGaP barriers. InGaP/GaAs multiple QWs with GaAs material grown at temperatures below 350°C under stoichiometric conditions show a decreasing GaAs optical signal intensity (compared to the InGaP buffer layer PL signal intensity) exceeding the lower detection limit for GaAs grown at 250°C. It is expected that deviations from a 1:1 As_2 :Ga ratio during the reduced temperature GaAs growth will further deplete the PL signal intensity.

Both InGaP/GaAs/ZnSe and ZnSe/GaAs/InGaP heterostructures show a detectable level of PL from the central GaAs layer. When the lower barrier layer is ZnSe, band-edge PL is detected from the GaAs layer only for a thick 100 nm layer. However, PL from a 6 nm GaAs QW heterostructure with a ZnSe upper barrier layer and an InGaP lower barrier layer is detected. Thus, effects of the nucleation layer have been shown not to significantly impact the optical properties of a GaAs layer as thin as approximately 20 monolayers.

5. Summary of material fabrication and optical characterization

This chapter begins with a summary of the results of the growth and optical characterization of the ZnSe/GaAs QWs and DBHs. The absence of an optical signal from these heterostructures is surprising, and in the middle of the chapter a set of five explanatory hypotheses are postulated. Finally, two approaches for examining these hypotheses are described; the latter is that used in this thesis.

5.1 Growth optimization

The growth of the ZnSe/GaAs QW and DBHs was achieved using a combination of MBE for the ZnSe layers and GSMBE for the III-V layers. Two challenges to the optimization of the ZnSe/GaAs QW are the mismatch in the optimal growth temperatures for the ZnSe and GaAs (280°C and 580°C, respectively), and the nucleation of the GaAs layer on the lower ZnSe barrier layer. A methodology defined as single-monolayer MBE (SM-MBE) was developed to nucleate the GaAs layer on the lower ZnSe barrier layer. The remainder of the GaAs QW layer was grown by standard MBE, but at a reduced substrate temperature of 350°C with a modified Group III-to Group V ratio. The ZnSe barrier layers were grown by standard MBE, with the nucleation of the ZnSe on the III-V layer initiated by 60 seconds of Zn introduction into the growth reactor before the onset of ZnSe growth.

5.2 Optical properties: PL

The optical properties of the ZnSe/GaAs QWs and DBHs were probed by low-temperature photoluminescence (PL) measurements. *The key result from this analysis was the unexpected absence of an optical signal from the central GaAs layer when ZnSe barriers were employed, regardless of the thickness of the GaAs layer.* Similarly grown GaAs was shown to luminesce when InGaP barriers layers were used. The ZnSe was

shown to exhibit band-edge luminescence, but also included a defect band feature indicating a deep level present in the thin ZnSe layers. The defect band is possibly a partial indication of the quality of the interface of the ZnSe layers with the III-V layers.

5.3 A set of hypotheses

Five explanatory hypotheses for the absence of a PL signal from the ZnSe/GaAs QW are presented. Each hypothesis presumes that a different characteristic of the heterostructure dominates. These characteristics are: interfacial roughness or interdiffusion, GaAs carrier lifetime, energy-band alignment, heterovalent interface properties, and defects and dislocations throughout the heterostructure.

5.3.1 Interfacial roughness or interdiffusion

The quality of a semiconductor heterointerface is crucial to the optical properties of the heterostructure. For a heterostructure composed of III-V compound semiconductors, such as InGaP and GaAs, an ideal heterointerface is both abrupt in the growth direction and flat along the growth front (as exhibited in Figure 5-1). An abrupt heterointerface does not possess any transitional monolayers composed of a combination of all of the constituent elements from the materials at either side of the interface. When such a transitional layer does exist, the heterointerface is considered interdiffused, and the transitional layer can contribute to the PL for the heterostructure by adding a feature corresponding to the transitional layer. For the ZnSe/GaAs heterostructure, an interfacial layer composed of the four constituent elements would have the potential to form a compound with a different lattice structure, such as Ga_2Se_3 which has a defect Wurzite lattice structure [11]. A non-FCC layer at the heterojunctions of the ZnSe/GaAs QW would both alter the energy-band structure and contribute to defects in the rest of the QW.

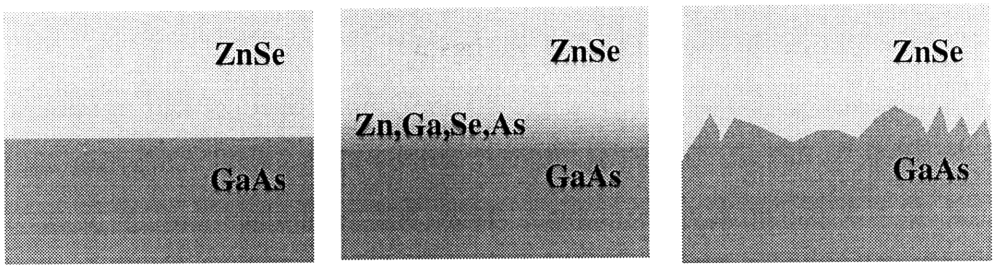

Figure 5-1. Schematics of the different possible conditions of the ZnSe/GaAs interface: abrupt, interdiffused, and rough.

A transitional layer at the ZnSe/GaAs heterointerface could also be composed primarily of either GaAs or ZnSe, with a high level of unintentional doping [97, 98]. For a GaAs-dominated transitional layer, the material can be acceptor impurity doped by interdiffused Zn. A ZnSe-dominated transitional layer can be donor impurity doped by interdiffused Ga. In either case, a high level of doping at the heterojunction between ZnSe and GaAs results in an electric field as the highly doped region interacts with the undoped layers. The electric fields bend the energy-band across the ZnSe/GaAs heterointerface which can inhibit carrier confinement in the GaAs QW [97].

A rough heterointerface, has been shown to affect the PL properties for QWs composed of III-V compound semiconductors [61, 65, 66]. The PL measurement probes the first confined state for both the electrons and holes in a QW. The confined energy for both carrier types is a function of the QW width. A modulation along the growth plane will effectively create a series of QWs of different widths along the length of the QW. As a result, the confined energies for the electrons and holes vary across the growth plane of the heterostructure, and the PL from the QW will thus have a range of energies. For interfacial roughness in a QW grown under two-dimensional conditions, the modulation in the growth plane would be on the order of a few atomic layers, and the PL from the QW would show one broadened, less intense feature [95]. *A decrease in PL signal intensity from a single QW with rough or interdiffused heterointerfaces could push the feature below the level of detection.*

5.3.2 Carrier lifetime in the GaAs QW material

The carrier lifetimes of GaAs and ZnSe grown under optimal conditions are both roughly 1 nsec. This is sufficient for carriers generated by the optical excitation in the PL measurement to radiatively recombine. However, materials grown with a high concentration of impurities, defects, or vacancies, can have a shortened carrier lifetime driven by non-radiative recombination, which can degrade or eliminate the respective PL feature. As previously discussed, GaAs grown under non-stoichiometric conditions at reduced temperatures has a significantly lower carrier lifetime (~ 50 psec for GaAs grown at 300°C).

Both the nucleation layer and the GaAs QW material in the ZnSe/GaAs QW are grown at reduced temperatures. The nucleation layer was grown under non-stoichiometric conditions at a reduced temperature. The first three monolayers of GaAs are deposited at 250°C with an As_2 :Ga ratio of 12:1. It is expected that the carrier lifetime of these three monolayers is below the time required for PL detection because of the absence of PL from GaAs grown at 250°C under stoichiometric conditions in an all III-V-based QW structure. The subsequent three monolayers of GaAs in the nucleation layer are grown at 300°C with an As_2 :Ga ratio of 3:1. PL has been demonstrated from GaAs grown at 300°C with an As_2 :Ga ratio of 1:1, although the signal intensity is very weak indicating that the non-stoichiometric GaAs grown at 300°C will not produce a detectable level of PL. The growth conditions for the bulk of the GaAs QW (350°C and an As_2 :Ga ratio of 1:1) have been shown to result in GaAs material characterized by PL that is within an order of magnitude of intensity of GaAs grown by standard conditions. *While PL has been measured from InGaP/GaAs multiple QWs with the GaAs grown at 350°C and As_2 :Ga ratio of 1:1, the combined properties of the nucleation layer and the GaAs QW could be sufficient to decrease the PL signal from the GaAs QW below the detection limit.*

5.3.3 Type II energy-band alignment

Up to this point, an assumption has been made that the energy-band alignment at the ZnSe/GaAs and the GaAs/ZnSe interfaces is type I. A type I heterojunction allows carrier

confinement in both the conduction and valence bands, as shown in the schematic for a ZnSe/GaAs QW with type I energy-band alignment in Figure 5-2 (a). However, in the instance of a type II energy-band alignment, only one type of carrier would be confined in a ZnSe/GaAs QW. In the schematic in Figure 5-2 (b),the holes are confined in the GaAs valence band, but there is now a barrier to electrons. For a heterostructure in this state, carriers generated across the GaAs band-gap would fall first to the lower energy level in the ZnSe conduction band, and then decay to the ZnSe valence band or tunnel to the GaAs valence band. In either case, the PL signal from the central GaAs layer would be eliminated.

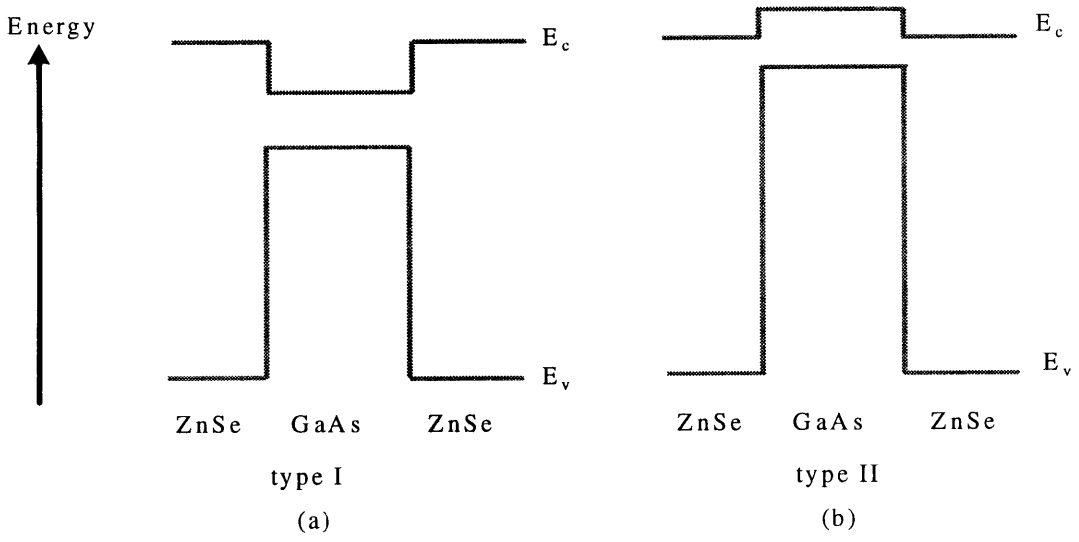

Figure 5-2. Schematic of energy-band diagram for a ZnSe/GaAs/ZnSe QW with type I (a) and type II (b) alignments.

There has been an extensive effort to determine the energy band alignment for the ZnSe on GaAs heterostructure. It is logical that the ZnSe-on-GaAs heterointerface in the ZnSe/GaAs QW aligns in a similar manner to that of ZnSe-on-GaAs grown at the optimal temperature of 580°C. However, little is known about the alignment of the GaAs on ZnSe heterointerface. The study of the InGaP on GaAs heterostructure has been shown to exhibit type II energy band alignment when the InGaP is grown at an elevated temperature [99]. *It is conceivable that the unique growth conditions under which the GaAs layer is nucleated on the ZnSe could form a similar type II interface.*

5.3.4 Heterovalent interface properties

If the ZnSe/GaAs interface is abrupt, the mismatch in the valences of the four elements will result in a sheet of electronic charge at the heterojunction. The electronic charge would be negative for an abrupt Ga-Se interface, and positive for an abrupt Zn-As interface [100]. According to electromagnetic field theory, the electric field that would result from a sheet of charge would be bound only by the surface/air interface of the heterostructure. The presence of such a field at two interfaces would either act to cancel the effects of the fields as they meet at the center of the QW, or would act to reinforce the overall field strength in the heterostructure. In either case, the presence of a strong electric field will alter the energy band of the heterostructure, and has the potential to deplete the area probed by the PL measurement of carriers faster than the carriers can radiatively recombine.

Kassel, *et al*, has measured an interfacial charge of roughly $1x10^{12}$ cm^{-2} for ZnSe/GaAs single heterostructures grown under optimal conditions [97]. Similar results have been found in the work by Dougherty [1]. To date, the GaAs/ZnSe heterostructure has not been probed to for interfacial charge. *Local carrier depletion caused by heterointerfacial charge has the potential to eliminate or reduce the radiative recombination in the ZnSe/GaAs QWs and DBHs.*

5.3.5 Dislocation and defects throughout the heterostructure

Crystal uniformity in the ZnSe/GaAs heterostructure is necessary to achieve an optical signal from the material. Defects such as vacancies that are incorporated during the growth can generate deep impurity levels in the band-gap of both the ZnSe and the GaAs. Larger defects, such as threading and misfit dislocations, can also generate deep levels within the heterostructure, but are more likely to be traps for non-radiative recombination.

The ZnSe-on-GaAs heterostructure has been extensively studied by the blue-green laser community in an effort to eliminate the occurrence of dislocations that spread during lasing, and cause a laser to self-destruct. The types of defects which are known to form at the ZnSe/GaAs heterointerface, and propagate into the ZnSe are fairly well understood.

Strain-reducing misfit dislocations in the form of 60° partial dislocations increase in density as the ZnSe layer approaches the critical thickness. Threading dislocations have also been identified to nucleate as a function of the ZnSe stoichiometry and the growth domain (two- or three-dimensional). Stacking faults have been shown to originate close to the ZnSe/GaAs heterointerface.

The defect structure for the GaAs-on-ZnSe heterointerface has not been thoroughly examined, and is expected to be strongly correlated with the GaAs nucleation process. The comparison of the different approaches to nucleating GaAs on ZnSe was made during the growth by assessing the RHEED surface pattern. Atomic force microscope measurements of the post-growth surface have shown complementary results to the RHEED surface pattern, indicating that the SM-MBE method to the nucleation of GaAs on ZnSe yields superior results to the other approaches taken. *However, a full assessment of the ZnSe/GaAs QW microstructure needs to be made to understand the defects which interrupt the crystal uniformity of the heterostructure and, hence, decrease or eliminate the PL signal intensity from the GaAs well.*

5.4 Description of approach to assessing each hypothesis

Each of the five hypotheses for explaining the absence of an optical signal from the GaAs QW material requires further analysis of the ZnSe/GaAs QWs. Two analytic approaches – optical and microstructural -- have been taken to probe the heterostructures. Optical analyses can provide further information regarding the carrier lifetime, energy-band alignment, and interfacial charge; this approach has been taken by David Dougherty [1]. Microstructural analyses can identify crystal imperfections such as defects, and interfacial roughness or interdiffusion. Three types of microstructural analysis were used to probe the ZnSe/GaAs QWs, and the results are presented in the second part of this thesis.

5.4.1 Optical analyses

The optical properties of the heterostructures have been studied by Dougherty to assess the energy-band alignment, the carrier lifetime and the presence of heterointerfacial electric fields. The methods employed include pump-probe measurements to measure the

carrier lifetimes in both the ZnSe and the GaAs layers. He also assessed the heterostructures, using a combination of photoreflectance and electroreflectance to measure both the energy-band alignment and the magnitude and orientation of interfacial electric fields. The preliminary analysis from these measurements revealed the complexity of probing low-dimensional multi-layer semiconductor heterostructures. As a result, the major part of Dougherty's complete analysis was completed on a the single ZnSe on GaAs heterostructure [1]. The experimental results from the ZnSe/GaAs QWs were not completely analyzed.

An important result from the work by Dougherty is the measurement of the electric field at the ZnSe-on-GaAs heterointerface, as a function of the GaAs doping and starting surface reconstruction. The results from these measurements are shown in Table 5-1. For the pseudomorphic ZnSe/GaAs heterostructures, the electric field is directed from the GaAs layer towards the ZnSe layer, due to a negative interfacial charge. The interfacial electric field increases with increasing n-type doping, as does the valence band offset. In conjunction with the theory by Kley, the negative interfacial charge corresponds to an abrupt Ga-Se interface [100]. In all cases, Dougherty measured a Type I energy-band alignment at the ZnSe-on-GaAs heterointerface. His results are for ZnSe/GaAs heterostructures grown in the same experimental system as the ZnSe/GaAs QWs in this study.

Sample	Thickness	GaAs doping	GaAs reconstruction	Electric field	Charge sign	Offset
	(μm)	(cm^{-3})		(V/cm)		(meV)
z222	0.12	$N_D=7x10^{17}$	4x4	$2.2x10^5$	-	160
z223	0.12	$N_D=8x10^{17}$	4x4	$2.3x10^5$	-	180
z194	0.10	$N_D=6x10^{17}$	4x4	$1.0x10^5$	-	180
n44	0.10	$N_D=1x10^{18}$	4x4	$8.8x10^5$	-	NA
n24	0.10	$N_D=1x10^{18}$	2x4	$7.8x10^5$	-	NA
z350	0.50	$N_D=1x10^{18}$	4x4	$9.5x10^5$	-	250
i44	0.10	SI	4x4	$4.2x10^4$	-	110
i24	0.10	SI	2x4	$3.5x10^4$	-	110
z345	0.50	SI	4x4	$2.8x10^4$	+	NA

Table 5-1. Summary of interfacial field and valence band offset for a ZnSe-on-GaAs heterostructure as a function of ZnSe thickness, GaAs doping (n-type=N_D, semi-insulating=SI), and GaAs starting surface reconstruction [1].

5.4.2 Microstructural analyses

The second approach to probing the ZnSe/GaAs heterostructures further is that of microstructural analysis, which is the work presented in the second part of this thesis. A combination of RHEED, atomic force microscopy, optical microscopy, electron microscopy, analytical electron microscopy and x-ray diffraction measurements have been used to probe for defects, interfacial width and interfacial coherence.

5.5 Microstructural analysis of ZnSe/GaAs heterostructures

The microstructural aspects of the ZnSe/GaAs QWs grown with a range of parameters and physical dimensions are examined using three different analytic techniques. Each of the three techniques provides a different type of information regarding the properties of the ZnSe/GaAs heterostructure. The first, energy dispersive x-ray spectroscopy, measures the spatial composition of the heterostructure and can probe for interdiffusion at the heterojunctions. The second technique, triple axis x-ray diffraction, probes the crystal uniformity within an area defined by a probe diameter of 1 mm. Finally, transmission electron microscopy provides information regarding the cross-section of the heterostructure with the capability of imaging the crystal lattice.

5.5.1 Comparison of methods

In order to understand the spatial resolution and probe depth for each method it is necessary to compare the different types of probes implemented in this study of ZnSe/GaAs QWs (see Table 5-2).

For the case of the photoluminescence measurements, optical excitation was employed using a combination of ultra-violet, red, and green light generated by a He-Cd, a He-Ne, and an argon laser, respectively. In all cases, the probe diameter was focused to a diameter of roughly 300 μm. The different optical sources have different absorption lengths in the ZnSe/GaAs QW, but probe no more than the top 2 μm of the sample. During growth, RHEED surface analysis was achieved with a low-energy, 10 keV, electron beam of diameter of roughly 1mm. The electron beam for the RHEED analysis impinges upon the sample surface at a low angle of 2°, and does not probe much more than 10 nm into the sample as a result.

For the microstructural analysis, an x-ray source and an electron source are implemented. The x-ray source generated from the K_α line for Cu is three orders of magnitude shorter in wavelength than the optical sources employed in the PL measurement. The x-ray source is directed upon the sample surface close to the Bragg angle, and has a varying degree of material penetration as the sample is rotated. However, the x-ray beam probes roughly 10 μm into the sample. The x-ray beam diameter is large enough, 1 mm, to probe almost an "infinite" number of unit cells in the heterostructure. The combination of the large beam diameter with the small wavelength for the x-ray source yields a high spatial resolution, so the x-ray measurement is important for assessing the defect structure over a long-range. The final two probes are electron beams used in the scanning transmission electron microscope and the transmission electron microscope. As high energy electrons are employed, the wavelength of the probe is short enough to allow for a spatial resolution capable of discerning the atomic lattice. For both measurements, the actual spatial resolution is limited by the chromatic and spherical aberrations in the electro-magnetic lenses. The electron beam for both measurements is capable of passing through up to 1

μm of material; however, thinner material is used to reduce the contribution of inelastic scattering to the measurement.

The different types of probes employed in the microstructural analysis are both complementary to the optical probes and to the RHEED electron beam. X-ray analysis can be expected to provide insight into the heterostructure over an area larger than the area probed by the PL measurement. The results from the RHEED surface analysis during the growth can be combined with the electron microscope measurements to understand and to assess the growth process for the ZnSe/GaAs QW.

Probe type	**λ (nm)**	**Probe diameter**	**Probe angle**
He-Ne laser	632.8	300 μm	0° - 10°
Argon laser	514.5	300 μm	0° - 10°
He-Cd laser	325	300 μm	0° - 10°
RHEED e-beam	0.122	1 mm	2°
X-ray Cu K_α	0.154	1 mm	θ_B
STEM (EDS) e-beam	0.0025	1 nm	0°
TEM e-beam	0.0027	1 nm - 10 μm	arbitrary

Table 5-2. Different types of probes implemented in this thesis and the probe dimensions, given in wavelength (λ) and probe diameter.

The analyses of the ZnSe/GaAs QW by x-ray and electron beam probes both rely upon diffraction of the probe by the atomic planes. In the following section, diffraction is discussed in direct relationship to the heterostructures analyzed in this study.

5.5.2 Introduction to diffraction

This section begins with a basic introduction to diffraction theory as applied to the ZnSe and GaAs crystal structures.

There are two different approaches to explaining the diffraction process: kinematical and dynamical. Kinematical diffraction theory assumes that diffraction is a result of single scattering events, and, thus, the crystal is either very small or the periodicity of the crystal structure is disrupted by imperfections. Dynamical diffraction theory allows for multiple scattering incidents contributing to the total diffraction process, and assumes a fairly

perfect crystal. Separately, both theories do not represent the experimental reality for the ZnSe/GaAs heterostructure. The discussion on diffraction is, as a result, given at a basic level with a more thorough explanation of some of the processes important to understanding the microstructural analysis presented in this thesis. Detailed descriptions of kinematical diffraction and dynamical diffraction can be found in several texts on the topic [101-103]. In the microstructural techniques employed, the quantitative analysis of the defect structure is based upon kinematical diffraction theory. Otherwise, dynamical diffraction theory applies more readily to the interpretation of the results.

Diffraction occurs when an electromagnetic wave impinges upon a crystal with a periodicity that exceeds the wavelength of the incident wave. The nature of the diffraction is a coherent form of scattering of the electromagnetic wave determined by the geometry of the material symmetry and periodicity. The diffracted wave is at its most intense when the excitation source is directed upon the material at an angle such that the path length of the electromagnetic wave is the same for the interaction with neighboring lattice planes or points. This relationship is defined by Eq. 1, where d is the lattice plane or point spacing, λ is the wavelength of the incident excitation source, and θ is angle of incidence. When θ is half of the full diffraction angle, it is called the Bragg angle.

$$\lambda = 2d \sin \theta \qquad \text{Eq. 1}$$

The Bragg intensity is a function of the crystal orientation. For the [001] growth plane, the Bragg angle of a GaAs layer is 33.026°, and for a ZnSe layer is 32.925°. For the ZnSe/GaAs heterostructure, the material is readily probed parallel, or perpendicular, to the growth surface (100). A schematic of a GaAs substrate is shown in Figure 5-3, with the crystallographic directions labeled. A cross-sectional view of a heterostructure is also shown, with the crystallographic directions labeled. As can be seen in Figure 5-3, the growth of the ZnSe/GaAs QWs is in the [100] direction. The basic crystal structure is zinc-blende cubic so natural cleavage {110} planes exist.

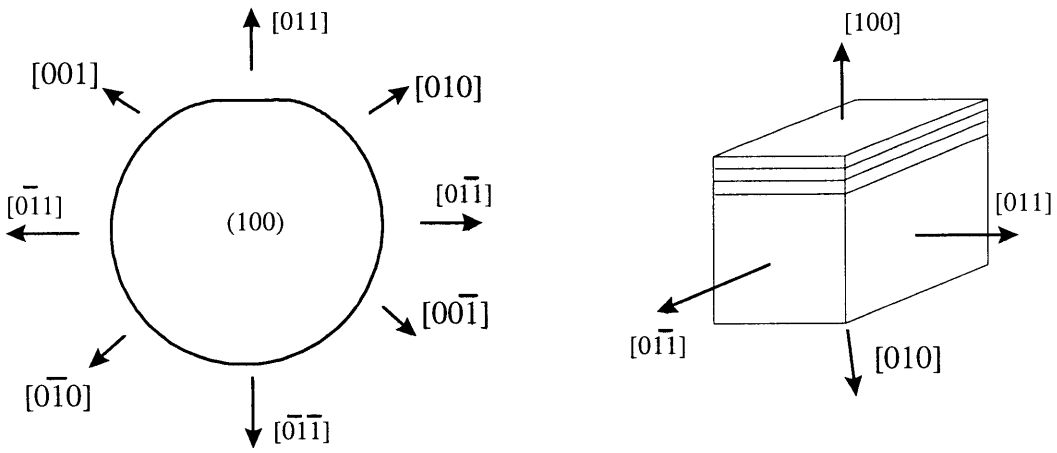

Figure 5-3. Crystallographic orientation of a GaAs (100) wafer, as seen from the surface and from the cross-section.

In x-ray diffraction measurements, the sample surface is probed by rotating the surface with respect to the x-ray beam. Variations in the diffraction intensity from the Bragg angle for the constituent layers in a heterostructure can be studied to understand the strain, defect density, and composition of the heterostructure.

For electron beam excitation, the electron beam is either aligned close to the [100] crystal axis in plan-view, or close to the [110] crystal axis in cross-sectional view. Cross-sectional alignment is useful for looking edge-on at the different layers in a heterostructure as shown in Figure 5-3. The interaction with the electron beam in either orientation is such that strong diffraction of the electrons by the periodic array of atoms occurs when the excitation is incident at the Bragg angle. A diffraction pattern characterized by a three-dimensional array of reciprocal lattice points related by Fourier transform to the crystal lattice results from the interaction of the electron beam with the crystal structure. The electron diffraction patterns for both sample orientation are shown in Figure 5-4, where the labels on the patterns correspond to reciprocal lattice points. Each reciprocal lattice point corresponds to a set of crystal planes. The forward scattered beam is the spot labeled 000.

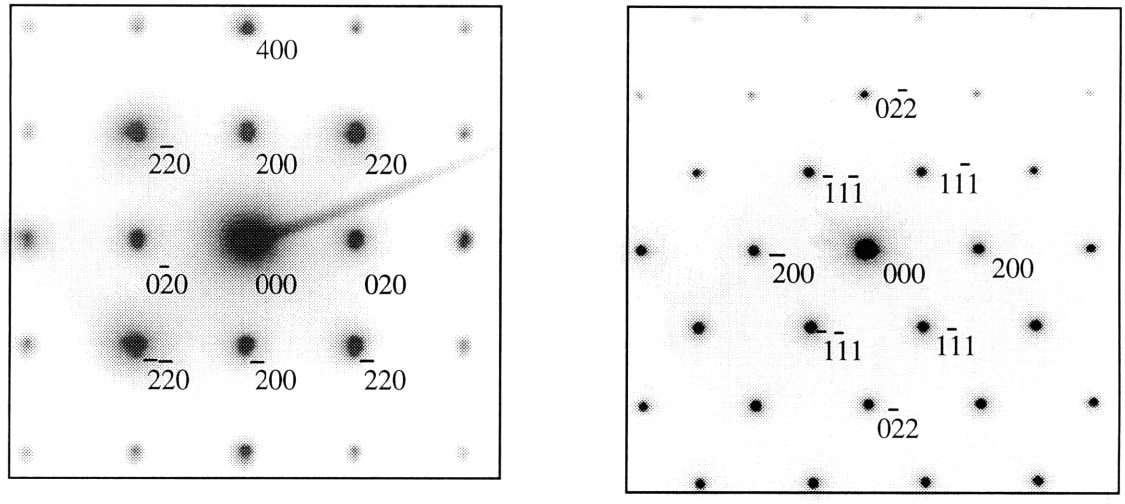

Figure 5-4. Electron diffraction patterns for GaAs in the [001] and the [011] directions.

Diffraction of x-rays from lattice planes parallel to the growth direction (100) is strongest for the (004) reciprocal lattice point. The (004) reciprocal lattice point is the first strong Bragg condition for the growth plane, although there is also an (002) reciprocal lattice point which is much weaker. The presence of an (002) reciprocal lattice point is unique to compound semiconductors. The (002) reflection is forbidden in single element zinc-blende crystal structures, such as Si. The difference in the structure factors for Zn and Se and for Ga and As allow for a weakly diffracting spot, which can be taken advantage of when studying compound semiconductor heterointerfaces. The relative intensities of the diffraction spots shown in Figure 5-4 indicate the orientation of the sample with respect to the electron beam. If the electron beam is slightly off the [001] or the [110] crystal axis, the Bragg condition for different lattice planes will be more likely to be satisfied, and the corresponding reciprocal lattice points will become illuminated. Aligning the sample with respect to its reciprocal lattice points is necessary to achieve high contrast, to identify defect type and orientation, and to adequately determine the physical dimensions of the heterostructure.

The information from the diffraction resulting from both x-ray and electron beam excitation can be used to assess the microstructure of the ZnSe/GaAs QW heterostructure.

Subsequent sections present the methodology and the results for compositional analysis by energy dispersive x-ray spectrometry and crystal quality by triple-axis x-ray diffraction and transmission electron microscopy. Each experimental technique is discussed in the section in which the data is presented.

6. Energy dispersive x-ray spectroscopy

Compositional analyses of semiconductor heterostructures are useful for identifying interdiffusion at the junction of heterolayers and the stoichiometry of each compound semiconductor layer. A technique which provides a high degree of spatial and compositional resolution is energy dispersive x-ray spectroscopy (EDS). This method is especially useful when used in conjunction with transmission electron microscopy. The following sections describe the approach taken to the compositional study of the ZnSe/GaAs QWs and DBHs using EDS. The goal of this study was to verify if there was a measurable amount of interdiffusion at the heterointerfaces between ZnSe and GaAs. Any measurable amount would indicate an amount of interdiffusion large enough to limit the optical properties of the GaAs QW.

A discussion of the method for EDS measurements is provided below with a description of the system that is used. The spatial and compositional limits to the measurement are investigated for the specific elements: Zn, Se, Ga, and As. The results from the measurements of the interfaces of ZnSe/GaAs QWs, DBHs, and all group III-V structures are compared. Finally, the relationship between the results from the compositional measurements and the heterointerfacial quality for the ZnSe/GaAs QWs is discussed.

6.1 Description of method for EDS

Energy dispersive x-ray spectroscopy (EDS) is a standard analytical tool that is part of a scanning transmission electron microscope (STEM) or a TEM. The measurements in this study were made in a VG HB603 STEM operating at 250 kV. An electron beam is generated from a tungsten field-emission tip, with a probe size of about 1 nm and current of about 10^{-10} Amps. During analysis, the sample sits in the column of the STEM at a vacuum of 10^{-9} Torr. The sample is illuminated by an incident electron beam that is rastered across the surface. A 30 mm^2 Si(Li) x-ray detector placed at an angle of 20° from

the sample surface detects x-rays which are emitted from the sample in the energy range of 0 keV to 20 keV. The energy resolution of the detector is 138 eV at an energy of 5.9 keV.

An x-ray that is detected from the sample as a result of interaction with the electron beam can be a result of two types of interactions with the resident atomic species. In one instance, an atomic species in the sample is ionized by the electron beam. The excited ion then decays to the ground state by emitting an x-ray photon. In the other case, energy is released in the form of an x-ray from the electron beam during an interaction with the nucleus of an atom in the sample. The EDS spectra in this case has a continuous background level called Bremsstrahlung radiation. The combined EDS spectra shows the Gaussian-shaped features which occur at energies related to the elemental composition of the sample superimposed on the background level. For the samples studied in this work, the K_α, K_β, and L_α x-rays are collected (Table 6-1). Other spurious features are often present in the EDS spectra including escape peaks which appear 1.74 keV below the characteristic energies of the elements in the sample.

	Zn	**Se**	**Ga**	**As**	**In**	**P**	**Cu**	**C**	**O**
Z	30	34	31	33	49	15	29	6	8
K_α (keV)	8.631	11.210	9.243	10.532	24.139	2.1	8.041	0.282	0.523
K_β (keV)	9.572	12.501	10.263	11.729	27.382		8.907		
L_α (keV)					3.287				

Table 6-1. Transition energies for K_α, K_β, and L_α for the constituent elements for the semiconductors of interest.

There is not a 1:1 correlation between the intensity of a given x-ray feature and the chemical composition. The x-ray detector is not uniformly sensitive over the full detection range of x-ray energies. Furthermore, if the sample has variations in thickness across the area of interest, the relative intensities of the x-ray features partially reflect these variations. The scattering in the sample by the electron beam increases with increasing sample thickness and thus increases the x-ray counts.

The composition of a given sample is determined by collecting x-rays for a set amount of time (long enough to exceed the noise level and short enough to avoid sample or electron beam drift effects) over a set area. Figure 6-1 demonstrates EDS results for both a layer of ZnSe and a layer of GaAs measured by holding the electron beam at a single point on the material surface for 300 seconds. The features in Figure 6-1 indicate the presence of the K_α and K_β lines for Zn, Se, Ga, and As.

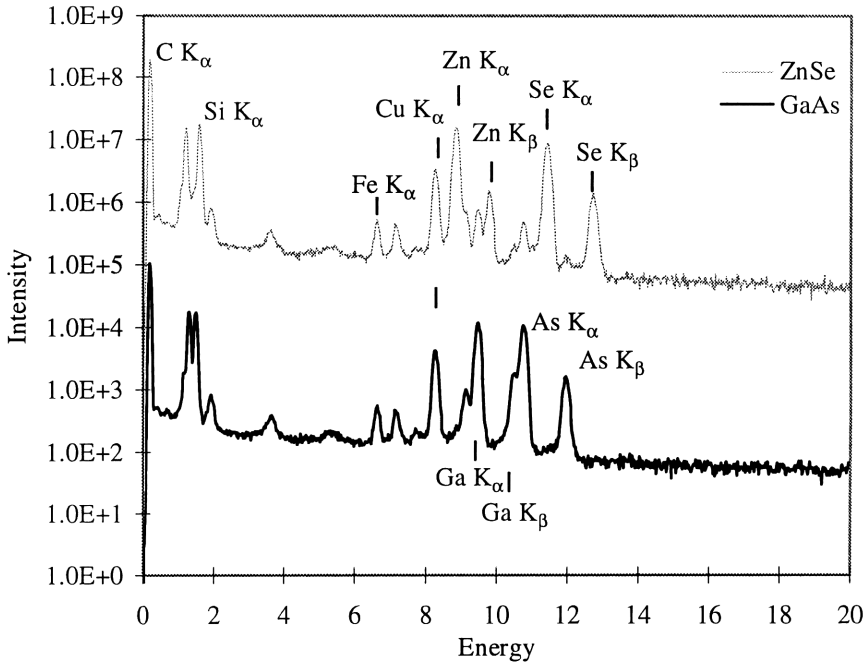

Figure 6-1. EDS measurements of GaAs and ZnSe, showing features for Ga, As, Zn, Se, and Cu. Also present are detectable levels of C, Si and Fe. The features to the left of the Cu peaks correspond to escape peaks resulting from x-ray interaction with the detector.

The elements of primary interest for ZnSe and GaAs are Zn, Se, Ga and As. The features corresponding to each of these elements in comparison to the background level shown in Figure 6-1 indicates that the K_α features are not of equal intensity. The differences in intensity do not necessarily reflect non-stoichiometric growth conditions. The sensitivity of the detector and the x-ray efficiency of each element must also be taken into consideration. However, this study is primarily interested in the spatial composition of the ZnSe/GaAs QW, because the relative intensities of the respective elemental features do

not contribute to this information. Other features in the EDS spectra shown in Figure 6-1 indicate the presence of Cu, C, Si, and Fe. The Cu originates from the grid upon which the sample is mounted. The C and Si are contaminants present both in the STEM column and on the sample. The presence of Fe is a result of the interaction with electrons and the walls of the STEM. The small peaks to the left of the Cu features are examples of escape peaks resulting from x-ray interaction with the detector. The downward slope in the EDS spectrum is a function of the Bremsstrahlung radiation caused by interactions between the electron beam and the atomic nuclei.

As the electron beam is transmitted through a sample, the emitted x-rays provide compositional information in the form shown in the EDS spectra in Figure 6-1. The information of primary interest is the compositional make-up of a ZnSe/GaAs heterostructure across the interfaces between the ZnSe and GaAs layers. An understanding of the theoretical limits of the EDS measurement are necessary to successfully assess the interfacial regions. Both the spatial resolution and the minimum mass detectable by the EDS measurement are a function of the materials being measured, the thickness of the sample, the electron beam diameter, and the x-ray detector resolution. The subsequent sections present the analysis of the beam spread caused by sample thickness effects in conjunction with the finite dimensions of the electron beam and resultant spatial resolution as a function of material thickness. This is followed by a discussion of the minimum detection level possible for the elements of interest for a sample of a given thickness.

6.2 Beam spread and minimum detection

The spread in the electron beam as it impinges upon a material has been approximated by a single-scattering model [104]:

$$b = 7.21 \times 10^5 \frac{Z}{E_0} \left(\frac{\rho}{A} \right)^{\frac{1}{2}} t^{\frac{3}{2}} \text{ (cm)} \qquad \text{Eq. 2}$$

In the above expression, t is the material thickness in units of cm, Z is the atomic number, E_0 is the beam energy in keV, ρ is the material density in g/cm^3, and A is the atomic weight in g/mole. When the parameters are estimated for ZnSe, GaAs, and InGaP, the beam spreading versus the thickness of the material results in the behavior shown in Figure 6-2. For comparison, the beam spread for iron is also given, as this is a common standard for EDS comparisons.

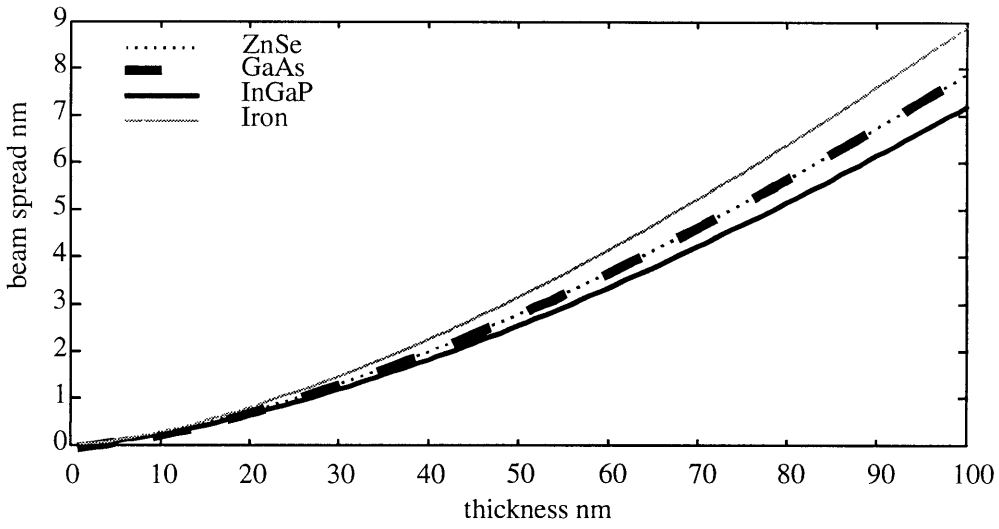

Figure 6-2. Beam spreading of the electron beam versus material thickness for ZnSe, GaAs, InGaP, and iron as calculated using the single-scattering model. The lines for ZnSe and GaAs overlap.

The overall spatial resolution for the EDS measurement is a combination of the beam diameter and the beam spreading. This is expressed in the following equations:

$$R_{\max} = \left(b^2 + d^2\right)^{\frac{1}{2}} \qquad \text{Eq. 3}$$

$$R = \frac{d + R_{\max}}{2} \qquad \text{Eq. 4}$$

where Eq. 3 represents the resolution (R_{max}) accorded to an electron beam (of diameter, d, beam spread, b) that has propagated through a sample of finite thickness. Eq. 4 takes the average of the top surface resolution and the bottom surface resolution.

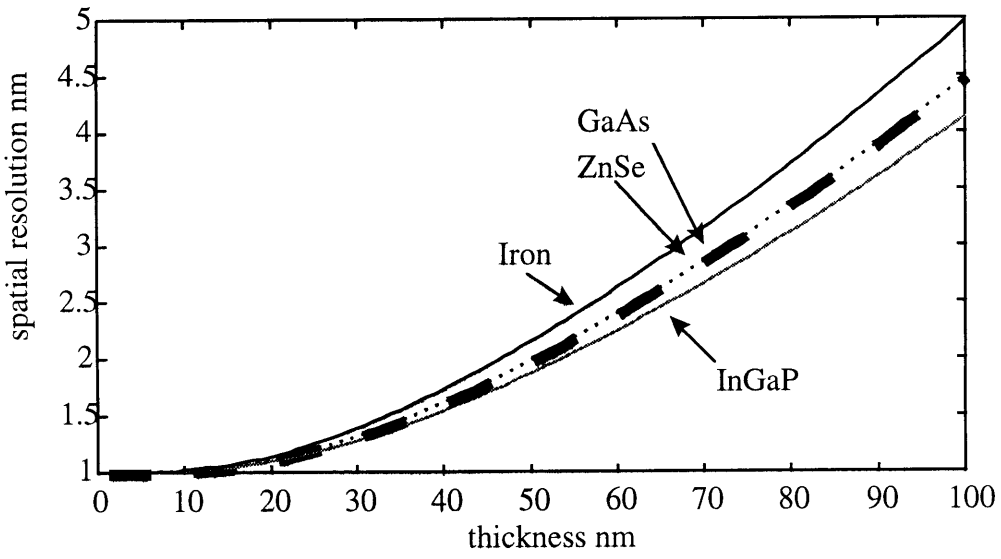

Figure 6-3. Spatial resolution of EDS measurement for ZnSe, GaAs, InGaP and iron.

Figure 6-3 shows a plot of the spatial resolution for the EDS measurement as a function of the sample thickness for ZnSe, GaAs, InGaP and iron. For very thin samples, thinner than 10 nm, the spatial resolution degrades by only 2% for an order of magnitude increase in the sample thickness. However, extrapolating the curve in Figure 6-3 for another order of magnitude increase in sample thickness, the spatial resolution will degrade by 50%. The samples for the EDS study have been studied by phase contrast imaging in the TEM, and in order to achieve this condition, the sample thickness needs to be on the order of 8 nm. Therefore, it is believed that the spatial resolution for the EDS measurement is between 1.0 nm and 2 nm.

6.2.1 Minimum detection

The minimum level of detection of a given material can be defined by the minimum mass fraction (MMF). The MMF is the smallest concentration of an element in weight percentage or parts per million that the EDS measurement can detect.

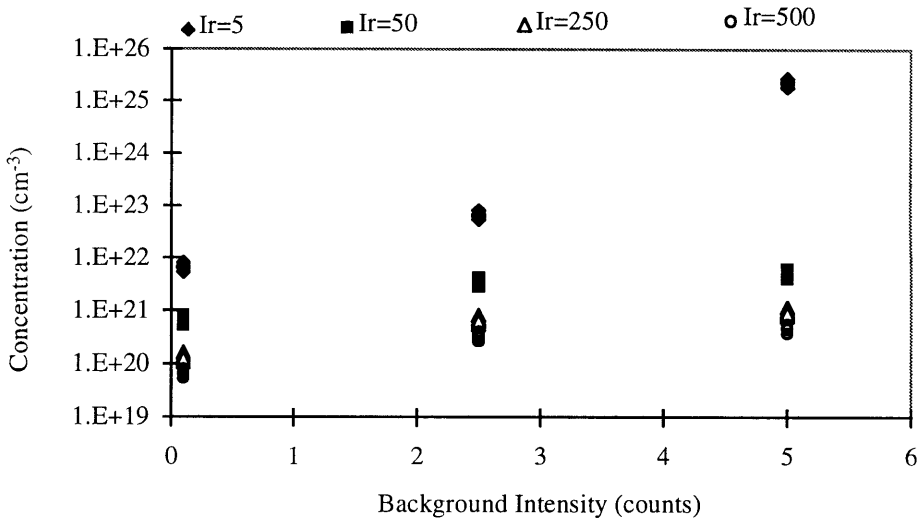

Figure 6-4. Minimum concentration of an element detectable as a function of the background intensity level and the integrated peak intensity (Ir) for Zn, Se, Ga, and As. The values for each element are grouped together according to the integrated peak intensity.

The minimum detectable level for each of the elements in ZnSe and GaAs is a function of the ratio of the background intensity to the integrated peak intensity for a given element. The background intensity is directly proportional to the sample thickness (as well as the beam current and detection time). Figure 6-4 shows in part this relationship for a fairly low integrated intensity ranging from 5 to 500 counts. The minimum detection level becomes less correlated with the background and integrated intensity as the integrated intensity approaches 500 counts, reaching a lower limit of roughly $7x10^{19}$ atoms/cm^3. In comparison to concentration levels often considered in semiconductor device design, this lower limit would be a very high level of doping. The diamond cubic lattice structures of ZnSe and GaAs have a molecular density of roughly $1x10^{23}$ molecules/cm^3. For a sample that is 8 nm thick, at the lowest limit of detection would correspond to the contribution of 10 atoms; for a sample that is 80 nm thick the lower detection limit corresponds to 100 atoms. Thus, a thicker sample is better for the detection of small concentrations of a material (although the spatial resolution is degraded with a thicker sample).

Given the analysis of the spatial resolution and the minimum mass detectable by the EDS measurement, interdiffusion at semiconductor interfaces would only be detected if the

interface had a width of a few nanometers. The interdiffusion at the heterointerface, to be detected, would have to be at least on the order of 2% of the molecular composition of the material for a sample 8 nm thick. These lower limits on the EDS measurement are sufficient to provide useful information on the heterointerfacial quality of the ZnSe/GaAs QWs. The approach to investigating these heterostructures is presented in the following sections.

6.3 Data acquisition

The EDS spectra shown in Figure 6-1 for ZnSe and GaAs are used as the basis for the acquisition of compositional data from an area of the sample. The energy-ranges defined by the FWHMs of the K_α features for Ga, As, Zn, and Se are monitored by the data acquisition system to determine the count-rate for each element during a linescan. As the electron beam is moved across the sample, the data acquisition program selectively measures the number of counts for each window. Two types of data are taken in this manner, a two-dimensional compositional map and a one-dimensional linescan. The linescan is more useful for quantitative analysis of the elemental composition of the sample with respect to translation across the sample. The compositional map is useful for the qualitative assessment of the composition of the specimen.

Compositional maps of small regions of both a ZnSe/GaAs 6 nm single quantum well (z302) and a 100 nm DBH (z255) were taken, in an effort to assess the "quality" of the heterostructure both parallel and perpendicular to the growth direction (see Figure 6-5). These two samples were selected because the TEM for each is very different, and the narrower GaAs region could serve to aid in experimentally evaluating the spatial resolution of the EDS measurement.

Any modulations in the composition perpendicular to the growth direction potentially indicate that the films were not successfully grown in a two-dimensional manner. Overlap in the spatial composition of the Zn and Se with the Ga and As elements is also an indicator of diffusion at the heterointerfaces.

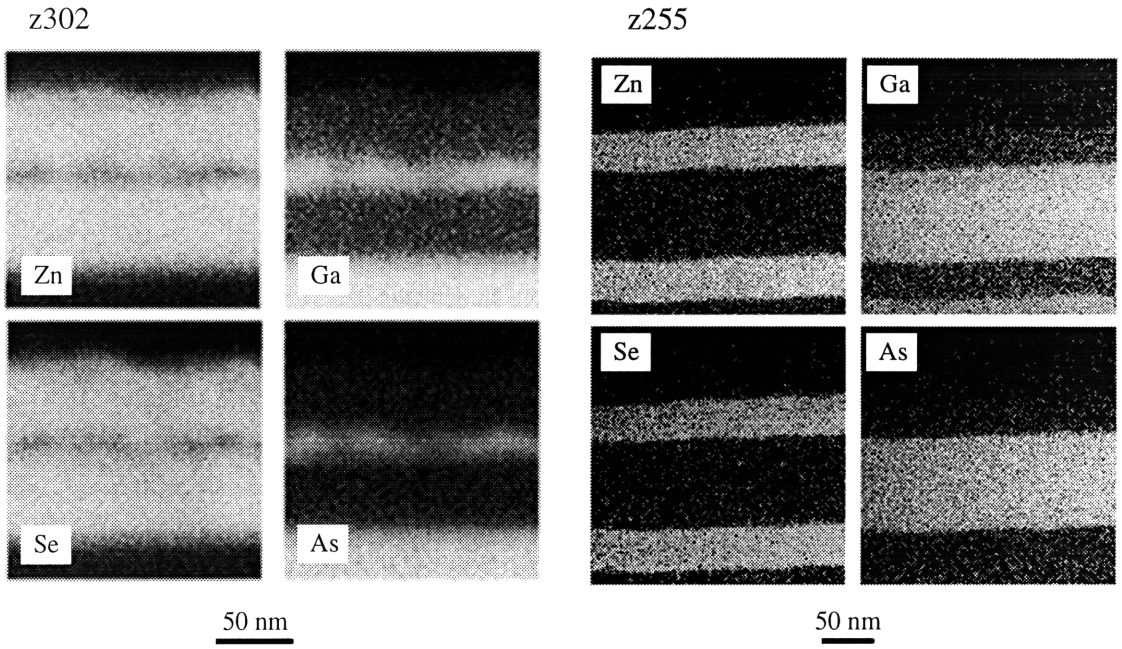

Figure 6-5. Compositional maps of a 6 nm (z302) and a 100 nm (z255) ZnSe/GaAs QW. The maps indicate the presence of Zn, Se, Ga, and As.

In Figure 6-5 the white bands in the left-hand set of images for both z255 and z302 are representative of the elemental concentrations of Zn (on top) and Se (on the bottom) from 50 nm ZnSe barrier layers. The EDS maps for sample z255 were taken at a different magnification from those of sample z302 in order to include the entire DBH in the map. As can be seen, there is a slight undulation in the top ZnSe layer in sample z302. Similar variations are present in z255, although not visible at the magnification the compositional map was taken. However, the spatial modulation of the composition at the heterointerfaces for sample z255 originates at the bottom III-V buffer layer upon which the heterostructure was grown. It is interesting that the undulation in this case propagates up through the entire structure.

Sample z255 shows very little overlap between the white bands representative of Zn and Se and the bands representative of Ga and As. In contrast, z302 shows the potential for a large overlap in the presence of ZnSe and GaAs in all layers. The background noise in the Ga and As plots for z302 is a function of Bremsstrahlung radiation which creates a fluorescence continuum during the EDS measurement. The background level is not as

evident in z255 because the region of the sample where the measurement was taken is thinner than the region of the sample over which the compositional map was taken for z302.

The compositional maps of the 6 nm and 100 nm ZnSe/GaAs QW structures shown in Figure 6-5 provide support for the EDS measurement as a feasible method for understanding the quality of the ZnSe/GaAs heterointerface region on a compositional basis. The 6 nm heterostructure shows the presence of a spatial modulation of the heterointerface perpendicular to the growth direction as well as some overlap between the constituent species of the ZnSe and the GaAs at the heterointerface.

Further assessment of the interfacial regions of the ZnSe/GaAs QWs are made using linescan analyses. All III-V heterointerfaces of InGaP/GaAs are also studied to compare to the ZnSe/GaAs interface as a base case for the EDS linescan measurement. The III-V/III-V heterointerface is expected to be abrupt, since the InGaP/GaAs heterostructure has been optically characterized by PL and shown to be of high quality. The lack of or the broadening of a PL signal from the InGaP/GaAs heterostructure would indicate a rough heterointerface.

The subsequent sections provide the linescan data from both the III-V and the II-VI/III-V heterostructures. First, the method by which the linescan data is processed is presented for an all III-V heterostructure. Next, the linescan data from a ZnSe/GaAs QW and the method by which the heterointerfaces are assessed are presented. Finally, the results are given from the linescan data for all of the heterostructures.

6.4 EDS linescans

The EDS linescans were taken by selecting an area of the sample of interest, scanning across the region, and sampling 128 data points for the elements that are preselected using the data from Figure 6-1. The number of data points is sufficient to ensure that several points are detected across an interface. The dwell time for each data point was set between 1 and 5 sec. A compromise exists in setting the dwell time. A longer dwell time

can produce a larger count level, and larger signal-to-noise ratio. However, a longer dwell time also results in increased surface contamination of the sample and an increase in the likelihood of sample or electron beam drift during the linescan. All of the negative results of an increased dwell time reduce the resolution of the EDS measurement. Hence, a variety of dwell times were chosen, depending on the signal from the sample (which is directly a function of the sample thickness).

The raw data from a linescan of an InGaP/GaAs multiple QW of well widths 2 nm and 4 nm are shown in Figure 6-6. The composition for the K_α lines of As, Ga, and P are shown. The In composition is measured from the L_α line. Two QWs can be detected in the linescan, most clearly defined by studying the As composition. The upward trend in the signal intensity with increasing depth indicates that the sample was becoming thicker as the scan progressed. The analysis of the heterointerfaces between the InGaP and the GaAs is complicated by the noise in the EDS spectra.

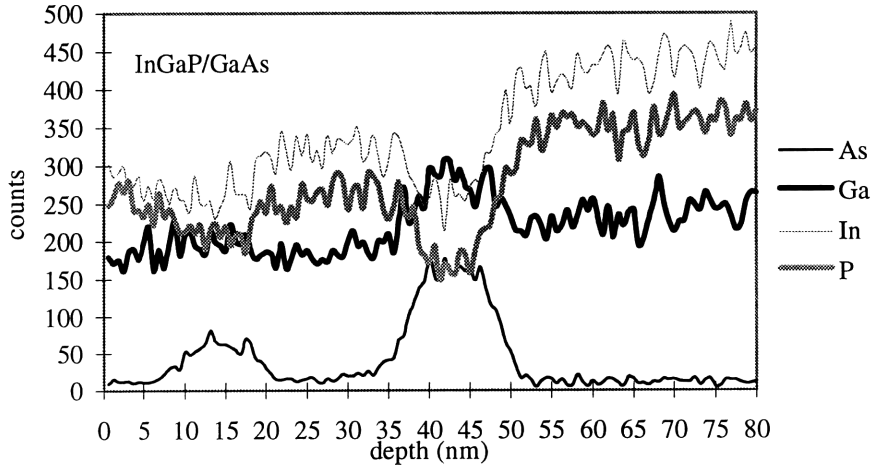

Figure 6-6. Linescan of an InGaP/GaAs multiple QW showing the presence of In, Ga, As, and P. The two GaAs QWs are 2 nm and 4 nm thick. The linescan is directed into the sample, as the depth increases, the substrate is approached.

The same sample was compositionally analyzed by EDS by taking a number of 3 minute long EDS spectra at 1 nm steps. This point-by-point approach is believed to result in higher compositional resolution without the issues of beam drift associated with long dwell time linescans, as each data point is selected by the STEM operator. However, a

degree of subjectivity exists in the data taking as there is a human component involved. The point-by-point data taken for the same InGaP/GaAs multiple QW measured in Figure 6-6 is shown in Figure 6-7. The resulting compositional results are somewhat clearer than the linescan in Figure 6-6, and the QWs are easier to discern by the analysis of the In, P, and As compositions. The Ga composition for this heterostructure is difficult to use for the assessment of spatial transitions, as all of the layers in the heterostructure have Ga. It is also important to note that the In and P compositions fall to a lower minimum in Figure 6-7 than in the linescan data from the same sample. This indicates that the compositional resolution of the linescan is exceeded at the small QW widths (2 nm and 4 nm).

Because the point-by-point method of taking the compositional data was so subjective and still appeared to have a similar amount of noise fluctuation, the linescan approach to taking EDS data was followed for the remainder of the samples studied. The limitations on the compositional resolution in the linescan data are considered in the analysis of the data.

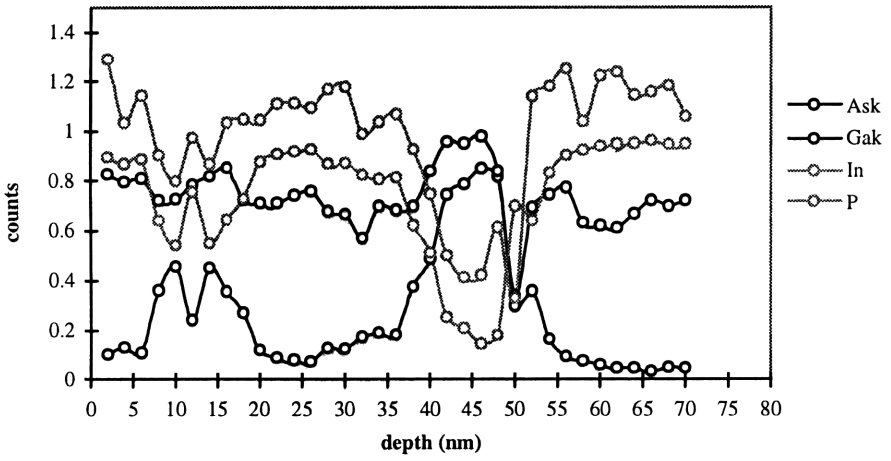

Figure 6-7. Compositional measurement of the 2 nm and 4 nm InGaP/GaAs multiple QW shown in Figure 6-6. The data was taken by measuring the integrated intensity of each element on a point-by-point basis. As the depth increases, the substrate is approached.

In order to better interpret the linescan data, a 3 point average of the data was applied 5 times. This filtering served to reduce the noise fluctuations in the data, as shown in Figure 6-8. Now, the QWs in the InGaP/GaAs heterostructure are more readily discerned, and

the heterointerfaces can be analyzed. The filtering method does not significantly alter the count/depth aspect ratio of the data.

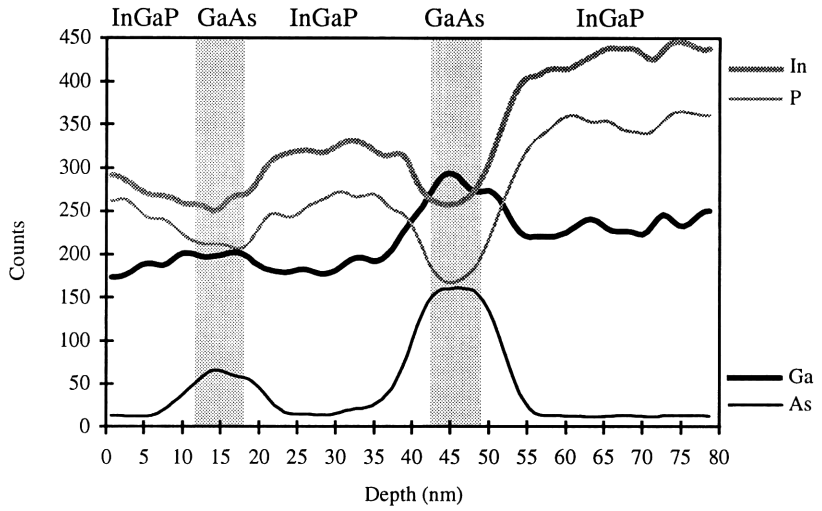

Figure 6-8. Filtered linescan EDS results from the 2nm and 4 nm InGaP/GaAs multiple QW. The linescan is directed into the sample, as the depth increases, the substrate is approached. The linescan data was filtered with a 3 point average applied 5 times. The shaded areas denote the regions where the GaAs QWs are believed to be.

The remainder of the EDS linescan data that will be discussed have been filtered in the same manner as in Figure 6-8. Since the goal of the compositional measurements by EDS was to assess the heterointerfaces of the ZnSe/GaAs QWs for the possibility of interdiffusion, the next section discusses how the heterointerface has been defined in relation to the data. The results for the different sample scanned are also presented.

6.5 Data Analysis

In order to assess the abruptness of the heterointerfaces in ZnSe/GaAs QWs, a uniform methodology needs to be applied for all types of samples. The linescan data in Figure 6-8 of an InGaP/GaAs multiple QW heterostructure show an increase in the As composition, accompanied by a decrease in the In and P compositions over regions believed to be occupied by GaAs. There is a region over which a transition occurs from material compositionally defined by the presence of In, Ga, and P to material compositionally defined by Ga and As. It would be logical to define this region as the heterointerface, with

a finite width. This, however, implies that the heterointerface of the InGaP/GaAs multiple QW heterostructure is not abrupt.

In comparison, the linescans of ZnSe/GaAs QWs with a GaAs layer thickness of 3 nm and 100 nm also show a similar region of transition (Figure 6-9 and Figure 6-10). In Figure 6-9, the region where the GaAs is believed to be according to the compositional profile is shaded gray. The transition region is shaded to an increasingly lighter tone. The transition from a GaAs to ZnSe is of a finite width, as with the InGaP/GaAs linescan data. The linescan data in Figure 6-9 show a similar limitation in the resolution in the EDS measurement as shown in Figure 6-8, as the Zn and Se compositions never fall to a background count level within the region believed to be the GaAs QW. In comparison, analysis of the wider 100 nm ZnSe/GaAs double heterostructure shown in Figure 6-10 indicates that the GaAs QW layer is in fact devoid of Zn and Se at levels within the detection limits of the EDS measurement. A quantitative assessment of the interface regions was carried out to better understand these results.

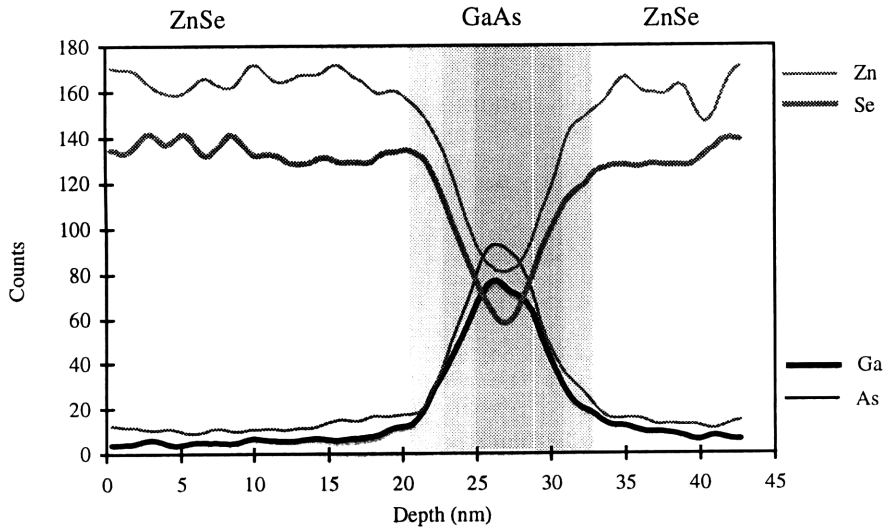

Figure 6-9. Linescan measurement of a 3 nm ZnSe/GaAs QW. The shaded background area indicates the presence of the GaAs QW, and the region over which the heterointerface is believed to occur.

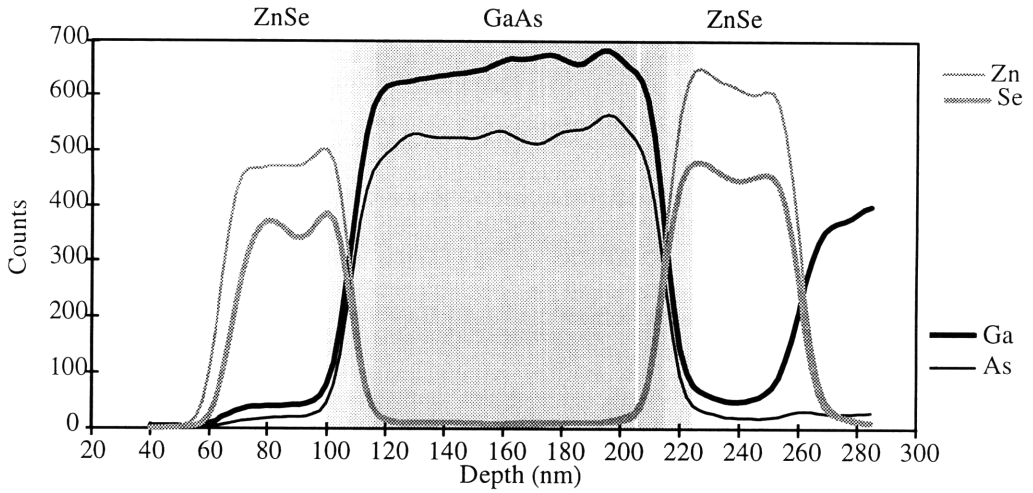

Figure 6-10. Filtered EDS linescan data for a ZnSe/100 nm GaAs DBH. The linescan is directed into the sample, as the depth increases, the substrate is approached. The GaAs region is shaded gray, and the heterointerfacial region is shaded incrementally from gray to white.

6.5.1 Definition of heterointerfacial thickness

The heterointerface was defined as the region over which the derivative of the elemental composition profile exceed 1.5 counts. This definition is more clearly shown in Figure 6-11 showing the As linescan data for the 100 nm ZnSe/GaAs DBH from Figure 6-10 along with the derivative of the data. A standard approach to defining transitions from one material to another is to take the 3% of and 97% of maximum values over the range of variation. A more generous definition for the heterointerface was used both to account for noise in the linescan and to avoid issues associated with the sample thickness variations across the scan area. As the linescan data for the ZnSe/GaAs QWs are studied in conjunction with InGaP/GaAs multiple QWs, the comparison of the widths of the heterointerfaces are more relevant than the absolute width in this study. Hence, the approach taken in defining the heterointerface shown in Figure 6-11 is a consistent methodology which can be used to compare across different samples.

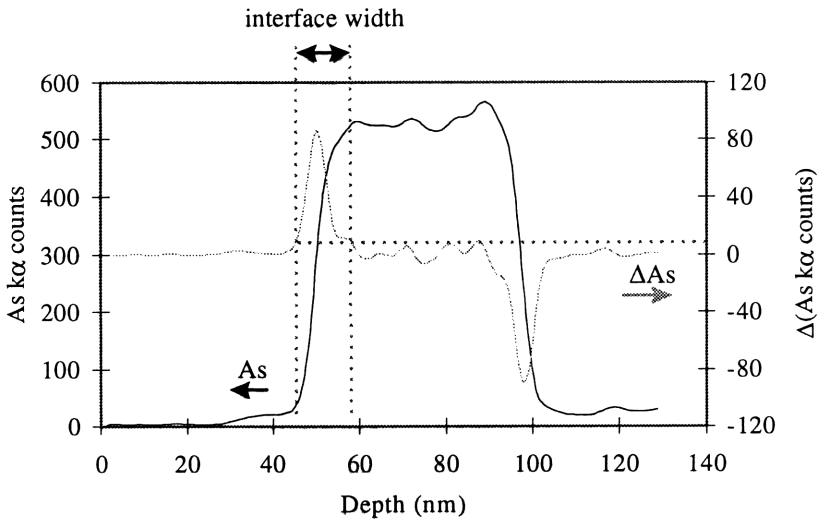

Figure 6-11. Determination of interface width for 100 nm ZnSe/GaAs DBH for As. The heterointerface is defined as the region over which the change between adjacent data points is greater than 1.5 counts. The change in As composition (ΔAs) is superimposed on the As composition. The linescan is directed into the sample, as the depth increases, the substrate is approached.

The interfacial width has been measured from the EDS linescan data for each of the constituent elements detected. The following sections present the results from the analysis of each of these elements in relation to the types of heterostructures.

6.5.2 Interfacial widths as measured by EDS

A series of samples of different materials and QW widths were investigated using EDS linescans. The samples and the linescan information are summarized in Table 6-2. In all of the samples measured, there are two interfaces of interest: the interface closest to the substrate (the lower interface) and the interface closest to the sample surface (the upper interface). Each of the samples studied has a GaAs layer, and hence at least one interface can be assessed by the Ga and As spatial composition. This commonality allows for comparison across the different heterostructures. Using the interface definition described in Figure 6-11, the linescan from each sample has been analyzed to see if there is a difference between the interfacial widths for the different material systems.

Sample	Structure	Dwell Time	Magnification
r239	InGaP/ 9 nm GaAs/InGaP	5 sec	500K
r292	InGaP/ 4 nm GaAs/InGaP	5 sec	1M
r485	AlGaAs/ 10 nm InGaP/GaAs	1 sec	1M
z272	ZnSe/ 3 nm GaAs/ ZnSe	1 sec	2M
z276	ZnSe/ 3 nm GaAs/ZnSe	1 sec	2M
z302	ZnSe/ 6 nm GaAs/ZnSe	3 sec	500K
z255	ZnSe/ 100 nm GaAs/ZnSe	5 sec	500K

Table 6-2. Summary of samples compositionally measured using EDS linescans, the structure of the samples, the dwell time per data point for the linescan and the magnification at which the linescan was taken.

The analysis of the EDS data accounts for differences in sample thickness and the dwell times used during the measurements. To a first approximation, if the measured count level from a sample for a given element is double that of another sample measured using the same dwell time then the thickness of the sample with the higher count level is twice that of the sample with the lower count level. There is also, to first approximation, a one-to-one correlation between the dwell time per data point and the count level. Hence, for sample r239 shown in Table 6-2, the dwell time is 5 sec per data point and would be expected to have a five-fold increase in As composition over sample r485 with a 1 sec dwell time per data point. The data was normalized for these different measurement conditions, first for dwell time. The normalization is important for clarifying whether or not sample thickness affects the measured value for the heterointerfacial width.

6.5.3 Comparison of GaAs-on-ZnSe and ZnSe-on-GaAs interfaces

For the ZnSe/GaAs QW structures, the nucleation conditions at each interface were different and the linescan data were studied to see if this difference was apparent in the composition profile. The compositional data for each of the ZnSe/GaAs QWs studied was converted to an interface width at both the upper and lower interfaces. To simplify the comparison, the interface width for the upper interface was subtracted from the interface width for the lower interface. If the upper interface is larger than the lower interface, subtracting the data would result in a positive value, and visa versa.

The data as a function of the GaAs QW width for the ZnSe/GaAs QWs is shown in Figure 6-12. The x-axis is plotted on a log scale in order to better differentiate the thinner QWs and the 100 nm DBH. The difference in the interface widths appears to be a function of the element studied. However, there is not a correlation between the interface width and the type of interface (upper or lower). In three out of the four cases measured, the Zn and Se show interfacial behavior that is counter to the results from the Ga and As linescans. For example, for the 6 nm QW, the Zn and Se show a slightly thinner upper interface while the Ga and As show a wider upper interface.

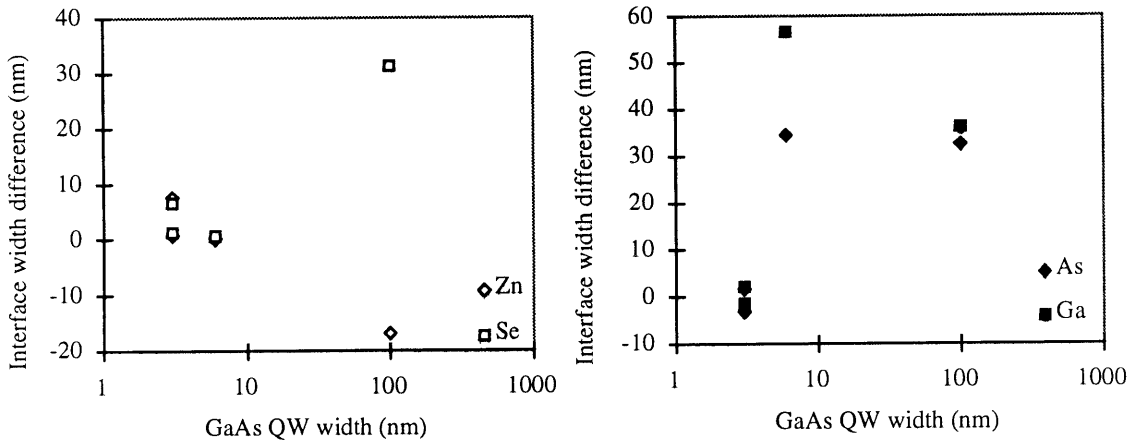

Figure 6-12. The subtraction of the interface widths from the upper and lower interfaces of a ZnSe/GaAs QW is plotted as a function of QW width. The data is shown from Zn, Se, Ga and As compositional data. There is no direct correlation between the type of interface and the interface width.

6.5.4 Comparison of ZnSe/GaAs and III-V/III-V heterointerfaces

The heterointerfaces for all of the samples studied were plotted as a function of the QW width in Figure 6-13. The As and Ga compositions are plotted for the upper (u) and lower (l) interfaces with the solid symbols representing the measured interfacial width of the III-V/III-V heterointerface and the open symbols representing the ZnSe/GaAs heterointerfaces. For the narrower QWs, the heterointerfacial width does not show any relationship between the type of interface, the materials at the interface or the interface width. There does not appear to be a strong relationship between the heterointerfacial width and the QW width for the ZnSe/GaAs heterointerface.

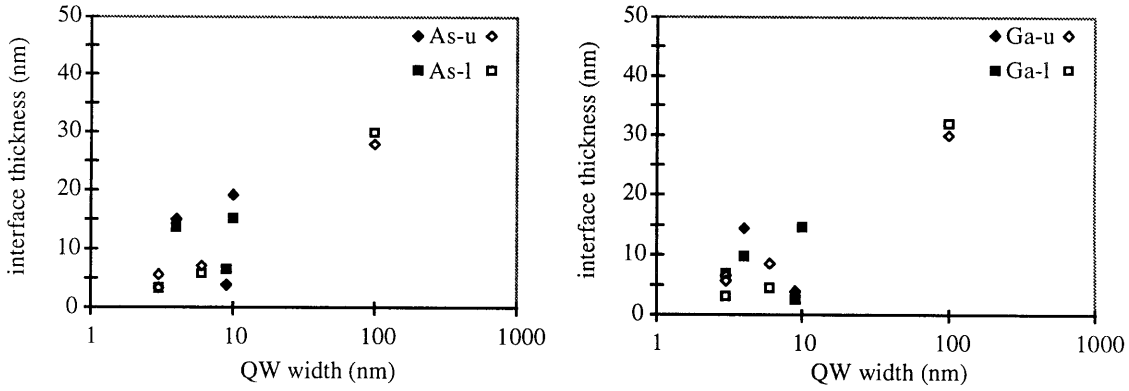

Figure 6-13. Interface thickness in nm as a function of well width for all samples studied. Solid symbols are for III-V/III-V heterointerfaces and open symbols are for ZnSe/GaAs heterointerfaces. The u and l denote the upper and lower heterointerface. The x-axis is plotted on a logarithmic scale to better differentiate amongst the data points from the narrower QWs. The plots indicate that there is no relationship between the QW width and the interface thickness, regardless of the heterostructure materials.

For the narrower QWs, of QW width 9 nm or less, the heterointerfacial width ranges from 3 nm to 20 nm. The 3 nm minimum heterointerfacial width is still much broader than expected for an abrupt semiconductor heterointerface, where the expected value would be 1 nm or less. Because the minimum heterointerface width is broader than expected, the possibility for sample thickness effects to contribute to the measured value for the heterointerface has been investigated. The same results in Figure 6-13 are plotted as a function of the relative thickness of the sample during the EDS linescan measurement as determined by the maximum count level for the respective element. These results are shown in Figure 6-14, and show a correlation between the measured interface width and the sample thickness.

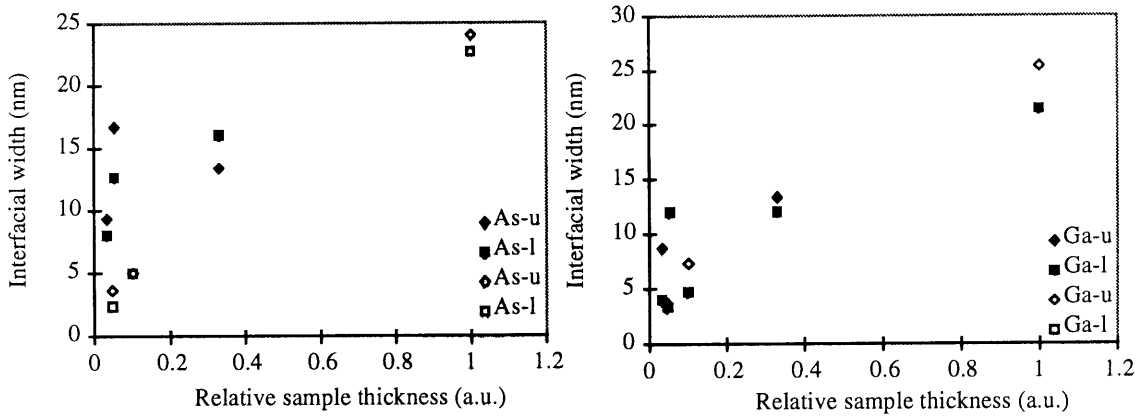

Figure 6-14. Interfacial width as determined from the spatial composition of As and Ga as a function of the relative sample thickness. The solid symbols represent the results from the III-V/III-V samples and the open symbols are from the ZnSe/GaAs samples. The upper (u) and lower (l) heterointerfaces are represented by diamonds and squares respectively. The results indicate that the interfacial width is largely a function of the relative sample thickness.

The relationship between the sample thickness during the EDS measurement and the interfacial width can be an indication of spatial resolution issues or of interfacial roughness. The electron beam spread, as previously discussed, reduces the effective spatial resolution of the EDS measurement. This is a conceivable result as the relative sample thickness range varies by an order of magnitude (as shown in Figure 6-14). Interfacial roughness is less probable for the InGaP/GaAs heterostructures probed, as the optical properties for these structures are indicative of high quality interfaces. Therefore the explanation for the trend seen in Figure 6-14 is believed to be a change in the spatial resolution as a function of beam spread.

The interface width as measured by the Zn and Se spatial compositions is shown in Figure 6-15. The relationship between the interfacial width and the QW width is shown in the left-hand plot. The relationship between the interfacial width and the relative sample thickness is shown in the right-hand plot. The upper heterointerface is denoted by the open symbols and the lower heterointerface is denoted by the solid symbols. A similar upward trend exists in the interfacial width as a function of QW width as shown in the data from the Ga and As spatial compositions in Figure 6-15. An upward trend does exist between the relative sample thickness and the interfacial thickness.

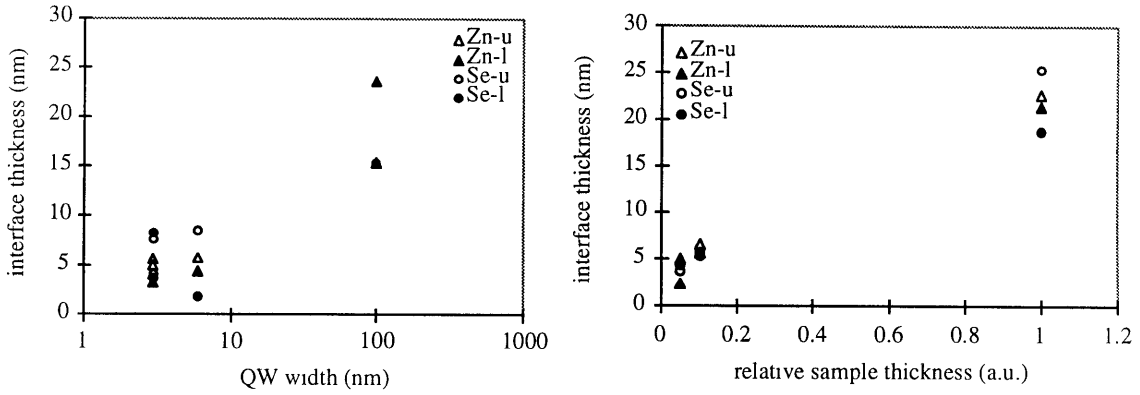

Figure 6-15. Interface width of ZnSe/GaAs heterointerface as measured by Zn and Se compositions as a function of QW width and the relative sample thickness. The letters u and l denote the upper and lower heterointerfaces. The x-axis is plotted on a logarithmic scale to differentiate amongst the data points from the narrower QWs. The plots show that the interface width is more strongly a function of the sample thickness than it is a function of the QW width.

It is difficult to determine whether the increase in the interfacial width as a function of an increase in the relative sample thickness shown in Figure 6-15 is a function entirely of beam spread or if there is a component of interfacial roughness contributing to this trend. As previously discussed, the upper and lower ZnSe/GaAs heterointerfaces were nucleated under different conditions. As the GaAs QW in these heterostructures was not grown under optimal conditions for GaAs it is plausible that the upper heterointerface would be rougher. The upper interface does appear to be slightly thicker than the lower interface as the relative sample thickness increases. However, the difference is fairly small, and the argument for beam spread affecting the spatial resolution cannot be discounted.

To better assess these results, a further study was done in which a ZnSe/GaAs heterostructure was annealed to ensure that interdiffusion occurred at the junction between the ZnSe and GaAs. The analysis of this heterostructure follows.

6.6 Diffusion: annealing study

The EDS linescan spectra of the ZnSe/GaAs QWs did not show conclusive evidence of interdiffusion at the ZnSe/GaAs interfaces. The degree of interdiffusion was measured in relation to the interfacial width of an InGaP/GaAs heterointerface. It is unclear whether the interfacial width for all of the structures measured corresponds to an interface that is

truly abrupt or if the spatial resolution of the EDS measurement has been reached. As a result, a ZnSe on GaAs sample was fabricated under conditions such that diffusion of the constituent species would occur at the ZnSe/GaAs interface in order to assess the practical detection limits of the EDS measurement.

For this experiment, a 100 nm ZnSe layer grown on a GaAs buffer layer with a starting c(4x4) surface reconstruction was compositionally analyzed by EDS (sample z369). Two pieces of sample z369 were also annealed at 600°C: one for 20 minutes, the other for 60 minutes, to force interdiffusion at the ZnSe/GaAs interface for the EDS measurement. Compositional maps and linescans of each sample were taken and compared. For the linescan data, three scans of each sample were taken at different locations along the thin area of the sample at a magnification of 500K with a dwell time of 1 sec per data point. Figure 6-16 shows an example of an EDS linescan from each sample, showing GaAs-to-ZnSe transition from left-to-right. The count level for the unannealed sample is roughly three times higher than that for the annealed case. The increase in the counts indicates that the area of the sample measured in the unannealed linescan is thicker than the area of the sample measured for the annealed case. In both scans shown in Figure 6-16, the downward trend in the count level also indicates that the sample is becoming thinner.

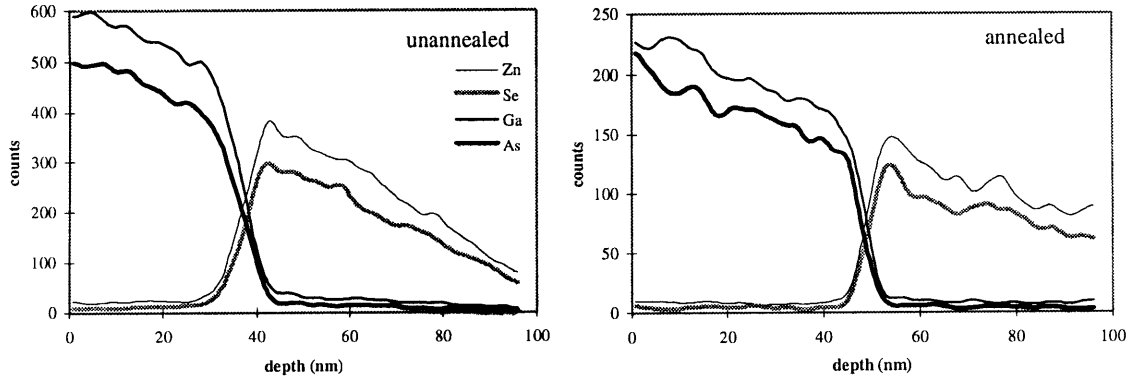

Figure 6-16. Linescan measurements of 100 nm of ZnSe on GaAs, showing the composition of Zn, Se, Ga and As. The count level decrease both of the linescans reflects the rapid change in the sample thickness.

All of the linescan data taken from z369 show the sample becoming thinner over the range of the linescan measurement. The analysis of the ZnSe/GaAs heterointerfacial is made by

the same process as that applied to previous EDS linescan data. For samples z369, the heterointerface width was defined as the region over which the change in the count level between two adjacent pixels exceeded 1.5 counts. Figure 6-17 shows linescan results for the Zn composition as a function of depth across a ZnSe/GaAs heterointerface. The change in the count level between adjacent pixels is superimposed. The left-hand y-axis shows the Zn count level and the right-hand y-axis shows the change in the Zn count level. The interface width is defined by the vertical dotted lines in Figure 6-17 which correspond to the range over which the change in the Zn level exceeds 1.5 counts.

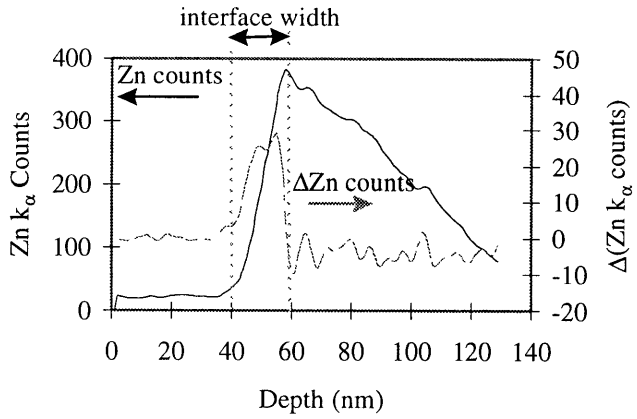

Figure 6-17. Method for determining the interfacial width for the ZnSe/GaAs single heterostructure. The EDS linescan data for Zn is shown, along with the change in the Zn counts as a function of depth from the ZnSe surface.

The ZnSe/GaAs interfacial widths measured from the EDS linescans for the unannealed and the annealed samples of z369 appear to be strongly dependent upon the thickness of the sample. The relative sample thickness at the location of the EDS measurement is determined from the maximum count level of the constituent elements. To a first approximation, doubling the sample thickness would double the x-ray count level for a given element in the EDS measurement. Figure 6-18 illustrates the interface width results as a function of the relative sample thickness for all cases of z369. The closed symbols are from linescan data for the unannealed z369 and the open symbols are from the linescan data for the annealed z369. In spite of the high-temperature anneal of z369, the

ZnSe/GaAs heterointerface does not appear to be significantly wider than that of the unannealed sample.

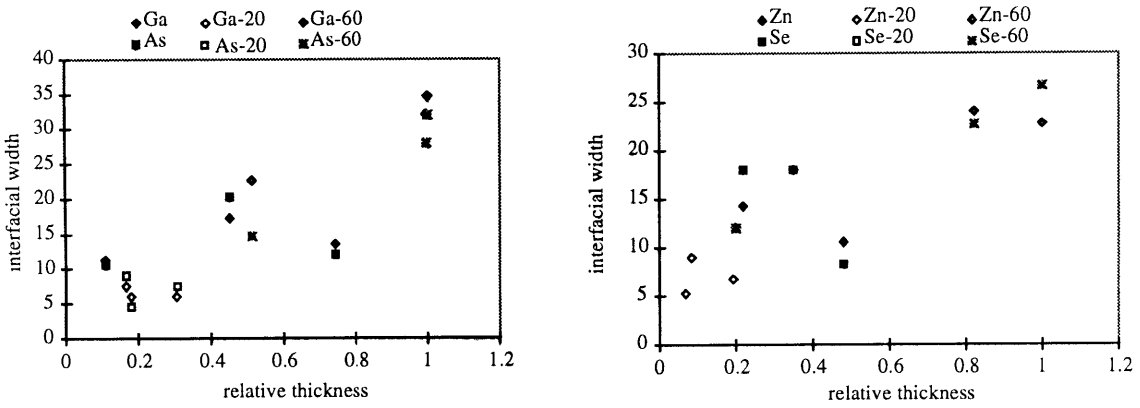

Figure 6-18. Interface width of ZnSe/GaAs heterojunction as measured by an EDS linescan as a function of the thickness of the sample during the measurement. The solid symbols are for the unannealed sample, the open symbols are for the annealed sample.

6.7 Summary

The compositional study of ZnSe/GaAs QWs by EDS has shown the limitations in the combined spatial and compositional resolution for the measurement. The theoretical resolution for the EDS measurement for a sample 8 nm thick is 1.015 nm. However, for an order of magnitude increase in sample thickness, the resolution degrades to 4.5 nm. The variation in spatial resolution over the expected range of sample thickness is high.

The minimum mass fraction has been calculated for a range of background intensities and integrated peak intensities corresponding to a specific element in the EDS measurement. For a high ratio of integrated peak intensity to the background intensity (of ~100), the composition detection lower limit is $1x10^{20}$ cm^{-3}. For an element in an 8 nm thick region of ZnSe or GaAs, and an electron beam diameter, this corresponds to the detection of 100 atoms of the respective element. In theory, the EDS measurement should be able to detect the presence of an element with this incidence in the sample.

Compositional maps of the cross-section of ZnSe/GaAs QWs indicated interdiffusion for the narrower QW, as well as interfacial roughness. The interdiffusion was represented by a

compositional overlap of the Ga and As atoms into the ZnSe barrier regions. The interface roughness appeared as a modulation of the surface or interface along the growth plane. The results from the compositional maps supported the theoretical analysis of the feasibility of the EDS measurement to provide insight into abruptness of the ZnSe/GaAs heterointerface.

However, EDS linescans taken across the cross-section of a series of ZnSe/GaAs, GaAs/ZnSe, III-V/GaAs heterointerfaces demonstrated the spatial and compositional resolution limits of the measurement. Spatial resolution limits for QW widths of less than 4 nm were shown in the measured presence of elements that are part of the barrier layers in the QW, contradicting the high-quality low-temperature PL signal measured from the QW. When a 100 nm ZnSe/GaAs DBH was compositionally evaluated by EDS, the central GaAs layer proved to be devoid of Zn and Se, indicating that the EDS measurement could spatially resolve the larger physical dimensions. Efforts to improve the spatial resolution were complicated by electron beam and sample drift.

Experimentally, the compositional resolution of the EDS measurement was shown to be worse than the theoretically calculated values. The limits to the compositional resolution were exhibited by the linescan measurement of a 100 nm thick ZnSe layer grown on a GaAs buffer layer that had been prepared three different ways: unannealed, annealed at 600°C for 20 minutes, and annealed at 600°C for 60 minutes. The cross-sectional bright and dark field images for the unannealed heterostructure indicate a high-quality ZnSe/GaAs interface. The sample that had been annealed for 20 minutes showed a high density of interfacial defects resulting from the relaxation of ZnSe on the GaAs and complicated by temperature induced defects. The sample annealed for 60 minutes showed a broad band of contrast near the region believed to be the heterointerface between the ZnSe and the GaAs. The region of different contrast between the ZnSe and the GaAs layers is believed to be strongly interdiffused. The interfacial widths of each of the three samples were compositionally assessed by linescan. In spite of the large variation in the heterointerfaces for the three samples, the heterointerface width was similar for all the of the samples.

In light of the compositional and spatial resolution limits probed in the experimental work, the fact that no relationship was found between the interfacial width and the materials on either side of the interface is not surprising. Instead, the heterointerfacial width has been shown to be directly related to the sample thickness during the measurement. The relative sample thickness was calculated to first approximation by comparing the count rate and the dwell time per data point. It is believed that this relationship would be more strongly presented if the effects of drift in the electron gun current were also incorporated into the analysis.

Because EDS is highly sensitive to sample thickness, a comparison was made for the interfacial width resulting from linescan data taken deliberately at different points on the same sample. When the sample is prepared for EDS analysis, there is a wedge shape to the area of interest. As a result, the sample thickness during the EDS measurement is strongly dependent upon the location on the wedge at which the linescan is taken. Taking a few linescans across regions of varying thickness allows for the comparison of the interfacial width as a function of relative thickness across different sample sets. This practice also eliminates the effects of the method of preparation of the samples, which result in a range of sample thicknesses, from the measurement.

As a technique for assessing the abruptness of semiconductor heterointerfaces, the EDS methodology lacks both the spatial and compositional resolution necessary. The information from the compositional maps is misleading when compared to the results from linescan data. The limitations of the EDS measurement are summarized by the comparison of the ZnSe layer grown on GaAs before and after annealing. In spite of the visible interdiffusion at the heterointerface after a 60 minute anneal, the ZnSe/GaAs heterointerfacial width is comparable to that of the unannealed sample.

7. Triple axis x-ray diffraction

Triple axis x-ray diffraction (TAD) measurements are used to assess the crystal quality in the ZnSe/GaAs DBH system on a more macroscopic basis than possible with TEM and HRTEM imaging. With a spatial resolution of ~1 mm and an absorption depth of roughly 10 μm, the TAD measurement provides insight in the statistical nature of the defect structure in the area probed. The diffuse scattering of x-rays taken during an x-ray rocking curve indicates the nature and presence of interfacial misfit dislocations by monitoring the strains present in the heterostructure, as shown in a recent study by Goorsky, *et al* [105]. The ZnSe/GaAs DBHs are probed using TAD to achieve a more macroscopic understanding of the defect structure in the materials. The following paragraphs provide a brief introduction to the types of data taken with the TAD measurement. Since the actual data are presented in subsequent sections, the background information necessary to assess the results is given first.

There are three different types of data acquired using the TAD measurement: θ/2θ scans, ω scans, and reciprocal space maps. A schematic of the relationship between the types of scans and the reciprocal lattice vectors is shown in Figure 7-1. The θ/2θ scans are made by rotating the sample and the detector with respect to the x-ray beam. When a Bragg angle for the sample is intersected during the rotation, the scattering from the x-ray beam is detected. A Gaussian-shape feature results. The angular location, intensity, and FWHM of the features in a θ/2θ scan are important. For a sample with multiple layers of different materials, the location of the peaks can be used to determine the layer thicknesses and composition. The in-plane lattice constant ($a_{\|}$) can be determined for the different layers. The relative intensity of the different features in a θ/2θ scan is representative of the layer thickness or the uniformity of a given layer across its thickness. The layer uniformity is also defined by the FWHM of the features in the θ/2θ scan. Any broadening of a peak is a measure of the crystallinity of the material in the sample. For the ZnSe/GaAs QWs, the

θ/2θ scans are useful indicators of layer thickness and the degree of strain relaxation in the heterostructure. When an InGaP or an InGaAs buffer layer is grown between the substrate and the ZnSe/GaAs QW, the θ/2θ scan is also used to determine the alloy composition and the strain imposed on the rest of the heterostructure by the buffer layer.

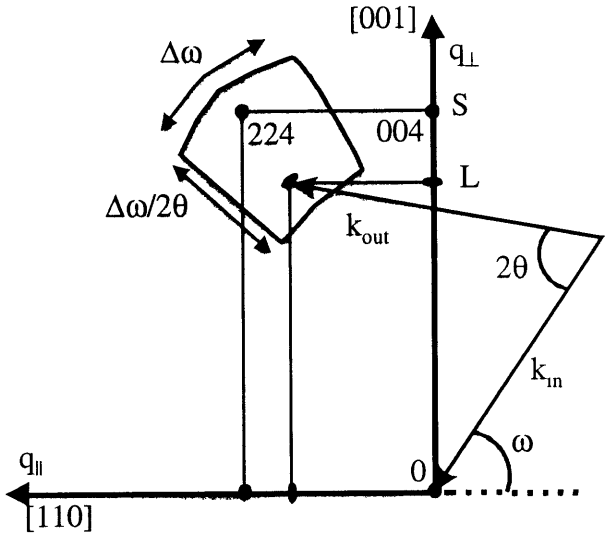

Figure 7-1. Schematic of reciprocal space measurement of the [001]-[110] cross-section of a substrate (S) and a strained layer (L). Typical reciprocal space scans in this study are made centered about the 004 reflection, however, the 224 reflection is also useful for evaluating layer tilt [106].

An ω scan is made by rotating the sample in the x-ray beam at the Bragg angle defined by the material in the sample. In general, an ω scan of the materials studied contains one feature. The intensity and FWHM of this feature provide insight into the defect structure and any fluctuation in $a_\perp$ of the layer (the lattice constant perpendicular to the growth direction). The ω scan is useful for assessing the layer uniformity from a lattice constant, mosaic, and/or defect perspective by comparing the integrated intensity of the data across a set of samples fabricated using different conditions.

A reciprocal space map (RSM), in its most basic form, is a series of θ/2θ and ω scans which results in a two-dimensional map of the reciprocal space vectors, $q_\parallel$ and $q_\perp$. The RSMs can be taken about different reciprocal lattice points to assess layer tilt and

asymmetry in the crystal structure. However, the RSMs in this study are all taken about the (004) diffracted beam. The mechanics of taking RSMs sometimes leads to acquisition times that are longer than the x-ray beam stability. As a result, larger rotational steps and shorter dwell times are used in RSMs for each data point than in $\theta/2\theta$ scans and ω scans. The data from an RSM are therefore more qualitative and provide a fairly graphic comparison of different samples.

The following sections present analyses of the ZnSe/GaAs QWs using all three types of data. A brief description of the physical system employed is given. Some of the system limitations are discussed at this point. A comparison of $\theta/2\theta$ scan data with simulated results follows. The ω scan results are then presented in an analysis of the diffuse scattering in relationship to the material parameters. Finally, the details behind the RSM data acquisition and results are given for the ZnSe/GaAs QWs. All of the data that is presented are compared to the base case of a GaAs substrate.

7.1 System Description

A Bede D^3 high-resolution diffractometer and a sealed tube Cu K_α source with generator settings of 40 kV and 150 mA is employed for the TAD measurements (see Figure 7-2). The x-ray beam is directed through a channel-cut collimator and a 111 Si crystal monochromator which selects a single wavelength of x-rays and collimates the beam with a resultant divergence of roughly 12 arcsec. The second axis is the sample, which is mounted on a stage that can be rotated with respect to the x-ray beam and the x-ray detector. The x-rays are detected by an EDR detector. Between the detector and the sample, further selection of the x-ray beam is completed by a third crystal axis of 111 Si. The third axis allows for the diffracted beam to be filtered in order to achieve a more highly selective probe of the sample structure.

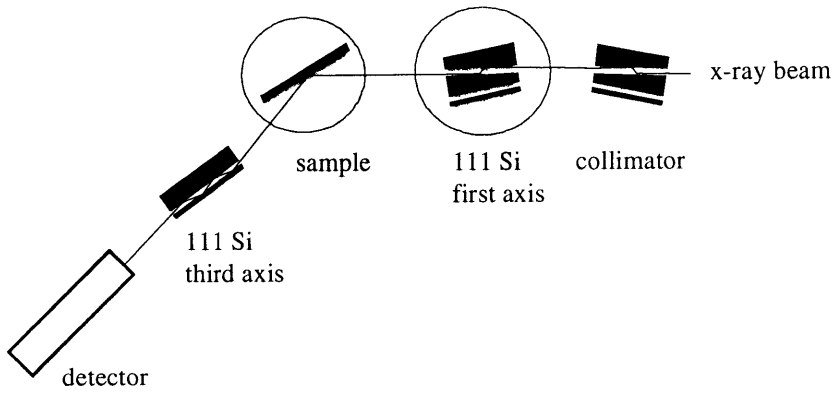

Figure 7-2. Schematic of the Bede D3 x-ray system. The first and third axes are 111 channel-cut Si crystals. The second axis is the sample. Before passing through the first axis, the x-ray beam is collimated by 111 channel-cut Si.

7.1.1 Curvature calibration

During the TAD measurement, the sample is mounted on a metal plate using either wax or crystal bond. Depending upon the mounting conditions, the sample has the potential to bow around the joint between the plate, the mounting material, and the sample. Furthermore, strain between layers in a heterostructure can be reduced by deformation of the substrate. The combination of these two effects results in some curvature across the sample, which causes broadening in the FWHM of the Bragg features. To understand the results from both the $\theta/2\theta$ and the ω scans, the degree of curvature and the amount of broadening that this curvature causes needs to be determined. The $\theta/2\theta$ results for a GaAs wafer were measured and compared to a simulation for an ideal GaAs wafer. The curvature on the simulation was increased until the data matched in FWHM. This match required a curvature of 25 arcseconds, which resulted in broadening a simulated GaAs feature from 7.5 arcsec to 26 arcsec in FWHM. The amount of curvature for all of the samples probed is not expected to be the same, and this inconsistency poses one of the difficulties in understanding TAD results. However, as all of the measurements were made with a similar method of mounting the sample onto the holder, and the sample size was fairly uniform, to a first approximation, an assumption is made that the wafer curvature does not vary significantly.

7.2 Results from θ/2θ scans

The θ/2θ scans of the ZnSe/GaAs QWs contribute to the understanding of the physical dimensions of the heterostructure in the growth direction, the degree of relaxation in the layers, and the alloy composition of any ternary layers in the heterostructure (InGaP or InGaAs). A typical θ/2θ scan of a ZnSe/GaAs QW is shown in Figure 7-3; in this case the GaAs well width is 100 nm. The data in the θ/2θ scans were taken with a rotational step size of 2 arcsec and a dwell time per data point of 2 sec. The primary feature in the θ/2θ scan corresponds to the GaAs substrate peak. As can be seen, the scan axis is usually set to zero at the maximum value in order to compare the angular separation between the substrate and the rest of the layers in the heterostructure.

A combination of simulation and direct measurement from the θ/2θ scan have been used to understand the physical dimensions of the ZnSe/GaAs DBH. When fringes are discernible in the data, as shown to the left of the GaAs peak in Figure 7-3, the width of the QW can be determined by the fringe period according to Eq. 5 [107]. The simulation of the θ/2θ scan was performed using RADS, a simulation program based upon dynamical diffraction theory [108].

$$\Delta\theta_p = \frac{\lambda}{t \sin\theta_B} \qquad \text{Eq. 5}$$

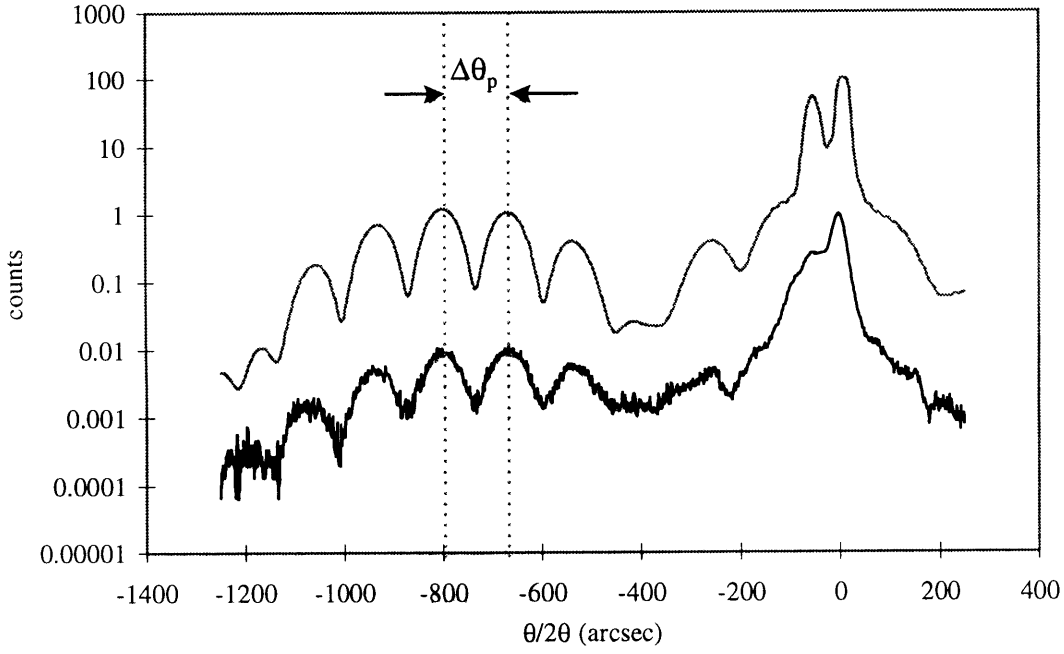

Figure 7-3. TAD θ/2θ scan of a 100 nm ZnSe/GaAs/ZnSe DBH. The black line indicates the experimental data, and the gray line the simulation of the heterostructure. The spacing of the fringes can be used to directly determine the GaAs layer thickness.

Based upon the fringe spacing in Figure 7-3 (130 arcsec), the actual GaAs width is 87 nm. This is within 4 atomic layers of the desired layer thickness for the GaAs. Because the fringe spacing is inversely related to the layer thickness, for narrower ZnSe/GaAs QWs, the θ/2θ scans show much broader fringes. For example, a 3 nm ZnSe/GaAs QW would have a fringe spacing of 340 arcsec. As a result, a comparison of the FWHM of the ZnSe-related feature in the ZnSe/GaAs heterostructure for different QW widths would reflect little beyond the changing thickness in the GaAs layer.

A comparison of the FWHM of the feature peaks in a θ/2θ scan for ZnSe/GaAs QWs grown with the same physical dimensions would provide insight into the uniformity of the lattice constant and diffracting planes for the respective layers. The FWHM of a GaAs θ/2θ scan has a theoretical limit of roughly 10 arcsec. Any broadening beyond the theoretical value is attributed to system limitations, curvature across the sample, strain between the different layers, and a misorientation of the crystal structure such that the Bragg condition is met over a wider angular range. For materials that are grown with

strain between different layers, the FWHM of a layer feature broadens when it begins to relax, and then narrows again once it has reached its natural lattice constant. The relationship between the FWHM of both the GaAs and the ZnSe features for 6 nm ZnSe/GaAs QWs where the GaAs QW was grown at different substrate temperatures is shown in Figure 7-4. As shown, with increasing substrate temperature, the FWHM of the GaAs feature becomes narrower. This improvement in the FWHM of the material is expected as the GaAs is grown at temperatures approaching the standard growth temperature of 580°C. At first consideration, the narrowing of the FWHM of the ZnSe feature with increasing GaAs growth temperature might also represent an improvement in the crystal quality. However, the reduction in the FWHM of the ZnSe feature could also indicate that the growth of GaAs at higher temperatures on the first ZnSe barrier layer has effectively energized relaxation mechanisms (i.e. interfacial defects). The ZnSe material for the GaAs QW material grown at the highest growth temperature is potentially relaxed.

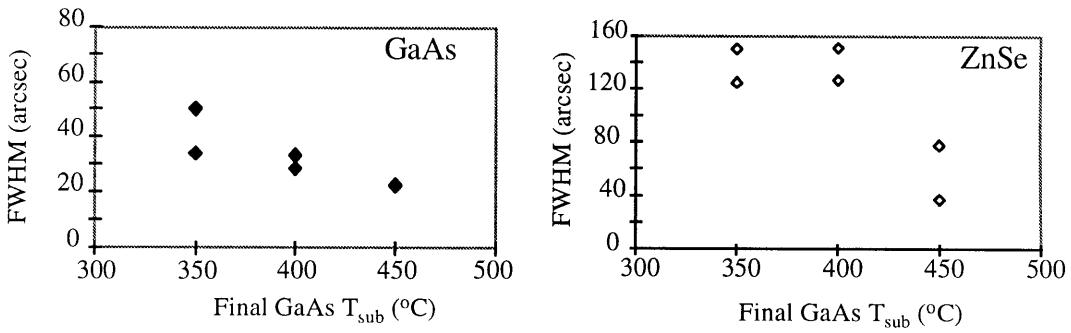

Figure 7-4. FWHM of the GaAs and the ZnSe features in TAD θ/2θ scans as a function of the final GaAs growth temperature. As shown, the FWHM of the respective features decreases with increasing final substrate temperature. For each growth temperature, the θ/2θ scan was taken with the sample in two orientations, 90° apart.

Further analysis of the x-ray diffraction measurements of the 6 nm ZnSe/GaAs QWs is necessary to understand the reduction in the FWHM of the ZnSe with increasing GaAs QW growth temperature. The θ/2θ scans can be used to provide further insight, as the data can offer information about the strain between two layers by studying the peak separation. If the ZnSe shows decreasing strain with increasing GaAs growth temperature, the ZnSe barrier layer has relaxed.

7.2.1 Strain determination between the ZnSe and the GaAs

The degree of strain between a semiconductor layer and the substrate can be probed by first measuring the difference in the lattice constant between the two materials perpendicular to the growth direction ($a_\perp$). The change is measured relative to the substrate lattice constant. The Bragg angles for the substrate peak, θ_s= 33.026°, and the layer peak, θ_l, can be determined from the $\theta/2\theta$ scan. The relationship between the change in the lattice constant, $a_\perp$, and the angular location of the x-ray features is given in Eq. 6 [106].

$$\left(\frac{\Delta a}{a}\right)_\perp = \frac{\sin\theta_s}{\sin\theta_l} - 1 \qquad \text{Eq. 6}$$

The perpendicular lattice constant for ZnSe can be determined from Eq. 6 and applied to Eq. 7 to determine the fractional strain, $\varepsilon_\perp$, between the two layers. The calculated lattice constant for ZnSe is compared to the known lattice constant of the GaAs substrate. The results from this calculation are shown in Figure 7-5 both as a function of the final GaAs QW growth temperature and the width of the QW for a series of ZnSe/GaAs QWs. A fully relaxed ZnSe layer on GaAs would have 0% strain.

$$\varepsilon_\perp = \frac{a_\perp - a_s}{a_s} \qquad \text{Eq. 7}$$

As can be seen, the strain between the GaAs and ZnSe is lower for the ZnSe/GaAs QW with the GaAs grown at the higher substrate temperature. This result fits with the argument that the ZnSe barrier layer is relaxed compared to the GaAs substrate. The lack of correlation between the degree of strain between the ZnSe and GaAs and the GaAs QW width also indicates that the growth of the QW at a substrate temperature of 350°C is sufficiently low to protect the first ZnSe barrier layer.

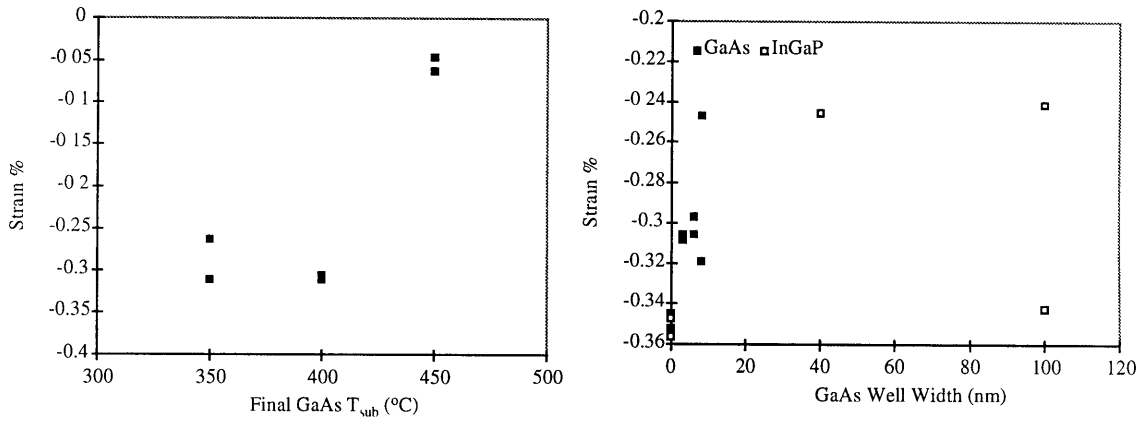

Figure 7-5 Strain % between the ZnSe and the GaAs layers based upon θ/2θ scans. The strain % is plotted as a function of the final GaAs substrate temperature (°C) and GaAs QW width (nm). For the plot of the strain as a function of QW width, the type of buffer layer employed is represented by the symbols. A solid symbol corresponds to a GaAs buffer layer and an open symbol corresponds to an InGaP buffer layer.

In summary, the results from the θ/2θ scans indicate that high quality ZnSe/GaAs QWs have been grown. For the standard growth conditions, the layers are shown to be pseudomorphic to the GaAs substrate regardless of QW width. Increasing the GaAs growth temperature in the ZnSe/GaAs QW has also been shown to decrease the critical thickness of the lower ZnSe barrier layer.

7.3 Results from ω scans

TAD ω scans were made by rotating the sample about the angles associated with the Bragg features measured in the θ/2θ scans and fixing the detector position in place while rotating the sample. The data were taken with a rotational step of 2 arcseconds and a dwell time per data point of 2 seconds. The ω scan GaAs wafer was measured in two different orientations with respect to the x-ray beam. The results from the GaAs wafer, shown in Figure 7-6, indicate that a minimum level of diffuse scattering from a semiconductor material has, on average, a FWHM of 13.5 arcseconds. In comparison, the ω scans from the same 100 nm ZnSe/GaAs/ZnSe DBH measured by θ/2θ scans in Figure 7-3 are much broader, as indicated by the plots shown in Figure 7-7.

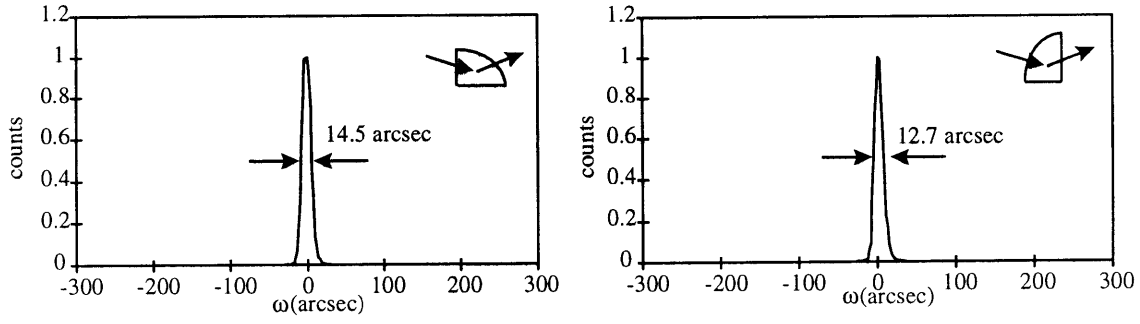

Figure 7-6. TAD ω scan results of a GaAs substrate at two different orientations to the x-ray beam as indicated by the schematics on each plot. The FWHM of each scan is also indicated. The data are normalized to the peak intensity for each orientation.

The ω scans shown in Figure 7-7 and Figure 7-8 show a directional variation in the lineshape of the data for a 100 nm ZnSe/GaAs DBH. The results in Figure 7-7 are measured at the Bragg angle for GaAs, while the results corresponding to the ZnSe layers are shown in Figure 7-8. If the ω scans were made in all four possible <110> directions, the second smaller peak that appears in one of the ω scans for both the ZnSe and the GaAs would move to the other side of the central peak.

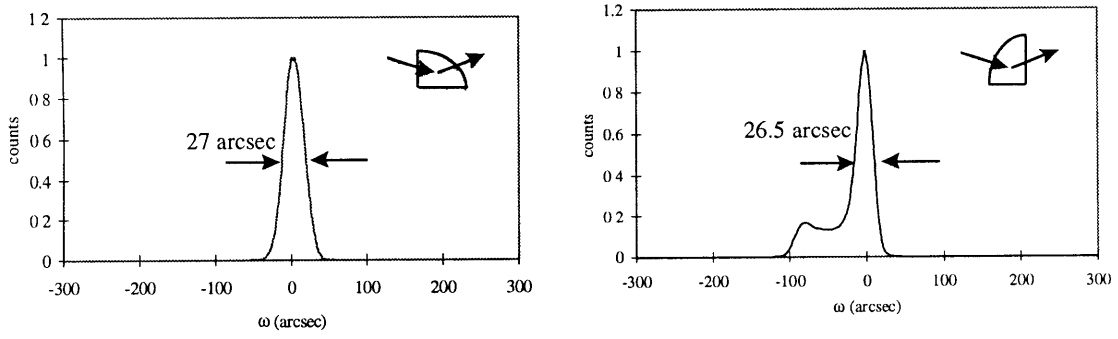

Figure 7-7. TAD ω scan results for a 100 nm GaAs layer and the GaAs substrate in a ZnSe/GaAs/ZnSe DBH taken in two orientations to the x-ray beam. Schematics of the sample orientation with respect to the x-ray beam are shown in each graph. The data are normalized to the peak intensity for each scan.

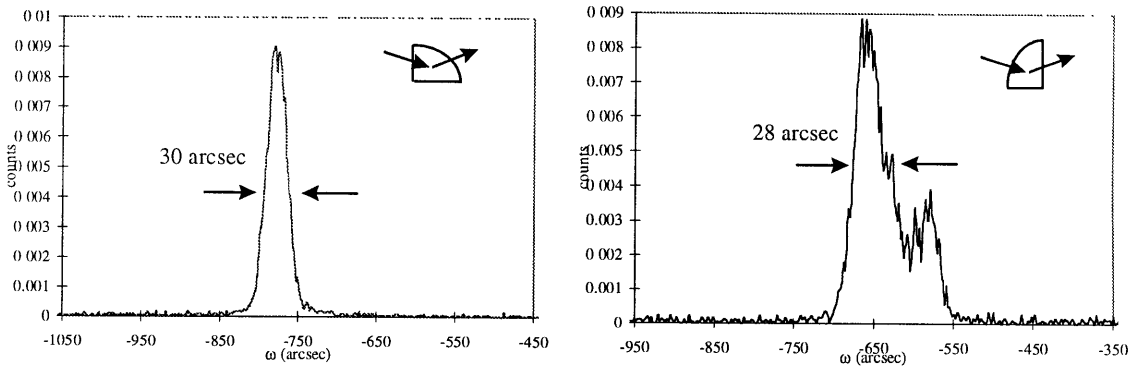

Figure 7-8 TAD ω scan results from the ZnSe barrier layers in a 100 nm ZnSe/GaAs/ZnSe DBH for two different orientations with respect to the x-ray beam (as indicated by the schematics in each graph). The data are normalized to the GaAs peak intensity in each orientation.

The ZnSe feature in both ω scans is roughly 1% as intense as the GaAs related feature. The reduction in intensity is a function of the layer thickness. The total ZnSe layer thickness in all of the ZnSe/GaAs QWs is roughly 100 nm. The x-ray diffraction measurement probes the top 10 μms of semiconductor material before absorption of the x-ray beam reduces the probe intensity to the noise level. Hence, it is logical that the ZnSe layer has a significantly smaller feature intensity. It is interesting, however, that the FWHM of the ZnSe ω scans is close to that of the GaAs material. This similarity in the FWHM of the four scans for the primary feature indicates that the GaAs ω scan features are not dominated by substrate effects, whereby the FWHM would be about half as large as the measurements from the ZnSe/GaAs QW. For the remainder of the ω scan analysis, the results from the GaAs material in the ZnSe/GaAs QWs are presented as the quality of the GaAs directly affects the quality of the rest of the heterostructure. The signal intensity from the ZnSe layers in these heterostructures is so low and sensitive to variations in the layer thicknesses that comparison across samples is complicated.

7.3.1 Diffuse scattering

Assessing the FWHM of the ω scan features is not sufficient to determine the degree of kinematical diffraction due to lattice imperfections in the TAD measurement. A better

approach is to determine the excess diffuse scattering in the material as a measure of crystal quality. The diffuse scattering is defined by Eq. 8 [109]:

$$I_{excess} = \int_{s_x,\min}^{s_x,\max} I_{net}(s_x,(s_z = 0))ds_x \qquad \text{Eq. 8}$$

where the variables, s_x and s_z represent the reciprocal lattice vectors. The equation for I_{excess} evaluates the integrated intensity of an ω scan, as represented by s_x with the z-axis of the crystal set to zero, or the Bragg peak angle for a given layer. The minimum level of diffuse scattering is set to subtract the dynamic scattering from the layer. In a method used by Goorsky, *et al* [105], the minimum diffuse scattering is defined as the integrated intensity of a GaAs wafer. The maximum diffuse scattering is determined by the instrumentation limits. The subsequent results present data that have taken the approach of Goorsky, *et al*, where the analysis of ω scans is generally made by normalizing the data to the peak intensity of the results from a high-quality bulk GaAs substrate.

If the growth of the ZnSe/GaAs QWs is a strong function of the quality of the GaAs layer, it would be expected that the diffuse scattering from the GaAs and the top ZnSe barrier layer would be reduced with increasing GaAs QW width. This improvement would be a result of increased growth time allowing the material to anneal into a smoother final layer. The GaAs QW can be considered a partially mosaic layer, because the growth temperature of 350°C is not sufficient to allow for a complete Ga migration on the GaAs surface to eliminate steps and pyramids. This hypothesis is tested in the TAD ω scan measurements of a series of ZnSe/GaAs QWs with a range of QW widths. The diffuse scattering is calculated in the form of integrated intensity normalized to a GaAs substrate ω scan. The results from this analysis are plotted in Figure 7-9. For each sample measured, the ω scan was taken in two orientations with respect to the x-ray beam, 90° out of phase. The integrated intensity results for the GaAs layer do reflect the expected behavior. The integrated intensity decreases with increasing GaAs QW width.

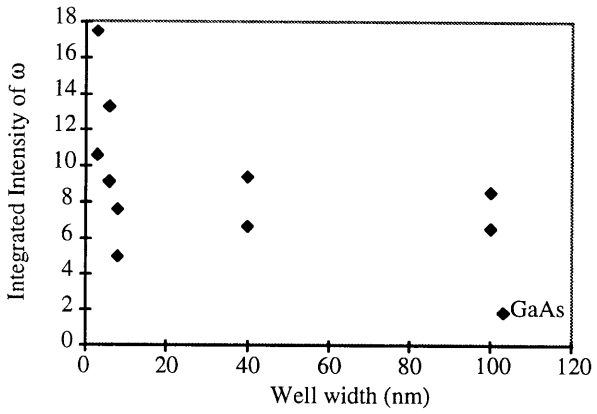

Figure 7-9. Integrated intensity of the GaAs feature in an ω scan using TAD as a function of GaAs QW width. The data are normalized to the peak value of an ω scan from a GaAs substrate.

Analysis of the integrated intensity for the ZnSe/GaAs QW as a function of the GaAs growth temperature was also studied. In the presentation of the θ/2θ results, the higher growth temperature was shown to have energized the lower ZnSe barrier to relax. The diffuse scattering should reinforce this argument, by increasing with an increase in the GaAs growth temperature as well. The integrated intensity of the set of 6 nm ZnSe/GaAs QWs as a function of the GaAs QW growth temperature is shown in Figure 7-10. The diffuse scattering from the GaAs material does increase with increasing growth temperature. The upward trend in the diffuse scattering for the GaAs as a function of GaAs QW growth temperature supports the previously presented θ/2θ data for the same samples, since the quality of the lower ZnSe barrier layer would affect the quality of the GaAs QW layer.

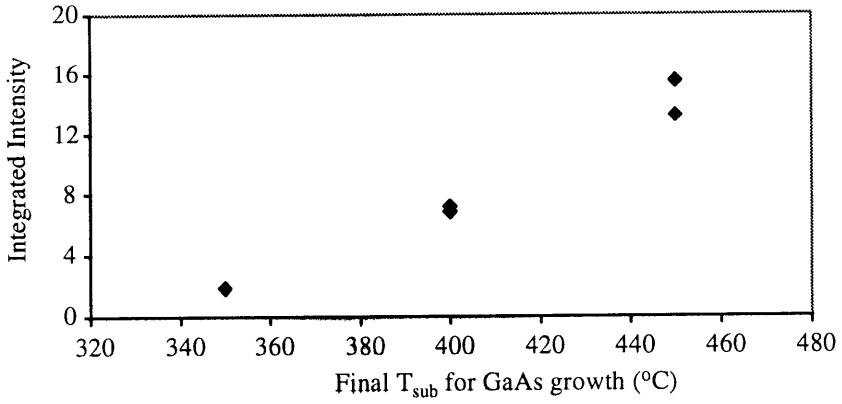

Figure 7-10. Integrated intensity of the GaAs feature in an ω scan using TAD as a function of the final substrate temperature (°C) during the growth of 6 nm GaAs QWs. The data are normalized to the peak value of an ω scan from a GaAs substrate.

The final set of ZnSe/GaAs QWs studied were the series of 6 nm QWs grown with a range of nucleation layer thicknesses. The nucleation layer is up to 10 monolayers of GaAs deposited on the lower ZnSe barrier layer. For these samples, the diffuse scattering from the GaAs in this heterostructure would be expected to decrease with a thicker nucleation layer. Based upon RHEED analysis during the nucleation of GaAs on ZnSe, full surface coverage of GaAs was not achieved until the third monolayer of deposition. Without this full coverage of GaAs, the remainder of the GaAs would have been grown in a more three-dimensional fashion, on GaAs islands. As a result, the mosaicity of the GaAs QW layer would be increased, as represented by the discontinuity of the material across the growth islands. The diffuse scattering in the TAD ω scans is expected to reflect this imperfection in the samples grown with thinner nucleation layers. In Figure 7-11 the diffuse scattering for this set of samples is plotted as the integrated intensity as a function of the number of monolayers of GaAs deposited at 250°C. For the GaAs material, the diffuse scattering does decrease with the thicker nucleation layer.

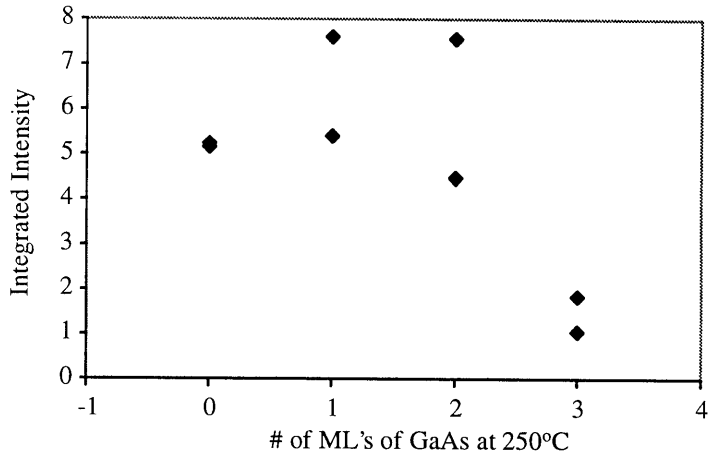

Figure 7-11. Integrated intensity of GaAs ω scan features from TAD measurements as a function of the number of ML's of GaAs deposited at 250°C for a 6 nm GaAs QW. The data are normalized to the peak value of the ω scan results from a GaAs substrate.

7.3.2 Dislocation density

The excess diffuse scattering in the ZnSe/GaAs QWs is a function of the dislocation density in the material. Although, while measuring the strain between the ZnSe and GaAs layers from the θ/2θ scans, the QWs were shown to be pseudomorphic to the GaAs substrate misfit dislocations are still probable at the ZnSe/GaAs heterointerface. Goorsky, *et al*, has determined that the TAD measurement is sensitive to dislocation densities of 1 μm^{-1}. In measuring the diffuse scattering and correlating it to the dislocation densities measured by plan-view TEM, Goorsky also has determined the relationship between the excess diffuse scattering and the dislocation density ($\rho_\perp$) to be:

$$\rho_\perp = 0.57(A_N - 1) \qquad \text{Eq. 9}$$

where A_N is the excess integrated intensity of the GaAs feature of an ω scan, and $\rho_\perp$ is measured in units of μm^{-1}. Applying the same equation to the excess integrate intensity measured for the ZnSe/GaAs QWs results in a range of misfit dislocation densities of 1 - 10 μm^{-1}. The relationship in Eq. 9 is relevant to the ZnSe/GaAs QW and DBH systems as Goorsky derived the equation based upon the diffuse scattering of GaAs. However, the potential does exist for the excess integrated intensity to be increased by wafer curvature

or rotational resolution and the multiplier, 0.57, might be specific to Goorsky's measurement.

The relationship between the sample orientation during the x-ray measurement and the misfit dislocation density was investigated by taking ω scans for two different orientations: the beam in the [011] or the [011] and the beam in the [011] or the [011] directions. The same trend is seen across all of the ZnSe/GaAs QW data sets: the misfit dislocation density is two times higher with the sample aligned such that the x-ray beam is parallel to the [011] direction. An example of this trend is shown in Figure 7-12. These results are unique to the x-ray diffraction measurement, as the area over which the sample is probed is large enough to see such low levels of dislocation densities. TEM analysis of these samples has the potential to look "between" dislocations at higher magnifications.

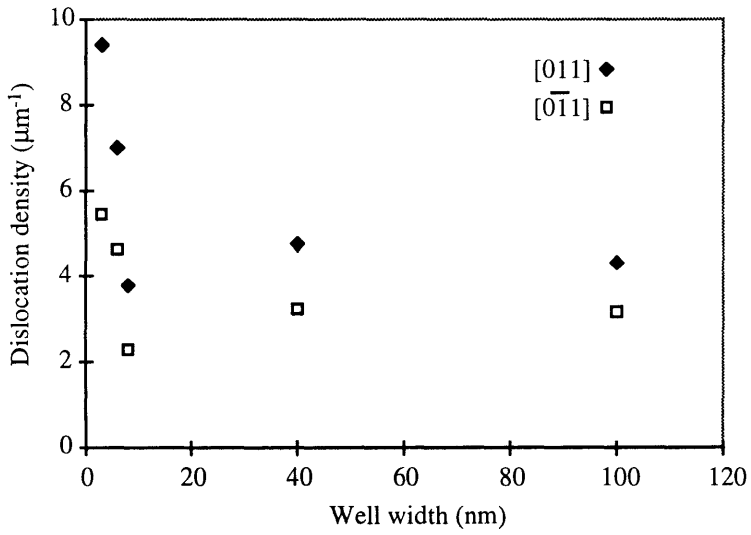

Figure 7-12. Dislocation density as a function of the ZnSe/GaAs QW width for both orientations measured. The dislocation density is higher when the x-ray beam was aligned parallel to the [011] direction.

To summarize, the data and analysis of the diffuse scattering for the ZnSe/GaAs QWs have indicated that the growth procedure for the heterostructure was optimized with respect to the nucleation layer and the GaAs growth temperature. The results also support the analysis of the θ/2θ scans, which suggested that the growth of the GaAs at a temperature of 450°C would force the lower ZnSe barrier layer to relax. The dislocation

density was calculated using the analysis presented by Goorsky, *et al*, with the end result that the ZnSe/GaAs QW shows evidence of a preferential direction for misfit dislocation formation.

The next step in the microstructural characterization of the ZnSe/GaAs QWs by TAD is to measure the (004) reciprocal space maps around the Bragg angles for the GaAs and ZnSe layers. These results are presented in the subsequent section.

7.4 Reciprocal space maps

The reciprocal space mapping (RSM) capability with the TAD measurement is a powerful tool for assessing the composition, strain, and defect density of a stack of materials. The ZnSe/GaAs QWs were initially assessed by this technique before the higher-resolution $\theta/2\theta$ and ω scans were taken in order to achieve a qualitative understanding of the relative quality of the QWs fabricated under different conditions. The details of the data acquisition and conversion to in-plane and perpendicular reciprocal lattice vector values follow. Next, the base case measurement of a GaAs substrate is presented. Finally, the RSMs for a series of ZnSe/GaAs QWs are shown and compared.

RSMs are taken by scanning the sample multiple times with small increments in $\theta/2\theta$ and ω, ultimately rotating the sample through a full two-dimensional region that incorporates both the Bragg angles of GaAs and ZnSe and the diffuse scattering associated with all of the layers in the ZnSe/GaAs QW heterostructure. The $\theta/2\theta$ axis was scanned in 5 arcsec steps, and the ω axis was scanned in 10 arcsec steps. The dwell time for each data point was 1 second. In comparison to the $\theta/2\theta$ scan and the ω scan results previously presented, the rotational resolution of the RSMs is reduced. This limitation arises because the data acquisition time inhibits smaller rotational steps. In general, the $\theta/2\theta$ scan range was 1700 arcsec and the ω scan range was 600 arcsec, resulting in a 7 hour data acquisition time. For a longer data acquisition time, x-ray beam and sample drift become more of an issue.

7.4.1 Conversion of θ/2θ and ω data to s_x and s_z

The in-plane and perpendicular reciprocal lattice vectors, s_x and s_z, can be determined from the following relationships [106]:

$$s_x = \frac{2}{\lambda}\sin\theta\sin(\omega-\theta) \qquad \text{Eq. 10}$$

$$s_z = \frac{2}{\lambda}\sin\theta\cos(\omega-\theta) \qquad \text{Eq. 11}$$

where θ and ω values come from the θ/2θ and the ω scans. The x-ray wavelength, λ, is 1.54 Å.

7.4.2 Base case: GaAs substrate

Two reciprocal space maps (RSMs) of a GaAs wafer manufactured by American Crystal Technology (AXT) were taken in the (004) orientation. The sample was aligned to the incident x-ray beam such that the beam was perpendicular to a sample edge, in a <110> direction, with the two (RSMs) taken with a 90° change in sample orientation. The RSMs from the GaAs sample were taken to assess the x-ray system performance in probing a high quality single crystal (see Figure 7-13). The contour maps for each orientation of GaAs are plotted to show 7 orders of magnitude of intensity on a logarithmic scale. The most intense contour is located in the center of the plot. The star-shaped profile of the contours demonstrates the large dynamic range in intensity of the RSM; the diagonal streaks result from diffraction from the analyzer crystal and the x-ray optics. The GaAs RSMs were plotted with axis dimensions that will be used for the ZnSe/GaAs QW RSMs. These plots enable a comparison to be made in the magnitude and breadth of the diffuse scattering between the GaAs substrate and the QWs.

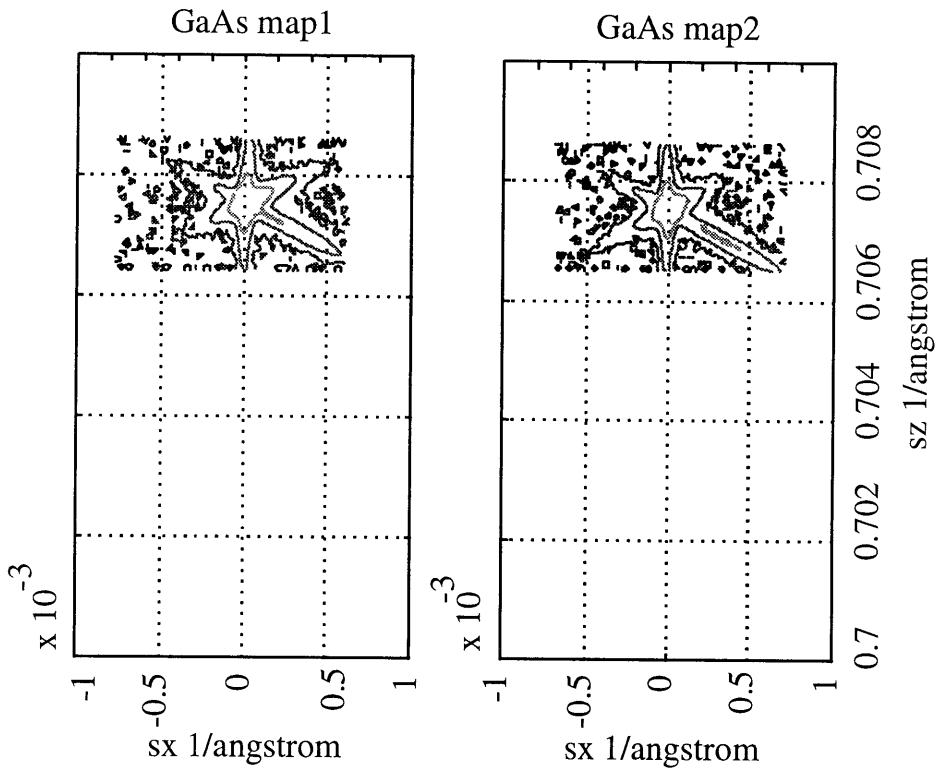

Figure 7-13. (004) RSM of a GaAs substrate in with the sample aligned to the x-ray beam in two orientations that are 90° apart.

The RSMs from the GaAs substrate shown in Figure 7-13 indicates that the diffuse scattering about the (004) reciprocal lattice point is symmetric. The FWHM of the features in both the s_x and the s_z direction are the same for both orientations. The diminished angular resolution for the RSM measurement due to the larger rotational step is also indicated in a slight broadening (of 2 arcesc) at the FWHM of the GaAs feature along the s_z axis.

The next sections present a series of RSMs for a 100 nm ZnSe layer grown on GaAs, a ZnSe/GaAs 100 nm DBH, and a ZnSe/GaAs 8 nm QW. The comparison to be made for this set of samples is the effect of the addition and width of the central GaAs layer on the TAD (004) RSM.

7.4.3 Data: ZnSe/GaAs heterostructures

The results from the (004) RSM of a 100 nm ZnSe layer on GaAs are shown in Figure 7-14. The contour map is plotted on a log scale, with 7 orders of elevation. The ZnSe layer is shown clearly centered around 0.703 $Å^{-1}$ on the s_z axis. The diffuse scattering in one direction is slightly broader than in the other. The broadening is evident in both the ZnSe- and the GaAs-related features, at 0.703 and 0.707 1/angstrom respectively.

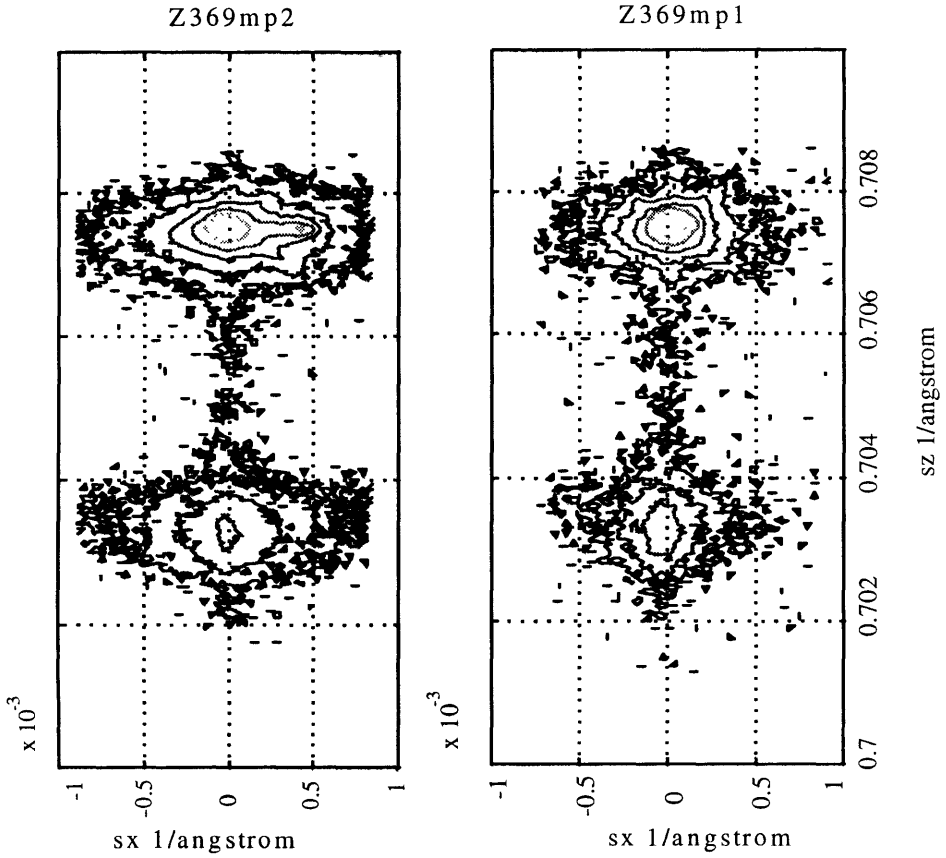

Figure 7-14. (004) RSMs of a 100 nm ZnSe layer on a GaAs buffer layer and substrate with the x-ray beam aligned in two orientations, 90° out of phase.

In comparison, the RSMs from two orientations of a 100 nm ZnSe/GaAs DBH plotted with the same range for the contours shows little evidence of broadening between the two different maps (see Figure 7-15). The variation between the two orientations occurs along the s_z direction, the direction of the perpendicular reciprocal lattice vector. The addition of a 100 nm thick GaAs layer between the ZnSe layer adds fringes to the ZnSe-related feature with a period discussed in a previous section. The splitting of the features shown

previously in the ω scans is also evident in the left-hand RSM, along the s_z axis. The splitting runs through the entire RSM.

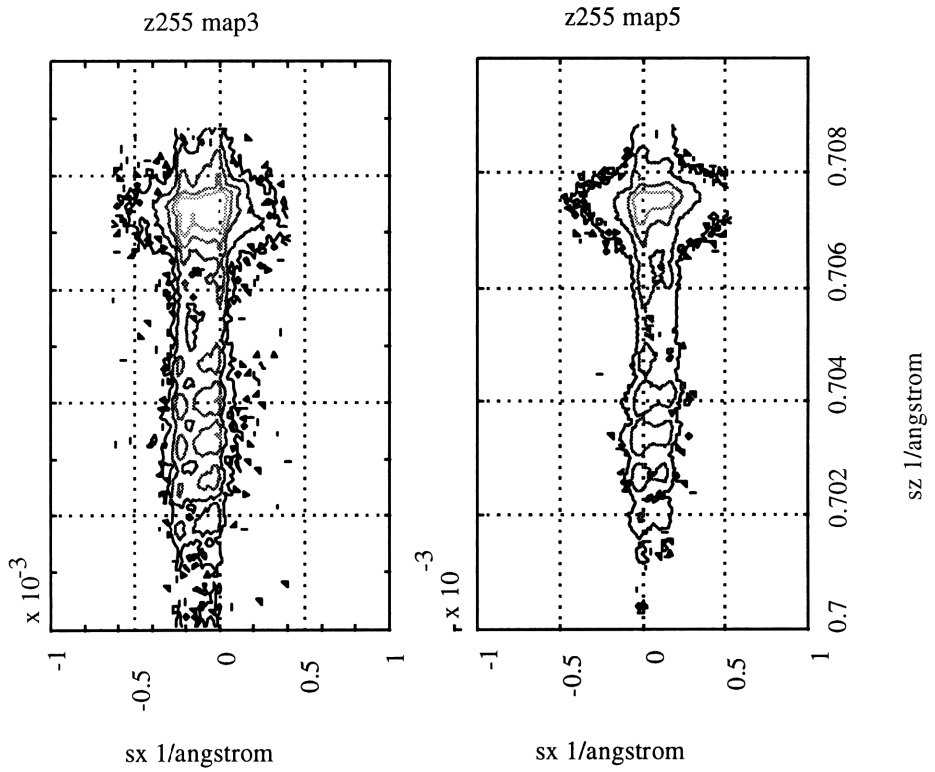

Figure 7-15. (004) RSMs of a 100 nm ZnSe/GaAs DBH, with the x-ray beam aligned at two orientations 90° out of phase.

The RSMs for a third heterostructure, an 8 nm ZnSe/GaAs QW, are shown in Figure 7-16. In these maps, the diffuse scattering is a function of the sample orientation to the x-ray beam. In the left-hand plot, the GaAs-related feature is close in lineshape to that of the GaAs substrate. However, the right-hand plot of the same sample, with a 90° rotation with respect to the left-hand plot, indicates a significant broadening in the GaAs feature. The feature corresponding to the ZnSe layer is similar in shape to the feature for the ZnSe layer in Figure 7-14. However, broadening also exists in the diffuse scattering of the left-hand plot. The broadening is an indication of a higher density of misfit dislocations, as discussed in a previous section. The RSM for this sample provides further support for analyzing the GaAs feature as a route to understanding the entire heterostructure, since the broadening appears to occur throughout the RSM.

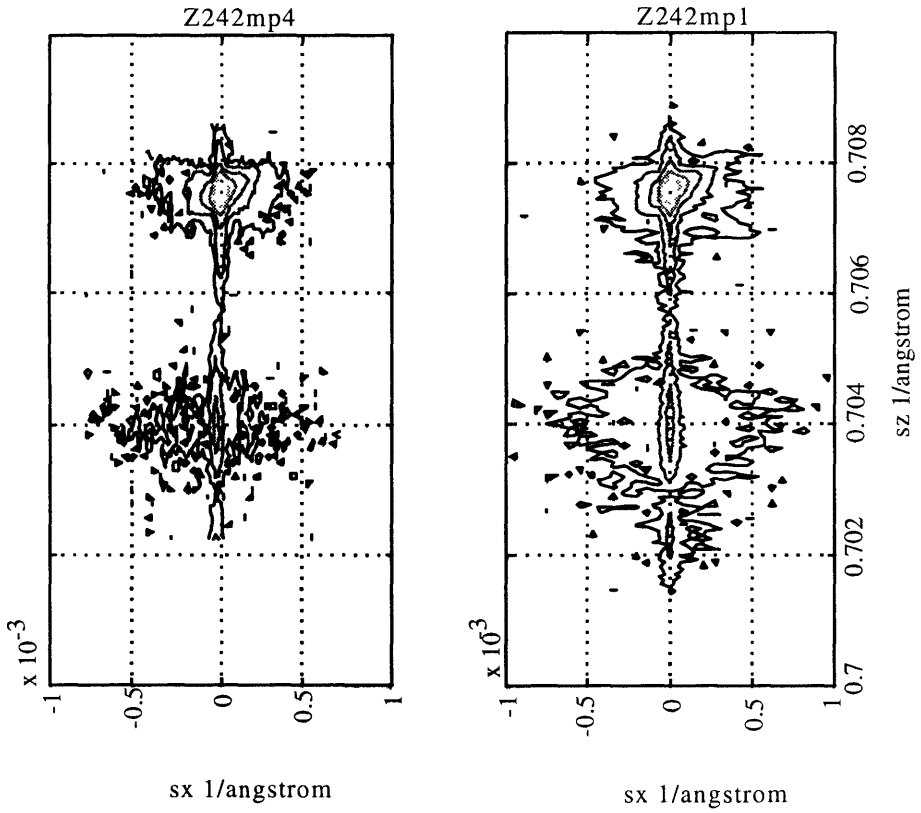

Figure 7-16. (004) RSMs of an 8 nm ZnSe/GaAs QW with the x-ray beam aligned in two orientations, 90° out of phase.

The fringes in the ZnSe feature seen in the 100 nm ZnSe/GaAs DBH (Figure 7-16) are not as evident in the RSM for the 8 nm ZnSe/GaAs QW since the fringe spacing is much larger for the narrower GaAs layer. The small feature at 0.702 $Å^{-1}$ marks the onset of the second fringe related to the presence of the GaAs QW. The fringe intensity is low, and subsequent fringes are below the range of detection.

The RSMs for the three different ZnSe/GaAs heterostructures indicate that the degree of diffuse scattering is not directly a function of the presence of a GaAs QW. The single ZnSe on GaAs heterostructure shows a large degree of diffuse scattering, and an orientational dependence on the magnitude of scattering. In comparison, the two ZnSe/GaAs heterostructures probed with a central GaAs layer, of thickness of either 100 nm or 8 nm, show a GaAs-related feature with a degree of diffuse scattering that approaches that seen in the GaAs substrate. The 8 nm QW also shows a directional

dependence on the sample orientation for the magnitude of the diffuse scattering, and this result has been discussed previously in the analysis of the ω scan results.

7.4.4 RSMs of GaAs on ZnSe

Thus far, the RSMs of the ZnSe/GaAs heterostructures have not shown a large deviation from the base case of a GaAs substrate. The limitations on the angular resolution as a function of the data acquisition parameters also limit the degree to which quantitative analysis can be made on the RSMs. Instead, the results from the straight one-dimensional scans have provided a great deal of insight into the properties of the ZnSe/GaAs QWs as a function of the growth parameters. In an effort to take advantage of the very graphic results the RSMs provide, the set of GaAs grown on ZnSe heterostructures were probed to see if a more significant comparison could be made amongst the samples. Following are the (004) RSMs of GaAs on ZnSe heterostructures nucleated by three different conditions: MBE, MEE, and SM-MBE. The RSMs for these three samples are plotted with a slightly larger scale on the s_x axis.

The RSMs for the 250 nm GaAs layer nucleated on ZnSe by standard MBE are shown in Figure 7-17. For both orientations of the sample measured, the feature intensity is weak and broad for both the ZnSe and the GaAs layers. In this instance, the GaAs layer is both thick and defective enough to dominate the properties of the GaAs-related feature. Though there does appear to be some dependence upon the sample orientation and the lineshape, it is more important to note that the GaAs-related feature is significantly broader than that of the GaAs-substrate base case.

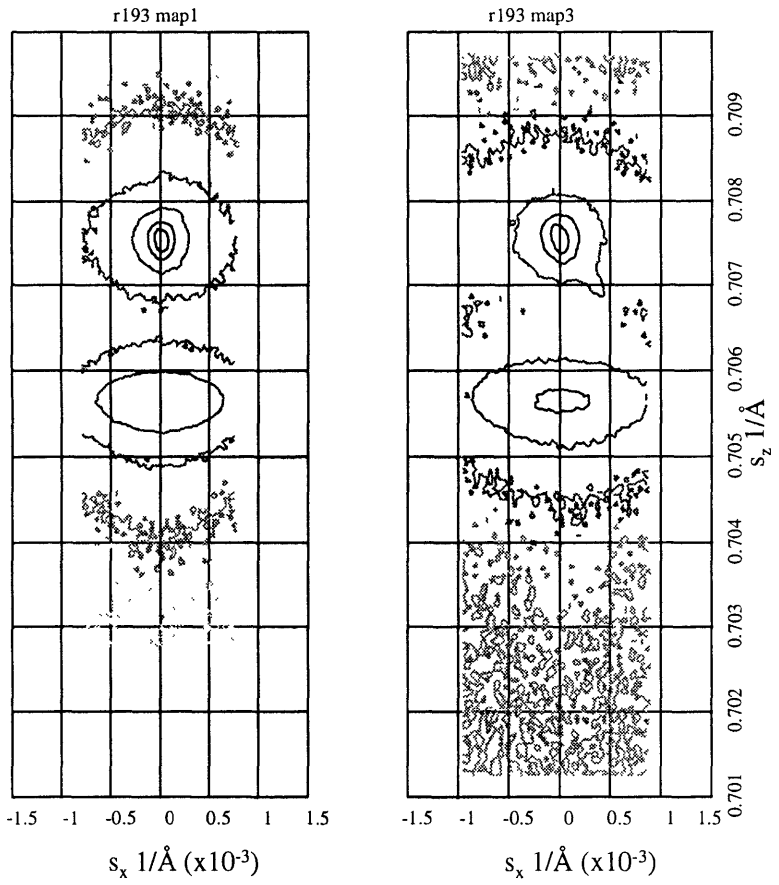

Figure 7-17. TAD (004) RSM of a 250 nm GaAs layer nucleated by standard MBE on a ZnSe layer. The signal intensity is both weak and broad for this sample, in both orientations.

In comparison, when the GaAs layer is nucleated on the ZnSe surface by MEE, the GaAs and the ZnSe features become more pronounced and the diffuse scattering narrows (see Figure 7-18). The GaAs-related feature reflects an intense central contribution from the substrate, but a large degree of diffuse scattering is still present. Based upon the RSMs for the MBE and the MEE nucleation of GaAs on ZnSe, an improvement in the GaAs quality appears to have resulted.

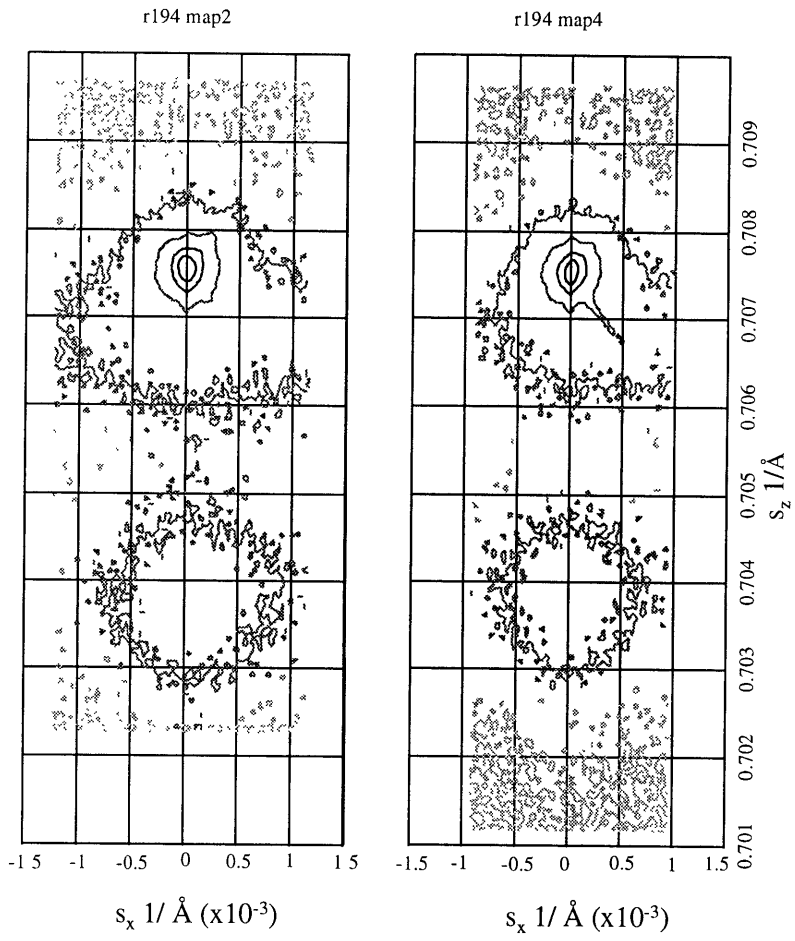

Figure 7-18. TAD (004) RSMs of a 250 nm GaAs layer nucleated on ZnSe by MEE using the methodology of Funato, *et al* [24].

The final nucleation sample, GaAs nucleation on ZnSe by SM-MBE shows the highest quality heterostructure of the three samples studied. The RSMs shown in Figure 7-19 for both orientations somewhat resemble the RSMs for the 8 nm ZnSe/GaAs QW. The GaAs-related feature is more intense and the degree of diffuse scattering is reduced in comparison to the GaAs on ZnSe nucleated by MBE and MEE. The ZnSe-related feature is also narrow and well-defined. A most encouraging result for the RSMs for this GaAs on ZnSe heterostructure are the appearance of fringes between the GaAs and the ZnSe feature, an indication that both the ZnSe-on-GaAs buffer layer and GaAs-on-ZnSe heterointerfaces are of similar quality.

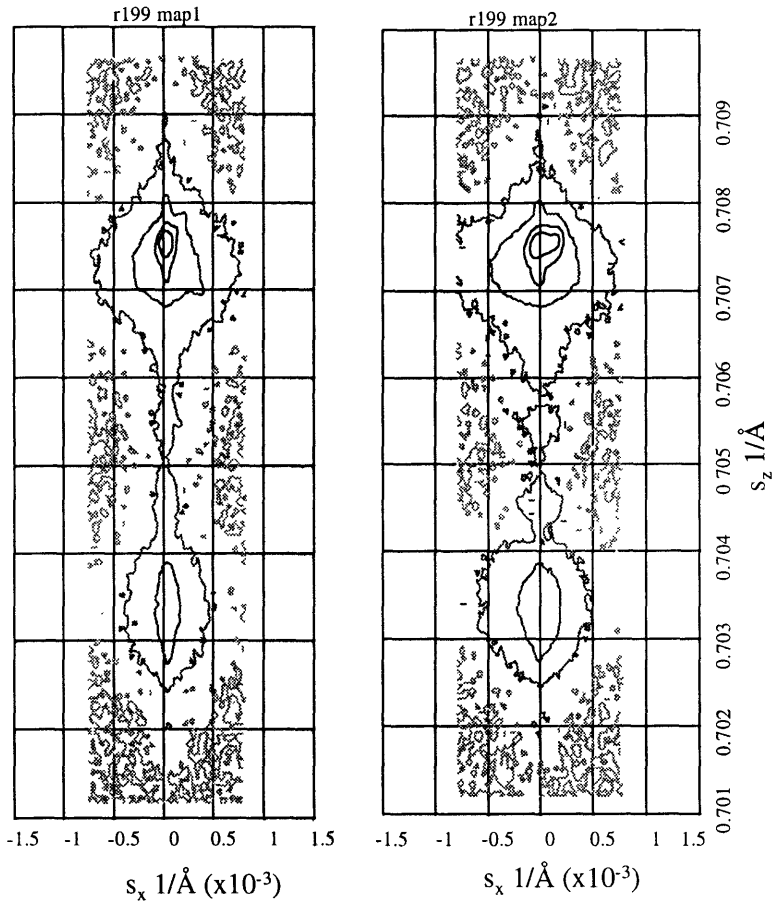

Figure 7-19. TAD (004) RSMs of a 250 nm GaAs nucleated on a thin ZnSe layer by SM-MBE. The interface between the GaAs layer on the ZnSe is of such high quality that fringes appear between the GaAs and the ZnSe features.

Based upon the results from the three GaAs/ZnSe heterostructures nucleated by different methods, the RSMs provide a clear comparison of the relative quality for large changes in the growth parameters.

7.5 Summary

The microstructural analysis of the ZnSe/GaAs QWs by x-ray TAD has provided insight into the long-range crystal properties of the heterostructures. The θ/2θ results were used to determine the degree of strain and the layer quality for the in-plane reciprocal lattice vector. The ZnSe/GaAs QWs were shown to be pseudomorphic to the GaAs substrate except for the instance in which the GaAs QW material was grown at an elevated temperature of 450°C. The increased growth temperature for the GaAs is believed to have

energized relaxation in the lower ZnSe barrier. This result is further supported in the analysis of the ω scan results for the same samples. The excess diffuse scattering was calculated from the ω scan data; it was measured by the integrated intensity of the ω scan feature normalized to a GaAs substrate peak and then subtracted from the integrated intensity of a GaAs substrate peak. For an increase in the GaAs growth temperature, the diffuse scattering for the GaAs layer was shown to increase, indicating a fluctuation of the perpendicular lattice constant which would be a function of dislocation density or mosaicity of the crystal structure. A similar increase in the diffuse scattering for ZnSe/GaAs QWs grown outside the optimized SM-MBE parameters was seen as a function of the thickness of the nucleation layer. This result is explained in conjunction with the RHEED patterns of the surface seen during the growth, which suggested that three-dimensional growth was more likely for the remainder of the growth if no nucleation layer existed. In the nucleation layer comparison, the cause of increased diffuse scattering can be attributed to mosaicity of the crystal structure caused by the formation of growth islands at the onset of the GaAs QW growths. The results from the diffuse scattering were also used to determine the range and orientation dependence on the misfit dislocation density in the ZnSe/GaAs QWs as a function of the QW width. The range of misfit dislocation densities are, to first approximation, between 1 and 10 μm^{-1}. However, the value of the dislocation density appears to be orientation dependent, with a two-fold increase of the density along the [011] direction over the [011] direction.

The study of the ZnSe/GaAs heterostructures by (004) RSMs indicated that the relative quality of the ZnSe/GaAs QWs was comparable to that of a GaAs substrate. The method appears to be more powerful as a tool to map heterostructures of very different physical dimensions and parameters. The RSM comparison of the GaAs nucleation on ZnSe by three different methods provided a graphic representation of the long-range improvement in the crystal structure when the growth was initiated by SM-MBE.

8. Transmission electron microscopy

The advent of the transmission electron microscope in the early 20th century gave scientists the ability to actually see the physical structure of materials down to the atomic level. This technological advance has become especially important in the semiconductor industry as the dimensions of both the materials and devices have shrunk below the resolution of optical microscopes. For the specific case of semiconductor heterostructure analysis, transmission electron microscopy (TEM) is used to identify defects and dislocations within the material with respect to orientations perpendicular or parallel to the surface of the heterostructure. The dimensions of the lattice planes, heterolayers, and other features of interest can also be determined.

The TEM analysis carried out in this study was completed at MIT's CMSE Electron Microscopy facility. Mass and phase contrast imaging was done on a JEOL 200CX with either a titanium and a LaB_6 filament. For higher resolution analysis, the Akashi 002B electron microscope with a LaB_6 filament was used, with a point-to-point resolution of 0.18 nm. In both cases, the operational voltage is 200 kV.

All of the ZnSe/GaAs heterostructures studied were analyzed by cross-sectional TEM. A ZnSe/GaAs single heterostructure was also studied by plan-view TEM in order clarify the defect structure visible in the cross-sectional images. The advantages of the cross-sectional analysis are the determination of the physical dimensions, the assessment of the heterointerfaces, and the ability to quantify the defect and dislocation density.

The following chapter is divided into two sections; one for TEM analysis and the other for high-resolution electron microscopy (HREM) analysis. The TEM section contains cross-sectional bright field images of a combination of ZnSe/GaAs heterostructures and III-V/III-V heterostructures. The goal of the TEM analysis is to identify the presence of defects and dislocations throughout the heterostructure as a function of the growth parameters for the ZnSe/GaAs heterostructures. In the second section of this chapter,

HREM imaging focuses on the ZnSe-on-GaAs and the GaAs-on-ZnSe heterointerfaces by imaging the atomic lattice.

8.1 Part I: TEM

The TEM results for the ZnSe/GaAs QWs and related heterostructures are given here. Material preparation issues are discussed first, and are followed by an assessment of the optimal bright field imaging condition of ZnSe to differentiate between preparation artifacts and structural information in the TEM images. Subsequent sections present the cross-sectional images of the heterostructures grown in the course of the ZnSe/GaAs QW optimization. The information to be gained from all of these results are: a visualization of the physical heterostructure, identification of defects in the heterostructure, and a comparison of the properties of the different heterostructures. All of the images shown in this section are oriented with the electron beam at or close to the [110] crystallographic direction.

8.1.1 Material preparation issues

One of the disadvantages of TEM analysis of ZnSe-based heterostructures is the sample preparation (see Appendix 2). The final process in the sample preparation, argon ion milling at 4 - 6 kV, determines the properties of the TEM sample. Although the energy of the argon beam is low in comparison to the electron beam, the argon ions have a stronger interaction with the material which can result in the formation of dislocation loops. The ion milling rate is material dependent, although for GaAs and ZnSe the difference is negligible unless the goal is to achieve lattice imaging. The largest problem with the ion milling process is the damage caused to the ZnSe material, which is shown in the subsequent TEM images.

During the ion milling process, the least stringent method was used to minimize material damage; the angle of impingement of the argon beam and the beam energy were minimized at 12° and 4 keV, respectively. The low angle of incidence for the argon ion beam reduces the penetration depth. The low energy reduces the defect formation in the sample must be thinner than 1 μm to achieve an adequate degree of forward scattering by

the electron beam. However, for lattice imaging, the sample needs to be roughly 10 nm thick. The argon ion milling process damages the ZnSe/GaAs heterostructures to the degree that the material is no longer crystalline at the thinnest parts. Hence, a compromise exists in achieving high-quality lattice images. The sample must be very thin, but the argon ion milling process destroys the lattice periodicity of the sample as it becomes very thin.

The imaging conditions for the ZnSe material was partially determined by the ion milling damage. Dark-field imaging was complicated by the contrast contribution from the dislocation loops in the damaged ZnSe material. A better approach appeared to be to image the samples under bright-field conditions (with the forward scattered beam centered down the optical-axis and in the selected area aperture).

8.1.2 Bright-field two-beam analysis

High contrast TEM images are achieved by minimizing the degree of inelastic scattering contributing to the sample image. A selected area aperture is placed in the path of the electron beam to allow selected diffracted beams (or reciprocal lattice points) to form the final sample image. Contrast is further increased by tilting the sample such that one diffracted spot is excited resulting in two intense diffraction beams: the forward scattered 000 beam and the excited diffracted beam. An excited diffraction beam corresponds to satisfying a Bragg condition for a crystal plane, as shown in the images of the electron diffraction patterns in Figure 8-1 showing the 200 and the 022 two-beam conditions. For compound semiconductors, the {200} beams are strongly related to the material composition, thus establishing a two-beam condition with either of these beams is useful for maximizing the contrast between the two materials [110, 111].

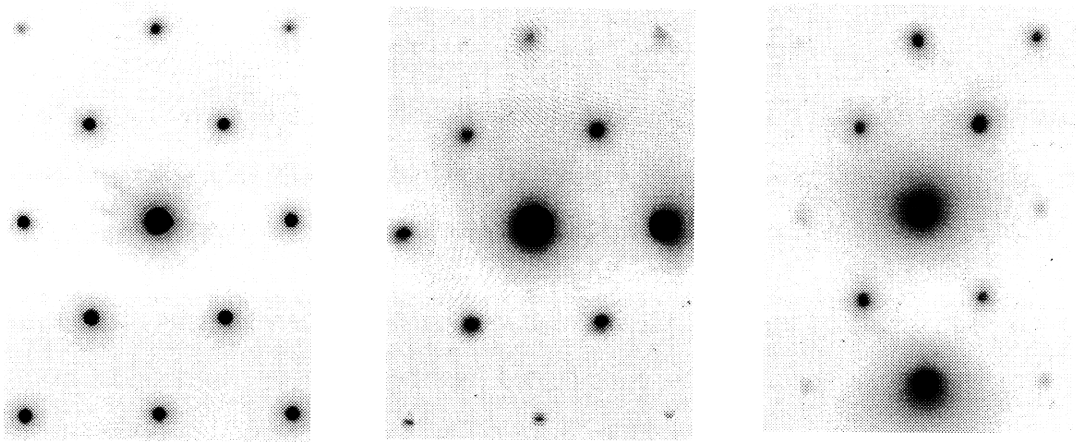

Figure 8-1. Electron diffraction patterns for the electron beam aligned down the [011] crystal axis, tilted to the 200 two-beam condition, and tilted to the 022 two-beam condition.

Figure 8-2 shows an example of an InGaP/GaAs multiple QW imaged with the sample titled in the path of the electron beam such that the electron beam is parallel to the (011) lattice plane or satisfies the 200 or the 022 Bragg conditions. When a Bragg condition is met, the contrast between the InGaP and the GaAs increases and both materials show more overall contrast. The contrast within the InGaP and GaAs layers is due to non-uniformity caused by thickness variations during the sample preparation. Regions in the images that are dark or light correspond to thicker or thinner areas of the sample.

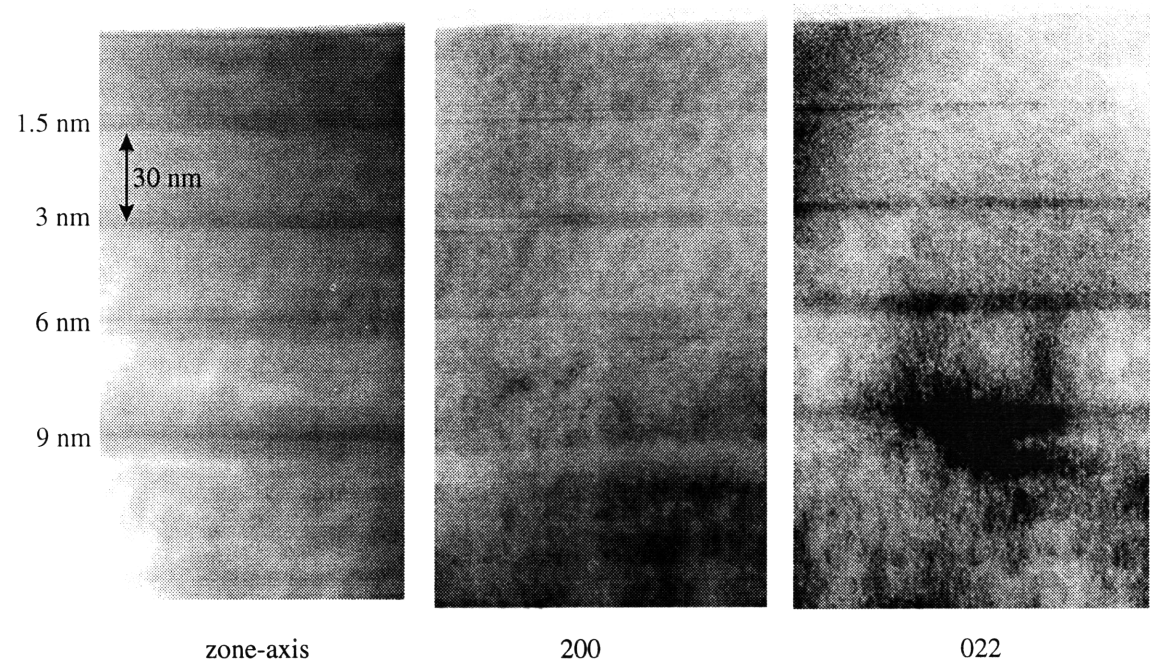

Figure 8-2. Bright-field TEM image of InGaP/GaAs multiple QW taken with the electron beam aligned in the [011] direction, tilted to a 200 two-beam condition, and tilted to a 022 two-beam condition. The two-beam images show a higher degree of contrast between the InGaP and the GaAs.

When imaging the ZnSe material, the ion milling damage is accentuated when first-order diffraction beams (the reciprocal lattice points closest to the forward scattered beam) are excited in achieving the two-beam condition. As a result, the TEM bright-field imaging of the ZnSe/GaAs heterostructure was done by exciting the second or third order diffraction beams.

8.1.2.1 Plan-view and cross-sectional analysis of ZnSe grown on GaAs

Initially, all of the heterostructures investigated were studied by cross-sectional TEM. Plan-view TEM analysis of a single ZnSe/GaAs heterostructure was studied because there was evidence of a high density of interfacial defects. The ZnSe layer for this heterostructure is 1 μm, beyond the critical thickness of ZnSe (~150 nm) when grown on GaAs, and the interfacial defects can be attributed to misfit dislocations formed during relaxation. In order to demonstrate a defective heterointerface, the combination of cross-sectional and plan-view TEM bright-field images for the ZnSe/GaAs single heterostructure is shown in Figure 8-3. Image (a) in Figure 8-3 shows the entire 1 μm ZnSe layer and

image (b) focuses in on the ZnSe/GaAs heterojunction. The defects at the heterointerface appear as dark lines of contrast. When imaged in plan-view, the ZnSe/GaAs heterointerface shows a high density of misfit dislocations aligned along the <011> directions (see image c). The dark lines in image (c) that run along a diagonal are believed to be threading dislocations that are bound by (001) planes, and thus seem to zigzag across the image. The types of defects present at the ZnSe/GaAs heterointerface in Figure 8-3 are typical of this heterostructure [9, 112-118].

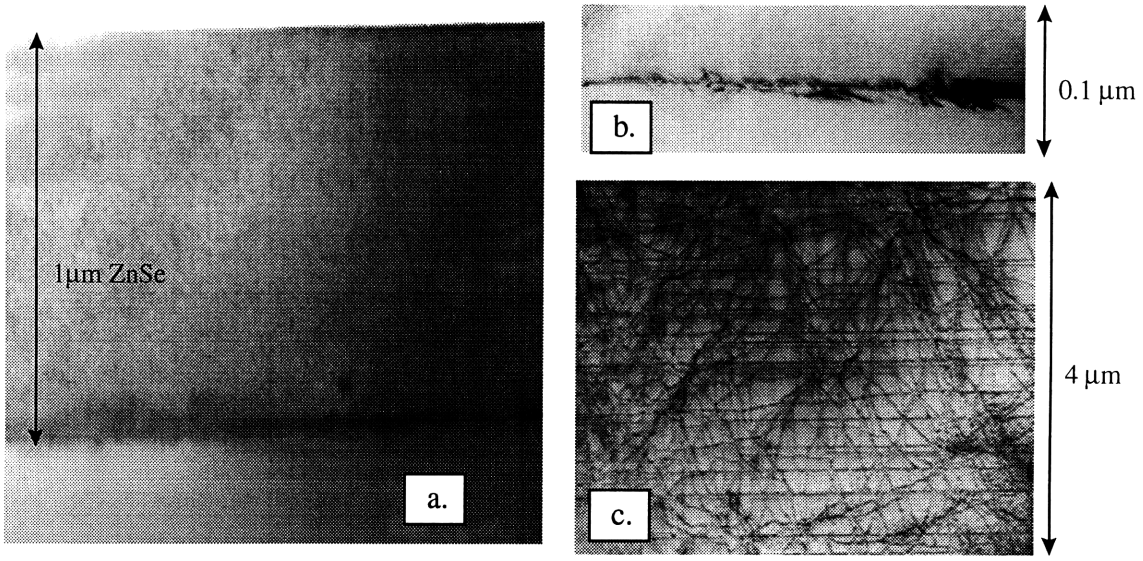

Figure 8-3. TEM of 1 μm ZnSe layer on GaAs. (a) Shows the cross-section of the entire ZnSe layer, (b) cross-section focuses in on the heterointerface and shows a series of defects, (c) plan-view image of the heterointerface showing a series of dislocations.

The origin of the majority of the heterointerfacial defects is the relaxation of the ZnSe layer on the GaAs. The rest of the heterostructures investigated are thin enough that relaxation is not expected to be a mechanism for defect generation at the heterointerfaces. Defects are also caused by the formation of the heterojunction, where the initial stages of nucleation for the ZnSe might not uniformly bond to the GaAs surface.

8.1.2.2 Pseudomorphic ZnSe/GaAs single heterostructure

A thin layer of ZnSe nucleated on GaAs under optimal conditions has a substantially lower defect density at the ZnSe/GaAs heterointerface than a thicker, relaxed ZnSe layer. Figure 8-4 shows the cross-sectional TEM image of a 285 nm thick ZnSe layer nucleated on

GaAs: without annealing, after a 20 minute anneal at 600°C, and after a 60 minute anneal at 600°C. This single heterostructure was previously discussed in regards to measuring interfacial roughness and interdiffusion by EDS. The unadulterated ZnSe/GaAs heterostructure shows a clean, defect-free heterointerface. The ZnSe material has little ion milling damage. However, as the sample is annealed, both the heterointerface and the ZnSe material becomes increasingly defective. A plot of the defect density along the heterointerface as a function of the 600°C anneal time is shown in Figure 8-5. The cross-sectional images indicate that the heterointerface is markedly altered during the anneal, which provides further evidence for the limitations of the EDS measurement for the compositional analysis of the ZnSe/GaAs heterointerface.

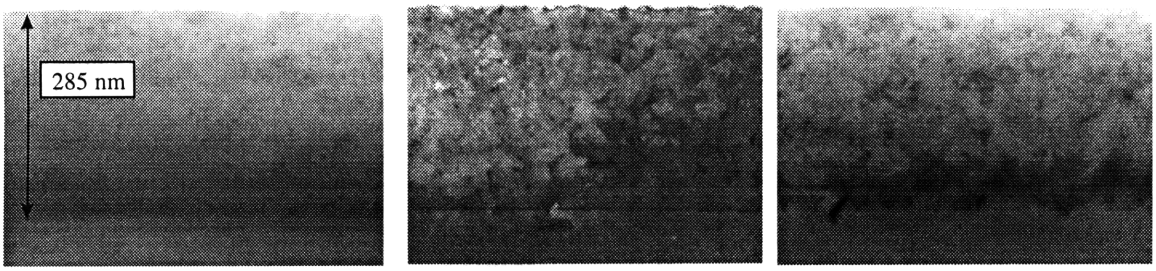

(a) no anneal (b) 20 min, 600°C (c) 60 min, 600°C

Figure 8-4. Bright-field cross-sectional TEM of a thin layer of ZnSe grown on GaAs with: no anneal, a 20 minute anneal at 600°C, and a 60 minute anneal at 600°C. The ZnSe layer relaxes when annealed, and becomes more damaged during ion milling.

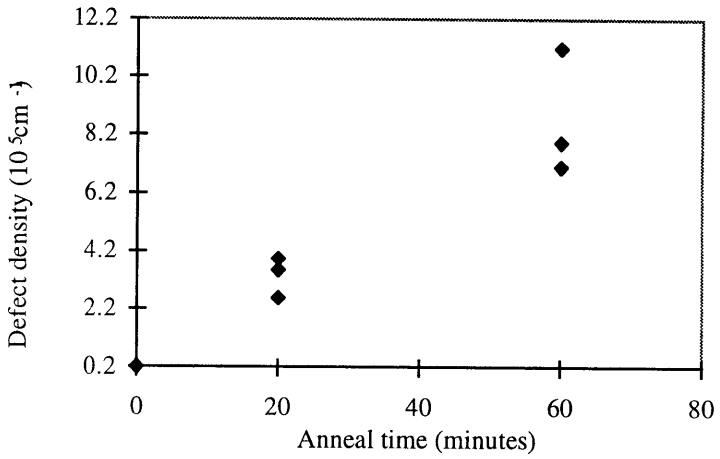

Figure 8-5. Defect density along the ZnSe/GaAs heterointerface as a function of the 600°C anneal time. The defect density increases with increasing anneal time.

The cross-sectional TEM analysis of the ZnSe-on-GaAs heterointerface indicates that the junction can be of high-quality for thin ZnSe layers. Also, the ZnSe material is shown to be more susceptive to ion milling damage as the material quality degrades. This relationship suggests that the thinning rate of the ion milling process is dependent on the ZnSe crystal orientation and quality.

8.1.2.3 Nucleation of GaAs-on-ZnSe

For the study of GaAs nucleation on ZnSe, the GaAs cross-section is expected to show the same crystal quality that was evident in the RHEED surface pattern during the GaAs growth. For the three different types of nucleation performed: standard MBE, MEE, and SM-MBE, the cross-section TEM images are shown in Figure 8-6. A ZnSe/GaAs DBH is shown for the GaAs nucleation by SM-MBE to demonstrate that the GaAs layer is of high enough quality for the upper ZnSe layer to be grown in a two-dimensional manner. The cross-sections of the GaAs-on-ZnSe heterostructures nucleated by standard MBE and by MEE indicate a high density of defects in the GaAs layer. The defects appear as dark lines which originate at the GaAs-on-ZnSe heterointerface. For the GaAs grown by MEE, the layer also shows a noticeable degree surface roughness. The TEM images in Figure 8-6 indicate that from a microstructural perspective, the SM-MBE GaAs nucleation methodology is superior to that previously reported by Funato, *et al.* [24, 25, 91].

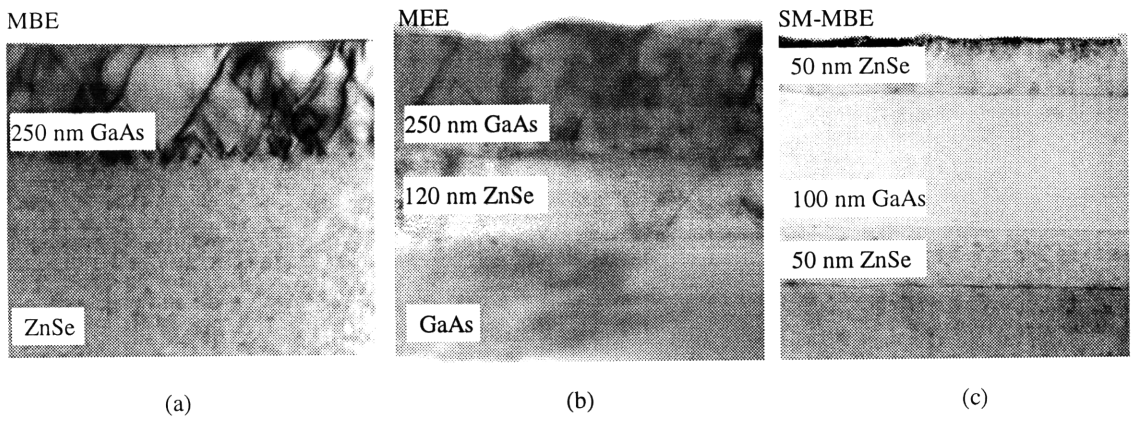

Figure 8-6. Cross-sectional bright-field TEM of GaAs layers nucleated on ZnSe by two different methods: standard MBE, MEE, or SM-MBE. A complete DBH is shown for the SM-MBE example to show that the top ZnSe layer is also of high quality.

8.1.2.4 Nucleation layer

Bright field, cross-sectional TEM images of 6 nm ZnSe/GaAs QWs grown with different GaAs nucleation layers are compared (see Figure 8-7). Shown are QWs grown with: an elevated GaAs QW temperature of 450°C, a standard SM-MBE nucleation layer, and no nucleation layer. The cross-sectional image of the sample grown with the standard SM-MBE nucleation layer shows each layer in the QW clearly. The other two samples imaged have such a large degree of contrast in the ZnSe barrier layers that the GaAs QW layer is not discernible. The upper ZnSe barrier layer for the 6 nm GaAs QW grown at 450°C has a high density of stacking faults originating at or near the region to believed to be the ZnSe-on-GaAs heterointerface. Further analysis of this heterostructure also shows that the stacking faults also originate in the lower ZnSe barrier layer.

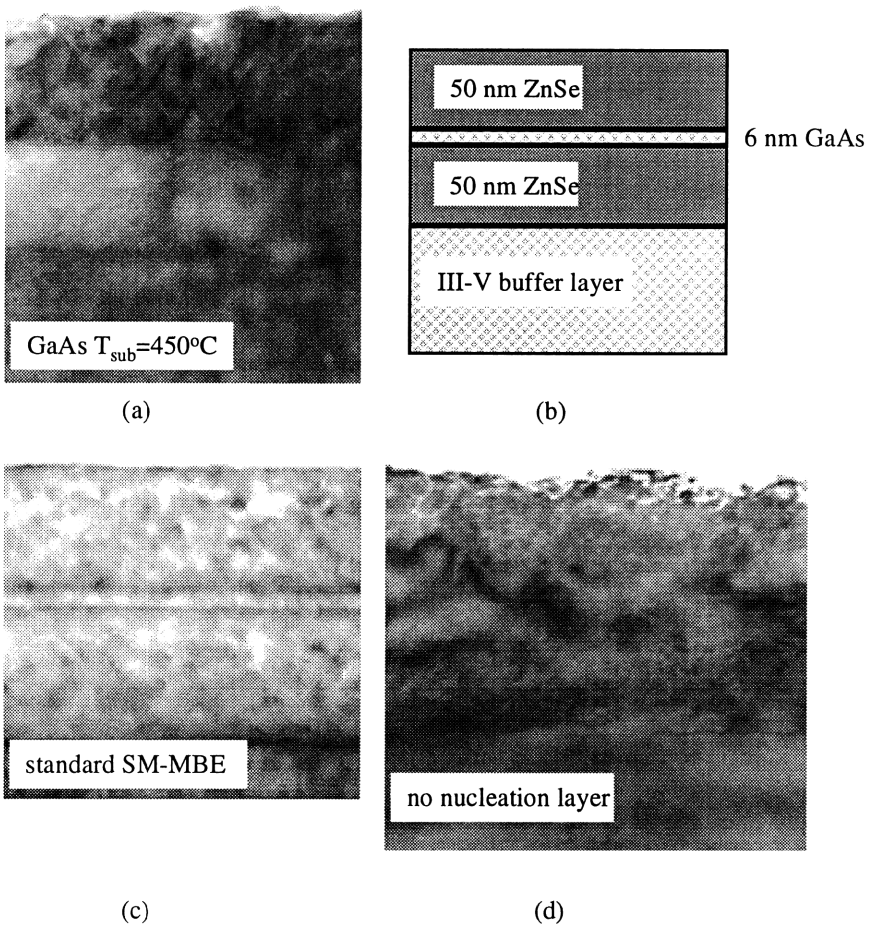

Figure 8-7. Cross-sectional bright-field TEM of 6 nm ZnSe/GaAs QWs grown under three different conditions: (a) GaAs growth temperature of 450C, (c) standard SM-MBE growth, (d) no nucleation layer. A schematic of the heterostructure is shown in figure (b). The cross-section of the 6 nm QW grown by standard conditions is of higher quality than the other two cases.

The large degree of contrast in the ZnSe barrier layers is due to the ion milling process. The ion mill has both damaged the ZnSe layers and preferentially milled the ZnSe according to crystal orientation. The 6 nm ZnSe/GaAs QW grown by standard SM-MBE shown in Figure 8-7c does show small amounts of ion milling damage and can be used as a comparison to understand the latter interaction of the ion mill with the ZnSe layers. It is believed that the ZnSe layers are more defective for the two other 6 nm QWs, and this is manifested by slightly misoriented growth islands in the ZnSe.

Figure 8-8 shows plots of the defect density of both the upper and lower ZnSe layers at the point of nucleation as a function of the nucleation growth parameters. The defect

density is a count of the number of point defects that result in the formation of stacking faults visible in the field of depth of the cross-section. The defect density along the heterointerfaces decreases with increasing GaAs nucleation layer thickness for both the upper and lower ZnSe barriers. It is surprising the quality of the lower ZnSe barrier is relationed to the GaAs nucleation layer thickness and not to the GaAs QW growth temperature. Instead, the upper ZnSe barrier shows an increasing defect density with increasing GaAs QW growth temperature.

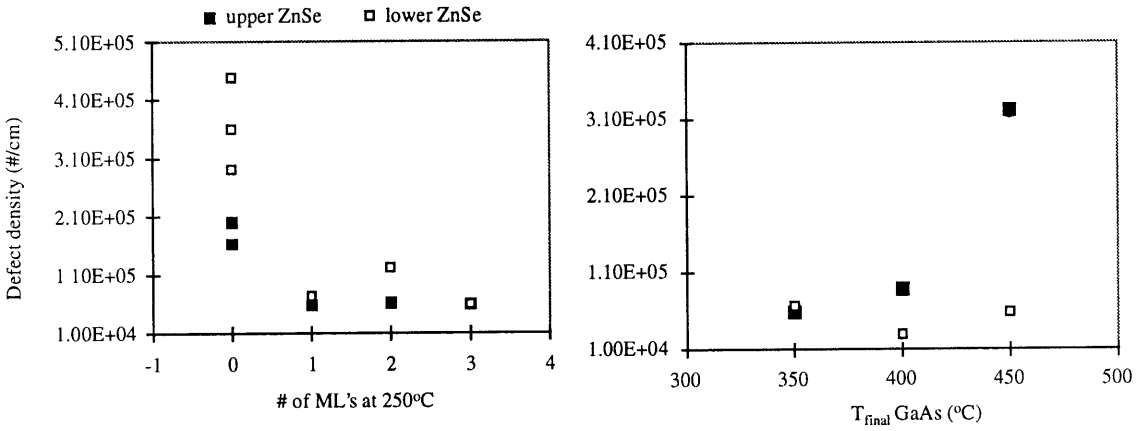

Figure 8-8. Defect density at the point of nucleation for the upper and lower ZnSe barriers for a series of 6 nm ZnSe/GaAs QWs as a function of the nucleation layer thickness and the GaAs QW growth temperature. The defect density decreases with increasing nucleation layer thickness for both ZnSe barriers. The defect density increases in the upper ZnSe barrier layer with increasing GaAs QW growth temperature.

The defect density at the upper ZnSe-on-GaAs heterointerface should reflect the defect density of the lower ZnSe on III-V buffer layer heterointerface because defects are expected to either propagate upwards through the heterostructure or roughen the GaAs nucleation surface. For the plot in Figure 8-8 of the defect density as a function of the GaAs nucleation layer thickness, both of the ZnSe barrier layers have the highest defect density when there is no nucleation layer. However, the upper ZnSe barrier layer has a defect density in excess of that of the lower ZnSe barrier layer; which is an indication that the defects at the upper ZnSe barrier layer on GaAs interface are also related to the ZnSe nucleation on the GaAs layer.

8.1.2.5 ZnSe/GaAs dimensions

The roughness seen in the upper ZnSe barrier layer in the ZnSe/GaAs QWs increases with decreasing QW width. Stacking faults are also more prevalent in the upper ZnSe barrier layer. The cross-sectional TEM images of ZnSe/GaAs DBHs and QWs with a central GaAs layer thickness of 100 nm, 40 nm, 6 nm, and 3 nm are shown in Figure 8-9. The GaAs QW is not visible in the 6 and 3 nm ZnSe/GaAs QWs. It is conceivable that the GaAs QW is of high quality, just not discernible from the ZnSe barrier layers though it is possible to differentiate between the upper and lower ZnSe barriers in both QWs.

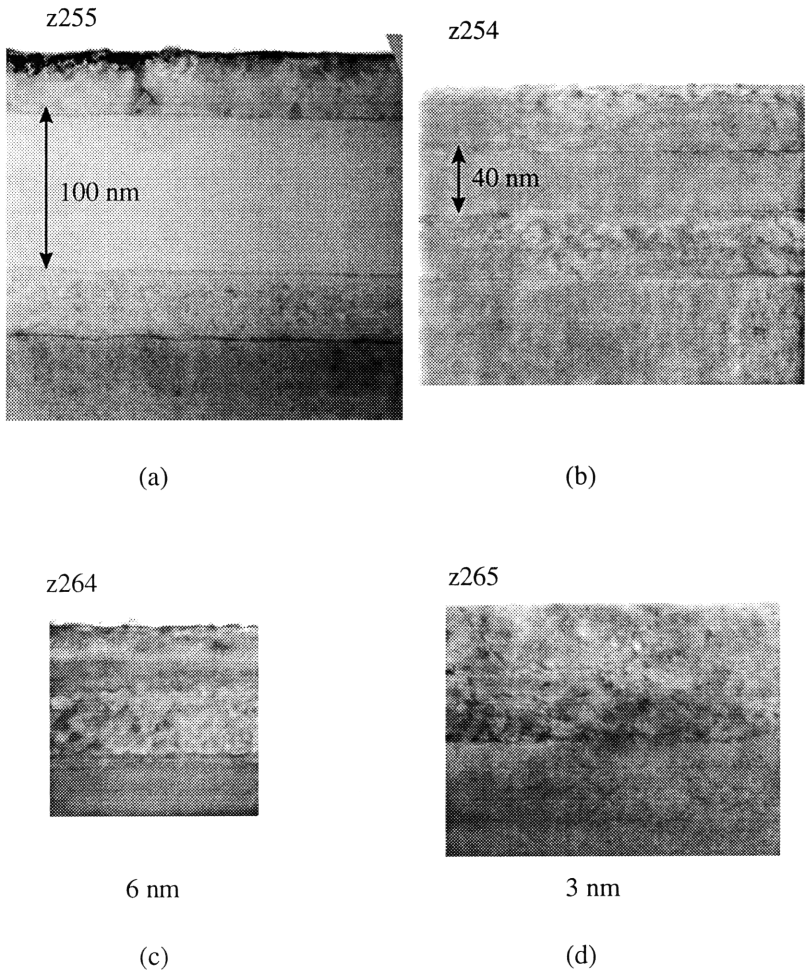

Figure 8-9. Bright field cross-sectional TEM of ZnSe/GaAs QWs and DBHs of GaAs layer thicknesses of: 100 nm, 40 nm, 6 nm, and 3 nm. The QW is not visible in the narrower QWs, but there is a visible increase in the roughness of the top ZnSe barrier layer.

The defect density at the nucleation plane for both ZnSe barrier layers as a function of the central GaAs layer width is shown in Figure 8-10. The defect density at the heterointerfaces shows a slight decrease with increasing GaAs width. However, there is a large spread in the defect density for the narrow QWs. The upper ZnSe barrier layer does have a high defect density than the lower barrier layer for the DBHs with wider GaAs layer thicknesses. The lower ZnSe barrier layer was nucleated on either a GaAs or an InGaP buffer layer. The defect density of the lower barrier does not reflect the different nucleation surface.

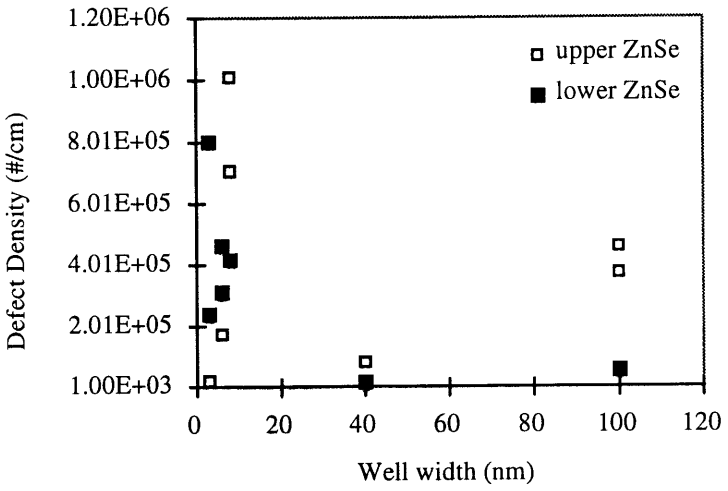

Figure 8-10. Defect density at the point of nucleation for both the upper and lower ZnSe barrier layers as a function of the width of the GaAs layer in a ZnSe/GaAs/ZnSe heterostructure. The defect density is shown to decrease with increasing GaAs width.

The increase in the defect density of the upper ZnSe barrier layer for the wider DBHs is counterintuitive. The GaAs surface is expected to be smoother with increasing thickness because the material has had longer to anneal during the longer growth. However, the plot of the defect density as a function of the central GaAs layer width only has two samples grown at the wider width for comparison. The spread in the defect density is conceivably as large for the wider DBHs as it is for the narrow QWs.

8.1.2.6 Buffer layers and substrate type

The ZnSe/GaAs DBHs and QWs were grown on several types of surfaces: GaAs, InGaP, InGaP/InGaAs, and ZnSe. The type of surface the heterostructure was grown on has microstructural implications, particularly in the case of InGaAs when a large degree of strain is introduced into the material system. The cross-sectional TEM images of the InGaP and InGaP/InGaAs buffer layers and the effects these buffer layers have on the ZnSe/GaAs heterostructure are presented in the next few paragraphs. This discussion is followed by an analysis of the use of ZnSe as the substrate for the ZnSe/GaAs DBHs.

InGaP buffer layers were grown between the ZnSe/GaAs DBHs and QWs and the GaAs substrate to eliminate the contribution of the GaAs substrate to the PL of the heterostructure. The growth parameters of the InGaP layer were established to achieve a lattice constant in the InGaP that was close to that of the GaAs (49% Ga). Initial TEM results of the cross-sections of the ZnSe/GaAs heterostructures and the InGaP/GaAs multiple QWs show a non-uniform InGaP buffer layer, characterized by a periodic variation in the contrast as shown in the multiple QW InGaP/GaAs heterostructure in Figure 8-11.

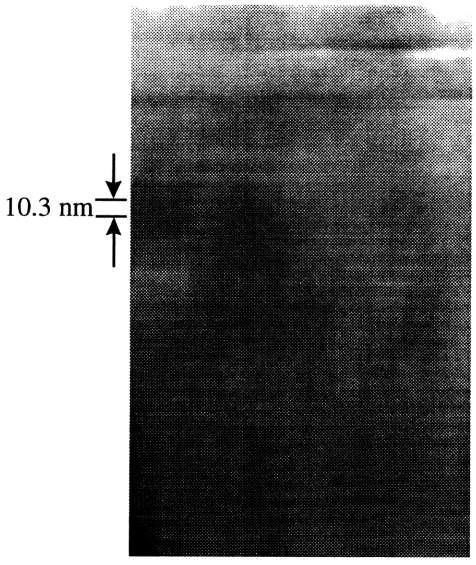

Figure 8-11. Cross-sectional TEM image of InGaP/GaAs multiple QW of well widths of 1.5 nm and 9 nm. The lower InGaP material shows a compositional fluctuation with a 10.3 nm periodicity.

The periodic contrast variation in the InGaP buffer layer has consequences for the ZnSe/GaAs QW and DBH optical properties. The contrast is a result of a small variation in the composition caused by a spatial separation of In and Ga in the growth reactor. During growth, the sample is rotated and thus a "superlattice" of two different compositions of InGaP results [119].

The fringes in the InGaP can be removed by altering the rotational speed of the sample during growth, as shown in Figure 8-12. The compositional variation in the InGaP material grown with the standard rotational speed is below the EDS detection limit, and TAD x-ray measurements show either a broad InGaP peak or two closely spaced InGaP peaks. However, even the slight variation in the composition can result in periodic electron confinement in the regions of the InGaP with a higher percentage of In. A 1 μm thick InGaP buffer layer with a superlattice period of 10.3 nm will have a more intense PL signal than an InGaP buffer layer without the periodicity in composition. PL measurements of ZnSe/GaAs DBHs with a He-Cd laser have an expected probe depth of roughly 300 nm. However, PL from the GaAs substrate at a depth of at least 1 μm from the surface has been measured. The strong PL from the InGaP buffer layer is believed to have back-pumped the GaAs substrate. The periodicity in the InGaP composition would have aided this process.

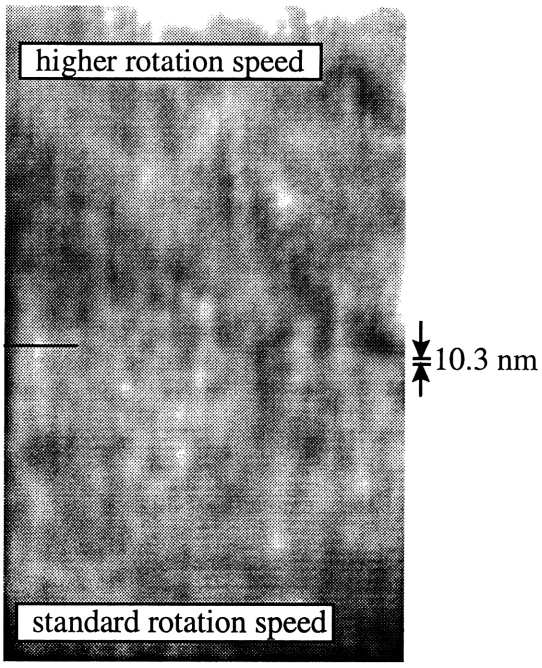

Figure 8-12. Cross-sectional bright field TEM of InGaP grown with two different substrate rotation speeds. The substrate rotation used for the ZnSe/GaAs QW growth results in InGaP buffer layers with compositional variation due to the relative proximity of the In and Ga to the sample during growth. The fringes are eliminated by increasing the speed of rotation.

InGaAs with a low percentage of In (< 6%) were incorporated into the buffer layer between the ZnSe/GaAs DBH in another effort to eliminate the GaAs substrate PL signal. However, the use of this buffer layer complicated the heterostructure by adding additional strain. Post-growth surface analysis of the heterostructures with InGaAs buffer layers show a cross-hatch visible by optical Nomarski phase-contrast microscopy measurements, indicating that the InGaAs layer is relaxed. The misfit dislocations which formed during the InGaAs relaxation propagate upwards through the rest of the heterostructure. A ZnSe/GaAs DBH with a GaAs thickness of 100 nm shows a defect density in the GaAs of roughly 1.6×10^4 cm^{-1}, whereas a similar heterostructure grown on only an InGaP buffer layer has a defect density below the detection level of the cross-sectional TEM measurement.

A third attempt to eliminate the contribution of the GaAs substrate from the PL signal originating from the ZnSe/GaAs DBHs and QWs was to grow the heterostructures on ZnSe substrates. Currently, ZnSe substrates are not manufactured with the same surface

quality as the GaAs substrates. The disparity between the two substrate types is partially a function of the surface oxide that natively forms on the GaAs surface and does not form on ZnSe. A native oxide protects the substrate surface after it has been chemical-mechanical polished. Another issue associated with the use of ZnSe substrates is the size limitation; the area of the ZnSe substrates is 1 cm^2. The quality of substrate degrades close to the edge, and the ZnSe substrate size results in a very small area for examination.

Careful preparation of the ZnSe substrate surface, followed by the growth of a thick ZnSe buffer layer was expected to isolate substrate surface effects from the final ZnSe/GaAs heterostructure. Appendix 2 describes the ZnSe surface preparation methods employed. The cross-sectional TEM images of a 40 nm ZnSe/GaAs DBH and an 8 nm ZnSe/GaAs QW are shown in Figure 8-13. The ZnSe substrates in these samples were prepared by a combination of degreasing, hydrogen plasma cleaning, and thermal cleaning. The homojunction shows a high density of defects which propagate up to the DBH. However, there is little evidence of defects originating at the GaAs-on-ZnSe and the ZnSe-on-GaAs heterointerfaces.

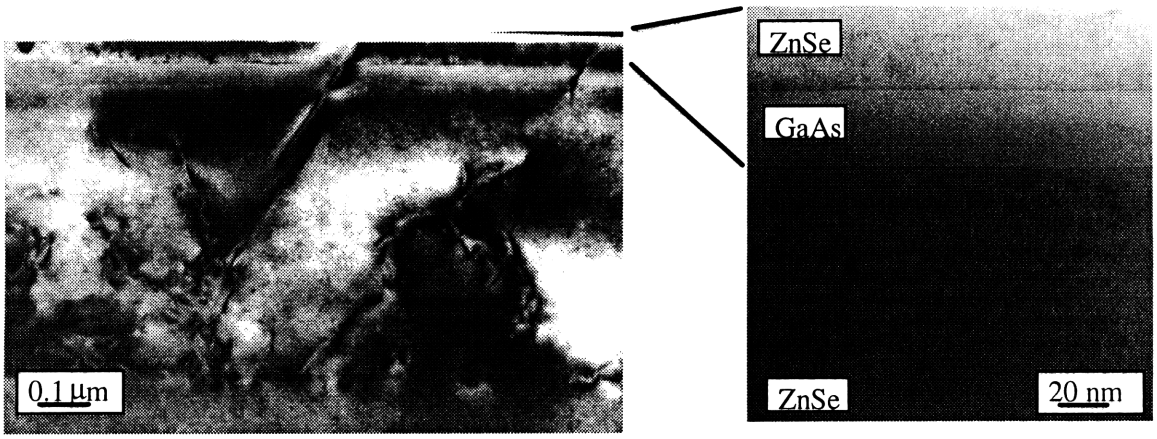

(a) (b)

Figure 8-13. Bright field cross-sectional TEM images of a 40 nm ZnSe/GaAs DBH grown on a ZnSe substrate. Figure (a) shows the entire heterostructure including the homojunction. Figure (b) shows a magnified view of the 40 nm GaAs layer.

8.1.3 Summary of cross-sectional TEM results

Cross-sectional TEM bright-field images of the compound semiconductor heterostructures investigated in this study have been presented. The nature of the ZnSe-on-GaAs heterointerface was investigated for ZnSe layer that is both lattice-matched to the GaAs substrate and relaxed. The ZnSe/GaAs interface in the relaxed structure shows a high density of misfit and threading dislocations both in cross-section and plan-view. Thinner ZnSe layers that are pseudomorphic to the GaAs substrate show defect-free heterointerfaces when grown under optimal conditions. Annealing the single heterostructure was shown to increase both the ion milling damage to the ZnSe during sample preparation and the density of point defects resulting in stacking faults at the heterointerface.

Images of a series of 6 nm ZnSe/GaAs QW cross-sections as a function of the GaAs nucleation layer thickness and the GaAs QW growth temperature show an upper ZnSe barrier layer more susceptive to ion milling damage. Both the presence of the GaAs nucleation layer and the growth of the GaAs QW at 350°C minimize the degree of ion milling damage that appears in the upper ZnSe barrier layer. The lower ZnSe barrier layer in the cross-sections studied show the presence of point defects at the ZnSe-on-buffer layer heterointerface with a density ranging from $1x10^4$ to $8x10^5$ cm^{-1}. The defects at the lower ZnSe barrier-on-buffer layer do not appear to be dependent upon to the type of buffer layer, and are indicative that, in general, the nucleation of the ZnSe on the buffer layer was not optimal.

The cross-sectional TEM images of ZnSe/GaAs DBHs of 40 nm and 100 nm show defect-free GaAs layers with a slightly higher defect density at the upper ZnSe barrier layer on GaAs heterointerface than at the plane of nucleation for the lower ZnSe barrier layer.

Buffer layers were grown between the ZnSe/GaAs DBH and QW to eliminate the contribution of the GaAs substrate to the PL signal. The InGaP buffer layer has a 10.3 nm compositional periodicity related to the rate of rotation of the substrate during growth. The periodicity is believed to have resulted in a superlattice with intensified PL, which

back-pumps the GaAs substrate. Narrow energy-gap InGaAs buffer layers were also employed as buffer layers, but even thin layers were shown to relax on the GaAs substrate and generate defects which reach the ZnSe/GaAs DBHs. Finally, ZnSe/GaAs DBHs were grown on ZnSe substrates to eliminate the GaAs substrate altogether. The ZnSe substrates are of a lower quality than the GaAs substrates due to the lack of a native oxide and the relatively new substrate manufacturing technology. The efforts to prepare the ZnSe substrate surface were not entirely successful in removing surface contaminants and providing a defect-free surface. As a result, the ZnSe/ZnSe homojunction is highly defective and contributes to the defect structure in the ZnSe/GaAs DBH.

8.1.4 Side note: cross-sectional imaging of III-V compounds

Additional cross-section TEM work was done to investigate III-V compound semiconductor heterostructures. AlGaAs, AlInGaAs, InGaAsP, and InP have all been prepared for and analyzed in the TEM. However, the preparation of materials containing either Al or In is more complicated than the preparation of ZnSe and GaAs. During the low temperature ion milling process, Al tends to oxidize (the vacuum in the ion mill is low $\sim 10^{-6}$ Torr) and In tends to melt. The oxidation of Al is not surprising, as this is a common issue in the initial fabrication of the material. However, the implications for the oxidation are the destruction of the lattice crystallinity and the tendency for the material to fall apart when it reaches a thickness that is electron "transparent". Materials containing In also tend to fall apart during the ion milling process. One approach to the fabrication of cross-sectional samples for Al- and In-containing materials is to rely entirely on mechanical polishing to reduce the material to a thickness that is appropriate for TEM imaging.

Another issue associated with the imaging of both Al- and In-containing materials is electron beam damage. During the imaging process the In-based materials appear to charge under the electron beam. The charging is manifested by bending of the crystal away from the electron beam. The bending changes the diffraction conditions that were set for imaging. One way to avoid this issue is to set the diffraction condition for imaging and focus at a region of the material that is thick enough that it will not bend under the electron beam. To take an image, move the thinner area of the sample into the electron

beam path, reduce the exposure time to account for the sample thickness, and take an image.

At higher magnifications, beam damage will also occur in both the Al- and In-containing materials. Under lattice imaging conditions, the beam damage is manifested by the appearance of either a diffraction pattern showing concentric rings or a bright-field image showing regions of amorphous materials. The best way to avoid this type of damage is to reduce the beam voltage. However, the TEMs used in this study operated at a relatively low voltage of 200 kV. Another option is to prepare a region of the sample for imaging and then move to another area of the sample a few seconds before taking an image.

8.2 Part II: HREM

The atomic lattice can be resolved using TEM if the proper imaging conditions (to achieve phase contrast imaging) are established and the sample is thin enough. The proper imaging conditions require careful alignment of the electron beam down the microscope column, voltage and current centering, and minimization of the astigmatism in the image caused by the objective lens and aperture. The sample thickness must be below 50 nm, in order to minimize inelastic scattering contributions to the image. The electron beam should be aligned down a zone-axis of the sample. In this study, both the [110] and [001] directions are employed. The image is formed by the contribution of at least the first order diffracted beams, although in this study all of the diffracted beams were collected unless otherwise noted.

The contrast between materials of different chemical composition is lessened when phase contrast imaging conditions are employed. The interface between ZnSe and GaAs is difficult to identify at magnifications such that atomic lattice is visible when the standard sample preparation results in an electron beam directed down the [110] axis. In this orientation, the contribution of several diffracted beams is as strong for both the ZnSe and the GaAs. Plots of the diffracted beam intensity as a function of material thickness are shown in Figure 8-14 for the electron beam oriented in the [110] and the [001] directions. For the electron beam aligned in the [001] direction, the diffracted beams overlap in

intensity for each material and there is an intensity difference for each material. For example, at a thickness of 30 Å's, the GaAs diffracted beams are almost twice as intense as the ZnSe diffracted beams. The HREM image of a ZnSe/GaAs heterostructure that is 30 Å's thick oriented with an [001] beam direction would show a more clearly defined junction between the ZnSe and the GaAs than imaging in the [110] direction or for a thickness of 50 Å's in the [001] direction.

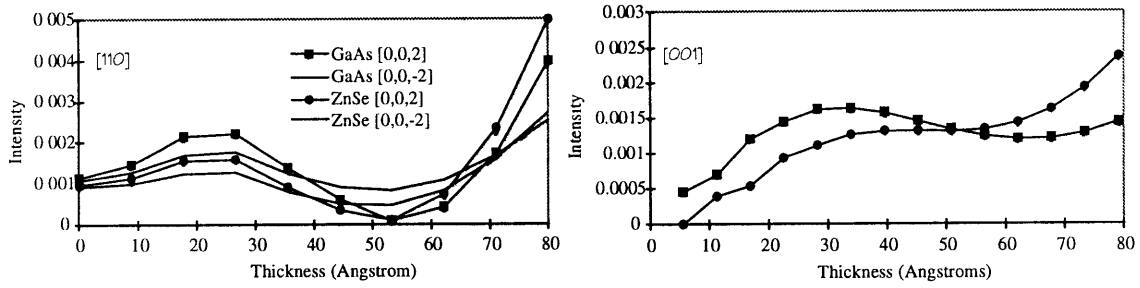

Figure 8-14. Pendellosung plots of the intensity of the diffracted beams as a function of sample thickness for the electron beam perpendicular to the [110] and the [001] directions.

The [110] results are intended as a comparison to the bright-field TEM images already shown. The [001] images will have an increased contrast between the ZnSe and the GaAs, and can provide more information at the heterointerfaces. The goal of the HREM imaging of the ZnSe/GaAs QWs and DBHs is to see if each heterointerface is coherent with a low defect density.

8.2.1 Lattice imaging of the [110] orientation

The ZnSe and the GaAs lattice structure in the [110] direction are very similar as the lattice constant and plane spacing of the materials is within 0.27%. Contrast between the two materials due to the different elemental mass is also small, because Zn, Se, Ga, and As are close in atomic number. Contrast in the HREM images in the [110] orientation is primarily enhanced by the difference in the ion milling rate for ZnSe and GaAs.

The lattice images of ZnSe and GaAs are shown for two different thicknesses in Figure 8-15. The thicker GaAs layer shows more contrast, but a less-resolved lattice. Both the ZnSe and the GaAs images are fairly noisy due to the contributions of inelastic scattering,

which is improved by applying a high-pass Gaussian filter to the image. Insets in the filtered images show simulations of each lattice, indicating that the images were taken at a defocus of -900 Å's for a ZnSe sample that is 40 Å's thick and a GaAs sample that is 80 Å's thick. The original ZnSe and GaAs images are from the same heterostructure, chosen to show the largest degree of contrast present between the two materials and the compromise that results due to the reduced resolution for the thicker GaAs sample. The difference in sample thickness for the ZnSe and the GaAs in the same cross-section reflects the difference in the ion milling rate for the two materials.

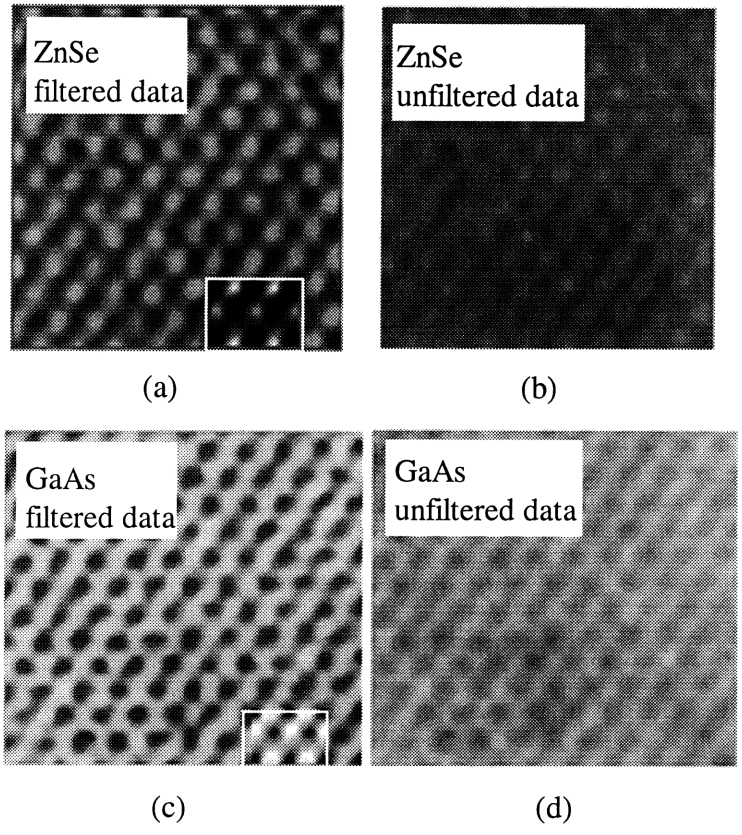

Figure 8-15. Lattice images of ZnSe and GaAs with the electron beam oriented down the [110] zone axis. The original image is shown next to data that has been Gaussian high-pass filtered. In the lower right-hand corner of the filtered data for both materials, an image simulation is shown corresponding to a 30 nm defocus for a 4 nm thick ZnSe sample and an 8 nm thick GaAs sample.

The HREM lattice image of a ZnSe/GaAs QW is shown in Figure 8-16(a), with an enlarged region shown of the GaAs QW and the heterointerfaces in Figure 8-16(b). The

contrast between the ZnSe and the GaAs is primarily due to a difference in the thickness in the two materials. The lattice of the ZnSe layers on either side of the GaAs material ranges from crystalline to amorphous, with regions that are damaged by the ion mill. The lattice of the GaAs material is fairly uniform across the QW. Both heterointerfaces are coherent, with a continuous crystal lattice present across the junction between the two different materials. At the GaAs-on-ZnSe heterointerface, a darker region appears for roughly 8 atomic layers in the ZnSe material. The difference in contrast is potentially a result of: a surface impurity on the ZnSe barrier layer, such as carbon, strain between the ZnSe and GaAs layer, or preferential ion milling. The contrast at the ZnSe-on-GaAs heterointerface is not as pronounced, but the lattice does show a region of discontinuity.

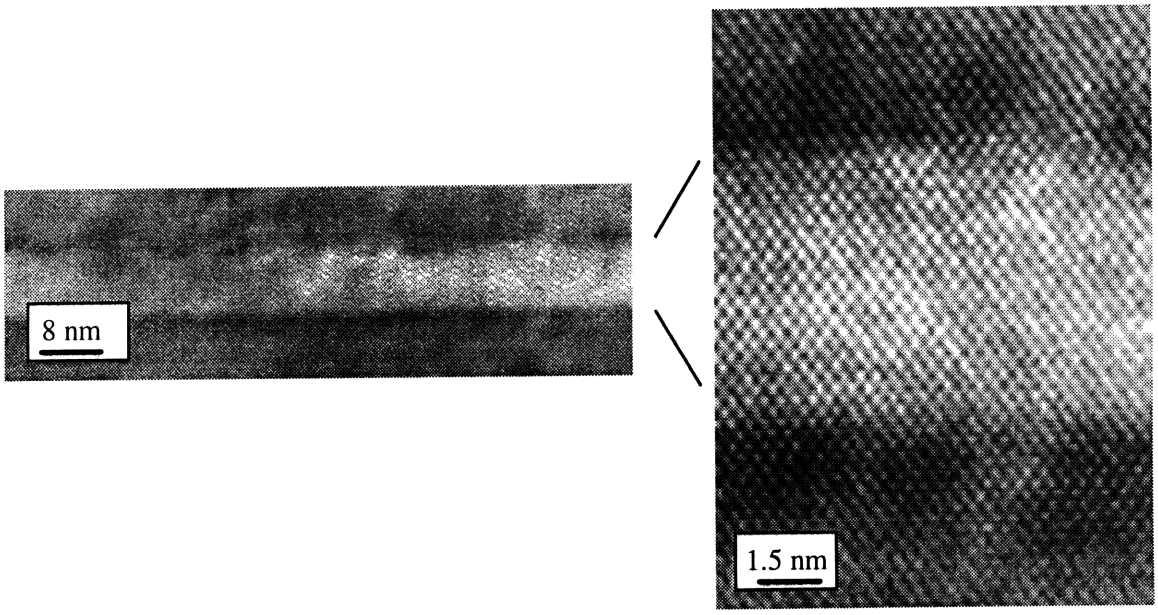

Figure 8-16. HREM image of 8 nm ZnSe/GaAs QW in the [110] orientation. The atomic lattice is visible in the image on the right, showing coherent heterointerfaces.

Figure 8-16(a) shows a flat GaAs-on-ZnSe heterointerface and a rough ZnSe-on-GaAs heterointerface. A closer inspection of the GaAs lattice shows no evidence of growth islands which would cause an undulation of the GaAs surface. The small degree of contrast at the upper heterointerface makes it difficult to accurately quantify the magnitude of the roughness. If the growth of the GaAs QW began in a three-dimensional

manner and annealed as the substrate temperature was raised, the undulation at the upper heterointerface could reflect the GaAs-on-ZnSe nucleation. For a ZnSe/GaAs DBH, the upper interface undulations are not as pronounced, indicating that the roughness initiated during the GaAs nucleation on ZnSe is increasingly annealed with a longer growth.

8.2.2 Lattice imaging of the [001] orientation

HREM lattice imaging in the [001] orientation is expected to magnify the contrast between the ZnSe and the GaAs due to the stronger (002) diffracted beam contributions to the image. However, the overall intensity of the diffracted beams is weaker in the [001] orientation, thus counteracting the contrast benefits for a sample of the same thickness as that imaged in the [110] orientation.

Achieving a high-quality ZnSe/GaAs QW or DBH cross-section has been somewhat elusive due to the damage caused by the ion mill to the ZnSe layers and the preferential ion milling for the two materials. The preparation of the samples in the [001] orientation requires a different procedure from that followed for the samples with a [110] orientation. The samples are sawed with a diamond-coated wire at a diagonal from the (110) planes. The [001] cross-sections were then thinned with a combination of polishing and ion milling. The ion milling rate for the [001]-oriented heterostructures is somewhat slower than for the [110] cross-sections, although this has not been thoroughly calibrated due to the equipment not being in an optimal state when those samples were prepared. The end result, in the preparation, is that the [001] cross-sections are damaged to the point of being amorphous by the ion mill for larger thicknesses than occurs in the [110] cross-sections.

The subsequent sections contain images from the HREM imaging of the [001] cross-sections. First, the lattice images from a ZnSe/GaAs DBH of the ZnSe and the GaAs are considered separately. This is followed by an examination of the two ZnSe/GaAs heterointerfaces and an 8 nm ZnSe/GaAs QW. Finally, the heterointerface roughness is quantified and discussed.

8.2.3 ZnSe/GaAs [001] lattice imaging

The HREM lattice images of GaAs and ZnSe are shown in Figure 8-18 (b) and (c), respectively. A two-beam image of the entire cross-section of a 100 nm ZnSe/GaAs DBH is shown in Figure 8-18 (a). The contrast between the ZnSe and the GaAs layers is not significantly enhanced by preparing the sample in the [001] orientation. However, the HREM lattice images show that the lattice is barely discernible for the GaAs and the ZnSe layers, indicating that the layers are thick (see Figure 8-18 (b) and (c)). Applying a filter similar to that in Figure 8-15 does not clarify the presence of the atomic lattice for these images.

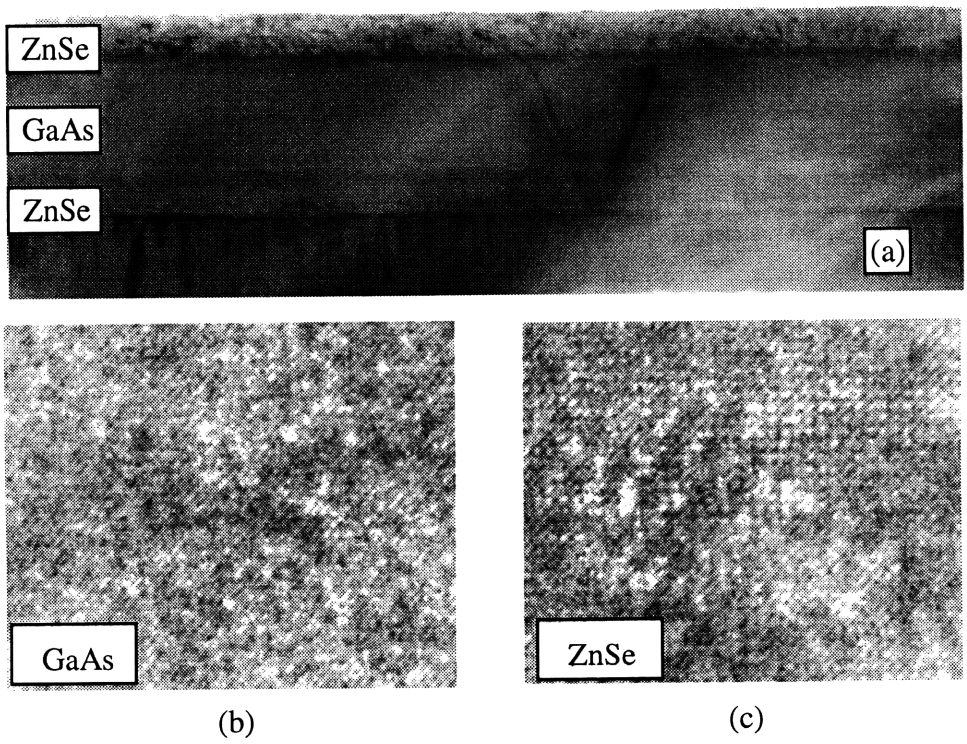

Figure 8-17. Cross-sectional TEM images of (a) 100 nm ZnSe/GaAs DBH, (b) lattice image of GaAs, (c) lattice image of ZnSe for a sample in the [001] orientation. The contrast between the ZnSe and GaAs lattice images is not significantly greater than that for the lattice images for samples oriented in the [110] direction.

The HREM images of the ZnSe-on-GaAs and the GaAs-on-ZnSe heterointerfaces for the cross-section shown in Figure 8-17 (a) show little contrast between the ZnSe and the GaAs layers. However, the heterointerfaces are visible, due to a combination of regions of

darker and lighter intensity. The heterointerfacial images are taken from the same region of the sample, resulting in some bending across the sample over the range of imaging. As a result, the diffraction conditions for the two heterointerfaces are different, with the upper heterointerface slightly bent away from the [001] zone axis. The atomic lattice appears as diagonal fringes because each diffraction beam is not uniformly contributing to the image. At the lower heterointerface, the material is slightly thicker, and correctly aligned to the electron beam. The atomic lattice is not as clearly visible than the lattice imaged in the [011] orientation in Figure 8-16. In general, there appears to be little gain in obtaining HREM images of the ZnSe/GaAs DBH in the [001] orientation because of material preparation limitations.

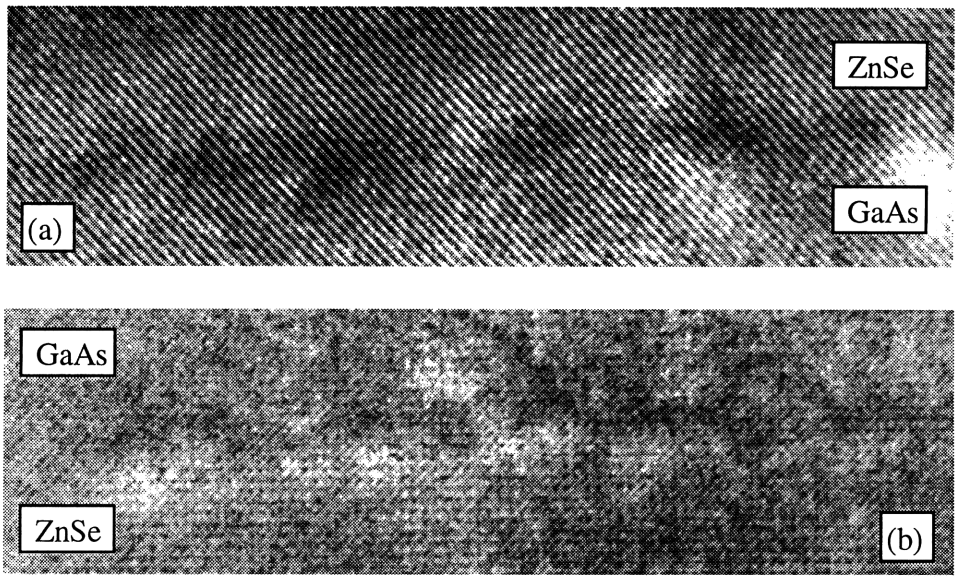

Figure 8-18. HREM [001] lattice image of the ZnSe-on-GaAs heterointerface and the GaAs-on-ZnSe heterointerface for the sample shown in Figure 8-17 (a). Thickness variation across the sample results in the upper interface showing fringes as opposed to the actual lattice.

A HREM image of a complete 6 nm ZnSe/GaAs QW is shown in Figure 8-19. The dimensions of the region examined are small enough that both the diffraction condition and thickness across the image are uniform. The atomic lattice is weakly discernible on either side of the GaAs QW layer, in the ZnSe barriers. The heterointerfaces are evident, but not as clearly for the ZnSe/GaAs DBH shown in Figure 8-17 and Figure 8-18. In both

cases, the defect density at the atomic level appears to be below the detection limit for this type of imaging.

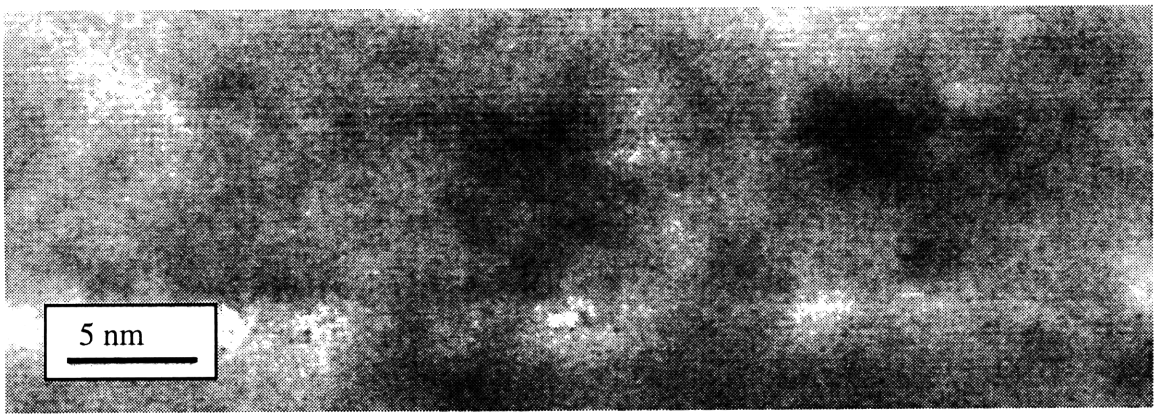

Figure 8-19. HREM [001] cross-sectional lattice image of a 6 nm ZnSe/GaAs QW. The sample is too damaged and too thick to resolve the atomic lattice.

The results from the [001] HREM cross-sectional imaging of the atomic lattice across the ZnSe/GaAs DBH and QW do not provide a great amount of information regarding the defect structure of the heterointerfaces. However, the ZnSe-on-GaAs heterointerface appears to have a different characteristic image than the GaAs-on-ZnSe heterointerface. The lower heterointerface appears, in general, as a thin white band with a width of a few atomic layers. It is unlikely that the white band at the GaAs-on-ZnSe heterointerface is caused by interdiffusion, as a similar band has been found to appear at a GaAs epilayer on GaAs substrate homojunction. The origin of the lighter intensity of the heterointerface is more likely a function of an increased concentration of surface contaminants on the ZnSe barrier layer or strain between GaAs QW layer and the ZnSe barrier layer. The upper heterointerface is marked by an undulation along the growth plane accompanied by regions of lighter and darker intensity (as compared to the lattice away from the heterointerface). These results are similar to those found for HREM images taken of samples in the [110] orientation.

8.2.4 Interface roughness and thickness

A quantitative assessment of the ZnSe/GaAs heterointerfaces studied in the [001] orientation was made by measuring the width of the white band defining the GaAs-on-

ZnSe heterointerface, and the width of the undulations in the growth planes for the ZnSe-on-GaAs heterointerface (see Figure 8-20).

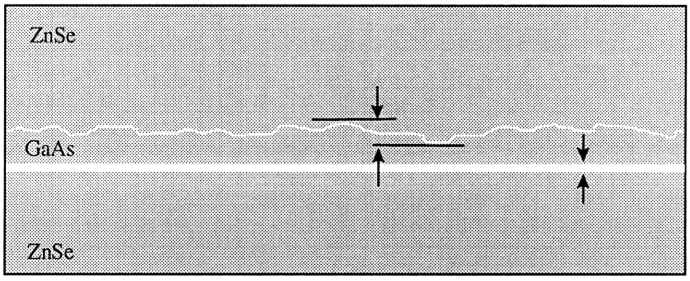

Figure 8-20. Schematic of ZnSe/GaAs QW cross-section showing the characteristic upper and lower ZnSe/GaAs heterointerfaces, and how the width of each interface is defined.

The ZnSe-on-GaAs heterointerface becomes smoother along the growth plane with a thicker nucleation layer. The width of the GaAs-on-ZnSe heterointerface does not reflect the thickness of the nucleation layer (see Figure 8-21). The upper ZnSe-on-GaAs heterointerface appears to be more sensitive to the nucleation and growth parameters for the GaAs QW. Increasing the temperature of the GaAs QW also increases the roughness of the ZnSe-on-GaAs heterointerface. Also, as the central GaAs layer width increases, the upper interface becomes flatter. All of these results are conducive to prior results found for cross-sections prepared in the [110] orientation.

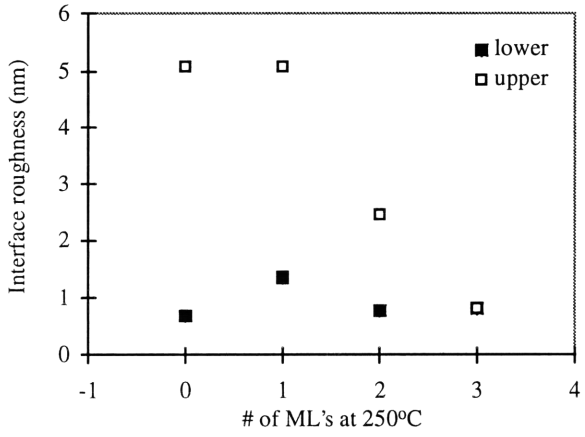

Figure 8-21. Plot of the interface roughness measured from HREM [001] lattice images as a function of the nucleation layer thickness. The GaAs-on-ZnSe interface is represented by the solid symbols, and the ZnSe-on-GaAs interface is represented by the open symbols.

The surface roughness of the 6 nm ZnSe/GaAs QWs was measured by atomic force microscopy (AFM) as a function of both the nucleation layer thickness and the growth temperature of the GaAs material. The surface roughness should reflect the upper interface roughness observed in the cross-sections. If the roughness at the upper heterointerface is enough to generate defects or prohibit two-dimensional ZnSe growth, the surface of the heterostructure would be rougher than it is at the heterointerface. However, if the roughness at the upper heterointerface is less severe, the growth of the upper ZnSe barrier layer could reduce the heterointerfacial roughness by a crystal-orientation dependent growth rate. The second instance appears to have occurred in the growth of the 6 nm ZnSe/GaAs QWs, as is shown in the summary plots in Figure 8-22. The surface roughness is roughly 50% of that measured at the upper ZnSe-on-GaAs heterointerface.

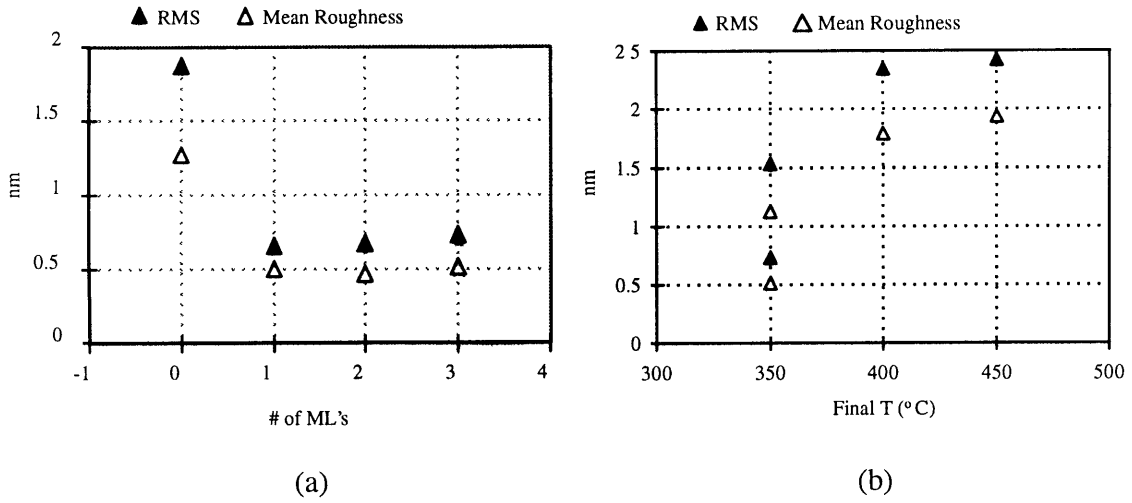

Figure 8-22. AFM surface roughness measurements of 6 nm ZnSe/GaAs QWs as a function of the GaAs fabrication. The surface roughness of the heterostructure as a function of the nucleation layer width in monolayers (ML's) is shown in (a) and as a function of the final GaAs growth temperature is shown in (b).

8.2.5 Summary of HREM imaging results

A series of ZnSe/GaAs QWs and DBHs have been investigated by HREM, to study the atomic lattice of each layer and heterointerface. The samples were prepared in two orientations: [110] and [001]. The [110] sample preparation is simplified by the presence

of natural <110> cleavage planes. However, the [001] sample orientation was expected to yield a higher degree of contrast between the ZnSe and the GaAs layers due to the larger contribution of the (200) diffraction beams to the image formation. The combined results of both types of sample orientations imaged exemplify the issues involved in preparing a semiconductor heterostructure for high resolution imaging.

The [110] oriented ZnSe/GaAs cross-sections showed a coherent crystal structure across both heterointerfaces. The GaAs-on-ZnSe heterointerface was demarcated by a dark line of contrast resulting from either strain between the GaAs and the ZnSe or impurity contamination present on the ZnSe surface during the GaAs nucleation. The ZnSe-on-GaAs heterointerface was accompanied by regions of both lighter and darker intensity than the surrounding lattice. The variations in intensity are expected to be due to a range of sample thickness, ion milling damage, and strain fields surrounding defect sites. The ZnSe-on-GaAs heterointerface also varies along the growth plane by several atomic layers, as a function of the growth conditions of the central GaAs layer.

Similar results were found in HREM images of [001] oriented ZnSe/GaAs cross-sections. However, the atomic lattice was not as readily imaged in these heterostructures as the samples tended to become amorphous when in the appropriate thickness range for lattice imaging. A series 6 nm ZnSe/GaAs QWs were studied by HREM imaging, and the upper ZnSe-on-GaAs heterointerface was found to have a roughness along the growth plane according to the nucleation layer parameters and the GaAs QW growth temperature.

9. Summary and Conclusion

The motivation for the study of ZnSe/GaAs QWs and DBHs was the fabrication of high speed optical switches. Amongst unique parameters of these heterostructures is the potential to achieve a large excitonic binding energy; this aides in the room-temperature device sensitivity. However, several experimental challenges are present in the fabrication of these heterostructures. This study set out to address these challenges.

The microstructural characterization of epitaxially-grown ZnSe/GaAs QWs and DBHs supports two hypotheses established to explain the absence of photoluminescence from the central GaAs layer. Interfacial roughness of the ZnSe-on-GaAs heterointerface and incorporation of carbon at the lower ZnSe barrier layer surface both appear to contribute to the reduction of the photoluminescence intensity from the central GaAs layer. The ZnSe-on-GaAs and the GaAs-on-ZnSe heterointerfaces seem to be abrupt, suggesting that a layer of interfacial charge could exist to drive carriers away or towards the heterointerfaces (in spite of the undulation along the growth plane of the ZnSe-on-GaAs heterointerface). Microstructural analysis does not confirm a third hypothesis, namely, that a high density of dislocations and defects throughout the heterostructure are acting as non-radiative recombination centers. The remaining two hypotheses are not addressed in the microstructural analysis: a low carrier lifetime in the GaAs reduces or eliminates radiative recombination, and the energy-band alignment is type II which results in a lack of carrier confinement in the GaAs.

This chapter has four parts. First, an overview of the work is given. Second, an assessment is made of the five explanatory hypotheses in light of both the microstructural results presented in this study, and the optical analysis by D. Dougherty. Third, the feasibility of achieving a detectable level of an optical signal from a GaAs QW with ZnSe barriers is discussed. Finally, recommendations are made for future research.

9.1 Overview of results

Both the fabrication and the characterization of the ZnSe/GaAs QW and DBH are presented in this study. In Chapter Two, a survey of the scientific literature is presented to establish the starting point for the growth procedures used in the fabrication of the ZnSe/GaAs QWs and DBHs. The details behind the fabrication and the optimization of the growth parameters for these heterostructures and the optical characterization follows in Chapter Three and Chapter Four. The first half of the thesis is concluded with a proposal of five hypotheses with the potential for explaining the absence of an optical signal from the central GaAs layer in the ZnSe/GaAs heterostructures, in Chapter Five. The subsequent chapters contain the experimental results from the microstructural characterization by three techniques: energy dispersive x-ray spectroscopy (Chapter Six), triple axis x-ray diffraction (Chapter Seven), and transmission electron microscopy (Chapter Eight).

The first task was the epitaxial growth and optimization of ZnSe/GaAs QWs and DBHs. *A methodology, defined as single-monolayer MBE (SM-MBE), was developed to nucleate the GaAs layer on the lower ZnSe barrier layer.* The remainder of the GaAs QW layer was grown by standard MBE, but at a reduced substrate temperature of 350°C with a modified Group III-to-Group V ratio. The ZnSe barrier layers were grown by standard MBE, with the nucleation of the ZnSe on the III-V layer initiated by 60 seconds of Zn introduction into the growth reactor before the onset of ZnSe growth. During the growth of a ZnSe/GaAs QW using this methodology, the RHEED pattern indicated a two-dimensional growth. The GaAs layer exhibited a c(4x4) RHEED surface reconstruction. The ZnSe layers exhibited a (2x1) RHEED surface reconstruction during growth, and a c(2x2) pattern upon growth completion.

The optical properties of the ZnSe/GaAs QWs and DBHs were probed by low-temperature photoluminescence (PL) measurements. *The key result from this analysis was the absence of an optical signal from the central GaAs layer when ZnSe barriers were employed, regardless of the thickness of the GaAs layer.* Similarly grown GaAs was shown to luminesce when InGaP barriers layers were used. The ZnSe was shown to

exhibit band-edge luminescence, but also included a defect band feature indicating a deep level present in the thin ZnSe layers. The defect band is possibly a partial indication of the quality of the interface of the ZnSe layers with the III-V layers.

The combination of the microstructural analysis, photoluminescence measurements, RHEED surface analysis, and AFM measurements show that the epitaxial growth of the central GaAs layer in the ZnSe/GaAs QWs and/or DBHs has been optimized. The GaAs nucleation layer is thick enough to allow for full surface coverage; and allows for two-dimensional growth of the subsequent GaAs QW. However, the growth regime of the nucleation layer is believed to have resulted in reduced-carrier lifetimes and, thus, is expected to inhibit radiative recombination from the GaAs material close to the GaAs-on-ZnSe heterointerface. The GaAs QW is grown at a temperature that is high enough to achieve GaAs of optical quality, and low enough to avoid relaxation in the lower ZnSe barrier layer.

The growth of the ZnSe barrier layers appears to be sub-optimal. The procedure followed for the epitaxial growth of ZnSe was established to replicate the method under which the highest quality ZnSe was reportedly grown. Although RHEED intensity oscillations of the lower ZnSe barrier layer were detected and used to measure the ZnSe growth rate, a high density of stacking faults occur during the nucleation of the ZnSe layer. Hence, *in situ* characterization by RHEED is not sufficient to assess the layer quality. The quality of the upper ZnSe barrier layer reflects both the ZnSe growth procedure and the quality of the central GaAs layer.

9.2 An assessment of the five candidate hypotheses

The results from the epitaxial growth and the optical characterization led to a further investigation into the properties of the ZnSe/GaAs QWs and DBHs. This investigation was based upon five hypotheses that hold promise for explaining the absence of an optical signal from the central GaAs layer. Each of the hypotheses are reassessed here in relationship to the microstructural characterization presented in the second half of this thesis.

9.2.1 Interface roughness and interdiffusion

> *For interfacial roughness in a QW grown under two-dimensional conditions, the modulation in the growth plane would be on the order of a few atomic layers, and the PL from the QW would show one broadened, less intense feature* [95]. *A decrease in PL signal intensity from a single QW could push the feature below the level of detection.*

For the ZnSe/GaAs QWs with GaAs layer thicknesses close to the excitonic diameter (~10 nm), this hypothesis is a legitimate explanation for explaining the absence of PL from the QW. HREM shows a rough ZnSe-on-GaAs heterointerface for the optimized growth procedure of about 1.5 nm, or 5 atomic layers. The modulation of the growth plane at the ZnSe-on-GaAs heterointerface increases with decreasing QW thickness. Hence, a GaAs QW designed to have a 6 nm QW width has a width ranging from 7.5 nm to 4.5 nm. The range of first confined energy states for these values of QW widths are 1.55 eV to 1.76 eV. The "periodicity" of the undulations at the upper heterointerface is roughly 25 nm, well within the dimensions of the optical excitation source (the diameter is ~ 300 μm). The ZnSe-on-GaAs heterointerfacial roughness is expected to be a contributor to the absence of PL in the GaAs QW for GaAs layers have a thickness close to the excitonic diameter.

The microstructural analysis showed no evidence of strong interdiffusion at the heterointerfaces in the ZnSe/GaAs QWs and DBHs. The EDS measurements were not at a high enough spatial and compositional resolution to accurately detect interdiffusion of the elemental species in the heterostructure. However, in the course of evaluating the EDS measurement, annealing studies revealed the nature of a grossly interdiffused ZnSe-on-GaAs heterointerface by bright field STEM imaging. Another set of images taken in the TEM gave further insight into the nature of the interdiffused heterointerface. In contrast, the heterointerfaces in the ZnSe/GaAs QWs and DBHs are very different from the annealed heterointerface as evaluated by TEM imaging. However, the possibility exists for a doping density level (~1×10^{18} cm^{-3}) of interdiffusion to be present at the ZnSe/GaAs heterointerfaces.

A single monolayer band of either lighter or darker contrast is evident at the GaAs-on-ZnSe heterointerface, and is also sometimes evident at the GaAs buffer layer on GaAs substrate homojunction. For the homojunction, the contrast is believed to be due to the incomplete oxide removal prior to growth. For the GaAs-on-ZnSe heterojunction, the band of contrast could be due to contamination of the ZnSe formed during the *in situ* transfer between growth reactors. The contamination would be primarily carbon, which could reside at interstitial sites in both the ZnSe and the GaAs, and form a deep level in the energy band-gap of either material.

9.2.2 Dislocations and defects

The defects that interrupt the crystal uniformity of the heterostructure can decrease or eliminate the PL signal intensity from the GaAs well.

The dislocation and defect density in the ZnSe/GaAs QWs and DBH has been found to be comparable to a pseudomorphic heterostructure composed of III-V compound semiconductors. TAD measurements have shown a directional variation in the misfit dislocation density; albeit at a low density (~ $1x10^4$ cm^{-2}). The cross-sectional TEM measurement has shown a consistent presence of stacking faults at the ZnSe-on-buffer layer and the ZnSe-on-GaAs heterointerfaces. The GaAs QW and DBH layers do not show defects originating at the GaAs-on-ZnSe heterointerface. The defects present in the GaAs layer originate in the lower ZnSe barrier layer, and occur at a density that is less than the scope of the TEM measurement.

The presence of the stacking faults at the ZnSe-on-III-V layer heterointerfaces explains the defect band in the ZnSe PL signal from the ZnSe/GaAs QWs and DBHs. However, the overall defect structure evident in the TEM and the TAD measurements is not present at a high enough density to eliminate the PL signal from the GaAs QW. Further support comes from the fact that a PL signal can be measured from 100 nm of ZnSe with a detectable defect density of stacking faults.

9.2.3 Heterovalent interfaces

Local carrier depletion caused by heterointerfacial charge has the potential to eliminate or reduce the radiative recombination in the ZnSe/GaAs QWs and DBHs.

The ZnSe/GaAs heterointerfaces appear abrupt (although undulating) and coherent in HREM images of cross-sections in the [110] and [001] orientation. However, the ion milling damage to the sample and the low contrast between the layers in both orientations complicates the evaluation of the heterointerfaces. Based upon the preliminary results of the HREM imaging, it is possible for both sides of the GaAs central layer to be abrupt enough for a charge imbalance to occur.

For the ZnSe-on-GaAs heterointerface, a sheet of charge has been measured in a ZnSe/GaAs single heterostructure by a combination of photoreflectance (PR) and electroreflectance (ER) measurements. The electric field caused by the sheet of charge is directed from the GaAs to the ZnSe. However, if the line of contrast at the GaAs-on-ZnSe heterointerface is due to carbon contamination of the ZnSe, it would have different electrical properties than the ZnSe-on-GaAs heterointerface.

Photoreflectance excitation (PRE) measurements were made of a series of ZnSe/GaAs 100 nm DBHs which had been annealed at 400°C, 500°C, and 600°C for 10 minutes each. The PRE measurement in part probes the electric fields present in the heterostructure. The probe energy of these measurements was held at the E_1 feature (430 nm) for GaAs in order to study the electric fields in the GaAs material. As the anneal temperature increases, the electric field strength decreases. The anneal is expected to energize diffusion across the heterointerfaces. Based upon the PRE measurement, at least one heterointerface in the ZnSe/GaAs DBH does possess a sheet of charge.

9.2.4 Carrier lifetime

While PL has been measured from InGaP/GaAs multiple QWs with the GaAs grown at 350°C and As_2 :Ga ratio of 1:1, the combined properties

of the nucleation layer and the GaAs QW could be sufficient to decrease the PL signal from the GaAs QW below the detection limit.

The carrier lifetime in the ZnSe/GaAs QWs and DBHs has been measured by D. Dougherty using a pump-probe technique. Although the data has not been thoroughly analyzed, a first interpretation indicates that the carrier lifetime exceeds 200 picosecond (the measurement limit). However, the lineshape of the data from the pump-probe measurement is similar to that previously seen in carrier lifetime measurements of low-temperature GaAs. Further analysis is required of these results.

The research by Missous, *et al* [31, 32], together with PL results of GaAs QWs with InGaP barriers, shows that lowering the GaAs growth temperature reduces the carrier lifetime and the PL efficiency. The GaAs nucleation layer is, as a result, believed to inhibit the generation of PL from the GaAs QW material close to the GaAs-on-ZnSe heterointerface.

9.2.5 Type II energy band alignment

The unique growth conditions under which the GaAs layer is nucleated on the ZnSe could form a similar type II interface.

The energy band alignment across the ZnSe/GaAs QWs and DBHs is not probed by the microstructural analysis. However, optical characterization by Dougherty has measured a type I energy band alignment for a ZnSe/GaAs single heterostructure. The energy band alignment of the GaAs-on-ZnSe heterointerface has yet to be measured.

9.3 The feasibility of detecting an optical signal

The feasibility of detecting an optical signal from a GaAs QW with ZnSe barriers is limited by the optimal epitaxial growth regime for both materials. If the measurement of the energy band alignment of the ZnSe/GaAs QW were to show evidence of both electron and hole confinement in the GaAs layer, the optical performance of the QW would be governed by the quality of each layer and the heterointerfaces. To some degree, the epitaxial growth of the ZnSe and the GaAs in the heterostructure can be optimized. Prior

to this study, an abrupt heterointerface was considered to be high quality. However, it is not clear what optimization means in this case. The properties of the heterointerfaces when abrupt possess a charge density and corresponding electric field that affects the optical signal from the QW. To form a heterointerface with a transitional width from one material to the next is expected to remove the interfacial charge, but has an unknown energy band alignment.

9.4 Suggestions for future work

There are several directions that can be taken in investigating ZnSe/GaAs QWs and DBHs. Before proceeding with the experimental research, it would be useful to develop a theoretical model for the optimal heterointerface for either side of the GaAs QW, and a set of experiments should be established to test this model. The characteristics in relationship to the formation of the GaAs-on-ZnSe heterointerface should also be studied experimentally. The pursuit of optical emission from the GaAs layer in a ZnSe/GaAs QW can be continued via further research on the fabrication and optical characterization of the heterostructures. Five aspects of the fabrication that can be manipulated with the potential to improve the ZnSe/GaAs QWs and DBHs are listed below.

- **Grow the entire structure in one system reactor**
  - Pro: reduce impurity contamination during transfers between growth reactors
  - Con: increased possibility of cross-contamination of the constituent species
- **Optimize the ZnSe growth**
  - Pro: reduce interfacial defect density
- **Investigate alternative substrates**
  - Pro: eliminate confusion in the analysis of the GaAs QW layer due caused by the presence of the GaAs substrate
  - Con: high quality, large area substrates of alternate materials are not readily available

- **Growth interruption and annealing of GaAs QW layer**
  - Pro: can achieve a smoother GaAs surface
  - Con: increased potential for impurity incorporation
- **Grow multiple QWs**
  - Pro: increase the PL intensity contribution from the GaAs QW layers
  - Con: relaxation of the ZnSe, longer growth time, more *in situ* transfers

A plan for evaluating the ZnSe/GaAs QWs and DBHs for the improvements in performance from each of these would be required. Although, microstructural analysis can evaluate the impact of each of the listed experiments, cross-sectional TEM and HREM analysis would be a more powerful technique if the sample preparation could be improved. This can be done by using either a low energy argon gun during the ion milling process or a different ion source, such as iodine.

Before pursuing the optimization of the fabrication of the ZnSe/GaAs QWs and DBHs, the work begun by Dougherty should be completed. A study of the GaAs-on-ZnSe heterointerface to assess the carrier lifetime, the energy-band alignment, and the interfacial charge density would provide the necessary information to ensure that a PL signal from the GaAs QW is possible.

10. Appendix 1. Preparation of TEM samples

A method for preparing the cross-sectional TEM samples used in this presented here. Although many of the sub-steps could be used for other material systems, some modifications might be necessary to avoid damaging the material during preparation.

There are four steps in the preparation. First, two pieces of the sample are epoxied face-to-face. Next, a piece of substrate material, such as GaAs, is epoxied to the backside of each sample. This epoxied stack of material constitutes the sample sandwich. The second step requires thinning and polishing the sample sandwich to a maximum thickness of 60 μm. Third, the thin sample is glued to a copper support grid. Finally, the sample on the copper grid is thinned with an ion mill until there is a hole in the center.

10.1.1 Step 1: The sample sandwich

1. Clean and cleave two pieces of the sample to be analyzed with dimensions: 3 mm x 1.5 mm.
2. Apply room temperature Mbond 610 epoxy resin to the surface of each sample piece.
3. Press the two sample pieces face-to-face.
4. Allow the epoxy to cure at 200°C for 90 minutes* .
5. Clean and cleave two piece of GaAs (or whatever substrate material was used in the sample to be analyzed) with dimensions: 3 mm x 1.5 mm.
6. Apply room temperature Mbond 610 epoxy resin to the backside of each sample piece.
7. Press the top surface of one piece of the GaAs substrate to each back side.
8. Allow the epoxy to cure at 200°C for 90 minutes.

---

* If the samples have indium on the backside, at this point, polish the indium off using 30 μm grit polishing paper. Rinse the sample sandwich afterwards in water to remove any residue.

10.1.2 Step 2: thinning and polishing

Mount the sample sandwich to a polishing chuck with crystal bond, or some mounting compound that can be removed with acetone. The polishing chuck in this instance is a cylindrical steel ingot roughly 1 cm in diameter. The ingot fits into a larger copper cylinder. The copper cylinder fits into a top-hat shaped copper polishing stand, with a base that is roughly 7 cm in diameter. The polishing stand is used to keep the sample parallel to the polishing surface.

Most of the TEM samples prepared in this study were polished on a series 6 inch diameter plastic films with aluminum oxide grit of different sizes on one side. The discs were pressed onto a damp glass plate to hold them flat. Water was sprayed on the polishing surface while the polishing chuck was manually moved around the disc. The sample was polished on one side with successively smaller grit sizes until the surface was both flat and mirror smooth. Then, the sample was removed from and turned over on the steel ingot by heating the ingot on a hot plate. The same polishing process was repeated, but the end result was to thin the sample to 60 μms or less. The sample thickness could be determined with a calibrated optical microscope. In general, the sample is pretty close to 60 μms thick if the crystal bond used to mount the sample is level with the sample surface.

step	grit size
1	30 μm
2	15 μm
3	5 μm
4	3 μm
5	0.3 μm

Table A1-1 Order of polishing and grit size used for cross-sectional TEM preparation.

In practice, the damage caused by a certain grit size is said to damage up to a depth of 3x the grit size into the sample. Therefore, the second side of to be polished should be polished to a thickness of at least 100 micron with the 30 micron grit, 45 micron with the 15 micron grit, etc.

10.1.3 Step 3: Mount to a grid

The thin sample sandwich is now mounted to a copper grid. Single 1 μm diameter aperture grids of roughly 50 μm thick were used in this study. The sample sandwich is still mounted to the steel ingot by crystal bond. It is important to have sharp tweezers and a microscope to correctly mount the sample.

1. Put a small amount of Hardman's epoxy resin on the copper grid surface and spread thin.
2. Place the grid with the shiny side to the sample surface onto the sample centering the epoxy line across the aperture. Take care not to get epoxy on the sample surface resting over the hole.
3. Allow the epoxy to cure for about 15 minutes at room temperature.
4. Heat the steel ingot on a hot plate until the crystal bond is watery.
5. Slide the copper grid off the chuck.
6. Soak the copper grid in acetone to remove any residual crystal bond.

10.1.4 Step 4: final thinning of the sample in the ion mill

The final step in cross-sectional TEM sample preparation is to thin the center of the sample sandwich until a hole is visible. An argon ion mill is used to sputter away the material in a controlled fashion. Redeposition of the sputtered material is avoided by maintaining a vacuum in the milling chamber of roughly 10^{-6} Torr. Uniform ion milling of the sample is achieved by rotating the sample.

The ion mill can heat the sample to 300°C. For ZnSe and In-containing materials, this temperature is high enough to actually destroy the material. Hence, care must be taken to allow the sample to cool the sample in liquid nitrogen during the ion milling process.

The penetration depth of the ion mill is a function of the milling angle, the angle of the ion guns to the sample surface, and power. In a fashion similar to the polishing and thinning step for TEM sample preparation, the power of the ion mill is reduced during the course

of the milling to remove and avoid damage to the sample. The milling angle for the samples in this study was held constant at 12°, which is pretty much the lowest angle the mill can be used at, and reduces the penetration depth of the argon ions.

When the ion guns on the ion mill are new (< 10 hours used), the milling rate at a voltage/current setting of 6 kV/1 mA is around 15 microns/hour. At a setting of 4 kV/0.25 mA, the milling rate is around 4 microns/hour. As the guns are used longer, the argon beams will tend to spread and the milling rate will subsequently decrease. The guns are changed roughly every 100 hours.

1. Mount the grid and sample onto a stage for the ion mill (Note: there are several different stages. For cold milling, use the stage with the rectangular copper legs.).
2. Evacuate the milling chamber.
3. Lower the stage into liquid nitrogen. Allow the sample to cool for 20 minutes.
4. Mill for 2.5 hours using the preset current and voltage values are 1.0 mA and 6 kV.
5. If the sample is thinning, a slight indentation in the sample within the grid aperture will be visible. If this is not visible, continue to ion mill at 1.0 mA/6kV for 30 minutes increments until the indentation can be seen.
6. Decrease the milling parameters: 4 kV, 0.25 mA. Ion mill for 2 hours, checking every 30 minutes until a hole is visible.

The sample with a hole in the center is ready for TEM analysis if the hole intersects the center epoxy line where the material of interest is. If the sample does not seem to thinning at the higher ion milling power, there might be epoxy on the sample surface, or the cover of the sample holder for the ion mill might not be screwed down tightly enough. In general, the above procedure will produce cross-sectional TEM samples with regions thin enough for phase-contrast imaging of the atomic lattice (no thicker than 8 nm).

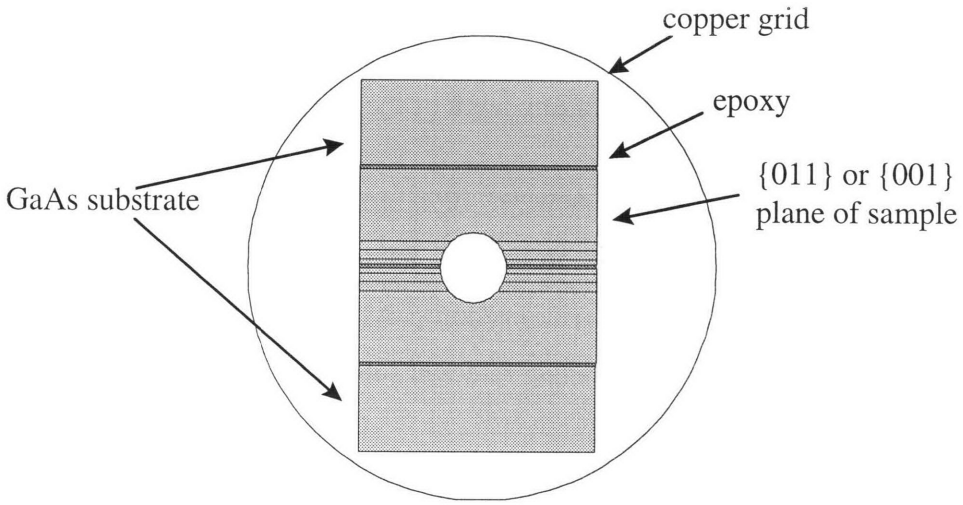

Figure A1-1. Fully prepared cross-sectional TEM sample, mounted on a single aperture copper grid.

11. Appendix 2. ZnSe substrate surface preparation

A series of ZnSe/GaAs QWs and DBHs were grown on semi-insulating ZnSe substrates manufactured by Sumitomo were used to eliminate the contribution of the GaAs substrate to the respective PL spectra. The geometry of the ZnSe substrates is either a 25 mm^2 or 100 mm^2 square cleaved along (011) planes. The substrates are single-side polished with an average polished surface roughness of 3.24 nm. In comparison, a GaAs wafer from the same manufacturer has an average surface roughness of 0.43 nm. Both the small geometry and the rough polished surface of the ZnSe substrates posed limitations on the ultimate quality of the epitaxially grown ZnSe/GaAs QWs and DBHs.

The ZnSe substrate does not have a thick native oxide which protects the surface from other impurity contamination. As a result, the ZnSe substrate shows a faint bulk RHEED reconstruction upon introduction to the growth reactor. Auger electron spectroscopy of the original substrate surface shows the presence of a O, Cl, C, Zn, and Se. In comparison, the surface of ZnSe epilayer that has been exposed to the room for several days shows the presence of O, C, Zn and Se; indicating that the Cl present in the ZnSe substrate is a remnant of the surface preparation technique followed by Sumitomo. Oxygen is roughly 5% of the surface composition of the ZnSe substrate; while, 25 % and 30% is C.

An investigation into the ZnSe surface preparation by degreasing, etching, thermal cleaning, and hydrogen plasma cleaning was done to eliminate the presence of O, C, and Cl. Degreasing was done by agitating the ZnSe substrate in a series of solvents to remove organic compounds and water from the surface. Etching was done with two different acids: bromine-methanol and hydrofluoric acid. Both hydrogen plasma cleaning and thermal cleaning were done in the growth reactor, under an ultra-high vacuum environment. The hydrogen plasma cleaning was done with a mixture of 85% H_2 and 15% Ar directed through a liquid nitrogen cooled plasma generator directed at the substrate surface. The thermal cleaning was done by heating the substrate. For each

surface preparation technique studied, Auger electron spectroscopy (AES) measurements were made of the ZnSe substrate surface to compare the surface composition. The ZnSe substrate surface was also monitored by RHEED to assess the surface roughness.

The AES results from a ZnSe substrate prepared by hydrogen plasma cleaning (H-cleaned), thermal cleaning, and degreasing are shown in Figure A2-1. The peak features in the graphs indicate the presence of a chemical element. Noted on the plots are N, O, C, Cl, Zn, and Se. The ZnSe substrate that has been hydrogen plasma cleaned has the lowest percentage of N, O, C and Cl of the three methods shown. However, all three surface preparation methods do not eliminate the C on the ZnSe surface.

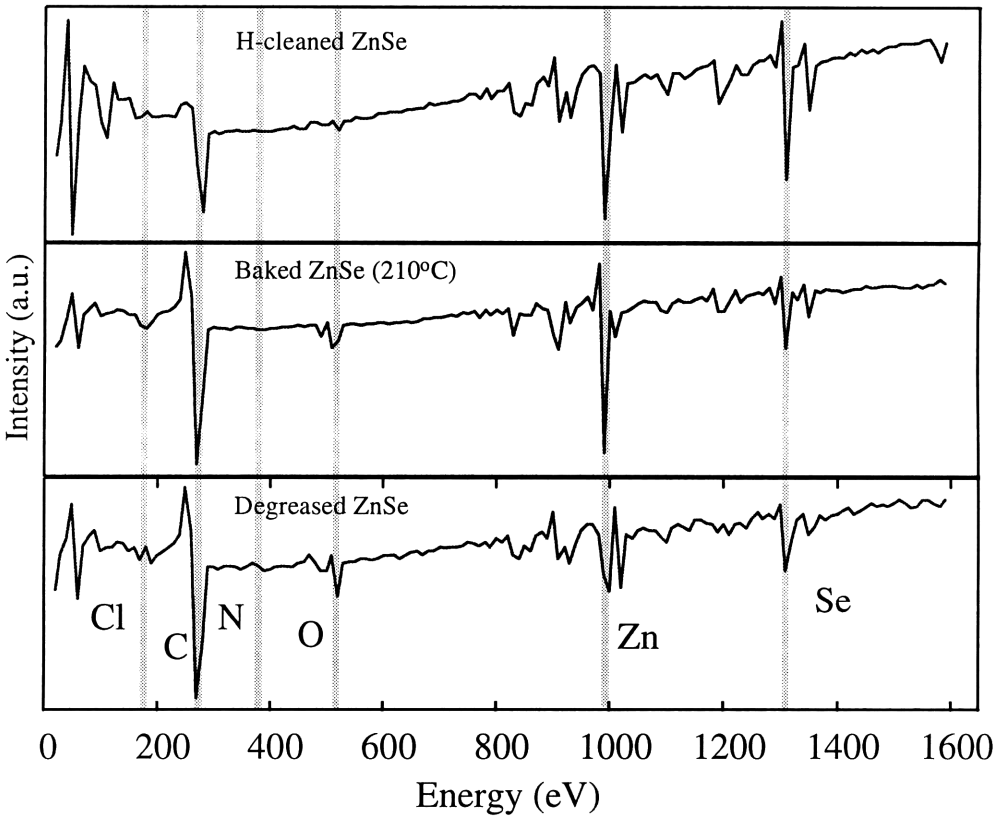

Figure A2-1. Auger electron spectra of ZnSe substrate surfaces as a function of the surface preparation: hydrogen plasma cleaned, thermally cleaned, and degreased.

The ZnSe substrate surface composition is compared as a function of the surface preparation in the bar charts in Figure A2-2 showing the fractional composition of C, O,

and Cl for a substrate: pre-surface preparation, after thermal cleaning, after degreasing, after hydrogen plasma cleaning. In all cases, the hydrogen plasma clean is the most successful at removing surface contamination. However, each method does reduce the amount of O and Cl at the surface.

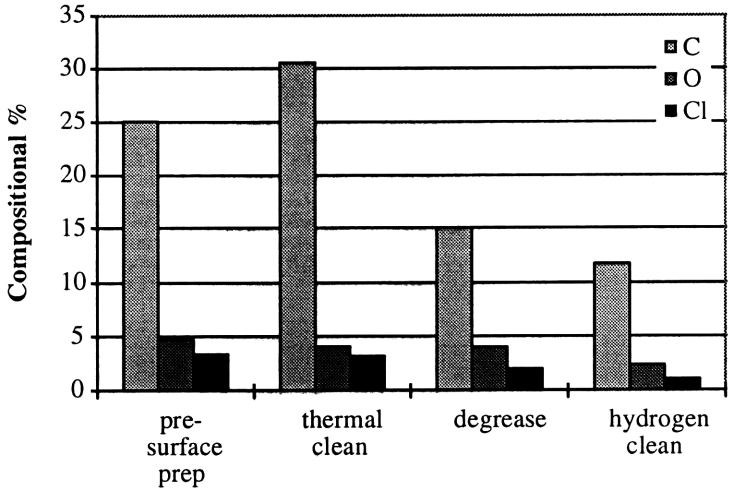

Figure A2-2. Fractional composition of C, Cl, and O present on the ZnSe surface as a function of the surface preparation method as measured by Auger electron spectroscopy.

Etching the ZnSe surface by bromine-methanol or hydrofluoric acid resulted in a surface that was too insulating to be analyzed by AES. The RHEED surface pattern of the ZnSe substrates prepared by etching was similar to the ZnSe substrate prepared by the other methods, showing a streaky bulk reconstruction.

The final ZnSe surface preparation method developed has three steps: degreasing, thermal cleaning, and hydrogen plasma cleaning. The sample was first degreased, then loaded into the growth reactor. Next, the substrate was heated to 300°C for 15 minutes. A hydrogen plasma was directed at the heated sample surface for 20 minutes. Within 10 minutes of the hydrogen plasma clean, a (2x1) surface RHEED reconstruction was visible (see Figure). In spite of the evidence of a reconstructed ZnSe surface, a high density of defects are nucleated at the homojunction between the ZnSe substrate and the ZnSe epilayer.

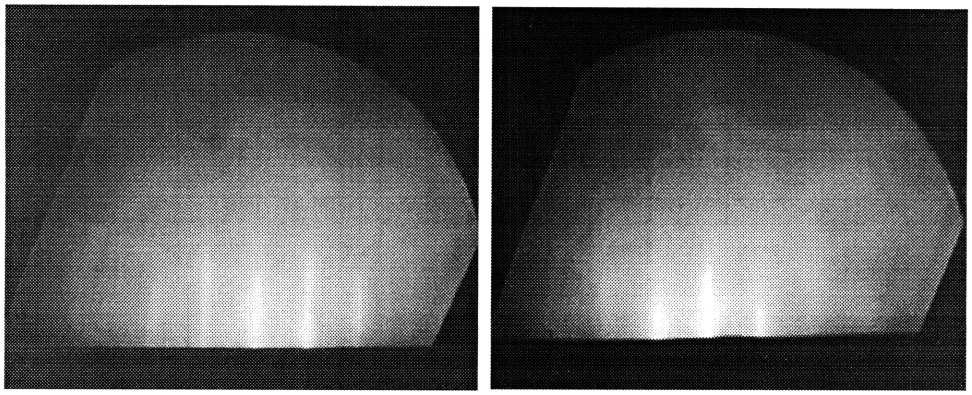

[011] [$0\bar{1}1$]

Figure A2-3. RHEED surface pattern of ZnSe substrate that has been thermally cleaned at 300°C and hydrogen plasma cleaned for 15 minutes, showing a (2x1) surface reconstruction.

The cross-sectional TEM images of the ZnSe/GaAs QWs and DBHs that were grown on ZnSe substrates show a high defect density at the ZnSe epilayer-ZnSe substrate homojunction, regardless of the surface preparation technique. When a (2x1) surface reconstruction was evident after the ZnSe substrate surface preparation, the homojunction shows the lowest defect density as indicated through qualitative cross-sectional TEM analysis. However, the defect density in this instance is still high enough to adversely affect the optical properties of the ZnSe/GaAs QWs and DBHs. As a result, the majority of these heterostructures were grown on the higher quality GaAs substrates.

Bibliography

1. Dougherty, D.J., *Femtosecond optical nonlinearities in ZnSe and characterization of ZnSe/GaAs heterostructures*, PhD. 1997, MIT: Cambridge.
2. Kumagai, M., T. Takagahara, *Excitonic and nonlinear-optical properties of dielectric quantum-well structures.* Physical Review B, 1989.**40**(18): p. 12,359.
3. Raichev, O.C., *Theory of hole conductivity in semiconductor superlattices.* Physical Review B, 1994.**50**(8): p. 5382.
4. Weisbuch, C., R. Dingle, A. C. Gossard, W. Wiegman,*Optical characterization of interface disorder in GaAs-Ga1-xAlxAs multi-quantum well structures.* Solid State Communications, 1981. **38**: p. 709.
5. Deveaud, B., J. Y. Emery, A. Chomette, B. Lambert, M. Baude, *Single monolayer well size fluctuations in the luminescence of GaAs-AlGaAs superlattices.* Superlattices and Microstructures, 1985. **1**(3): p. 205.
6. Tamargo, M.C., J.L. de Miguel, D.M. Hwang, H.H. Farrell, *Structural characterization of GaAs/ZnSe interfaces.* Journal of Vacuum Science and Technology B, 1988. **6**(2): p. 784-787.
7. Tamargo, M.C., J.L. de Miguel, F.S. Turco, B.J. Skromme, M.H. Meynadier, R.E. Nahory, D.M. Hwang, H.H. Farrell, *Multiple chamber molecular beam epitaxy growth system: growth of GaAs/ZnSe heterostructures.* Proceedings of the SPIE, Los Angeles, 1988.
8. Tamargo, M.C., J.L. de Miguel, F.S. Turco, B.J. Skromme, D.M. Hwang, R.E. Najory, H.H. Farrell. *Growth of II-VI/III-V mixed heterostructures.* in *Molecular Beam Epitaxy 1988*. 1988. Sapporo, Japan.
9. Gunshor, R.L., L.A. Kolodziejski, M.R. Melloch, N. Otsuka, A.V. Nurmiko.*II-VI/III-V heterointerfaces: epilayer-on-epilayer structures.* in *Molecular Beam Epitaxy 1988*. 1988. Sapporo, Japan.
10. Kobayashi, N., *ZnSe/GaAs heterointerface stabilization by high-temperature Se treatment of GaAs surface.* Japanese Journal of Applied Physics, 1988.**27**(9): p. L1597-L1599.
11. Qiu, J., D.R. Menke, M. Kobayashi, R.L. Gunshor, D. Li, Y. Nakamura, N. Otsuka, *Characterization of Ga_2Se_3 at ZnSe/GaAs heterovalent interface.* Applied Physics Letters, 1991.**58**(24): p. 2788-2790.
12. Qiu, J., Q.-D. Qian, R.L. Gunshor, M. Kobayashi, D.R. Menke, D. Li, N. Otsuka, *Influence of GaAs surface stoichiometry on the interface state density of as-grown epitaxial ZnSe/epitaxial GaAs heterostructures.* Applied Physics Letters, 1990. **56**(13): p. 1272-1274.
13. Qian, Q.-D., J. Qiu, M. Kobayashi, R.L. Gunshor, L.A. Kolodziejski, M.R. Melloch, J.A. Cooper, J.M. Gonsalves, N. Otsuka, *Low interface state density at*

pseudomorphic ZnSe/epitaxial GaAs interface. Materials Research Society Symposium Proceedings, 1989. **145**: p. 423-428.

14. Chikyow, T., Nobuyuki Koguchi, *MBE growth method for pyramid-shaped GaAs micro crystals on ZnSe(001) surface using Ga droplets.* Japanese Journal of Applied Physics, 1990. **29**: p. L2093-L2095.

15. Chikyow, T., Satoshi Takahashi, Nobuyuki Koguchi, *Surface structure dependence of GaAs microcrystals size grown by As-incorporation into Ga droplets.* Surface Science, 1992. **267**: p. 241-244.

16. Bringans, R.D., D.K. Biegelsen, L.-E. Swartz, F.A. Ponce, J.C. Tramontana, *Use of ZnSe as an interlayer for GaAs growth on Si.* Applied Physics Letters, 1992. **61**(2): p. 195-197.

17. Romano, L.T., Bringans, R.D., Knall, J., Biegelsen, D.K., Garcias A., Northrup, J.E., O'Keefe, M.A., *Atomic rearrangement at the interface of annealed ZnSe films grown on vicinal Si(001) substrates.* Physical Review B, 1994. **50**(7): p. 4416-4423.

18. Ramesh, S., N. Kobayashi, Y. Horikoshi, *Migration-enhanced epitaxy growth and characterization of high quality ZnSe/GaAs superlattices.* Applied Physics Letters, 1990. **57**(11): p. 1102.

19. Ramesh, S., N. Kobayashi, Y. Horikoshi, *Study of high-quality ZnSe/GaAs/ZnSe single quantum well and ZnSe/GaAs heterostructures.* Journal of Crystal Growth, 1991. **115**: p. 333-337.

20. Zhang, S., N. Kobayashi, *Photoluminescence and structure properties of GaAs/ZnSe quantum wells.* Applied Physics Letters, 1992. **60**(7): p. 883.

21. Zhang, S., N. Kobayashi, *X-ray diffraction study of annealed ZnSe/GaAs superlattices.* Applied Physics Letters, 1992. **60**(20): p. 2499.

22. Kobayashi, N., Y. Horikoshi, *Growth of ZnSe/GaAs Superlattices by Migration-Enhanced Epitaxy.* Japanese Journal of Applied Physics, 1990. **28**(2): p. L236.

23. Fujita, S., Prakash A. Murawala, Seiji Maruo, Osamu Tsuji, Shizuo Fujita, *Organometallic vapor-phase epitaxial growth and characterization of GaAs/Zn(S,Se) multilayered structures.* Japanese Journal of Applied Physics, 1991. **30**(1B): p. 78-81.

24. Funato, M., M. Ishii, P. A. Murawala, *Metalorganic vapor phase epitaxial growth and characterization of ZnSe-GaAs multilayered structures.* Journal of Crystal Growth, 1992. **117**: p. 543.

25. Funato, M., S. Fujita, S. Fujita, *Structural analysis of ZnSe-GaAs quantum wells.* Japanese Journal of Applied Physics, 1993. **32**(8): p. 3396.

26. Liu, X., A. Prasad, W.M. Chen, A. Kurpiewski, A. Stoschek, Z. Liliental-Weber, E.R. Weber, *Mechanism responsible for the semi-insulating properties of low-temperature-grown GaAs.* Applied Physics Letters, 1994. **65**(23): p. 3002- 3004.

27. Luo, J.K., H. Thomas, D.V. Morgan, D. Westwood, *Transport properties of GaAs layers grown by molecular beam epitaxy at low temperature and the effects of annealing.* Journal of Applied Physics, 1996.**79**(7): p. 3622- 3629.

28. Matyl, R.J.M.R.M.J.M.W., *High resolution x-ray diffraction analysis of annealed low-temperature gallium arsenide.* Applied Physics Letters, 1992.**60**(21): p. 2642-2644.

29. Melloch, M.R., N. Otsuka, J.M. Woodall, A.C. Warren, J.L. Freeouf, *Formation of arsenic precipitates in GaAs buffer layers grown by molecular beam epitaxy at low substrate temperatures.* Applied Physics Letters, 1990.**57**(15): p. 1531- 1533.

30. Mirin, R.P., J.P. Ibbetson, U.K. Mishra, A.C. Gossard, *Low temperature limits to molecular beam epitaxy of GaAs.* Applied Physics Letters, 1994.**65**(18): p. 2335-2337.

31. Missous, M., S. O'Hagan,*Nonstoichiometry and dopants related phenomena in low temperature GaAs grown by molecular beam epitaxy.* Journal of Applied Physics, 1994.**75**(7): p. 3396- 3401.

32. Missous, M., *Stoichiometric low-temperature GaAs and AlGaAs: A reflection high-energy electron-diffraction study.* Journal of Applied Physics, 1995.**78**(7): p. 4467- 4471.

33. O'Hagan, S., M. Missous,*Effect of As4/Ga flux ratio on electrical and optical properties of low temperature GaAs grown by molecular beam epitaxy.* Journal of Applied Physics, 1994.**75**(12): p. 7835- 7841.

34. O'Hagan, S.P., M. Missous.*Dopant and As4/Ga flux ratio influence on the electrical and structural properties of LT GaAs.* in *Compound Semiconductor Symposium.* 1994. San Francisco, CA.

35. Smith, F.W., A.R. Calawa, C-L. Chen, M.J. Manfra, L.J. Mahoney,*New MBE buffer layer used to eliminate backgating in GaAs MESFET's.* IEEE Electron Device Letters, 1988. **9**(2): p. 77- 80.

36. Warren, A.C., J.M. Woodall, J.L. Freeouf, D. Grischkowsky, M.R. Melloch, N. Otsuka, *Arsenic precipitates and the semi-insulating properties of GaAs buffer layers grown by low-temperature molecular beam epitaxy.* Applied Physics Letters, 1990. **57**(13): p. 1331- 1333.

37. Yu, K.M., Z. Liliental-Weber,*Lattice site locations of excess arsenic atoms in gallium arsenide grown by low-temperature molecular beam epitaxy.* Applied Physics Letters, 1991. **59**(25): p. 3267- 3269.

38. Viturro, E.R., M. R. Melloch, J.M. Woodall, *Optical emission properties of semi-insulating GaAs grown at low temperatures by molecular beam epitaxy.* Applied Physics Letters, 1992. **60**(24): p. 3007 - 3009.

39. Sinha, S., B.M. Arora, S. Subramanian, *Photoreflectance and photoluminescence spectroscopy of low-temperature GaAs grown by molecular-beam epitaxy.* Journal of Applied Physics, 1996.**79**(1): p. 427- 432.

40. Knox, W.H., G.E. Doran, M. Asom, G. Livescu, R. Leibenguth, S.N.G. Chu, *Low-temperature-grown GaAs quantum wells: Femtosecond nonlinear optical and parallel-field transport studies.* Applied Physics Letters, 1991. **59**(12): p. 1491-1493.

41. Gupta, S., M.Y. Frankel, J.A. Valdmanis, J.F. Whitaker, G.A. Mourou, F.W. Smith, A.R. Calawa, *Subpicosecond carrier lifetime in GaAs grown by molecular beam epitaxy at low temperatures.* Applied Physics Letters, 1991. **59**(25): p. 3276- 3278.

42. Kaminska, M.E.R.W., Z. Liliental-Weber, R. Leon, Z.U. Rek,*Stoichiometry-related defects in GaAs grown by molecular-beam epitaxy at low temperatures.* Journal of Vacuum Science Technology B, 1989. **B 7**(4): p. 710 - 713.

43. Kaminska, M., Z. Liliental-Weber, E.R. Weber, T. George, J.B. Kortright, F.W. Smith, B-Y. Tsaur, A.R. Calawa, *Structural properties of As-rich GaAs grown by molecular beam epitaxy at low temperatures.* Applied Physics Letters, 1989. **54**(19): p. 1880 - 1883.

44. Melloch, M.R., Annual Review of Material Science, 1995.**25**: p. 547-600.

45. Harrison, W.A., E. A. Kraut, J. R. Waldrop, R. W. Grant, *Polar Heterojunction Interfaces.* Physical Review B, 1978. **18**(8): p. 4402.

46. Harrison, W.A., *Theory of band line-ups.* Journal of Vacuum Science and Technology B, 1985. **3**(4): p. 1231-1238.

47. Van Vechten, J.A., *Ionization potentials, electron affinities, and band offsets.* Journal of Vacuum Science and Technology B, 1985.**3**(4): p. 1240-1244.

48. Van de Wall, C.G., Richard M. Martin, *Theoretical calculations of semiconductor heterojunction discontinuities.* Journal of Vacuum Science and Technology B, 1986. **4**(4): p. 1055-1059.

49. Ruan, Y.-C., W.Y. Ching, *An effective dipole theory for band lineups in semiconductor heterojunctions.* Journal of Applied Physics, 1987.**62**(7): p. 2885-2897.

50. Murayama, M.T.N., *Chemical trend of band offsets at wurtzite/zinc-blende heterocrystalline semiconductor interfaces.* Physical Review B, 1994. **49**(7): p. 4710-4724.

51. Duggan, G., *A critical review of heterojunction band offsets.* Journal of Vacuum Science and Technology B, 1985. **3**(4): p. 1224-1230.

52. Nicolini, R., L. Vanzetti, G. Mula, G. Bratina, L. Sorba, A. Mura, J.E. Angelo, W. W. Gerberich, A. Franciosi,*Local interface composition and band offset tuning in ZnSe-GaAs(001) heterostructures.* Physical Review Letters, 1994. **72**: p. 294.

53. Bonanni, A., L. Vanzetti, L. Sorba, A. Franciosi, M. Lomascolo, P. Prete, R. Cingolani, *Optimization of interface parameters and bulk properties in ZnSe-GaAs heterostructures.* Applied Physics Letters, 1995. **66**(9): p. 1092-1094.

54. Bratina, G., L. Vanzetti, R. Nicolini, L. Sorba, X. Yu, A. Franciosi, G. Mula, A. Mura, *Microscopic control of ZnSe-GaAs heterojunction band offsets.* Physica B, 1993. **185**: p. 557-565.

55. Bratina, G., R. Nicolini, L. Sorba, L. Vanzetti, Guido Mula, X. Yu, A. Franciosi, *ZnSe-GaAs heterojunction parameters.* Journal of Crystal Growth, 1993. **127**: p. 387-391.

56. Bratina, G., L. Vanzetti, L. Sorba, G. Biasiol, A. Franciosi, M. Peressi, S. Baroni, *Lack of band-offset transitivity for semiconductor heterojunctions with polar orientation: ZnSe-Ge(001), Ge-GaAs(001), and ZnSe-GaAs(001).* Physical Review B, 1994. **50**(16): p. 11,723.

57. Franciosi, A., L. Vanzetti, L. Sorba, A. Bonanni, R. Cingolani, M. Lomascolo, D. Greco, *Band offset engineering of II-VI/III-V heterointerfaces.* Materials Science Forum, 1995. **182-184**: p. 17-22.

58. Ota, K., Hiroyuki Yaguchi, Kentaro Onabe, Ryoichi Ito, Yasuhiro Shiraki,*Effect of growth interruption on the interface flatness in metalorganic vapor phase epitaxy-grown GaAs/GaAsP heterostructures.* Journal of Crystal Growth, 1994. **145**: p. 819-823.

59. Geurts, J., J. Finders, J. Woitok, D Gnoth, A. Kohl, K. Heime, *Chracterization of the interface abruptness of $In_{0.53}Ga_{0.47}As/InP$ multi quantum wells by Raman spectroscopy, x-ray diffractometry and photoluminescence.* Journal of Crystal Growth, 1994. **145**: p. 813-818.

60. Krispin, P., R. Hey, H. Kostial, *Intrinsic origin and composition dependence of deep-level defects at the inverted $GaAs/Al_xGa_{1-x}As$ interface grown by molecular-beam epitaxy.* Journal of Applied Physics, 1995.**77**(11): p. 5773-5781.

61. Hayakawa, T., T. Suyama, K. Takahashi, M. Kondo, S. Yamamoto, S. Yang, T. Hijikata, *Interface disorder in GaAs/AlGaAs quantum wells grown by MBE.* Surface Science, 1986. **174**: p. 76-81.

62. Juang, F.-Y., P. K. Bhattacharya, J. Singh, *Determination of the microscopic quality of InGaAs-InAlAs interfaces by photoluminescence- Role of interrupted molecular beam epitaxial growth.* Applied Physics Letters, 1986. **48**(4): p. 290-292.

63. Lahiri, I., D. D. Nolte, J. C. P. Chang, J. M. Woodall, M. R. Melloch, *The role of excess arsenic in interface mixing in low-temperature-grown AlAs/GaAs superlattices.* Applied Physics Letters, 1995. **67**(9): p. 1244-1246.

64. Lew, A.Y., C. H. Yan, C. W. Tu, E. T. Yu, *Characterization of arsenide/phosphide heterostructure interfaces grown by gas-source molecular beam epitaxy.* Applied Physics Letters, 1995. **67**(7): p. 932-934.

65. Wolford, D.J., , G. D. Gilliland, T. F. Kuech, J. F. Klem, H. P. Hjalmarson, J. A. Bradley, C. F. Tsang, J. Martinsen, *Compaison of transport, recombination, and interfacial quality in molecular beam epitaxy and organometallic vapor-phase*

epitaxy GaAs/$Al_xGa_{1-x}As$ structures. Applied Physics Letters, 1994. **64**(11): p. 1416-1418.

66. Liu, W., Desheng Jiang, Kejian Luo, Yachui Zhang, Xiaoping Yang,*Broadening of the excitonic linewidth due to scattering of two-dimensional free carriers.* Applied Physics Letters, 1995. **67**(5): p. 679-681.

67. de Miguel, J.L., S.M. Shibli, M.C. Tamargo, B.J. Skromme,*Planar doping with gallium of molecular beam epitaxial ZnSe.* Applied Physics Letters, 1988. **53**(21): p. 2065-2067.

68. Miyajima, T., Katshiro Akimoto, Yoshifumi Mori,*Deep levels in Ga-doped ZnSe grown by molecular-beam epitaxy.* Journal of Applied Physics, 1990. **67**(3): p. 1389-1392.

69. Niina, T., Tetsuo Minato, Kiyoshi Yoneda,*Ga-doped ZnSe grown by molecular beam epitaxy for blue light emitting diodes.* Japanese Journal of Applied Physics, 1982. **21**(6): p. L387-L389.

70. Wood, C.E.C., *'Surface exchange' doping of MBE GaAs from S and Se 'captive sources'.* Applied Physics Letters, 1978. **33**(8): p. 770-772.

71. Tu, D.-W., Kahn, A., *ZnSe- Se-GaAs interfaces.* Journal Vacuum Science and Technology A, 1985. **3**(3): p. 922-925.

72. Lannoo, M., *Basic principles governing the surface atomic structure of zinc blende semiconductors.* Materials Science and Engineering, 1993.**B22**: p. 1-8.

73. Harbison, J., H. Farrell,*Molecular-beam epitaxial growth mechanisms on the GaAs(100) surface.* Journal of Vacuum Science Technology B, 1988. **6**(2): p. 733.

74. Farrell, H., M. C. Tamargo, S. M. Shibli,*The Structure of the ZnSe(100) c(2x2) surface.* Journal of Vacuum Science Technology B, 1990. **8**(4): p. 884.

75. Chen, W., A. Kahn, P. Soukiassian, P. S. Mangat, J. Gaines, C. Ponzoni, D. Olego, *ZnSe(100) surface: atomic configurations, composition, and surface dipole.* Physical Review B, 1994. **49**(15): p. 10,790.

76. Coronado, C.A., E. Ho, P.A. Fisher, J.L. House, K. Lu, G.S. Petrich, and L.A. Kolodziejski,*Gas Source Molecular Beam Epitaxy of ZnSe and ZnSe:N.* Journal of Electronic Materials: Special Issue on Wide Bandgap II-VI Semiconductors for Blue/Green Emitters, 1994. **23**(3): p. 269-274.

77. Fisher, P.A., J.L. House, E. Ho, C.A. Coronado, G.S. Petrich, L.A. Kolodziejski, *GSMBE Growth of ZnSe on Novel Buffer Layers.* Journal of Vacuum Science Technology, B, 1994. **B12**(2): p. 1153-1155.

78. Fisher, P.A., E. Ho, J.L. House, G.S. Petrich, L.A. Kolodziejski. *P- and N-type Doping of ZnSe Using GSMBE.* in Materials Research Society Symposium. 1994. San Francisco, CA.

79. Fisher, P.A., E. Ho, J.L. House, G.S. Petrich, L.A. Kolodziejski, J. Walker, N.M. Johnson, *P- and N-Type Doping of ZnSe: Effects of Hydrogen Incorporation.* Journal of Crystal Growth, 1995. **150**(1-4): p. 729.

80. Ho, E., C.A. Coronado, P.A. Fisher, J.L. House, K. Lu, G.S. Petrich, and L.A. Kolodziejski. *Gas Source Epitaxy of ZnSe:MOMBE and GSMBE*. in International Conference on Chemical Beam Epitaxy and Related Growth Techniques. 1993. Nara, Japan.

81. Ho, E., Fisher, P.A., J.L. House, G.S. Petrich, and L.A. Kolodziejski. *The Doping of ZnSe using Gas Source Molecular Beam Epitaxy*. in SPIE's International Symposium on Photonic Sensors and Controls for Commercial Applications. 1994. Boston, MA.

82. Ho, E., P.A. Fisher, J.L. House, G.S. Petrich, L.A. Kolodziejski, J. Walker, N.M. Johnson, *Hydrogen Passivation in Nitrogen- and Chlorine-Doped ZnSe Films Grown by Gas Source Molecular Beam Epitaxy.* Applied Physics Letters, 1995. **66**(9): p. 1062-1064.

83. Lu, K., J.L. House, P.A. Fisher, C.A. Coronado, E. Ho, G.S. Petrich, and L.A. Kolodziejski. *(In,Ga)P Buffer Layers for ZnSe-Based Visible Emitters*. in *International Conference on II-VI Semiconductors and Related Optoelectronic Materials*. 1993. Newport, RI: Journal of Crystal Growth.

84. Lu, K., J.L. House, P.A. Fisher, C.A. Coronado, E. Ho, G.S. Petrich, L.A. Kolodziejski, G.C. Hua, and N. Otsuka,. *GSMBE Growth of ZnSe on (In,Ga)P*. in Materials Research Society Symposium. 1994. San Francisco, CA.

85. He, X., R. Manijeh, *Optical investigations of GaAs-GaInP quantum wells grown on the GaAs, InP, and Si substrates.* Applied Physics Letters, 1992. **61**(14): p. 1703.

86. Atique, N., E. S. Harmon, J. C. P. Chang, J. M. Woodall, M. R. Melloch, N. Otsuka, *Electrical and structural properties of Be- and Si- doped low-temperature grown GaAs.* Journal of Applied Physics, 1995.**77**(4): p. 1471.

87. Mirin, R.P., J. P. Ibbetson, U. K. Mishra, A. C. Gossard, *Low temperature limits to molecular beam epitaxy of GaAs.* Applied Physics Letters, 1994. **65**(18): p. 2335.

88. Missous, M., S. O'Hagen, *Nonstoichiometry and dopants related phenomena in low temperature GaAs grown by molecular beam epitaxy.* Journal of Applied Physics, 75(7), pp. 3396, 1994. **75**(7): p. 3396.

89. Gupta, S., M. Y. Frankel, J. A. Valdamanis, J. F. Whitaker, G. A. Mourou, F. W. Smith, A. R. Calawa, *Subpicosecond carrier lifetime in GaAs grown by molecular beam epitaxy at low temperatures.* Applied Physics Letters, 1991. **59**(25): p. 3276.

90. Knox, W.H., G.E. Doran, M. Asom, G. Livescu, R. Leibenguth, S.N.G. Chu, *Low-temperature growth GaAs quantum wells: Femtosecond nonlinear optical and parallel-field transport studies.* Applied Physics Letters, 1991. **59**(12): p. 1491.

91. Funato, M., Shizuo Fujita, Shigeo Fujita, *Metalorganic vapor phase epitaxial growth of GaAs on ZnSe on the flow sequence of source precursors at the interface.* Journal of Crystal Growth, 1994. **145**: p. 616-621.

92. House, J.L., *Optical characterization of ZnSe by photoluminescence., Masters thesis in Electrical Engineering*. 1994, MIT: Cambridge.

93. Petrich, G., *designer of PL acquisition software*, . 1992.

94. Yao, T., Y. Okada, S. Matsui, K. Ishida, I. Fujimoto, *The effect of lattice deformation on the optical properties and lattice parameters of ZnSe grown on (100)GaAs.* Journal of Crystal Growth, 1987. **81**: p. 518-523.

95. Seifert, W., N. Carlsson, M.-E. Pistol, L. Samuelson, *Metalorganic vapour phase epitaxy grown quantum-well structures within barriers of InP and GaInP- a comparison.* Journal of Crystal Growth, 1994. **145**: p. 758-763.

96. Coronado, C.A., E. Ho. P.A. Fisher, J.L. House, K. Lu, G.S. Petrich, L.A. Kolodziejski, *Gas source molecular beam epitaxy of ZnSe and ZnSe:N.* Journal of Electronic Materials, 1994. **23**(3): p. 269-273.

97. Kassel, L., , J. W. Garland, P. M. Raccah, M. A. Haase, H. Cheng, *Effects of Zn and Ga interdiffusion on ZnSe/n+ GaAs interfaces.* Semiconductor science and technology, 1991. **6**(9A): p. A146-A151.

98. Lin, H.T., D. H. Rich, D. B. Wittry, *Cathodoluminescence study of domains, defects, and interdiffusion in ZnSe/GaAs(100).* Journal of Applied Physics, 1994. **75**(12): p. 8080.

99. Liu, Q., S. Derksen, A. Lindner, F. Scheffer, W. Prost, F.-J. Tegude, *Evidence of type-II band alignment at the ordered GaInP to GaAs heterointerface.* Journal of Applied Physics, 1995.**77**(3): p. 1154-1158.

100. Kley, A., J. Neugebauer, *Atomic and electronic structure of the GaAs/ZnSe(001) interface.* Physical Review B, 1994.**50**(12): p. 8616-8628.

101. Edington, J.W., *Electron diffraction in the electron microscope*. Practical electron microscopy in materials science. Vol. 2. 1975, East Kilbride: Philips. 122.

102. Hirsch, P.B., A. Howie, R.B. Nicholson, D.W. Pashley, M.J. Whelan, *Electron microscopy of thin crystals*. 2 ed. 1977, Malabar: Robert E. Krieger Publishing Company. 563.

103. Cowley, J., *Diffraction physics*. 2 ed. 1990, Amsterdam: Elsevier Science Publishers B.V. 430.

104. Williams, D.B., C. Barry Carter, *Transmission Electron Microscopy.* Spectrometry. Vol. 4. 1996, New York: Plenum Press.

105. Goorsky, M.S., M. Meshkinpour, D.C. Streit, T.R. Block, *Diffuse x-ray scattering from misfit dislocations at semiconductor hetero-interfaces.* Journal of Physics D: Applied Physics, 1995.**28**: p. A92-A96.

106. Sluis, P.v.d., *Determination of strain in epitaxial semiconductor structures by high-resolution x-ray diffraction.* Applied Physics A, 1994.**A 58**: p. 129-134.

107. Meshkinpour, M., M.S. Goorsky, K.M. Matney, D.C. Streit, T.R. Block, *Characterization of buried pseudomorphic InGaAs layers using high-resolution x-ray diffraction.* Journal of Applied Physics, 1994.**76**(6): p. 3362-3366.

108. *RADS dynamical simulation*, . 1992, Bede Scientific Ltd: United Kingdom.

109. Wang, V.S., Matyi, R.J., *Triple crystal x-ray diffraction analysis of chemical-mechanical polished gallium arsenide.* Journal of Applied Physics, 1992.**72**(11): p. 5158-5164.

110. Ourmazd, A., K. Ahlborn, K. Ibeh, T. Honda, *Lattice and atomic structure imaging of semiconductors by high resolution transmission electron microscopy.* Applied Physics Letters, 1985.**47**(7): p. 685-688.

111. Ourmazd, A., *Semiconductor interfaces: abruptness, smoothness, and optical properties.* Journal of Crystal Growth, 1989. **98**: p. 72-81.

112. Sinclair, R., F.A. Ponce, T. Yamashita, D.J. Smith.*High resolution electron microscopy of II-VI compound semiconductors.* in *Microscopy of semiconducting materials conference.* 1983. Oxford, England: Institute of Physics.

113. Brown, P.D., A.P.C . Jones, G.J. Russell, J. Woods, B. Cockayne, P.J. Wright. *In plane anisotropy of the defect distribution in ZnSe, ZnS and ZnSe/ZnS epilayers grown on (001) GaAs by MOCVD.* in *Microscopy of semiconducting materials conference.* 1987. Oxford, England: Institute of Physics.

114. Sant, S.B., J. Kleiman, M. Melech, R.M. Park, G.C. Weatherly, R.W. Smith, K. Rajan. *Defect characterization of MBE grown ZnSe/GaAs and ZnSe/Ge heterostructures by cross-sectional and planar transmission electron microscopy.* in *Microscopy of semiconducting materials conference.* 1987. Oxford, England: Institute of Physics.

115. Hua, G.C., D. C. Grillo, T. B. NG, C. C. Chu, J. Han, R. L. Gunshor, A. V. Nurmiko, *Study on stacking faults and microtwins in wide bandgap II-VI semiconductor heterostructures grown on GaAs.* Journal of Electronic Materials, 1996. **25**(2): p. 263.

116. Guha, S., H. Munekata, L. L. Chang, *Structural quality and the growth mode in epitaxial ZnSe/GaAs(100).* Journal of Applied Physics, 1993.**73**(5): p. 2294.

117. Chen, Y., X. Liu, E. Weber, E.D. Bourret, Z. Liliental-Weber, E. E. Haller, J. Washburn, D. J. Olego, D. R. Dorman, J. M. Gaines, N.R. Tasker, *Structures and electronic properties of misfit dislocations in ZnSe/GaAs(001) heterojunctions.* Applied Physics Letters, 1994.**65**(5): p. 549.

118. Grillo, D.C., W. Xie, M. Kobayashi, R. L. Gunshor, G. C. Hua, N. Otsuka, H. Jeon, J. Ding, A. V. Nurmiko, *MBE growth and microstructural evaluation of Zn(S,Se)-based LEDS and diode lasers.* Journal of Electronic Materials, 1993. **22**(5): p. 441.

119. Xiaoguang, H., Manijeh Razeghi, *Investigation of the heteroepitaxial interfaces in the GaInP/GaAs superlattices by high-resolution xray diffractions and dynamical simulations.* Journal of Applied Physics, 1993.**73**(7): p. 3284-3290.